

Cold Atom Interferometry in Optical Potentials

Gordon Douglas McDonald



A thesis submitted for the degree of
Doctor of Philosophy at
The Australian National University

August 2015

© Gordon Douglas McDonald 2015

Declaration

To the best of my knowledge and except where acknowledged in the customary manner, the material presented in this thesis is original and has not been submitted in whole or part for a degree in any university. Where work has been performed in collaboration with others, I have acknowledged the contributions of all authors.

Gordon Douglas McDonald

9 December 2015

Stopping by Woods on a Snowy Evening

Whose woods these are I think I know.
His house is in the village, though;
He will not see me stopping here
To watch his woods fill up with snow.

My little horse must think it queer
To stop without a farmhouse near
Between the woods and frozen lake
The darkest evening of the year.

He gives his harness bells a shake
To ask if there is some mistake.
The only other sound's the sweep
Of easy wind and downy flake.

The woods are lovely, dark, and deep,
But I have promises to keep,
And miles to go before I sleep,
And miles to go before I sleep.

Robert L. Frost (1874–1963)

Acknowledgments

There are many people who have helped guide me to this point, all of which deserve my gratitude. To my supervisor, mentor and friend Nick Robins, I offer my most heartfelt thanks. Without your tireless help and guidance none of this would have been achievable. Thank you especially for encouraging me through innumerable experimental failures on to some brilliant successes. Your puns are what drive us crazy, and your tenacious enthusiasm is what drives this group on to greatness. To my lab-mate, friend and Thai-boxing partner Carlos Kuhn, I am so glad that you decided to make the move to Australia, to be a part of our group. Your energy, resourcefulness and determination were an integral part of many of the results presented in this thesis, and the many barbecues you hosted for us all were always a wonderful experience. I wish you, Barbara and Yasmin the brightest of futures.

There are so many fellow students I have had the privilege of sharing my time here with. These are Daniel Döring, Paul Altin, Rachel Poldy, Graham Dennis, Michael Hush, John Debs, Stuart Szigeti, Shayne Bennetts, Kyle Hardman, Patrick Everitt, Hannah Keal, Thanh Nguyen, Paul Wigley, Christopher Bentley, Ethan Bardean, and Ciaron Quinlivan. I've had countless invigorating discussion about physics, life and banter with each of you, which will always be remembered fondly. For academic and thesis-related advice, help understanding physics and stimulating discourse I thank John Close, Mattias Johnsson, Craig Savage, Joe Hope, Cristina Figl and Hans Bachor. Thank you also to Seruni Freisleben for the wonderful opportunity to be a guest lecturer at the University of Indonesia.

Good friends can make the worst times into the best times, and I have had two of the best in Young Lee and Lisa Walker. You have both been there with me throughout our studies, and now as we each find our way in the world I know that our friendship will only grow. Thank you to David Shellard for introducing me to mountain-biking, writing your thesis along side me and pondering the meaning of it all. Thank you to all my friends and to the many people I have met since beginning to dance only a few years ago, you helped keep me sane and happy through everything.

My family have always provided a supportive and encouraging environment for a budding scientist. My grandparents Pam and Graham were always teaching me how to build, create and think through problems. My mother Debbie has always unconditionally supported me through life's dramas, and her partner Rob can find humour anywhere with his sharp wit. My father Doug, his wife Endah and my brothers Kevin and Alfred are my second home, of which I am proud to be a part.

Thank you all.

Abstract

This thesis describes recent advances in ultra-cold atom interferometry. A common theme in the work described here is that the experiments are conducted on a Bose-Einstein condensate in an optical waveguide. This optical potential confines the atoms against gravity in the vertical dimension, guiding them to freely propagate along one horizontal dimension. Being supported against gravity enables long expansion times of hundreds of milliseconds, which facilitates techniques such as delta-kick cooling.

There are two main advantages of using ultra-cold atoms, rather than simply cold atoms, as a source for interferometry. Firstly, the coherence of an ensemble of atoms (as measured by either coherence length or coherence time) increases with a reduction in temperature. This means that a larger signal-to-noise may be obtained for a greater perturbation to ideal conditions, such as imperfect beam alignment, vibrations, intensity fluctuations etc. Conversely, this also means that such perturbations must be better understood so as to remove their systematic shift from a measurement of a quantity of interest. The second advantage to using an ultra-cold source cloud is its small size and small momentum width, as compared with a thermal source. Their small positional width means that clouds separated by only a small amount in momenta can easily be spatially separated and separately counted without the need for (magnetic) state labelling. Their small momentum width (and thus low spatial dispersion) means that better mode-matching is possible at the end of the interferometer, and that less-imperfect beam-splitter pulses are able to be used over the whole cloud.

The beamsplitters themselves would ideally impart a large momentum splitting between the interfering states as the signal of the interferometer is proportional to this splitting. The effective use of such a large momentum splitting, however, requires both an even narrower momentum width source and a system free of vibrations to at least a certain level. Otherwise such confounding factors can prevent any useful signal from being measured in such a device. Three such techniques were investigated in this thesis: reflection from a repulsive light potential barrier, Bragg transitions from an optical lattice (which are effectively bouncing atoms off a moving grating), and Bloch-acceleration by loading the atoms into such an optical lattice and then accelerating the combined system. It is found that a combination of both Bragg and Bloch provides the most promising route to truly large momentum transfer in a system which is sensitive only to acceleration. Lastly, large-momentum transfer techniques

can be used to effectively increase the way in which the output signal scales with time, creating interferometers which generate the same sensitivity faster (increasing the bandwidth of a sensor), or generate a much better sensitivity in the same time.

The atom chosen for use in such a system depends largely upon what is easy to condense in a given lab, but it also depends upon which knobs one would like to be able to play with. A BEC of Rubidium-87 is comparatively easy to produce thanks to favourable collisional properties and the availability of diode lasers at the correct wavelength. However if one would like more control over the properties of the condensed cloud, including its collisional self-interaction strength, one must move to a different species. Conveniently also present in natural-abundance Rubidium sources, the collisional properties of Rubidium-85 can be modified by applying an external magnetic field, at an easy-to-experimentally-reach value of between 150-170G. Inconveniently, it is difficult (although not impossible) to condense by itself, so a sympathetic cooling technique in which ^{87}Rb is used as an expendable coolant to acquire a cold sample of ^{85}Rb is used in this thesis. This technique works surprisingly well thanks to yet more fortunate coincidences of the atomic properties of each atom. One benefit of requiring cold ^{87}Rb to produce cold ^{85}Rb is that it is easy to then produce a condensate of each species simultaneously in the same trap. It turns out that this combination of atomic isotopes is ideal for an interferometric test of the weak equivalence principle, one of the underpinnings of General Relativity. In fact, space missions are currently being proposed and funded on this combination of isotopes. This thesis also presents the results of the first Bose-condensed version of such a dual-species interferometer. As could well be expected, inter-atomic interactions play a large role in determining the output of such an interferometer and much further study is required before such a system could be deployed in space.

By ensuring there is no ^{87}Rb left after condensation, we have created a pure ^{85}Rb BEC. Using this we can now explore how the inter-atomic interactions affect the phase shift of a condensed atom interferometer, as we have complete control over the interaction strength. Two especially interesting cases are the following. Firstly, a condensate with no inter-particle interactions should not exhibit this effect at all, allowing a clean comparison point. Secondly, with a small attractive interaction between atoms, it is possible to create a self-trapped cloud of atoms which propagates dispersionlessly, even in the presence of a repulsive trapping potential. This cloud is known as a soliton, and it is predicted to have even more interesting quantum mechanical properties. For example it is predicted that by colliding two such solitons, an entangled state can be generated. Our results indicate that the dispersionless character of the soliton out-performs all other interaction strengths in an atom interferometer, including even the non-interacting cloud.

Throughout this thesis I have gained a better understanding of how ultra-cold atom interferometers work and what can be done to improve and extend their capabilities into new and exciting directions, and hopefully after reading this thesis, you will too.

Contents

Stopping by Woods on a Snowy Evening	v
Acknowledgments	vii
Abstract	ix
1 Introduction	1
1.1 What Is An Atom Interferometer?	1
1.2 Practical considerations	4
1.3 Free vs. Trapped atom interferometry	8
1.4 Thesis Outline	9
1.5 List of Publications	10
I Pieces of the atomic jigsaw puzzle	13
2 Two level atoms	15
2.1 Hamiltonian	15
2.2 Coherent Evolution	17
2.3 Pulses	19
2.4 Coherent Evolution with Decay	19
2.5 Steady State	20
2.6 Forces on the atoms	21
2.7 Examples of the Dipole Force	22
2.7.1 Blue-detuned beam as an atom-optic mirror	22
2.7.2 Blue-detuned beam as a vertical beamsplitter	24
2.7.3 Red-detuned beam as a Dipole trap	26
2.7.4 Two photon transitions	28
2.7.5 Optical Lattices	29
2.7.6 Bragg diffraction	30
2.7.6.1 Bragg resonance	30
2.7.6.2 Rabi frequency	33
2.7.7 Bloch oscillations	33
2.7.7.1 Adiabatic loading	37
2.7.7.2 Adiabatic acceleration	39
2.8 Scattering Force	41

2.8.1	Magneto-Optical Trapping	42
2.8.2	Imaging	42
3	Atom Interferometer Theory	45
3.1	Atom-light interactions	45
3.2	Interferometer Phase Shift	46
3.2.1	Action	46
3.2.2	Time Symmetries	50
3.2.3	Laser Phase	51
3.3	Extensions	51
3.3.1	Constant energy offset	51
3.3.2	Vibrations and time-varying \mathbf{g}	52
3.3.2.1	Fourier series decomposition	53
3.3.3	Coriolis Effect	54
3.3.4	Separation Phase	55
3.4	Example Interferometer Configurations	57
3.4.1	Mach-Zehnder (MZ)	57
3.4.2	Continuous-Acceleration Bloch (CAB) sequence	58
3.4.3	Butterfly configuration	62
3.4.4	Recoil sensitive interferometers	64
4	Dual-Species $^{87}\text{Rb}/^{85}\text{Rb}$ BEC Machine	67
4.1	Laser System	68
4.2	Science Table	71
4.3	Optical Lattice Beams	75
4.4	Fourier Decomposition Algorithm	77
II	A selection of interferometers	79
5	Optically Guided Interferometry	81
5.1	Why guided interferometry?	81
5.2	Magnetic Waveguides	82
5.3	Optical Waveguide	82
5.4	Optically Waveguided Interferometer	85
5.4.1	Phase Noise	87
5.4.2	Summary	88
5.5	Repulsive optical barrier as a horizontal mirror	89
5.6	Butterfly configuration	92
6	Large Momentum Transfer in Atom Interferometry	95
6.1	Some history of Large Momentum Transfer (LMT)	96
6.2	Space-time Area and LMT	98
6.3	Experimental set-up	99

6.4	Delta-kick cooling for a narrow momentum width source	99
6.5	Interferometer Pulse Sequences	103
6.5.1	Mach-Zehnder sequence	104
6.5.2	CAB sequence	104
6.5.3	CAB2 sequence	106
6.5.4	Calibration of Bloch Lattice	106
6.5.5	Detection	106
6.6	Gradiometer to measure waveguide curvature	111
6.7	A faster sensitivity scaling	112
6.8	Extension to T^n scaling	114
6.9	Future Directions	114
6.10	Discussion	115
7	Variable Scattering Length Interferometry	117
7.1	Feshbach resonance	117
7.2	Soliton Formation	120
7.3	Soliton Interferometry	125
7.4	Summary and Future Directions	129
8	Dual Isotope Interferometry	131
8.1	Equivalence Principle Measurements	131
8.2	Dual Species condensate	132
8.3	Simultaneous Interference Fringes	133
8.4	Systematic phase shifts between isotopes	138
8.5	Summary	143
9	Conclusion and Outlook	145

Introduction

Light interferometry has been used for just over 130 years to investigate the properties of the world around us in finer detail [169, 170]. Since its inception, interferometry has blossomed into a wide ranging field using not only light, but also electrons [224], neutrons [142, 102, 225, 101, 196, 215], neutral atoms [136, 58, 22], Boes-Einstein condensates [15], ions [116], superfluid ^3He and ^4He [205, 218, 122, 131] and larger molecules [115]. Neutral atoms in particular are a versatile tool for interferometry as they are sensitive to gravity and other accelerations through their mass, to magnetic fields through the Zeeman shift and their magnetic dipole moment, and sensitive to electric fields through their electric polarisability.

1.1 What Is An Atom Interferometer?

An atom interferometer takes a source of atoms, which could be a cold cloud or a beam of atoms, and splits it along two (or more¹) trajectories in space-time. These two trajectories experience different environments, and they are then brought back together and compared, to see the difference in phase accumulated between the two paths. For example, in a Mach-Zehnder configuration [Fig. 1.1 (a)], some of the atoms are initially diffracted to a faster moving state. After a time T , the speed of the two clouds of atoms is swapped, and after a further time T all the atoms are overlapping again. At this point the atoms are diffracted once again and hence interfered. The fractional number in each of the two output clouds carries the information we require. If, for example, we vary the position of the last diffraction grating, we will change the additional phase ϕ which it applies. By plotting the fraction of atoms in one of the two output states we will get a sinusoidal graph which looks like Fig. 1.1 (b), and the offset of this cosine from zero is the phase difference Φ between what was accumulated along each of the two paths. This relative phase is used to

¹In general it can of course compare the relative phase along many different paths as in Talbot-Lau interferometry, for example.

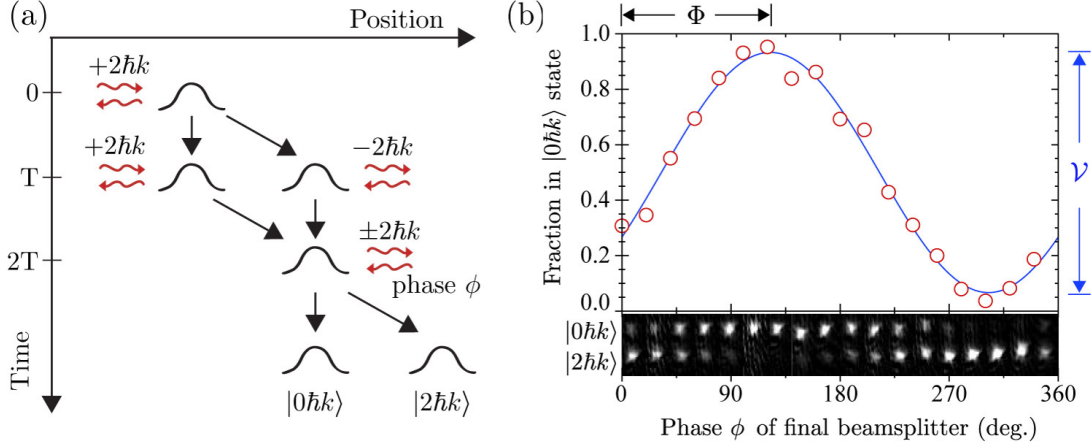


Figure 1.1: **(a)** Space-time diagram for a Mach-Zehnder atom interferometer. First, the initial cloud of atoms is split by a laser pulse between two momenta, zero and two photon recoils. A time T later, a second laser pulse swaps the momenta of the two clouds of atoms. After an additional time T the two clouds overlap once again and are recombined and interfered by a final laser pulse. The clouds are then allowed to separate before an image is taken to count how many atoms are in each final momentum state. **(b)** An example interference fringe from an atom interferometer, which will be shown again as Fig 7.6. As the phase ϕ of the last beam-splitter is varied, the fraction of atoms in the $|0\hbar k\rangle$ state traces out a cosine fringe. Also indicated are the important parameters extracted from the fit, the fringe visibility \mathcal{V} and the interferometric phase Φ . At the bottom the raw absorption images after each run are shown.

infer a measurement of a quantity of interest, for example, the value of local gravity \mathbf{g} , the strength of the local magnetic field \mathbf{B} , or the rotation rate of the earth Ω_e .

Applications for atom interferometers include (but are not limited to) inertial measurement, measurement of electric and magnetic fields, measurement of time and measurements of light fields and surfaces. With small changes to the interferometric sequence or direction, atom interferometers can also measure gradients and higher derivatives of all of these quantities.

Gravimetry

The phase of an interferometer with space-time area $\mathcal{A} = \int_{t_{\text{start}}}^{t_{\text{finish}}} \Delta\mathbf{x} dt$, constructed with an atom of mass m is sensitive to local gravity \mathbf{g} through the relation (to be presented in Chapter 3)

$$\Phi = \frac{m}{\hbar} \int_{t_{\text{start}}}^{t_{\text{finish}}} \Delta\mathbf{x} dt \cdot \mathbf{g} \quad (1.1)$$

$$= \frac{m}{\hbar} \mathcal{A} \cdot \mathbf{g} \quad (1.2)$$

Measurements of local gravity \mathbf{g} [124, 187, 7] can be used to look at tidal fluctuations, earthquakes, plate tectonics and other geophysical phenomena. Maps of the spatial variation in local gravity $\mathbf{g}(x, y)$, the gravity gradient $\frac{d\mathbf{g}(x,y)}{dz}$ [222, 221] or even the gravity curvature $\frac{d^2\mathbf{g}(x,y)}{dz^2}$ [200] can be used for mineral exploration, groundwater mapping, navigation and climate change modelling. They can also be used in searching for bunkers or tunnels buried underground. Another use is to compare the gravitational acceleration of two different atoms in order to test the weak equivalence principle, and this will be discussed further in Chapter 8. Careful differential gravimetry with calibrated source masses can be used to measure Newton's gravitational constant G to higher precision [201].

Magnetometry

The magnetic sensitivity of an atom interferometer can be used to create spatial maps of the naturally occurring magnetic field $\mathbf{B}(\mathbf{r})$ and its spatial derivatives [244, 18], which could again have applications in mineral exploration and geodesy. The magnetic sensitivity is derived from the Zeeman shift

$$U = \mu \cdot \mathbf{B} \quad (1.3)$$

where μ is the magnetic dipole moment of the atoms. An atom interferometer will detect a difference in the Zeeman shift between two trajectories according to

$$\Phi = \frac{m}{\hbar} \int_{t_{\text{start}}}^{t_{\text{finish}}} \Delta U dt. \quad (1.4)$$

From Eq. (1.3), the atoms will experience an acceleration due to a spatial gradient in magnetic field, according to

$$\mathbf{a}_{\text{mag}} = -\frac{1}{m} \mu \cdot \nabla \mathbf{B} \quad (1.5)$$

and this can be detected by an inertially sensitive interferometer. Magnetically sensitive atom interferometers could also be used to map out the magnetic properties of a nearby surface [179], e.g. a new magnetic material or new design of atom chip. Atom interferometers can be designed to be sensitive to only certain frequencies of oscillatory magnetic fields [35] by carefully utilising time symmetry in the design of the sequence.

Inertial measurements

Atom interferometers can sense both linear accelerations \mathbf{a} [164] and rotations $\boldsymbol{\Omega}$ [19], which are a vital source of information for dead-reckoning navigation systems. Linear accelerations are detected according to Equation (1.1) by re-

placing \mathbf{g} with \mathbf{a} . Rotations are sensed according to the Sagnac Phase shift

$$\Phi = \frac{2m}{\hbar} \boldsymbol{\Omega} \times \mathbf{A} \quad (1.6)$$

where \mathbf{A} is the vector-area enclosed by the atom interferometer, and $\boldsymbol{\Omega}$ is the rotation being detected. As atom interferometers are highly sensitive to vibrations at very low frequencies, this makes them ideal tool for the search for gravity waves in this frequency range [100]. These concepts will be developed in Chapter 3.

Light

The change in potential V felt by the atoms due to the Stark shift of a beam of light can be measured by its effect on the phase of the atoms which pass through it, by comparing with other atoms with a different Stark shift, according to the usual relation

$$\Phi = \frac{m}{\hbar} \int_{t_{\text{start}}}^{t_{\text{finish}}} \Delta V dt. \quad (1.7)$$

It is also possible to perform a precision measurement of the recoil frequency, $\omega_r = \frac{\hbar k^2}{2m}$. This allows a precision measurement of the fine-structure constant $\alpha = \frac{e^2}{4\pi\epsilon_0\hbar c} \approx \frac{1}{137}$ as the other factors are already known to high precision [32].

1.2 Practical considerations

The field of atom interferometry began in 1991 with thermal beams of atoms being split using nano-fabricated diffraction gratings [136], double slits [41], and 1-photon [197] or 2-photon [134] transitions. By the year 2000, atom interferometry had surpassed other techniques for measuring rotations [107]. The following year, atom interferometers had equalled the gravitational sensitivity and long-term absolute accuracy of its nearest competitor, the falling corner cube [187]. This record stood unchallenged for more than a decade, and it was only in 2013 that another atom interferometer beat it by a factor of two [124].

What stands in the way of further progress? To answer this question we must examine the factors which determine the precision of an atom interferometer. In the specific case of a Mach-Zehnder atom interferometer, the smallest achievable acceleration sensitivity Δa in a single run goes as

$$\Delta a = \frac{1}{\sqrt{N} k_{\text{eff}} T^2 \mathcal{V}} \quad (1.8)$$

where N is the number of atoms used in the run, k is the momentum separation between the two trajectories along the direction in which we wish to measure the acceleration \mathbf{a} , T is the interferometer time ($2T$ is the time from the beginning to the end of the interferometer) and \mathcal{V} is the fringe visibility, the amplitude of a sinusoidal fit to the interference fringe, which is between 0 and 1. Let us examine each of the parts of this expression in turn.

Atom number N

The appearance of \sqrt{N} on the denominator of Eq. (1.8) is a result of simple binomial statistics. If a coin is flipped N times, the expected fraction of heads will be 50%. But the standard deviation around this value will go as $1/\sqrt{N}$. The same is true for atoms which can be in one of two output ports of an interferometer, and here it is known as the quantum projection-noise limit. This limit can be surpassed, tending towards $1/N$, using quantum entanglement in condensed sources [77, 179, 23] but as yet this is impractical for a large enough number of atoms to be metrologically useful. This scaling with the square root of the number of atoms means that to produce a device which is an order of magnitude more sensitive, the number of atoms needs to be increased by two orders of magnitude.

Momentum Transfer k_{eff}

The momentum k_{eff} transferred to the atoms by the atomic beam-splitter is equivalent to the momentum separation between the two trajectories which make up the interferometer. The signal in an interferometer can therefore be increased by increasing this momentum splitting. One way to do this is simply using a repulsive barrier in direct analogy to the optical beamsplitter, as will be discussed in Sections 2.7.2 and 5.5. Another way is to impart many photon-recoils of momentum to the atoms using an optical lattice, which is a key result of this thesis and will be discussed in Chapter 6. Of course in order to achieve such large momentum transfer it is necessary to have a very low-dispersion source [233] and so we study two approaches to this problem. In Chapter 6 we use delta-kick cooling to collimate the wavefront of our expanding condensate before applying the interferometer, and in Chapter 7 we will use the interatomic interactions to cancel out the spatial dispersion and create a soliton as the source cloud for our atom interferometer.

Interferometer Time T

In the example of a Mach-Zehnder interferometer, the T^2 in the denominator of Eq. (1.8) is as a result of the space-time area \mathcal{A} in that particular interferometer

going as $\sim k_{\text{eff}}T^2$ [c.f. Eq. (1.2)], and the theory behind this will be explored in more detail in Chapter 3. This scaling means that if the interferometer time can be increased two-fold, the uncertainty in acceleration can be decreased four-fold. We will also show theoretically in Chapter 3 and experimentally in Chapter 6 that by using large momentum transfer, this scaling can be increased to T^3 or even higher powers of T .

Fringe visibility \mathcal{V}

The fringe visibility \mathcal{V} , shown in Fig. 1.1 (b), also appears in the denominator of Eq. (1.8). It is the amplitude of a sinusoidal fit to the interference fringe. If $\mathcal{V} = 1$ it means that there is perfect coherence and all the atoms contributed to the interferometer signal. If $\mathcal{V} < 1$ it means that something in the interferometer did not go perfectly, for example some of the atoms did not interfere, some of the atoms interfered with a different phase offset, or some noise has crept into the detection process. If $\mathcal{V} = 0$, it means that the interferometer is unable to perform any measurement of the quantity of interest.

However these are not the only factors that need to be taken into account. By definition, a precise accelerometer is sensitive to very small accelerations. These may be from the signal of interest, say local gravity \mathbf{g} , or they may be from some unwanted mechanical vibrations of the room or the apparatus. Therefore, a common restriction on the acceleration sensitivity of an atom interferometer is the level to which it can be isolated from background vibrations. These must be well below the desired level of acceleration sensitivity for a good measurement, and in fact are the main limiting factor in current state-of-the-art acceleration measurements with atom interferometry. Phase noise on the diffraction grating will couple in exactly the same as a vibration and so the relative phase of two laser beams generating the diffraction grating must be controlled precisely as well.

Dispersion of the interferometric wave packet can reduce the efficiency of diffraction pulses [233]. Dispersion throughout the interferometer will also cause phase inhomogeneities across the cloud, which will lower the overall fringe visibility when averaged at the end of the interferometer. For these reasons interferometers are being constructed which rely upon colder and colder sources, which have a narrower momentum width and consequently less spatial dispersion. Thermal sources are, roughly speaking, in the range of a few mili-Kelvin to hundreds of nano-Kelvin, and consequently have a momentum width between one and a hundred photon recoils². The colder the thermal source is to begin with, the lower the loss involved in selecting a velocity class to use for the interferometer. This is analogous to using a light bulb as a source for a light interferometer. The light can be filtered to provide a suitable source for an interferometer, but it will still have a much shorter coherence length and larger angular divergence than a laser beam. Similarly, a cold but incoherent

²These numbers are based upon ^{87}Rb and using the D2 line at 780nm, and will vary depending upon the atom or transition chosen.

thermal source of atoms can be filtered (velocity selected) to form a source for interferometry. However this will also have a short coherence length and large spatial divergence as compared with a coherent atomic source, a Bose-Einstein Condensate.

Indistinguishable bosons will condense if they fulfil the phase-space density criteria [17, 188]

$$\rho \lambda_{\text{dB}}^3 \gtrsim 2.6 \quad (1.9)$$

for 3D density ρ , thermal de Broglie wavelength $\lambda_{\text{dB}} = \sqrt{\frac{2\pi\hbar^2}{mk_B T}}$, temperature T , and Boltzmann's constant k_B . This regime is roughly described by particles which are separated by less than λ_{dB} , so that inter-particle interactions become important. A BEC will have a momentum width on the order of 0.01-0.1 photon recoils, which in the absense of inter-particle interactions is determined by the momentum width of the ground state of the trap in which it is held. Repulsive interactions will tend to make the condensate larger (in-trap) and hence lower the momentum width. However, once the condensate is allowed to expand, it can convert the energy stored in the interparticle interactions into kinetic energy, and can become broader in momentum width [5]. In addition, condensed atoms are now phase-coherent, which allows the possibility of multiple particles interfering with each other.

To explore the effect of both temperature and condensation on an atom interferometer we compared three source clouds in the same interferometric sequence; a thermal cloud cooled to $1.3 \mu\text{K}$, a thermal cloud cooled to 75nK , and a Bose-Einstein Condensate. In Figure 1.2 the fringe visibility \mathcal{V} is shown for a Mach-Zehnder interferometer constructed in an optical waveguide in our setup. Each source cloud had a small section selected from it with the same axial momentum width, so that the differences between them will occur because of differences in the transverse momentum width and phase coherence between across multiple atoms in the condensate. These results are published in Ref. [114]. It is clear that the interference is more robust against small mode-mismatching in the output states from the condensed source, as it has a higher visibility \mathcal{V} than the two thermal source clouds.

In analogy to reducing the dispersion of a light beam by collimating it with a lens, the dispersion of a matter-wave can be collimated by briefly applying a trapping potential, and this is known as delta-kick cooling. Section 6.4 describes our implementation of this process and shows how drastic the improvement in fringe visibility is in our atom interferometer. This process can only fractionally reduce the momentum width of a given source cloud, so the colder you start, the colder you get. Another advantage of BEC is that its density can be high enough to take advantage of inter-particle interactions. A BEC will follow a Schrödinger-like equation, the Gross-Pitaevski Equation

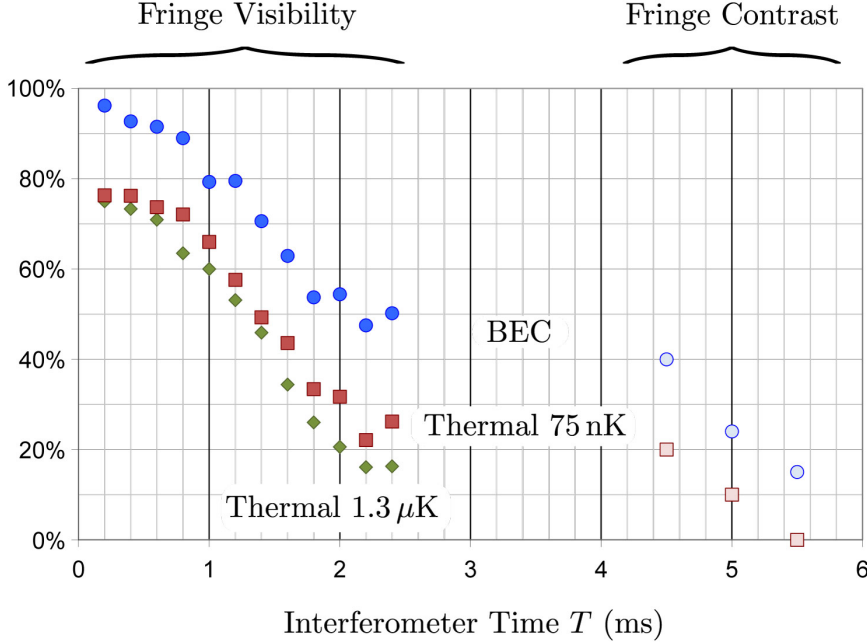


Figure 1.2: This figure shows the effect of transverse temperature and condensation on coherence. Each source cloud has been velocity selected to be the same momentum width along the axis of the interferometer. Published in Ref. [114].

$$-i\hbar \frac{d}{dt} \Psi = \frac{\hbar^2}{2m} \nabla \Psi + V(\mathbf{x})\Psi + U |\Psi|^2 \Psi \quad (1.10)$$

where $U = \frac{8\pi a}{\hbar^2}$ governs the strength of the interactions, and a is the s -wave scattering length of the atoms. If U is positive, the interactions are repulsive, and if U is negative the interactions are attractive. The influence of repulsive interactions on an atom interferometer have been studied previously [5, 62]. In Chapter 7 I will use an attractive inter-particle interaction to cancel out the Heisenberg-limited dispersion of a BEC, creating a soliton. I will then show that this source cloud maximises the visibility \mathcal{V} of the interferometer among other choices of the inter-particle interaction strength.

1.3 Free vs. Trapped atom interferometry

State-of-the-art atom interferometers used in precision measurement of time, rotation and gravity currently perform an interferometer on the atoms while they are in free-fall in order to decouple them as much as possible from the environment. This is because it requires fewer parts to be vibrationally isolated to such a high level. For

example, in the case of a gravimeter, it only requires one mirror to be well isolated from background vibrations. On the other hand, this restricts the maximum interferometer time and hence the signal of an atom interferometer by the vertical height of the vacuum system, according to the time it takes to fall a certain distance under gravity, $h = \frac{1}{2}gt^2$. This means that a vacuum system 10 m tall can accommodate a fall time of just under 1.5 s, which can be doubled if the atoms are launched from the bottom instead of being dropped from the top. These systems can quickly become unwieldy if a portable measurement device is the desired outcome, and this has led to interest in trapped and guided atom interferometers which can perform such measurements with a more compact setup. The disadvantage is that the entire guiding potential must also be isolated from environmental vibrations and noise so as to not disturb the signal we are trying to measure. In principle this is possible but has proven difficult in practice. Here I demonstrate an arrangement for horizontal acceleration sensitivity by suspending the atoms in a horizontal far-detuned optical dipole trap, which we term the optical waveguide. In principle this should allow long time interferometry in that direction, although in practice long times have not yet been achieved in this configuration. In the future a defined axis sensor could be built by combining many of these, aligned along each axis to measure accelerations and rotations in each direction simultaneously.

1.4 Thesis Outline

Part I of this thesis introduces the concepts, techniques and experimental details which will be required for understanding the main results of this thesis. Chapter 2 refreshes the theory of the two-level atom and shows how it underpins many of our techniques in manipulating atoms with the use of light. Chapter 3 outlines a geometric approach to understanding the primary measure at the conclusion of an interferometer, the phase difference accumulated between the two paths travelled by the atoms. Chapter 4 introduces the experimental apparatus in which all the experiments are performed and outlines the steps to achieve Bose-Einstein Condensation of either or both of the naturally abundant isotopes of rubidium. This forms the starting point for condensed-atom interferometry.

Part II comprises the main results of this thesis. Chapter 5 presents the first incarnation of optically-guided atom interferometry on ^{87}Rb . In this chapter I also demonstrate an entirely novel kind of ‘triangle’ interferometer incorporating a blue-detuned barrier as an atom-optic mirror, to bring the two paths back together again. Chapter 6 presents a new design of interferometer which achieves both the largest momentum separation between the two interfering paths in an acceleration-measuring interferometer to date, and a scaling law in interferometric acceleration sensitivity which scales as the cube of the interferometer time, bettering the usual quadratic relation.

Chapter 7 shows the effect on both the phase and visibility of an interferometer, of being able to vary the scattering length (and thus the collisional properties) of the interfering atoms. These experiments are performed through the use of an easily accessible Feshbach resonance in ^{85}Rb . Surprisingly, the highest visibility is achieved not when the interactions are turned off, but when they are tuned to be attractive, so as to produce a cloud of constant phase-space density - a matter-wave soliton. Finally, Chapter 8 experimentally investigates the simultaneous operation of an interferometer on overlapping condensates of both ^{87}Rb and ^{85}Rb . Such a technique is proposed for space missions to test the weak equivalence principle, i.e. the principle that objects of different mass will accelerate at the same rate in a given gravitational field, in the absence of other effects such as air resistance.

1.5 List of Publications

The following is a list of publications produced during the course of this thesis, in reverse chronological order.

A Bose-condensed, simultaneous dual species Mach-Zehnder atom interferometer

C. C. N. Kuhn, G. D. McDonald, K. S. Hardman, S. Bennetts, P. J. Everitt, P. A. Altin, J. E. Debs, J. D. Close, and N. P. Robins.
New J. Phys. **16**, 073035 (2014).

A Bright solitonic matter-wave interferometer

G. D. McDonald,* C. C. N. Kuhn, K. S. Hardman, S. Bennetts, P. J. Everitt, P. A. Altin, J. E. Debs, J. D. Close, and N. P. Robins.
Phys. Rev. Lett. **113**, 013002 (2014).

External cavity diode lasers with 5 kHz linewidth and 200 nm tuning range at 1.55 μm and methods for linewidth measurement

S. Bennetts, G. D. McDonald, K. S. Hardman, J. E. Debs, C. C. N. Kuhn, J. D. Close, N. P. Robins.
Opt. Express **22**, 10642 (2014).

A faster scaling in acceleration-sensitive atom interferometers

G. D. McDonald,* C. C. N. Kuhn, S. Bennetts, J. E. Debs, K. S. Hardman, J. D. Close, and N. P. Robins.
Europhysics Letters **105**, 63001 (2014).

Construction and Characterization of External Cavity Diode Lasers for Atomic Physics

K. S. Hardman, S. Bennetts, J. E. Debs, C. C. N. Kuhn, G. D. McDonald, N. P. Robins.
J. Vis. Exp. **86**, e51184 (2014)

The role of source coherence in atom interferometry

K. S. Hardman*, C. C. N. Kuhn, G. D. McDonald, J. E. Debs, S. Bennetts, J. D. Close, and N. P. Robins.

Phys. Rev. A **89**, 023626 (2014).

80 $\hbar k$ momentum separation with Bloch oscillations in an optically guided atom interferometer

G. D. McDonald,* C. C. N. Kuhn, S. Bennetts, J. E. Debs, K. S. Hardman, M. Johnsson, J. D. Close, and N. P. Robins.

Phys. Rev. A **88**, 053620 (2013).

Precision atomic gravimeter based on Bragg diffraction

P. A. Altin, M. T. Johnsson, V. Negnevitsky, G. R. Dennis, R. P. Anderson, J. E. Debs, S. S. Szigeti, K. S. Hardman, S. Bennetts, G. D. McDonald, L. D. Turner, J. D. Close and N. P. Robins.

New J. Phys. **15**, 023009 (2013).

From apples to atoms: measuring gravity with ultra cold atomic test masses

J. E. Debs, K. S. Hardman, P. A. Altin, G. D. McDonald, J. D. Close and N. P. Robins.
Preview **164**, 30 (2013)

Optically guided linear Mach-Zehnder atom interferometer

G. D. McDonald*, H. Keal, P. A. Altin, J. E. Debs, S. Bennetts, C. C. N. Kuhn, K. S. Hardman, M. T. Johnsson, J. D. Close, and N. P. Robins.

Phys. Rev. A **87**, 013632 (2013).

11 W narrow linewidth laser source at 780nm for laser cooling and manipulation of Rubidium

S. S. Sané, S. Bennetts, J. E. Debs, C. C. N. Kuhn, G. D. McDonald, P. A. Altin, J. D. Close and N. P. Robins.

Opt. Express **20**, 8915 (2012).

Optically trapped atom interferometry using the clock transition of large ^{87}Rb Bose-Einstein condensates

P. A. Altin, G. D. McDonald, D. Döring, J. E. Debs, T. H. Barter, J. D. Close, N. P. Robins, S. A. Haine, T. M. Hanna and R. P. Anderson

New J. Phys. **13**, 065020 (2011).

Optically trapped atom interferometry using the clock transition of large ^{87}Rb Bose-Einstein condensates : Addendum

P. A. Altin, G. D. McDonald, D. Döring, J. E. Debs, T. H. Barter, J. D. Close, N. P. Robins, S. A. Haine, T. M. Hanna and R. P. Anderson

New J. Phys. **13**, 119401 (2011).

Collapse and three-body loss in a ^{85}Rb Bose-Einstein condensate

P. A. Altin, G. R. Dennis, G. D. McDonald, D. Döring, J. E. Debs, J. D. Close, C. M. Savage and N. P. Robins.

Phys. Rev. A **84**, 033632 (2011).

Cold-Atom gravimetry with a Bose-Einstein condensate

J. E. Debs*, P. A. Altin, T. H Barter, D. Döring G. R. Dennis, G. D. McDonald, R. P. Anderson, J. D. Close, and N. P. Robins.

Phys. Rev. A **84**, 033610 (2011).

Quantum-projection-noise-limited interferometry with coherent atoms in a Ramsey-type setup

D. Döring, G. D. McDonald, J. E. Debs, C. Figl, P. A. Altin, H.-A. Bachor, N. P. Robins and J. D. Close.

Phys. Rev. A **81**, 043633 (2010).

Part I

Pieces of the atomic jigsaw puzzle

Two level atoms

The simplest model for interactions between atoms and light is the two-level atom. This chapter will derive some common two-level atom results and then show several examples of how they apply when manipulating atoms with light. These examples include Rabi flopping, the dipole force and how it is used to create conservative potentials for the atoms, the scattering force and how it is used in a MOT, and two-photon transitions such as Bragg scattering of the atoms. Some of these examples form the basis of techniques used in the rest of this thesis.

To begin we will derive the optical Bloch equations for a two-level system. This form has the benefit of a readily visualisable mental picture of what is going on, which is known as the Bloch sphere.

2.1 Hamiltonian

Define the Rabi frequency Ω by the applied electric field times the electric dipole moment of the transition between the ground $|g\rangle$ and excited $|e\rangle$ state

$$\Omega = \frac{\mathbf{d} \cdot \mathbf{E}}{\hbar} \quad (2.1)$$

$$= \frac{-e}{\hbar} \mathbf{E} \cdot \langle e | \mathbf{r} | g \rangle \quad (2.2)$$

Start with the following hamiltonian

$$\hat{\mathcal{H}} = \frac{\hbar\omega_0}{2} (|e\rangle\langle e| - |g\rangle\langle g|) + \frac{\hbar\omega}{2} (|g\rangle\langle g| - |e\rangle\langle e|) + \hbar\Omega \cos(\omega t + \phi) (|g\rangle\langle e| + |e\rangle\langle g|) \quad (2.3)$$

where ω_0 is the resonant frequency of the atom, and ω is the frequency of the photon. This can be written in matrix notation as

$$\hat{\mathcal{H}} = \underbrace{\frac{\hbar\omega_0}{2} \begin{pmatrix} 1 & 0 \\ 0 & -1 \end{pmatrix}}_{\text{atom energy}} + \underbrace{\frac{\hbar\omega}{2} \begin{pmatrix} -1 & 0 \\ 0 & 1 \end{pmatrix}}_{\text{light energy}} + \underbrace{\hbar\Omega \cos(\omega t + \phi) \begin{pmatrix} 0 & 1 \\ 1 & 0 \end{pmatrix}}_{\text{interaction}} \quad (2.4)$$

Transforming into the rotating frame which rotates with angular frequency ω , and averaging over many periods of the fast rotating terms which have an angular frequency of 2ω gives¹

$$\hat{\mathcal{H}} = \underbrace{\frac{\hbar\omega_0}{2} \begin{pmatrix} 1 & 0 \\ 0 & -1 \end{pmatrix}}_{\text{atom energy}} + \underbrace{\frac{\hbar\omega}{2} \begin{pmatrix} -1 & 0 \\ 0 & 1 \end{pmatrix}}_{\text{light energy}} + \underbrace{\frac{\hbar\Omega}{2} \begin{pmatrix} 0 & e^{i\phi} \\ e^{-i\phi} & 0 \end{pmatrix}}_{\text{interaction}} \quad (2.5)$$

Defining the detuning between the resonant frequency and the applied frequency as $\Delta = \omega_0 - \omega$ we have

$$\hat{\mathcal{H}} = \frac{\hbar}{2} \begin{pmatrix} \Delta & \Omega e^{i\phi} \\ \Omega e^{-i\phi} & -\Delta \end{pmatrix} \quad (2.6)$$

We can write this in terms of a vector of Pauli matrices² $\vec{\sigma} \equiv \{\hat{\sigma}_x, \hat{\sigma}_y, \hat{\sigma}_z\}$ as

$$\hat{\mathcal{H}} = \frac{\hbar}{2} (\vec{W} \cdot \vec{\sigma}) \quad (2.7)$$

where the Rabi vector is $\vec{W} = \{\Omega \cos \phi, -\Omega \sin \phi, \Delta\}$

¹This is known as the rotating wave approximation

²The Pauli matrices are given by $\sigma_x = \begin{pmatrix} 0 & 1 \\ 1 & 0 \end{pmatrix}$, $\sigma_y = \begin{pmatrix} 0 & -i \\ i & 0 \end{pmatrix}$ and $\sigma_z = \begin{pmatrix} 1 & 0 \\ 0 & -1 \end{pmatrix}$. All 2×2 matrices A can be written in the form $A = \frac{1}{2}(cI + \vec{v} \cdot \vec{\sigma})$ because the Pauli matrices, together with the identity matrix, form an orthogonal basis set. To find the coefficients one can use $c = \text{Tr}\{A\}$ and $\vec{v} = \text{Tr}\{\vec{\sigma}A\}$.

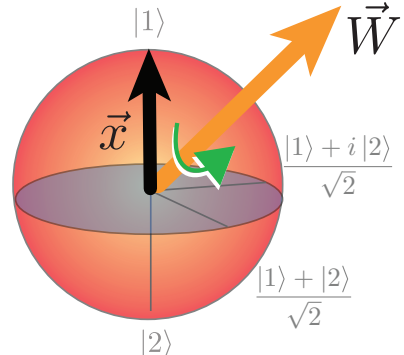


Figure 2.1: The Bloch sphere picture. The Bloch vector \vec{x} , which describes the quantum state of the two-level system, rotates according to Eq. (2.15) around the Rabi vector $\vec{W} = \{\Omega \cos \phi, -\Omega \sin \phi, \Delta\}$, itself describing the atom-light interaction.

2.2 Coherent Evolution

The density matrix $\hat{\rho}$ evolves coherently according to the von Neumann equation,

$$i\hbar \frac{d\hat{\rho}}{dt} = [\hat{\mathcal{H}}, \hat{\rho}] \quad (2.8)$$

in the absence of any spontaneous decay from the excited to the ground state.

We can write the density matrix in terms of pauli matrices as

$$\hat{\rho} = \frac{1}{2} (I + \vec{x} \cdot \vec{\sigma}) \quad (2.9)$$

and we can call $\vec{x} = \{x, y, z\}$ the Bloch vector. For a pure state $|\vec{x}| = 1$ while for a mixed state $|\vec{x}| < 1$. So the commutator $[\hat{\mathcal{H}}, \hat{\rho}]$ is given by

$$[\hat{\mathcal{H}}, \hat{\rho}] = \frac{\hbar}{4} (\vec{W} \cdot \vec{\sigma}) (I + \vec{x} \cdot \vec{\sigma}) - (I + \vec{x} \cdot \vec{\sigma}) \frac{\hbar}{4} (\vec{W} \cdot \vec{\sigma}) \quad (2.10)$$

$$= \frac{\hbar}{4} (\vec{W} \cdot \vec{\sigma}) (\vec{x} \cdot \vec{\sigma}) - \frac{\hbar}{4} (\vec{x} \cdot \vec{\sigma}) (\vec{W} \cdot \vec{\sigma}) \quad (2.11)$$

$$= \frac{i\hbar}{2} (\vec{W} \times \vec{x}) \cdot \vec{\sigma} \quad (2.12)$$

where on the last line we have used the identity $(\vec{a} \cdot \vec{\sigma}) (\vec{b} \cdot \vec{\sigma}) = ((\vec{a} \cdot \vec{b}) I + i(\vec{a} \times \vec{b}) \cdot \vec{\sigma})$ and Eq. (2.8) becomes

$$i\hbar \frac{d}{dt} (I + \vec{x} \cdot \vec{\sigma}) = i\hbar (\vec{W} \times \vec{x}) \cdot \vec{\sigma} \quad (2.13)$$

$$\frac{d\vec{x}}{dt} \cdot \vec{\sigma} = (\vec{W} \times \vec{x}) \cdot \vec{\sigma} \quad (2.14)$$

$$\frac{d\vec{x}}{dt} = \vec{W} \times \vec{x} \quad (2.15)$$

which is the vector differential equation describing the Bloch vector \vec{x} rotating around the Rabi vector \vec{W} in three dimensions, at a rate $|\vec{W}| = W$ rad/s⁻¹. On the last line we were able to ‘undo’ the dot product by equating the coefficient of each orthogonal Pauli matrix. For a given initial Bloch vector \vec{x}_0 , and constant Rabi vector \vec{W} , Eq. (2.15) has the solution

$$\vec{x}(t) = \cos(Wt)\vec{x}_0 + \sin(Wt)(\vec{w} \times \vec{x}_0) + [1 - \cos(Wt)](\vec{w} \cdot \vec{x}_0)\vec{w} \quad (2.16)$$

where we have defined the unit Rabi vector $\vec{w} = \vec{W}/W$. Let us now simplify to the case where the initial state is the ground state, i.e. the initial Bloch vector is $\vec{x}_0 = \{0, 0, -1\}$. In this case, the z-projection of the Bloch vector (which is the fraction in the excited state minus the fraction in the ground state) is given by

$$z(t) = \vec{e}_z \cdot \vec{x}(t) \quad (2.17)$$

$$= \cos(Wt)(\vec{e}_z \cdot \vec{x}_0) + \sin(Wt)(\vec{x}_0 \times \vec{e}_z) \cdot \vec{w} + [1 - \cos(Wt)](\vec{w} \cdot \vec{x}_0)(\vec{w} \cdot \vec{e}_z) \quad (2.18)$$

$$= -\cos(Wt) - \frac{\Delta^2}{W^2}[1 - \cos(Wt)] \quad (2.19)$$

and so the probability that the atom is in the excited state is given by $\rho_{ee} = \langle e | \hat{\rho} | e \rangle$ is given by

$$\rho_{ee}(t) = \frac{1 + z(t)}{2} \quad (2.20)$$

$$= \frac{1}{2} \left(1 - \frac{\Delta^2}{W^2} \right) [1 - \cos(Wt)] \quad (2.21)$$

$$= \frac{\Omega^2}{W^2} \sin^2 \left(\frac{Wt}{2} \right) \quad (2.22)$$

while the probability of the atom being in the ground state is of course given by

$$\rho_{gg}(t) = 1 - \rho_{ee}(t). \quad (2.23)$$

2.3 Pulses

For an initial ground state $\vec{x} = \{0, 0, -1\}$, a π pulse is defined (for a pulse of constant intensity light for a time τ) by $W\tau = \pi$, so that ρ_{ee} is maximised, i.e. as much population has been transferred into the excited state as possible. Ideally this pulse is on-resonant and so $\Delta = 0$ and the efficiency of the transfer is 100%. In the more general case of arbitrary pulse shapes (for example a gaussian pulse which minimises its Fourier frequency width for a given pulse duration) the π pulse is defined by

$$\int W(t)dt = \pi \quad (2.24)$$

which also maximises transfer between the ground and excited states. For a resonant π pulse and an arbitrary initial state, the component in the ground and excited state are swapped (while maintaining coherence) and so this pulse is also called a mirror pulse.

A $\pi/2$ pulse is defined similarly by $\int W(\tau)dt = \pi/2$. If the $\pi/2$ pulse is resonant and all the atoms are in either the ground or excited state to begin with, then afterwards the atoms will be equally distributed between $|g\rangle$ and $|e\rangle$. For this reason this pulse is also known as a beam-splitter pulse.

2.4 Coherent Evolution with Decay

Including spontaneous emission (at a rate Γ) in Eq. (2.8) we arrive at the master equation

$$i\hbar \frac{d\hat{\rho}}{dt} = [\hat{\mathcal{H}}, \hat{\rho}] + i\hbar\Gamma\mathcal{D}[\hat{\sigma}_-]\hat{\rho} \quad (2.25)$$

where $\hat{\sigma}_- = \frac{1}{2}(\hat{\sigma}_x - i\hat{\sigma}_y)$ is the decay operator $|g\rangle\langle e|$ and the decoherence superoperator \mathcal{D} is given by

$$\mathcal{D}[\hat{c}]\hat{\rho} = \hat{c}\hat{\rho}\hat{c}^\dagger - \frac{1}{2}(\hat{c}^\dagger\hat{c}\hat{\rho} + \hat{\rho}\hat{c}^\dagger\hat{c}) \quad (2.26)$$

so that

$$\mathcal{D}[\hat{\sigma}_-]\hat{\rho} = -\frac{1}{2}(x\hat{\sigma}_x + y\hat{\sigma}_y) - (1+z)\hat{\sigma}_z \quad (2.27)$$

and

$$\frac{d\vec{x}}{dt} = \vec{W} \times \vec{x} - \frac{\Gamma}{2} \begin{pmatrix} x \\ y \\ 2+2z \end{pmatrix} \quad (2.28)$$

which can be solved analytically for constant \vec{W} by rewriting it as a matrix equation:

$$\frac{d\vec{x}}{dt} = A\vec{x} + \vec{b} \quad (2.29)$$

for $A = \begin{pmatrix} -\frac{\Gamma}{2} & -\Delta & -\Omega \sin \phi \\ \Delta & -\frac{\Gamma}{2} & \Omega \cos \phi \\ \Omega \sin \phi & -\Omega \cos \phi & -\Gamma \end{pmatrix}$ and $\vec{b} = \begin{pmatrix} 0 \\ 0 \\ -\Gamma \end{pmatrix}$ (2.30)

which has the solution

$$\vec{x}(t) = \int_0^t e^{A(t-s)} ds \cdot \vec{b} + e^{At} \cdot \vec{x}(0) \quad (2.31)$$

which is unfortunately not particularly illuminating when written out in full.

2.5 Steady State

Let us now look at the steady-state solution when $\frac{d\vec{x}}{dt} = 0$, which can be written as the matrix equation

$$A\vec{x} = -\vec{b} \quad (2.32)$$

and upon solving for \vec{x} we find

$$\vec{x} = \frac{1}{1+\delta^2+\mathcal{I}} \begin{pmatrix} \sqrt{2\mathcal{I}}(\sin \phi - \delta \cos \phi) \\ \sqrt{2\mathcal{I}}(\cos \phi + \delta \sin \phi) \\ -(1+\delta^2) \end{pmatrix} \quad (2.33)$$

for unitless detunings and intensities

$$\delta = \frac{2\Delta}{\Gamma}, \quad \mathcal{I} = \frac{2\Omega^2}{\Gamma^2} = \frac{I}{I_{sat}} \quad (2.34)$$

2.6 Forces on the atoms

Adopt the Hamiltonian including kinetic energy:

$$\hat{\mathcal{H}} = \frac{\mathbf{p}^2}{2m} + \hat{\mathcal{H}}_A + \hat{\mathcal{H}}_I \quad (2.35)$$

$$(2.36)$$

where the interaction Hamiltonian $\hat{\mathcal{H}}_I = \hbar\Omega \cos(wt - \mathbf{k.r} + \phi) (|g\rangle\langle e| + |e\rangle\langle g|)$ is the coupling term. The force on the atom is now given by

$$\mathbf{F} = \frac{d}{dt} \langle \hat{\mathbf{p}} \rangle \quad (2.37)$$

$$= \frac{i}{\hbar} \langle [\hat{\mathcal{H}}, \hat{\mathbf{p}}] \rangle \quad (2.38)$$

$$= -\langle \nabla \hat{\mathcal{H}}_I \rangle \quad (2.39)$$

Now assuming the positional dependence is not in the atom's internal energy or the photon's energy, it can only be in the coupling term, in the electric field strength.

$$\mathbf{F} = -\langle \nabla \hat{\mathcal{H}}_I \rangle \quad (2.40)$$

$$= -\hbar \langle \nabla (\Omega \hat{\sigma}_x \cos(wt - \mathbf{k.r} + \phi)) \rangle \quad (2.41)$$

$$= -\hbar \langle \hat{\sigma}_x [(\nabla \Omega) \cos(wt - \mathbf{k.r} + \phi) + \Omega \nabla \cos(wt - \mathbf{k.r} + \phi)] \rangle \quad (2.42)$$

$$= -\hbar \langle \hat{\sigma}_x [(\nabla \Omega) \cos(wt - \mathbf{k.r} + \phi) + \Omega \sin(wt - \mathbf{k.r} + \phi) \nabla (\mathbf{k.r})] \rangle \quad (2.43)$$

$$= -\hbar \langle \hat{\sigma}_x [(\nabla \Omega) \cos(wt - \mathbf{k.r} + \phi) + \mathbf{k}\Omega \sin(wt - \mathbf{k.r} + \phi)] \rangle \quad (2.44)$$

which can be written in the frame rotating at speed ω (and with the rotating wave approximation) as

$$\mathbf{F} = -\hbar \langle \hat{\sigma}_x [\nabla \Omega \cos \phi + \mathbf{k}\Omega \sin \phi] + \hat{\sigma}_y [-\nabla \Omega \sin \phi + \mathbf{k}\Omega \cos \phi] \rangle \quad (2.45)$$

$$= -\frac{\hbar}{2} \vec{x} \cdot \vec{y} \quad \text{for} \quad \vec{y} = \begin{pmatrix} (\nabla \Omega) \cos \phi + \mathbf{k}\Omega \sin \phi \\ -(\nabla \Omega) \sin \phi + \mathbf{k}\Omega \cos \phi \\ 0 \end{pmatrix} \quad (2.46)$$

Using the steady state solution for \vec{x} in Eq. (2.33) we find

$$\mathbf{F} = \underbrace{\frac{\hbar \mathbf{k} \Gamma}{2} \frac{\mathcal{I}}{1 + \delta^2 + \mathcal{I}}}_{\text{Scattering Force}} + \underbrace{\frac{\hbar \Delta}{2} \frac{\nabla \mathcal{I}}{1 + \delta^2 + \mathcal{I}}}_{\text{Dipole Force}} \quad (2.47)$$

As this dipole force $\mathbf{F}_{\text{dip}} = -\nabla U_{\text{dip}}$ is the negative gradient of a potential function

$$U_{\text{dip}} = \frac{\hbar \Delta}{2} \ln \left(1 + \frac{\mathcal{I}}{1 + \delta^2} \right) \quad (2.48)$$

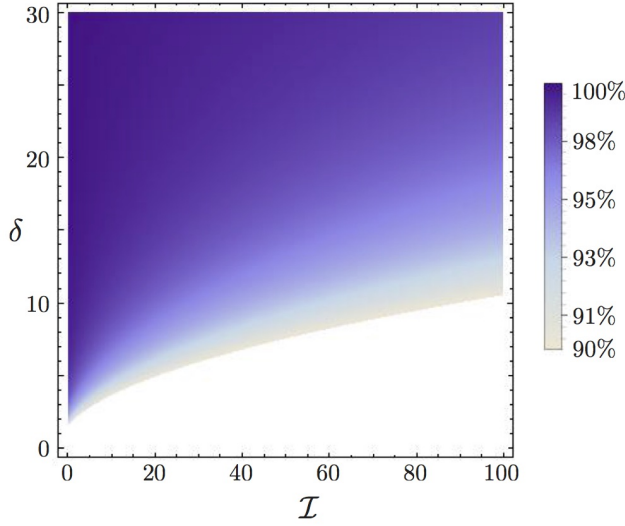


Figure 2.2: This figure shows the ratio of the correct expression for the dipole force [Eq. (2.48)] to the approximate expression [Eq. (2.49)]. In the far-detuned limit, the dipole potential can be well approximated by the simpler expression Eq. (2.49).

it is a conservative force. Regions of high intensity form an attractive potential for $\Delta < 0$, known as red detuning, or a repulsive potential for $\Delta > 0$, known as blue detuning. In the far detuned limit $\Delta \gg \Omega$ (equivalent to $\delta \gg \sqrt{I}$) this potential approximates to

$$U_{\text{dip}} \approx \frac{\hbar\Gamma}{4\delta} I \quad (2.49)$$

which is inversely proportional to the detuning in linewidths. The validity of this approximation is shown graphically in Figure 2.2.

2.7 Examples of the Dipole Force

The conservative dipole potential of Eq. (2.48) and (2.49) is ubiquitous in atom-optics, and is used heavily in this thesis. It is worthwhile taking some time here to examine some examples of atoms interacting with an optical dipole potential. We will examine a repulsive barrier formed from a blue-detuned beam with $\delta > 0$, an attractive trapping potential formed from one or more red-detuned beams with $\delta < 0$, and optical lattices which are formed from two counter-propagating laser beams which interfere to create a standing wave.

2.7.1 Blue-detuned beam as an atom-optic mirror

A perfect experiment to demonstrate the conservative nature of the dipole force is that of atoms bouncing off a repulsive, blue-detuned light sheet. We used 4W of

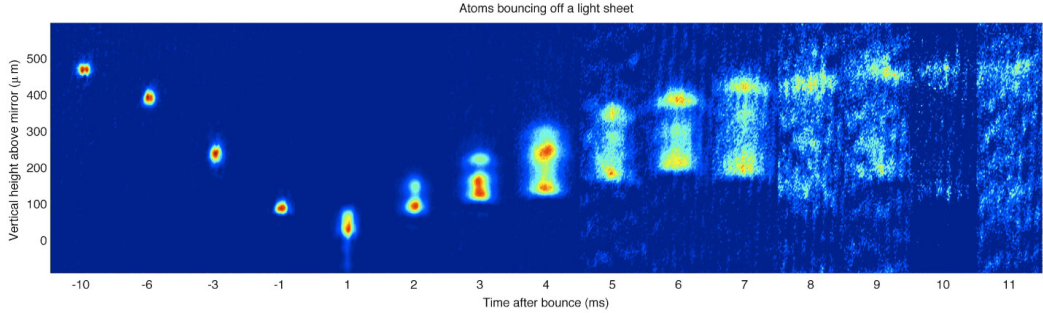


Figure 2.3: A ^{87}Rb BEC bouncing off of a blue-detuned light sheet. In contrast to the classical case, a “quantum” bounce has a less well-defined position (although the center-of-mass position is the same, by Ehrenfest’s theorem), and is a combination of Airy functions given in Eq. (2.51). This work, performed in our lab, is similar to the experiments in Ref. [28, 185, 16, 55, 11] for an optical mirror, but also has analogues in the case of ultra cold neutrons [103, 127] and photons [64]. As the reflecting barrier was not perfectly level, the atoms bounced away from the camera and thus do not reach the same average height as when they were released.

green light at 532nm (Sourced from a Coherent Verdi Laser) which was focussed into a light sheet of around $20\mu\text{m}$ thickness, via a $f=15\text{cm}$ cylindrical lens. The light sheet was positioned 0.5mm below the position where we form a ^{87}Rb Bose-Einstein condensate. This green light was shuttered so it would only turn on after the condensate was formed, otherwise stray light caused heating and prevented condensation formation. By capturing a time-series of 1ms spaced images after release of the condensate, (see Figure 2.3) we are able to observe the atoms reflecting from the blue-detuned light sheet. By comparing Eq. (2.49) to the gravitational potential energy of the atoms, we can see that the potential energy of the barrier is about 200 times the kinetic energy of the atoms at the time of impact.

The eigenstates of the free-particle on a gravitational incline in the z -direction are Airy functions [96, 24]

$$\psi_j(z) = N_j \text{Ai} \left(\frac{z}{l_g} - \alpha_j \right). \quad (2.50)$$

$$\approx \left[\frac{2\pi^2}{3(j-1/4)} \right]^{\frac{1}{6}} \text{Ai} \left(\frac{z}{l_g} - \left[\frac{3\pi}{2}(j-1/4) \right]^{\frac{2}{3}} \right) \quad (2.51)$$

where on the last line approximations to the normalisation constant and zero of the Airy function for large j are used. The wave function for the so-called "Quantum

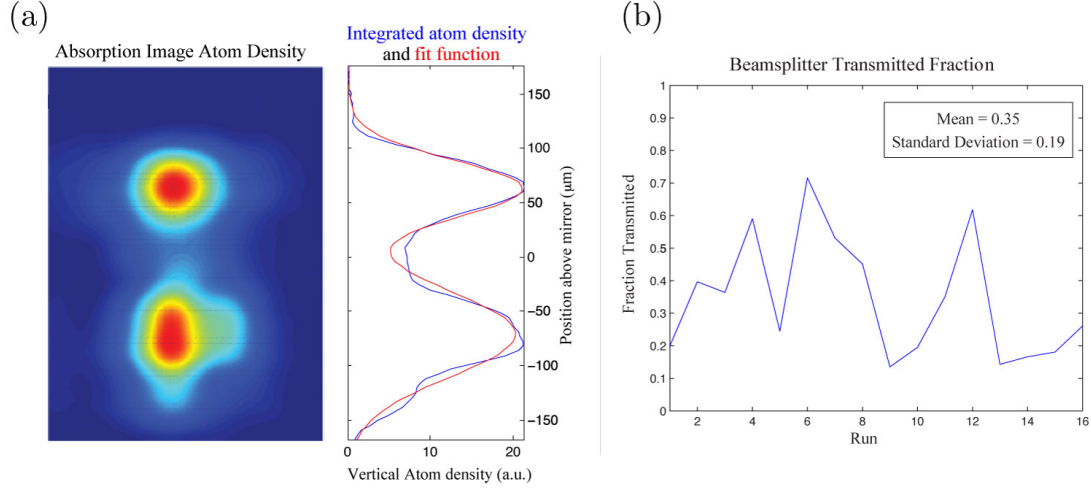


Figure 2.4: A blue-detuned light sheet was used as a matter-wave beam splitter. In (a) the bottom cloud has passed through the barrier, while the top cloud was reflected. As the transmitted fraction [shown for several realisations in (b)] depends quite sensitively [Eq. (2.53)] upon the height of the optical potential, it was not very stable. The energy of the cloud as it encountered the barrier was controlled by varying the position of the blue-detuned barrier below the position at which the BEC was formed, while the energy of the barrier was controlled by varying the intensity of the blue-detuned light. The atom cloud had been falling for 11ms at the time at which it encountered the optical potential.

"Bouncer", a free particle on an incline with an infinite potential wall trapping the particle, is a sum over those Airy functions which go to zero at the infinite wall at $z = 0$ [93]. The center-of-mass position $\langle \hat{x} \rangle$ is of course the same as the classical case, by Ehrenfest's theorem. This quantum-bouncing behaviour can be seen clearly from $t \approx 2\text{ms}$ onwards in Figure 2.3.

2.7.2 Blue-detuned beam as a vertical beamsplitter

By lowering the intensity of the beam creating the optical potential barrier until some fraction of the atoms pass by and remainder does not, we can create a matter-wave beam-splitter. An experimental realisation of this is presented in Fig. 2.4. As a first order analytic approximation we can treat it like a plane wave with incident energy $E = \frac{(\hbar k_1)^2}{2m}$ impacting upon a finite square barrier of width a and potential height V so that the transmission probability p_T is given by [219]

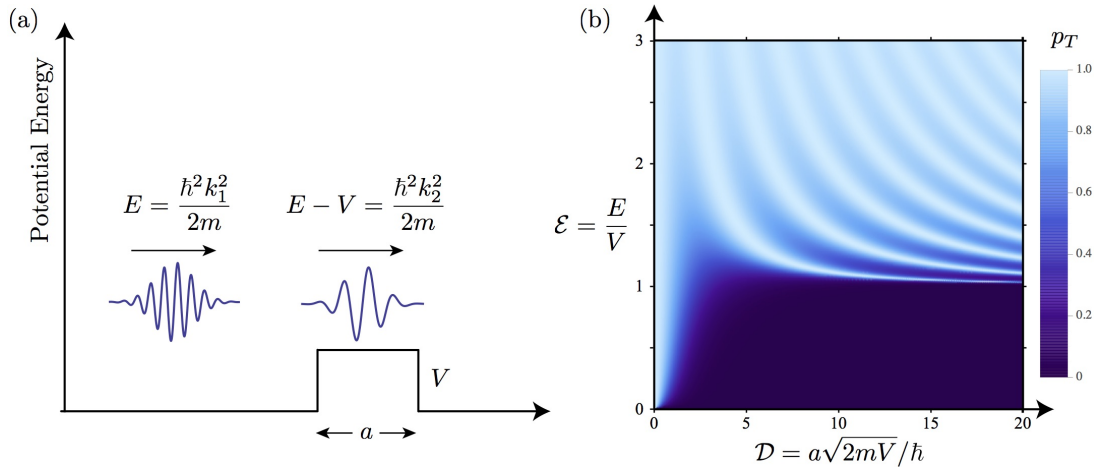


Figure 2.5: (a) Diagram illustrating transmission of a plane-wave through a square barrier of width a and potential energy height V . (b) Transmission probability p_T as a function of unitless incoming energy \mathcal{E} , and barrier width \mathcal{D} , as per Equation (2.53). Tunnelling occurs in the classically forbidden region in the bottom left of the plot where $\mathcal{E} < 1$.

$$p_T = \frac{1}{1 + \frac{1}{4} \left(\frac{k_1}{k_2} - \frac{k_2}{k_1} \right)^2 \sin^2(k_2 a)} \quad (2.52)$$

where $k_2 = \sqrt{\frac{2m(E-V)}{\hbar^2}} \leq k_1$ is the wavenumber of the matter-wave while it is on top of the potential barrier. This can be re-written in terms of the dimensionless barrier width $\mathcal{D} = a\sqrt{2mV}/\hbar$ and incoming energy $\mathcal{E} = E/V$ as

$$p_T = \frac{1}{1 + \frac{\sin^2(\mathcal{D}\sqrt{\mathcal{E}-1})}{4\mathcal{E}(\mathcal{E}-1)}} \quad (2.53)$$

This probability is illustrated in Figure 2.5. In order to realise a truly quantum beam splitter we want each atom to have roughly a 50% chance of being split either way, as opposed to simply filtering a cloud of atoms with a spread in energy into high and low energy atoms.

An advantage of such a beam splitter is a very fine dependence upon the input wave function, colloquially a 'hair trigger'. So in the first instance it could be used as a sensitive measuring device, to measure fluctuations in drop height for example. However it is also very sensitive to the properties of the blue-detuned beam used, so it could be used as a beam-measurement tool.

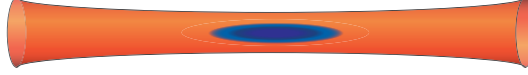


Figure 2.6: A representation of atoms suspended in a red-detuned optical waveguide.

Another possible use of such a beam splitter is atom-number squeezing. Schemes exist for the generation of NOON states $\frac{1}{\sqrt{2}}(|N,0\rangle + |0,N\rangle)$ by colliding bright matter-wave solitons with repulsive barriers [94, 26]. These NOON states can then be converted into metrologically useful squeezing by further state manipulation.

2.7.3 Red-detuned beam as a Dipole trap

A key component for the experiments in the remainder of this thesis is the horizontal optical waveguide.

For a gaussian beam with total power P , focus at the origin, Rayleigh length $x_R = \frac{\pi w_0^2}{\lambda}$ and radial width $w(x) = w_0 \sqrt{1 + \left(\frac{x}{x_R}\right)^2}$, the intensity profile is given by

$$I(x, r) = \frac{2P}{\pi w(x)^2} \exp\left(\frac{-2r^2}{w(x)^2}\right). \quad (2.54)$$

Restricting ourselves to the x - z plane we can set $r = |z|$, and introducing $P_{sat} = \frac{I_{sat}}{2} \pi w_0^2$ for $w_0 = w(0)$ we have the normalised intensity as

$$\mathcal{I}(x, z) = \frac{P}{P_{sat}} \left(\frac{w_0}{w(x)}\right)^2 \exp\left(\frac{-2z^2}{w(x)^2}\right). \quad (2.55)$$

The dipole-force potential energy landscape is given by Eq. (2.49),

$$U_{dip} \approx \frac{\hbar\Gamma}{4\delta} \mathcal{I}(x, z) \quad (2.56)$$

$$= \frac{\hbar\Gamma}{4\delta} \frac{P}{P_{sat}} \left(\frac{w_0}{w(x)}\right)^2 \exp\left(\frac{-2z^2}{w(x)^2}\right) \quad (2.57)$$

but for the total potential energy we must add gravity,

$$U_{tot} = U_{dip} - mgz \quad (2.58)$$

$$= \frac{\hbar\Gamma}{4\delta} \frac{P}{P_{sat}} \left(\frac{w_0}{w(x)}\right)^2 \exp\left(\frac{-2z^2}{w(x)^2}\right) - mgz. \quad (2.59)$$

To find the vertical minimum $z_{min}(x)$ in this potential we must set the vertical com-

ponent of the force equal to zero,

$$0 = -\frac{dU_{tot}}{dz} \quad (2.60)$$

$$= mg + \frac{\hbar\Gamma}{\delta} \frac{P}{P_{sat}} \left(\frac{w_0}{w(x)} \right)^2 \frac{z_{min}}{w(x)^2} \exp \left(\frac{-2z_{min}^2}{w(x)^2} \right). \quad (2.61)$$

This equation has the real solution

$$z_{min}(x) = \frac{i}{2} \frac{w(x)}{w_0} \sqrt{W \left(-4f^2 \left[\frac{w(x)}{w_0} \right]^6 \right)} \quad (2.62)$$

where we have defined the unitless constant

$$f \equiv \frac{mgw_0}{\hbar\Gamma} \frac{\delta}{P/P_{sat}} \quad (2.63)$$

and $W(\xi)$ is the Lambert W-function, i.e. the solution to the transcendental equation

$$\xi = W(\xi)e^{W(\xi)}. \quad (2.64)$$

For $W(\xi)$ to be real we must have its argument $\xi \geq -\frac{1}{e}$. This gives us the criteria for a trapping potential to exist for the given parameters,

$$\left(\frac{w(x)}{w_0} \right)^3 f < \frac{1}{2\sqrt{e}} \quad (2.65)$$

$$\frac{mgw_0}{\hbar\Gamma} \frac{\delta}{P/P_{sat}} \left[1 + \left(\frac{x}{x_R} \right)^2 \right]^{\frac{3}{2}} < \frac{1}{2\sqrt{e}} \quad (2.66)$$

which for $x = 0$ gives the criterion $f < 1/2\sqrt{e}$ or

$$\frac{mgw_0^3}{\hbar\Gamma} \frac{I_{sat}\delta}{P} < \frac{1}{\pi\sqrt{e}} \quad (2.67)$$

$$\approx 0.2 \quad (2.68)$$

For small $|\xi|$, we have $e^\xi \approx 1$ and so we can approximate $W(\xi) \approx \xi$. In this small f limit the solution becomes

$$z_{min}(x) \approx - \left(\frac{w(x)}{w_0} \right)^4 f. \quad (2.69)$$

As the width of the gaussian beam is given by $w(x) = w_0 \sqrt{1 + \left(\frac{x}{x_R} \right)^2}$ for the Rayleigh

length $x_R = \frac{\pi w_0^2}{\lambda}$, we have

$$z_{\min}(x) \approx - \left(1 + \left[\frac{x}{x_R} \right]^2 \right)^2 f \quad (2.70)$$

$$\approx - \left(1 + 2 \left[\frac{x}{x_R} \right]^2 \right) f \quad (2.71)$$

$$= - \frac{mgw_0}{\hbar\Gamma} \frac{\delta}{P/P_{sat}} \left(1 + 2 \left[\frac{x}{x_R} \right]^2 \right) \quad (2.72)$$

$$= - \frac{mgw_0}{\hbar\Gamma} \frac{\delta}{P/P_{sat}} \left(1 + 2 \left[\frac{x\lambda}{\pi w_0^2} \right]^2 \right). \quad (2.73)$$

The curvature κ of the potential minimum z_{\min} near $x = 0$ is given by

$$\kappa = \frac{d^2 z_{\min}}{dx^2} \Big|_{x=0} \quad (2.74)$$

$$= - \frac{4f}{x_R^2} \quad (2.75)$$

$$= - \frac{2\lambda^2}{\pi w_0} \frac{mg}{\hbar\Gamma} \frac{\delta}{P} I_{sat} \quad (2.76)$$

from which it can be seen that to reduce the curvature of the waveguide potential energy minimum, we would like the largest possible waist w_0 and power P in the beam.

2.7.4 Two photon transitions

It is possible to create a system whereby single photon transitions (which involve spontaneous emission) are highly improbable, while two-photon transitions (involving stimulated absorption and emission) are the dominant interaction. Such schemes depend upon a three-level system in which an intermediate atomic state is never very highly populated, but simply couples the two other states. Figure 2.7 shows a ‘lambda’ type of three-level system in which two meta-stable ground states $|1\rangle$ and $|2\rangle$ are coupled via a higher-energy excited state $|e\rangle$ and the exchange of two photons. If the detuning Δ_1 is chosen such that the lasers are far-detuned from the excited state (i.e. there will be no macroscopic population of the excited state followed by spontaneous emission) then the system can be again treated as a two-level system via adiabatic elimination. This is well treated in several places [5, 62]. The result is that the effective two-level Rabi frequency is given by

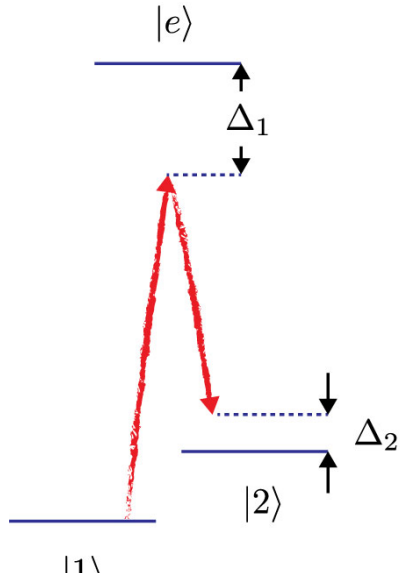


Figure 2.7: Energy level diagram for a 3-level system undergoing a 2-photon transition.

$$\Omega_{2,\text{eff}} = \frac{\Omega_{1e}\Omega_{2e}}{\Delta_1} \quad (2.77)$$

while the effective two-level detuning is given simply by Δ_2 . The advantage to such a scheme is that stimulated processes dominate over spontaneous ones, allowing complete control over a coherent system over longer timescales. Such a scheme is used in Raman, and Bragg transitions, and even the dipole force can be formulated in this way.

2.7.5 Optical Lattices

So let's say you shine two plane-wave laser beams with slightly different frequencies (so that k is roughly the same for both) in opposite directions on top of one another. The resulting electric field

$$E = E_1 \cos(w_1 t - \mathbf{k} \cdot \mathbf{r} - \phi) + E_2 \cos(w_2 t + \mathbf{k} \cdot \mathbf{r} + \phi) \quad (2.78)$$

when squared to give the intensity, and averaged over many optical periods, gives

$$I = \frac{c\epsilon_0}{2} |E|^2 \quad (2.79)$$

$$= \frac{c\epsilon_0}{2} \left(\frac{E_1^2 + E_2^2}{2} + E_1 E_2 \cos(2\mathbf{k}\cdot\mathbf{r} - [w_2 - w_1]t + \phi) \right) \quad (2.80)$$

$$= \frac{I_1 + I_2}{2} + \sqrt{I_1 I_2} \cos(2\mathbf{k}\cdot\mathbf{r} - [w_2 - w_1]t + \phi) \quad (2.81)$$

$$= \frac{I_1 + I_2}{2} + \sqrt{I_1 I_2} \cos(2\mathbf{k}\cdot[\mathbf{r} - \mathbf{r}_0 + \mathbf{v}_L t]) \quad (2.82)$$

which is a lattice with a wavevector $\mathbf{k}_L = 2\mathbf{k}$, moving with a phase velocity given by $\mathbf{k}_L \cdot \mathbf{v}_L = w_1 - w_2$, and with a phase offset determined by the location of an arbitrary reference position $\phi = \mathbf{k}_L \cdot \mathbf{r}_0$. According to Eq. (2.49) and assuming $I_1 = I_2 = I$ this gives a lattice potential for the atoms of

$$U_{\text{dip}} \approx \frac{\hbar\Gamma\mathcal{I}}{4\delta} \{1 + \cos(2\mathbf{k}\cdot\mathbf{r} - [w_2 - w_1]t + \phi)\} \quad (2.83)$$

$$\equiv \frac{U_0}{2} [1 + \cos(2\mathbf{k}\cdot\mathbf{r} - [w_2 - w_1]t + \phi)] \quad (2.84)$$

For zero phase offset $\phi = 0$ and in the Doppler-shifted velocity frame in which equal frequencies are coming from either direction, this becomes the standing wave

$$U_{\text{dip}} = \frac{U_0}{2} [1 + \cos(2\mathbf{k}\cdot\mathbf{r})]. \quad (2.85)$$

2.7.6 Bragg diffraction

By briefly applying an optical lattice to the atoms (with the correct resonance condition), it is possible to split the cloud into two momentum states, separated by $2n$ photon recoils, where the Bragg order n is an integer. This can also be treated as a $2n$ -photon transition. The atoms which are kicked by the Bragg lattice obey the same energy and momentum conservation laws as a tennis ball bouncing off a brick wall, i.e. in the lattice frame it acts like a perfectly elastic collision with an immovable lattice. This picture can be handy to keep in mind.

2.7.6.1 Bragg resonance

The de Broglie wavevector of an atom moving at velocity \mathbf{v}_{atom} is given by

$$m\mathbf{v}_{\text{atom}} = \hbar\mathbf{k}_{\text{atom}}$$

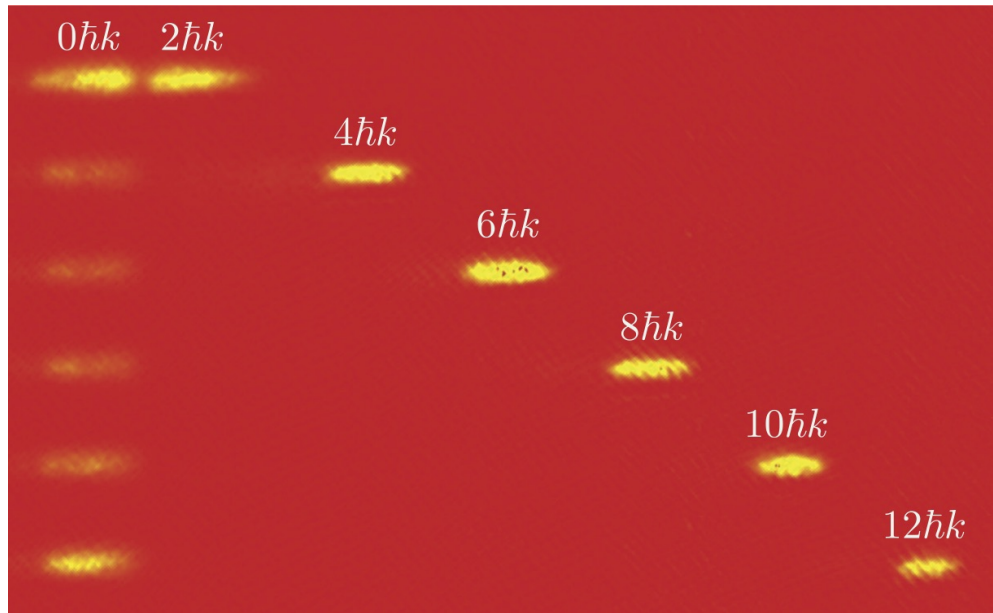


Figure 2.8: Demonstration of n -th order Bragg transitions along the waveguide for $n = 1$ to $n = 6$.

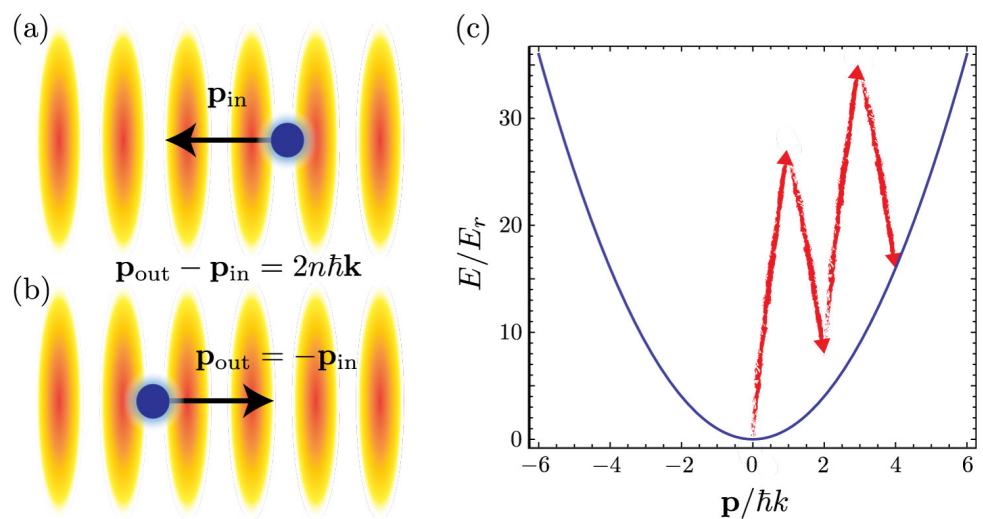


Figure 2.9: (a) In the frame of the lattice, the atom has a certain incoming momentum. (b) If the incoming momentum is an even-integer multiple of the photon momentum $\hbar k$ then the atom can be kicked by the lattice through the exchange of $2n$ photons, reversing its initial momentum. (c) Energy diagram for the Bragg resonance of a $4\hbar k$ transition, in the frame in which the atom is initially at rest.

Now in the velocity frame of the lattice, we want $\mathbf{v}_{atom} = \pm \mathbf{v}_L$ for atoms coming towards and reflecting off from the lattice respectively (where \mathbf{v}_L is the velocity of the lattice in the frame in which the atoms are initial stationary), so

$$\hbar \mathbf{k}_{atom} = m \mathbf{v}_L \quad (2.86)$$

$$= \frac{m \Delta \omega}{\mathbf{k}_L} \quad (2.87)$$

$$= \frac{m \Delta \omega}{2 \mathbf{k}} \quad (2.88)$$

for a lattice with frequency difference $\Delta\omega$ in the frame of the atoms.

We also want the constructive resonance condition³ for an n th order kick (for lattice wavelength $\Lambda = \frac{2\pi}{|\mathbf{k}_L|} = \frac{\pi}{|\mathbf{k}|}$)

$$n \lambda_{atom} = 2 \Lambda \quad (2.89)$$

$$\therefore \mathbf{k}_{atom} = \frac{n \mathbf{k}_L}{2} \quad (2.90)$$

$$= n \mathbf{k} \quad (2.91)$$

which simply says that the wavefunction of atoms reflecting from successive peaks of the lattice must add constructively. Putting Eq. (2.86) and (2.91) together we have

$$\hbar n \mathbf{k} = \frac{m \Delta \omega}{2 \mathbf{k}} \quad (2.92)$$

$$\Delta \omega = \frac{2n\hbar |\mathbf{k}|^2}{m} \quad (2.93)$$

$$= 4n\omega_r \quad (2.94)$$

where we have defined the recoil frequency to be $\omega_r \equiv \frac{\hbar |\mathbf{k}|^2}{2m}$. In the case where the two beams are not counter-propagating, this result generalises to

$$\Delta \omega = 4n\omega_r \sin^2 \left(\frac{\theta}{2} \right) \quad (2.95)$$

where θ is the angle between the two beams which make up the lattice, i.e. $\theta = 0$ for two overlapping, co-propagating beams and $\theta = \pi$ for counter-propagating beams. This means that the energy transferred is given by (number of 2-photon

³The constructive resonance condition here is different to the case of an optical cavity because the reflective surfaces in a cavity face opposite directions, so only one gets a π phase shift for reflection, whereas if both cavity mirrors pointed in the same direction then the resonance conditions would be the same as for this Bragg case.

pairs) \times (energy per 2-photon pair):

$$\begin{aligned}\Delta E &= n\hbar\Delta\omega \\ &= 4n^2\hbar\omega_r \\ &= 4n^2E_r\end{aligned}$$

where $E_r \equiv \hbar\omega_r$. This expression is quadratic in n , as it must be in order to satisfy the dispersion relation for matter, $E = \frac{|\mathbf{p}|^2}{2m}$ as depicted in Figure 2.9 (c).

2.7.6.2 Rabi frequency

As n -th order Bragg diffraction is a $2n$ photon process, the laser power required to drive higher-order transitions increases quite rapidly. The comparable expression to Eq. 2.77 for the effective $2n$ -photon Rabi frequency is [233]

$$\Omega_{2n,\text{eff}} = \frac{\Omega_{2,\text{eff}}^n}{(8\omega_r)^{n-1} [(n-1)!]^2}. \quad (2.96)$$

2.7.7 Bloch oscillations

If we instead turn up the lattice intensity slowly, while the lattice is co-moving with the atoms, we can load the atoms into the new perturbed energy eigenstates, which are depicted in Figure 2.10. To work out what these are exactly, let us consider an atom in one dimension experiencing a periodic potential caused by the optical lattice,

$$U_{\text{dip}}(\mathbf{r}) = \frac{U_0}{2} [1 + \cos(2\mathbf{k} \cdot \mathbf{r})] \quad (2.97)$$

$$= \frac{U_0}{4} [2 + e^{2\mathbf{k} \cdot \mathbf{r}} + e^{-2\mathbf{k} \cdot \mathbf{r}}]. \quad (2.98)$$

The eigenfunctions of the system are thus subject to the following Schrödinger equation

$$H\psi_n(\mathbf{r}) = \left[\frac{\hat{p}^2}{2m} + U_{\text{dip}}(\mathbf{r}) \right] \psi_n(\mathbf{r}) \quad (2.99)$$

$$= E_n \psi_n(\mathbf{r}) \quad (2.100)$$

By Floquet's theorem, the eigenfunctions can be expressed as a plane wave $e^{\frac{i\mathbf{q}\cdot\mathbf{r}}{\hbar}}$ multiplied by a function $\phi_n(\mathbf{q}, \mathbf{r})$ with the periodicity of the lattice

$$\psi_n(\mathbf{q}, \mathbf{r}) = e^{\frac{i\mathbf{q}\cdot\mathbf{r}}{\hbar}} \phi_n(\mathbf{q}, \mathbf{r}).$$

As $\phi_n(\mathbf{q}, \mathbf{r})$ has the periodicity of the lattice (i.e. repeats every $2\mathbf{k} \cdot \mathbf{r}$) we can write it as the following sum,

$$\phi_n(\mathbf{q}, \mathbf{r}) = \sum_{j=1}^{\infty} c_j(\mathbf{q}, \mathbf{r}) e^{ij2\mathbf{k}\cdot\mathbf{r}}$$

so that

$$\psi_n(\mathbf{q}, \mathbf{r}) = e^{\frac{i\mathbf{q}\cdot\mathbf{r}}{\hbar}} \sum_{j=1}^{\infty} c_j(\mathbf{q}, \mathbf{r}) e^{ij2\mathbf{k}\cdot\mathbf{r}} \quad (2.101)$$

$$= \sum_{j=1}^{\infty} c_j(\mathbf{q}, \mathbf{r}) e^{i(2j\mathbf{k} + \mathbf{q}/\hbar) \cdot \mathbf{r}} \quad (2.102)$$

and Eq. (2.100) becomes

$$H\psi_n(\mathbf{q}, \mathbf{r}) = \left[\frac{1}{2m}(q + 2\hbar kj)^2 + U_{\text{dip}}(\mathbf{r}) \right] \psi_n(\mathbf{q}, \mathbf{r}) \quad (2.103)$$

$$= \left[\frac{1}{2m}(q + 2\hbar kj)^2 + \frac{U_0}{4} (2 + e^{2\mathbf{k}\cdot\mathbf{r}} + e^{-2\mathbf{k}\cdot\mathbf{r}}) \right] \sum_{j=1}^{\infty} c_j(\mathbf{q}, \mathbf{r}) e^{i(2j\mathbf{k} + \mathbf{q}/\hbar) \cdot \mathbf{r}} \quad (2.104)$$

$$\therefore H\phi_n(\mathbf{q}, \mathbf{r}) = \left[\frac{1}{2m}(q + 2\hbar kj)^2 + \frac{U_0}{4} (2 + e^{2\mathbf{k}\cdot\mathbf{r}} + e^{-2\mathbf{k}\cdot\mathbf{r}}) \right] \phi_n(\mathbf{q}, \mathbf{r}) \quad (2.105)$$

This Hamiltonian can be represented in matrix form as

$$H = \frac{U_0}{2} \mathbb{1} + \begin{pmatrix} \ddots & \frac{U_0}{4} & 0 & 0 & 0 & \dots & 0 & 0 & 0 \\ \frac{U_0}{4} & \left(\frac{q}{\hbar k} - j\right)^2 & \frac{U_0}{4} & 0 & 0 & & & 0 & 0 \\ 0 & \frac{U_0}{4} & \ddots & \ddots & \ddots & & & & 0 \\ 0 & 0 & \ddots & \left(\frac{q}{\hbar k} - 1\right)^2 & \frac{U_0}{4} & 0 & & & \vdots \\ 0 & 0 & \ddots & \frac{U_0}{4} & \left(\frac{q}{\hbar k}\right)^2 & \frac{U_0}{4} & \ddots & 0 & 0 \\ \vdots & & & 0 & \frac{U_0}{4} & \left(\frac{q}{\hbar k} + 1\right)^2 & \ddots & 0 & 0 \\ 0 & & & & \ddots & \ddots & \ddots & \frac{U_0}{4} & 0 \\ 0 & 0 & & & 0 & 0 & \frac{U_0}{4} & \left(\frac{q}{\hbar k} + j\right)^2 & \frac{U_0}{4} \\ 0 & 0 & 0 & \dots & 0 & 0 & 0 & \frac{U_0}{4} & \ddots \end{pmatrix} \quad (2.106)$$

To find the eigenenergies $E_n(q)$ we must find the roots of the polynomial

$$\|H - E_n(q)\mathbb{1}\| = 0.$$

In practice this is difficult for the full Hamiltonian, but luckily it is sufficient to solve the same problem for an $(2l+1) \times (2l+1)$ truncated Hamiltonian instead of the $\infty \times \infty$ Hamiltonian, as long as $l \gg n$ [104, 227, 52]. In Figure 2.10 I have truncated to $l = 10$. The parabolic energy dispersion relation at zero lattice intensity, $E = (q + n\hbar k)^2/2m$, contains several degeneracies, some at $q = 0$ for $\pm n \neq 0$ and some at $q = \hbar k$ for all n . The end result of increasing the lattice depth is the creation of several avoided crossings, as seen in Figure 2.10(b).

Two interesting cases deserve special mention. For $E_n(q) \gg U_0$, i.e. a low lattice depth or a high relative velocity between the atoms and the lattice, the atoms simply experience the average value of the lattice depth, and so their energy is shifted by the average Stark shift of the lattice, $U_0/2$, i.e.

$$E_n(q) \approx \begin{cases} (n + \frac{|q|}{\hbar k})^2 E_r + \frac{U_0}{2} & n \text{ even} \\ (n + 1 - \frac{|q|}{\hbar k})^2 E_r + \frac{U_0}{2} & n \text{ odd} \end{cases} \quad (2.107)$$

and as such the atoms are not trapped by the lattice. For $E_n(q) \ll U_0$ i.e. a high lattice depth and the lattice and atom frames are coincident, the lower energy levels correspond to tight binding in lattice sites which look approximately like harmonic oscillators with $\omega_{HO} = 2\sqrt{U_0\omega_r/\hbar}$, and thus have energies

$$E_n(q) \approx (2n + 1)\sqrt{U_0 E_r} \quad (2.108)$$

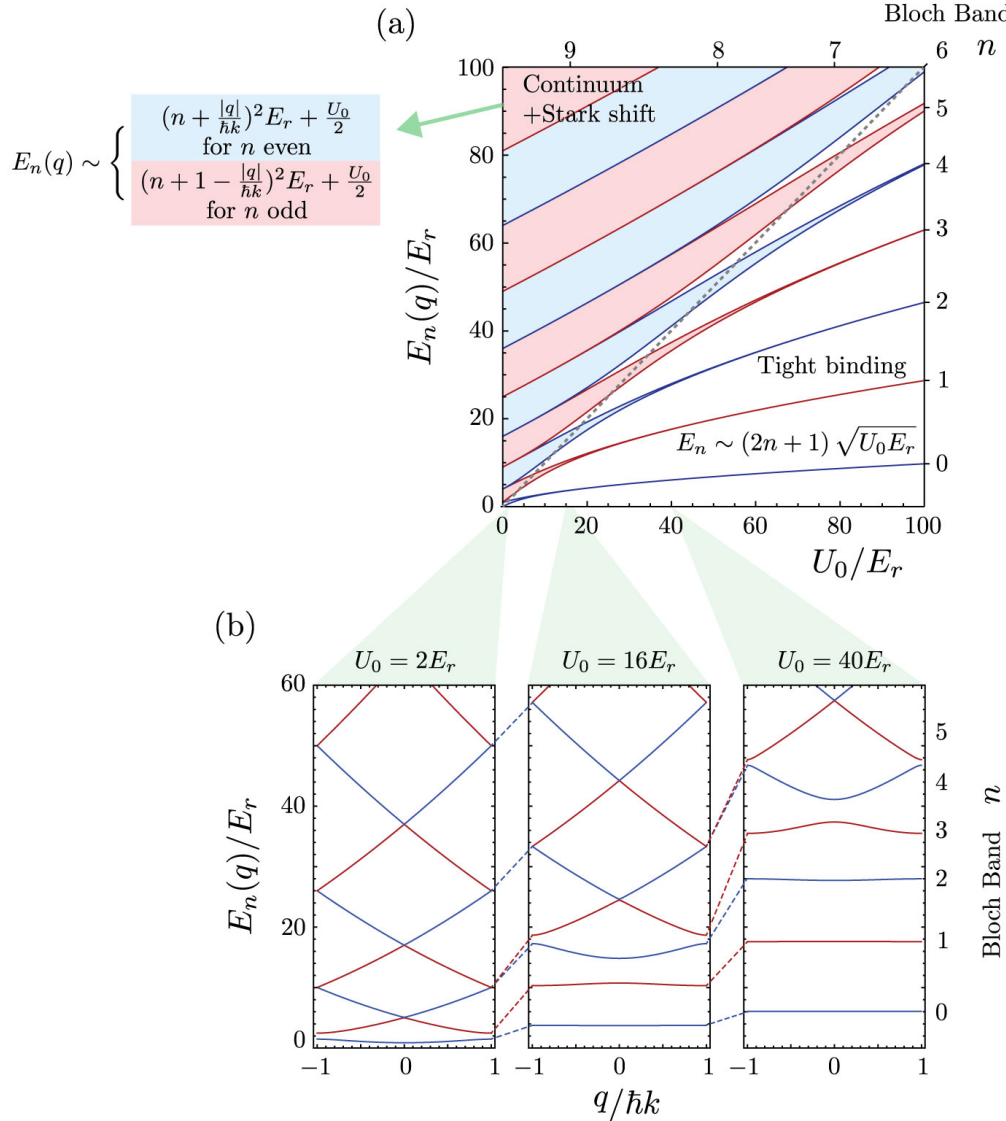


Figure 2.10: Energy $E_n(q)$ of atoms in the n th Bloch band of an optical lattice with quasi momentum q . (a) Diagram illustrating the band structure of moving atoms in the presence of an optical lattice. In the top-left half, where the atoms have more kinetic energy than the lattice depth, $E_n(q) > U_0$, the atoms propagate freely albeit with their energy Stark-shifted by the average value of the lattice intensity. In the bottom right half, where the lattice is deeper than the kinetic energy of the atoms (i.e. each atom is tightly bound to a given lattice site), the energy levels separate out and discretise according to the levels of a harmonic oscillator. After Ref. [227]. (b) Levels splitting as a function of quasi momentum q for several lattice depths. With almost no lattice, kinetic energy follows the familiar quadratic relationship with momentum. As the lattice becomes deeper, the discrete harmonic-oscillator-like energy levels begin to appear. After Ref. [104].

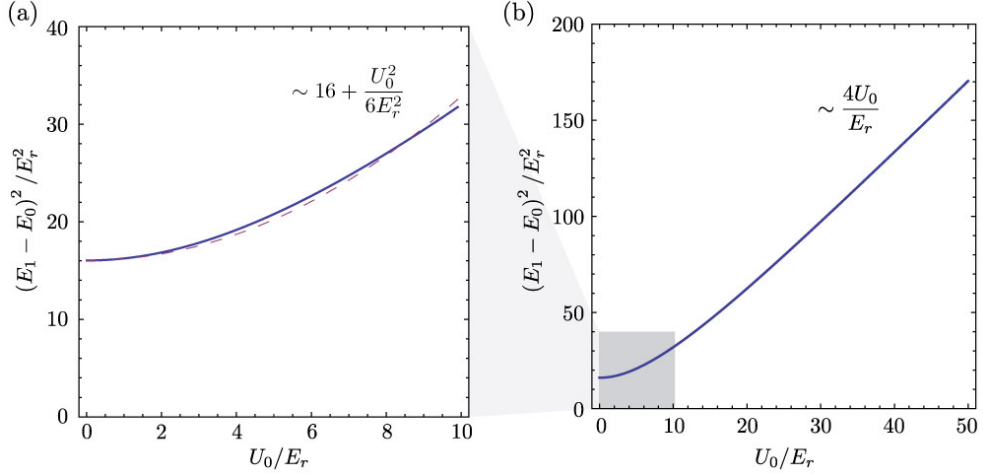


Figure 2.11: Plots of $(E_1 - E_0)^2 / E_r^2$ at $q = 0$ against U_0 / E_r , in order to examine the right-hand side of Eq. (2.109), the adiabaticity criterion for loading into the lowest band of a Bloch lattice. (a) For small U_0 the RHS of the criterion is quadratic with increasing lattice depth, whereas (b) for large depth, it is linear again. The dashed line in (a) is a quadratic approximation $\sim 16 + \frac{U_0^2}{6E_r^2}$.

2.7.7.1 Adiabatic loading

In order to adiabatically load atoms which are stationary in the lattice frame it is necessary to raise the lattice intensity sufficiently slowly. Denoting the eigenstates by $|n, q\rangle$, an exact adiabatic loading criterion is given by the formula [67, 145]

$$\left| \langle 1, q | \frac{\partial H}{\partial t} | 0, q \rangle \right| \ll \frac{(E_1(q) - E_0(q))^2}{\hbar}. \quad (2.109)$$

The left hand side of this equation can be seen from the matrix in Eq. (2.106) to be

$$\left| \langle 1, q | \frac{\partial H}{\partial t} | 0, q \rangle \right| = \frac{1}{4} \frac{dU_0}{dt} \quad (2.110)$$

The energy difference on the right hand side of Eq. (2.109) will be maximum at $q = 0$, i.e. the atoms are precisely stationary in the lattice frame, and it can be determined approximately by truncating the Hamiltonian as above. The result of this has been plotted in Figure 2.11, but we can employ the previous two simplifying cases (low or high lattice depth U_0) and examine the behaviour in each. In the low lattice depth $U_0 \lesssim 10E_r$ regime we have⁴

⁴The quadratic term should actually be the Stark shift squared, $\frac{U_0^2}{4}$, but empirically $\frac{U_0^2}{6}$ approximates the function better over a larger range.

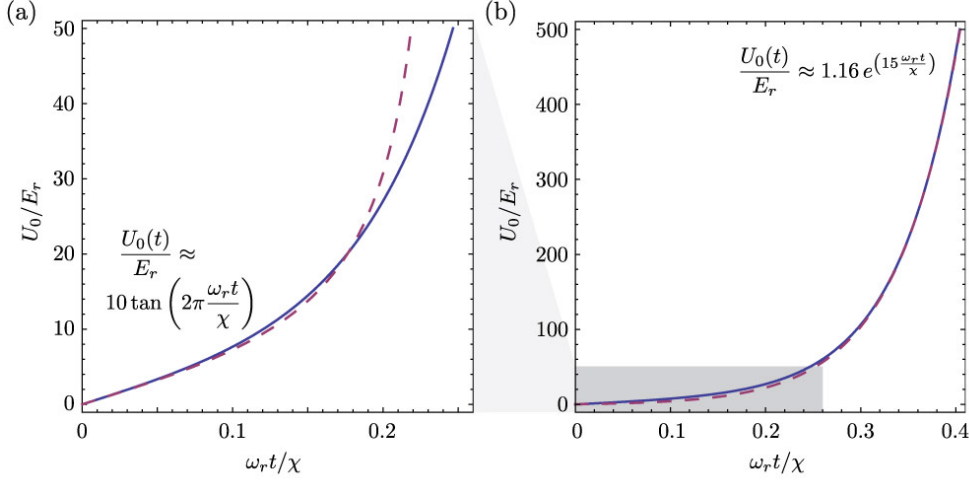


Figure 2.12: Plot of the lattice depth $U_0(t)/E_r$ over time for the fastest possible load rate, while satisfying the adiabaticity criterion Eq. (2.109) by a factor of χ . The solid line in both subfigures is numerically evaluated. The dashed line in (a) is the approximation for small $U_0 \lesssim 20$ of $U_0(t) \approx 10E_r \tan\left(2\pi \frac{\omega_r t}{\chi}\right)$, while the dashed line in (b) is the approximation for large $U_0 \gtrsim 100$ of $U_0(t) \approx 1.16 E_r e^{\left(15 \frac{\omega_r t}{\chi}\right)}$.

$$(E_1(0) - E_0(0))^2 \approx 16E_r^2 + \frac{U_0^2}{6} \quad (2.111)$$

and so the adiabatic loading criterion (2.109) becomes

$$\frac{dU_0}{dt} \ll \frac{1}{\hbar} \left(64E_r^2 + \frac{2U_0^2}{3} \right) \quad (2.112)$$

Assuming “ \ll ” implies at least factor of χ difference, (for example $\chi = 10$) then the maximum increase rate is given by

$$\left. \frac{dU_0}{dt} \right|_{\max} \approx \frac{1}{\chi \hbar} \left(64E_r^2 + \frac{2U_0^2}{3} \right) \quad (2.113)$$

$$\therefore U_{0\max}(t) = 4\sqrt{6}E_r \tan\left(\frac{8}{\chi} \sqrt{\frac{2}{3}} \omega_r t\right) \quad (2.114)$$

$$\approx 10E_r \tan\left(2\pi \frac{\omega_r t}{\chi}\right) \quad (2.115)$$

In the large U_0 limit the maximum lattice depth increase rate is proportional to the current lattice depth so we would expect an exponential rise. Heuristically this rise fits well to the relation

$$U_0(t) \approx 1.16 E_r e^{(15 \frac{\omega_r t}{\chi})} \quad (2.116)$$

in the large U_0 limit, as shown in Figure 2.12 (b).

2.7.7.2 Adiabatic acceleration

Once the lattice is loaded, we would like to accelerate it along with the atoms we have loaded into it. In order to accelerate the atoms without allowing them to fall behind, we have another adiabaticity criterion to follow. We want the atoms to remain in the lowest Bloch band and oscillate in quasimomentum q . As the atoms reach $\mathbf{q} = \hbar\mathbf{k}$ they should be Bragg-kicked back to $\mathbf{q} = -\hbar\mathbf{k}$, and the acceleration can continue. The probability for this to fail in one Bloch oscillation is given by the Landau-Zener formula

$$P_{LZ} = e^{-\frac{\pi}{16} \left[\frac{E_1(\hbar k) - E_0(\hbar k)}{E_r} \right]^2 \omega_r \tau_b} \quad (2.117)$$

where τ_b is the time for one Bloch oscillation. This formula again involves the difference in energy between the two lowest Bloch bands, but this time at the edges of $q = \pm\hbar k$ instead of at the centre, as this is where the Bragg transition will occur. Casting the problem in terms of the acceleration a_b we apply to the Bloch lattice, we can re-write $\omega_r \tau_b = a_r / a_b$ for a newly-defined recoil acceleration $a_r \equiv \frac{\hbar^2 k^3}{m^2}$. So the probability can also be written as

$$P_{LZ} = e^{-\frac{\pi}{16} \left[\frac{E_1(\hbar k) - E_0(\hbar k)}{E_r} \right]^2 \frac{a_r}{a_b}} \quad (2.118)$$

Now the probability for n_b successful Bloch oscillations is

$$P_{n_b} = (1 - P_{LZ})^{n_b} \quad (2.119)$$

$$\approx 1 - n_b P_{LZ} \quad (2.120)$$

where the approximation is for small probability of failure P_{LZ} on each oscillation. So we want $n_b P_{LZ}$ to be small. The energy part of the exponential in Eq. (2.118) is plotted in Figure 2.13 (a) it is reasonably well approximated for small lattice depths $U_0 \lesssim 10E_r$ by the average stark shift squared, $[E_1(\hbar k) - E_0(\hbar k)]^2 \approx U_0^2/4$. In this regime the probability of n_b successful Bloch oscillations is given by

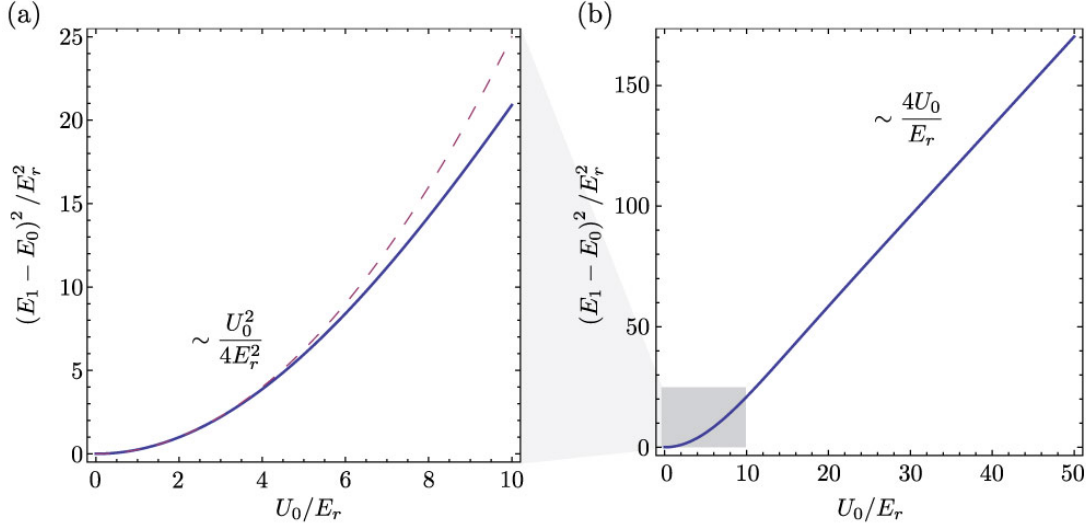


Figure 2.13: Plots of $(E_1 - E_0)^2 / E_r^2$ at $q = \hbar k$ against U_0 / E_r , in order to examine the Landau-Zener formula [Eq. (2.118)], the criterion for remaining in the lowest band of a Bloch lattice while accelerating the lattice. (a) For small U_0 the energy difference squared is quadratic with increasing lattice depth, whereas (b) for large depth, it is linear again. The dashed line in (a) is the quadratic approximation $\frac{U_0^2}{4E_r^2}$.

$$P_{n_b} \approx 1 - n_b e^{-\frac{\pi}{64} \left(\frac{U_0}{E_r} \right)^2 \frac{a_r}{a_b}}. \quad (2.121)$$

For the probability of failure to remain at the same small value we must require that

$$\frac{U_0^2}{a_b} \ln n_b = \text{constant} \quad (2.122)$$

and so for a constant number of Bloch oscillations n_b , the maximum adiabatic Bloch acceleration rate a_b scales quadratically with lattice depth, and hence also scales quadratically with available laser power, in this small lattice depth regime of $U_0 \lesssim 10E_r$. This agrees with previous experimental results (see Fig. 12 of Ref. [184]).

For higher lattice depths the energy difference squared becomes linear, $[E_1(\hbar k) - E_0(\hbar k)]^2 \approx 4U_0 E_r$, [see Fig. 2.13(b)] and so the probability tends towards

$$P_{n_b} \approx 1 - n_b e^{-\frac{\pi}{4} \frac{U_0}{E_r} \frac{a_r}{a_b}}. \quad (2.123)$$

In this case, for the probability of failure to remain at the same small value we must require that

$$\frac{U_0}{a_b} \ln n_b = \text{constant} \quad (2.124)$$

and so for a constant number of Bloch oscillations n_b , the maximum adiabatic Bloch acceleration rate a_b scales linearly with lattice depth, and hence also scales linearly with available laser power, in this large lattice depth regime of $U_0 \gtrsim 10E_r$.

2.8 Scattering Force

The scattering force [the first term of Eq. (2.47)] for a two level atom is conveniently given by the momentum of the absorbed photon $\mathbf{p} = \hbar\mathbf{k}$ times the scattering rate R_{scatt} for a two-level system

$$\mathbf{F}_{scatt} = \frac{\hbar\mathbf{k}\Gamma}{2} \frac{\Omega^2}{\Delta^2 + \frac{\Omega^2}{2} + \frac{\Gamma^2}{4}} \quad (2.125)$$

$$= \frac{\hbar\mathbf{k}\Gamma}{2} \frac{\mathcal{I}}{1 + \delta^2 + \mathcal{I}} \quad (2.126)$$

The scattering rate (number of photons scattered per atom per unit time) is then given by

$$R_{scatt} = \frac{\Gamma}{2} \frac{\Omega^2}{\Delta^2 + \frac{\Omega^2}{2} + \frac{\Gamma^2}{4}} \quad (2.127)$$

$$= \frac{\Gamma}{2} \frac{\frac{I}{I_{sat}}}{1 + \frac{I}{I_{sat}} + \left(\frac{2\Delta}{\Gamma}\right)^2} \quad (2.128)$$

$$= \frac{\Gamma}{2} \frac{\mathcal{I}}{1 + \mathcal{I} + \delta^2} \quad (2.129)$$

The scattering force is important for laser-cooling of atoms, and must be considered as a source of unwanted heating when using dipole potentials. The scattering rate also determines how much light is redirected by a cloud of atoms during absorption imaging.

2.8.1 Magneto-Optical Trapping

The Magneto-Optical Trap (MOT) has been a mainstay of cold-atom physics since its realisation in 1987 [193]. In a 3D MOT (depicted in Figure 2.14) atoms are collected and cooled thanks to the scattering force with a combination of the Doppler and Zeeman effects. The scattering occurs from six optical beams of the correct polarisation, coming in along the positive and negative x , y and z axes. These beams are red-detuned from resonance so that the Doppler shift will bring them closer to resonance as the atom is moving towards a given beam. Near the centre of the MOT the atoms experience a large, linear magnetic field gradient thanks to the quadrupole coil arrangement, which crosses through zero magnetic field at the centre of the trap. The important results are derived elsewhere [85, 168] and shown in Fig. 2.14.

2.8.2 Imaging

The scattering rate is also important in absorption and fluorescence imaging. In absorption imaging, near-resonant light is incident upon a cloud of atoms. The atoms absorb some of this light and scatter it in a random direction. Here we assume all of this light is lost, and only the un-scattered light remains, and is captured on the camera. Thus we take a picture of the “shadow” of the atoms. The intensity of the light, with photons of energy $E_\nu = \hbar\omega$ passing through a given area A , is

$$I = \frac{E_\nu}{A} \times \frac{\text{number of photons}}{\text{time}} \quad (2.130)$$

and this will decrease as it passes through a cloud of two-level atoms as

$$\frac{dI}{dz} = \frac{E_\nu}{A} \times \underbrace{\frac{\text{number of photons}}{\text{time} \times \text{number of atoms}}}_{R_{scatt}} \times \underbrace{\frac{\text{number of atoms}}{\text{volume}}}_{\rho} \times A \quad (2.131)$$

$$= E_\nu \times R_{scatt} \times \rho \quad (2.132)$$

for 3D density of atoms ρ . Inserting Eq. (2.129),

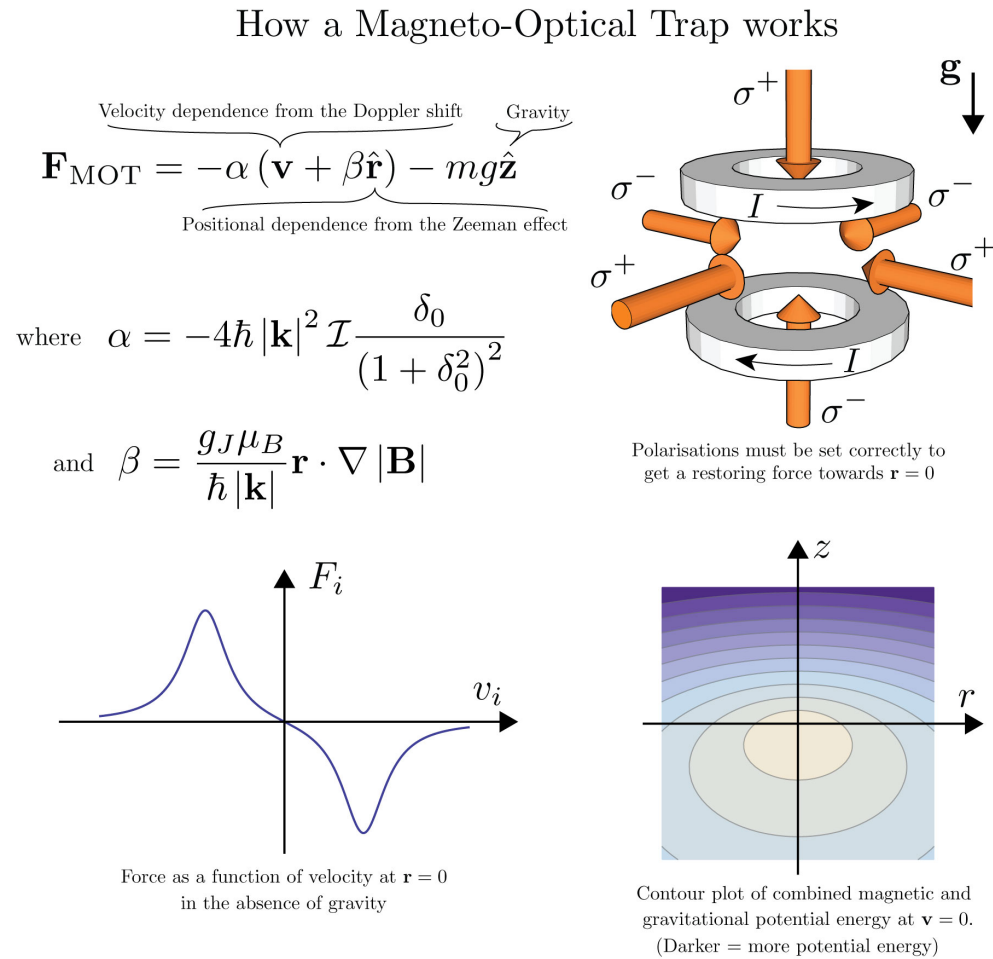


Figure 2.14: This graphic briefly explains the workings of a Magneto-Optical Trap. The two graphs at the bottom use arbitrary, illustrative parameters.

$$\frac{dI}{dz} = \rho E_\nu R_{scatt} \quad (2.133)$$

$$= \rho \frac{hc}{\lambda} \frac{\Gamma}{2} \frac{\mathcal{I}}{1 + \mathcal{I} + \delta^2} \quad (2.134)$$

$$= \rho I \frac{hc\Gamma}{2\lambda I_{sat}} \frac{1}{1 + \mathcal{I} + \delta^2} \quad (2.135)$$

and using $I_{sat} = \frac{\pi h c \Gamma}{3\lambda^3}$,

$$\frac{dI}{dz} = \rho I \frac{3\lambda^2}{2\pi} \frac{1}{1 + \mathcal{I} + \delta^2} \quad (2.136)$$

$$= \rho I \frac{\sigma_0}{1 + \mathcal{I} + \delta^2} \quad (2.137)$$

$$= \rho I \sigma \quad (2.138)$$

where we have defined the resonant, low intensity cross-sectional area of the two-level atom as $\sigma_0 \equiv \frac{3\lambda^2}{2\pi}$ and the full cross-sectional area as

$$\sigma \equiv \frac{\sigma_0}{1 + \mathcal{I} + \delta^2}. \quad (2.139)$$

For low intensity light, $\mathcal{I} \ll 1 + \delta^2$, the cross-sectional area is $\sigma \approx \frac{\sigma_0}{1 + \delta^2}$ and Eq. (2.138) has the solution

$$I_f = I_0 e^{-\sigma \int \rho dz} \quad (2.140)$$

$$= I_0 e^{-n\sigma} \quad (2.141)$$

Thus, we can find the integrated atom density $n = \int \rho dz$ by taking a picture with atoms I_f and without atoms I_0 and computing

$$n = \frac{1}{\sigma} \ln \frac{I_0}{I_f} \quad (2.142)$$

pixel-wise over the image. Sometimes we will refer to Optical Depth (OD), which is simply given by $OD = n\sigma$. Further details on the imaging process and calculation are explained in detail elsewhere [163].

Atom Interferometer Theory

It is commonly stated that the acceleration sensitivity of an atom interferometer is proportional to the space-time area enclosed between the two interfering arms [189, 150, 63]. Here we derive the interferometric phase shift for an extensive class of interferometers, and explore the circumstances in which only the inertial terms contribute. We then analyse various interferometer configurations in light of this geometric interpretation of the interferometric phase shift.

3.1 Atom-light interactions

If a particle experiences a linearly varying potential term $V(\mathbf{x}) = m\mathbf{g} \cdot \mathbf{x}$ and is otherwise free, it will experience an acceleration \mathbf{g} . The two arms of the interferometer, labelled a and b , experience accelerations $\mathbf{a}_a(t)$ and $\mathbf{a}_b(t)$ respectively at time t , which we shall define from $t = 0$ in the middle of our interferometer as in Fig. 3.1. These accelerations may comprise both the inertial acceleration \mathbf{g} and any other acceleration $\tilde{\mathbf{a}}_a(t)$ and $\tilde{\mathbf{a}}_b(t)$ from time-varying potentials used to generate the interferometer (e.g. Bragg diffraction pulses, Bloch lattice accelerations, magnetic field gradients etc.).

For example, to treat a Bragg diffraction pulse at time t_1 which imparts a downwards velocity kick of $2n\hbar\mathbf{k}/m$ to path b , (see Figure 3.2) we can write the kicked path's acceleration in the inertial frame as $\tilde{\mathbf{a}}_b(t) = -\delta(t - t_1)\frac{2n\hbar\mathbf{k}}{m}$, and the acceleration of the un kicked path (also in the inertial, freely-falling frame) as $\tilde{\mathbf{a}}_a(t) = 0$. For a more complicated sequence of kicks, we can simply take the sum of each one.

As another example, constant acceleration in an optical Bloch lattice can be expressed as a classical acceleration $\tilde{\mathbf{a}}_b(t) = \frac{2n_b\hbar\mathbf{k}}{m\tau_b}$ where the number of Bloch oscillations is given as n_b and the time for a single oscillation is τ_b . Alternatively, it may be expressed as one $2\hbar\mathbf{k}$ kick every Bloch oscillation period τ_b , starting $\tau_b/2$ from the beginning, e.g. $\tilde{\mathbf{a}}_b(t) = \sum_{i=1}^{n_b} \frac{2\hbar\mathbf{k}}{m} \delta(t - t_i)$ where $t_i = t_0 + \tau_b(i + 1/2)$ and t_0 is start

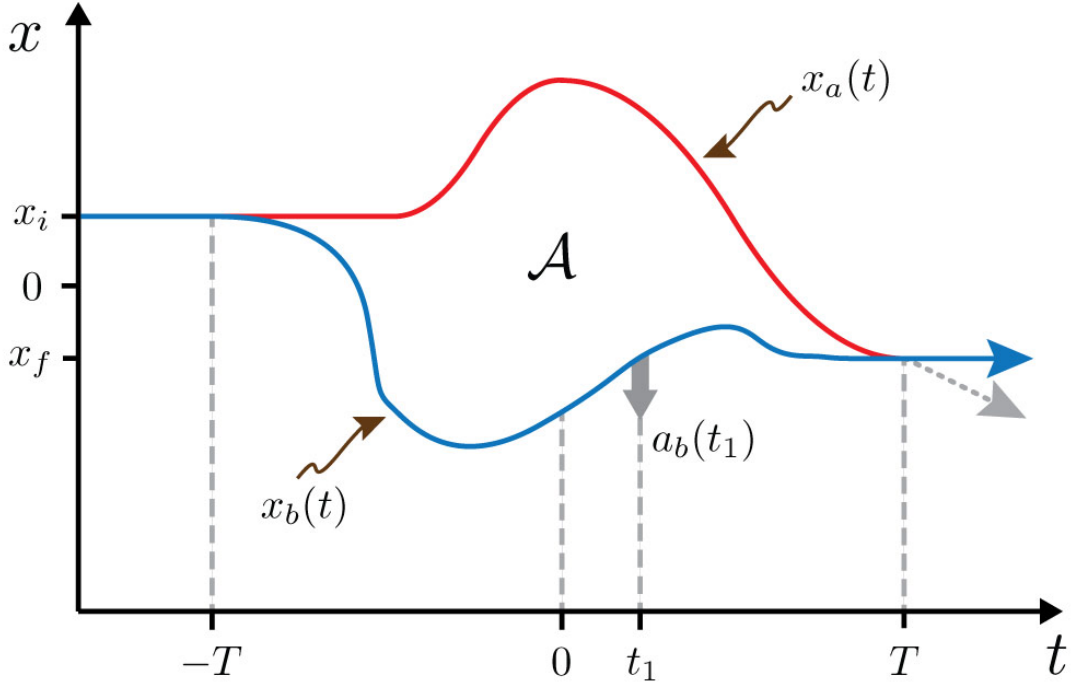


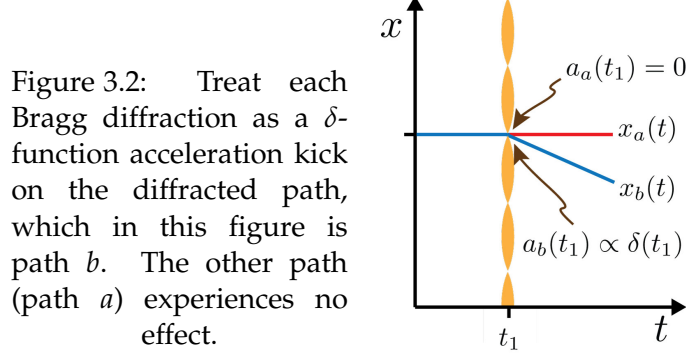
Figure 3.1: (Color online) The two paths a and b form an arbitrary closed interferometer. For clarity, the diagram is drawn with $\mathbf{g} = 0$. We are calculating the difference in phase accumulated along two paths which exit the interferometer at the same place and with the same final velocity, here shown as a blue arrow. The alternate exit path is shown as a grey dotted arrow. The area enclosed between the two paths in this space-time diagram is the space-time area, \mathcal{A} .

time of the Bloch lattice acceleration. Either treatment gives the same space-time area in the total interferometer. For such a treatment to correctly account for the phase shift along each path individually the atoms must experience a whole number of Bloch oscillations. A small correction when this is not the case has been investigated in Ref. [145].

3.2 Interferometer Phase Shift

3.2.1 Action

The phase shift of an atom interferometer can be calculated by the path integral formalism. Consider the classical action S_a of a particle of mass m moving along a path $\mathbf{x}_a(t)$ with velocity $\mathbf{v}_a(t)$ and experiencing an acceleration $\mathbf{a}_a(t)$,



$$S_a = \int_{-T}^T K_a - V_a dt \quad (3.1)$$

$$= m \int_{-T}^T \frac{v_a^2}{2} + \mathbf{a}_a \cdot \mathbf{x}_a ds. \quad (3.2)$$

where we have defined the potential term $V_a(t) = -m\mathbf{a}_a(t) \cdot \mathbf{x}_a(t)$. The phase shift of an interferometer consisting of arms traversing the classical paths a and b is given by

$$\Delta\Phi = \frac{\Delta S}{\hbar} \quad (3.3)$$

$$= \frac{S_a - S_b}{\hbar} \quad (3.4)$$

$$= \frac{m}{\hbar} \int_{-T}^T \frac{v_a^2 - v_b^2}{2} + \mathbf{a}_a \cdot \mathbf{x}_a - \mathbf{a}_b \cdot \mathbf{x}_b ds \quad (3.5)$$

$$= \frac{m}{\hbar} \int_{-T}^T \frac{\Delta[v^2]}{2} + \Delta[\mathbf{a} \cdot \mathbf{x}] ds. \quad (3.6)$$

If we now make the distinction between the acceleration \mathbf{g} the atoms would experience inertially, in absence of the interferometric sequence and the acceleration $\tilde{\mathbf{a}}_i$ the atoms feel along path i specifically because of the sequence, along with the corresponding separations for velocity and position,

$$\mathbf{a}_i = \tilde{\mathbf{a}}_i + \mathbf{g} \quad (3.7)$$

$$\mathbf{v}_i = \tilde{\mathbf{v}}_i + \mathbf{v}_g \quad (3.8)$$

$$\mathbf{x}_i = \tilde{\mathbf{x}}_i + \mathbf{x}_g \quad (3.9)$$

we can expand the kinetic energy term in the integrand of equation (3.6) to be

$$\frac{\Delta [v^2]}{2} = \frac{\tilde{\mathbf{v}}_a^2 - \tilde{\mathbf{v}}_b^2}{2} + \mathbf{v}_g(\tilde{\mathbf{v}}_a - \tilde{\mathbf{v}}_b) \quad (3.10)$$

while the potential term in the integrand of equation (3.6) becomes

$$\Delta [\mathbf{a} \cdot \mathbf{x}] = \tilde{\mathbf{a}}_a \cdot \tilde{\mathbf{x}}_a - \tilde{\mathbf{a}}_b \cdot \tilde{\mathbf{x}}_b + (\tilde{\mathbf{a}}_a - \tilde{\mathbf{a}}_b) \cdot \tilde{\mathbf{x}}_g + \mathbf{g} \cdot \Delta \tilde{\mathbf{x}} \quad (3.11)$$

If we consider just the integral of the potential term, and integrate by parts

$$\int_{-T}^T \Delta [\mathbf{a} \cdot \mathbf{x}] dt \quad (3.12)$$

$$= \int_{-T}^T \tilde{\mathbf{a}}_a \cdot \tilde{\mathbf{x}}_a - \tilde{\mathbf{a}}_b \cdot \tilde{\mathbf{x}}_b + (\tilde{\mathbf{a}}_a - \tilde{\mathbf{a}}_b) \cdot \mathbf{x}_g + \mathbf{g} \cdot \Delta \tilde{\mathbf{x}} dt \quad (3.13)$$

$$= [\tilde{\mathbf{v}}_a \cdot \mathbf{x}_a - \tilde{\mathbf{v}}_b \cdot \mathbf{x}_b]_{-T}^T - \int_{-T}^T \tilde{v}_a^2 - \tilde{v}_b^2 dt \\ - \int_{-T}^T \mathbf{v}_g(\tilde{\mathbf{v}}_a - \tilde{\mathbf{v}}_b) dt + \int_{-T}^T \mathbf{g} \cdot \Delta \tilde{\mathbf{x}} dt \quad (3.14)$$

then Eq. (3.6) becomes

$$\Delta\Phi = \frac{m}{\hbar} \int_{-T}^T \frac{\Delta [v^2]}{2} + \Delta [\mathbf{a} \cdot \mathbf{x}] ds. \quad (3.15)$$

$$= \frac{m}{\hbar} \left([\tilde{\mathbf{v}}_a \cdot \mathbf{x}_a - \tilde{\mathbf{v}}_b \cdot \mathbf{x}_b]_{-T}^T - \frac{1}{2} \int_{-T}^T \tilde{v}_a^2 - \tilde{v}_b^2 dt + \int_{-T}^T \mathbf{g} \cdot \Delta \tilde{\mathbf{x}} dt \right) \quad (3.16)$$

Let us call the boundary term $\Delta\Phi_{\text{sep}}$, the separation phase

$$\Delta\Phi_{\text{sep}} = \frac{m}{\hbar} [\tilde{\mathbf{v}}_a \cdot \mathbf{x}_a - \tilde{\mathbf{v}}_b \cdot \mathbf{x}_b]_{-T}^T \quad (3.17)$$

$$= [\tilde{\mathbf{k}}_a \cdot \mathbf{x}_a - \tilde{\mathbf{k}}_b \cdot \mathbf{x}_b]_{-T}^T \quad (3.18)$$

$$= \tilde{\mathbf{k}}_a(T) \cdot \mathbf{x}_a(T) - \tilde{\mathbf{k}}_b(T) \cdot \mathbf{x}_b(T) - \tilde{\mathbf{k}}_a(-T) \cdot \mathbf{x}_a(-T) + \tilde{\mathbf{k}}_b(-T) \cdot \mathbf{x}_b(-T) \quad (3.19)$$

For the final states to interfere they must have the same final position $\mathbf{x}_b(T) = \mathbf{x}_a(T)$, and for this interference to persist in the far-field they must have the same final velocity, $\tilde{\mathbf{k}}_b(T) = \tilde{\mathbf{k}}_a(T)$ so the separation phase depends only upon the initial states,

$$\Delta\Phi_{\text{sep}} = \tilde{\mathbf{k}}_b(-T) \cdot \mathbf{x}_b(-T) - \tilde{\mathbf{k}}_a(-T) \cdot \mathbf{x}_a(-T). \quad (3.20)$$

In the case that the initial velocities are the same then the separation phase becomes

$$\Delta\Phi_{\text{sep}} = -\tilde{\mathbf{k}}(-T) \cdot \Delta\mathbf{x}(-T) \quad (3.21)$$

$$= -\tilde{\mathbf{k}}_i \cdot \Delta\mathbf{x}_i. \quad (3.22)$$

and if the initial separation $\Delta\mathbf{x}_i = 0$ (i.e. the interferometer is closed) then there is no contribution from the separation phase.

The kinetic term can be re-written in terms of frequency, through $\tilde{E}_{\text{kin}} = \hbar\tilde{\omega} = \frac{\hbar^2 k^2}{2m}$

$$\Delta\Phi_{\text{kin}} = -\frac{m}{2\hbar} \int_{-T}^T \tilde{v}_a^2 - \tilde{v}_b^2 dt \quad (3.23)$$

$$= \int_{-T}^T \tilde{\omega}_b - \tilde{\omega}_a dt \quad (3.24)$$

So the total interferometer phase shift becomes

$$\Delta\Phi = -\tilde{\mathbf{k}}_i \cdot \Delta\mathbf{x}_i + \int_{-T}^T \tilde{\omega}_b - \tilde{\omega}_a dt + \frac{m}{\hbar} \int_{-T}^T \mathbf{g} \cdot \Delta\tilde{\mathbf{x}} dt \quad (3.25)$$

$$= \Delta\Phi_{\text{sep}} + \Delta\Phi_{\text{kin}} + \Delta\Phi_{\text{inertial}} \quad (3.26)$$

There are many ways (through various symmetries) in which to make $\Delta\Phi_{\text{kin}} = 0$, which we will discuss in the next section. In any of these cases, for a closed interferometer, the phase shift simplifies to

$$\Delta\Phi = \Delta\Phi_{\text{inertial}} \quad (3.27)$$

$$= \frac{m}{\hbar} \int_{-T}^T \mathbf{g} \cdot \Delta\tilde{\mathbf{x}} dt \quad (3.28)$$

and for a constant acceleration \mathbf{g} this can be pulled out of the integral,

$$\Delta\Phi = \frac{m}{\hbar} \mathbf{g} \cdot \int_{-T}^T \Delta\tilde{\mathbf{x}} dt \quad (3.29)$$

$$= \frac{m}{\hbar} \mathbf{g} \cdot \mathcal{A} \quad (3.30)$$

where we have defined the space-time area on the last line, $\mathcal{A} \equiv \int_{-T}^T \Delta\tilde{\mathbf{x}} dt$.

To include the possibility of different internal magnetic states of the atoms, an additional phase shift $\Delta\Phi_{\text{mag}}$ must be added. As the potential energy of a magnetic

dipole with dipole moment μ in a magnetic field is given by $U = -\mu \cdot \mathbf{B}$, the phase shift is given by

$$\Delta\Phi_{\text{mag}} = - \int_{-T}^T \Delta U dt \quad (3.31)$$

$$= \int_{-T}^T \mathbf{B} \cdot \Delta\mu dt \quad (3.32)$$

This will apply to Raman interferometry in particular, whereas in Bragg interferometry the atoms stay in the same internal state and so this shift is zero.

3.2.2 Time Symmetries

There are many arbitrary ways to create an interferometer in which $\Delta\Phi_{\text{kin}} = 0$. One way is to enforce either of the following velocity symmetries

$$\tilde{\mathbf{v}}_a(t) = \tilde{\mathbf{v}}_b(-t) \quad (i) \quad (3.33)$$

or

$$\tilde{\mathbf{v}}_a(t) = -\tilde{\mathbf{v}}_b(-t) \quad (ii) \quad (3.34)$$

from which it follows that

$$\tilde{\mathbf{v}}_a^2(t) = \tilde{\mathbf{v}}_b^2(-t) \quad (3.35)$$

$$\int_{-T}^T \tilde{\mathbf{v}}_a^2(t) dt = \int_{-T}^T \tilde{\mathbf{v}}_b^2(-t) dt \quad (3.36)$$

$$\int_{-T}^T \tilde{\mathbf{v}}_a^2(t) - \tilde{\mathbf{v}}_b^2(t) dt = 0 \quad (3.37)$$

$$\Delta\Phi_{\text{kin}} = 0 \quad (3.38)$$

These symmetries also help to cancel other shifts in real interferometers such as Stark shifts and others as described in Section 3.3.1.

3.2.3 Laser Phase

Any laser interaction which kicks a path in such a way to increase the space-time area of the interferometer, its phase should be added, and any interaction which kicks a path in such a way as to decrease the interferometer's space-time area, its phase should be subtracted. Thus

$$\phi_L = \sum_{\text{increases } \mathcal{A}} \phi_i - \sum_{\text{decreases } \mathcal{A}} \phi_i \quad (3.39)$$

where each ϕ_i is the laser phase accumulated along a certain path when that path experiences a $2n_i$ -photon-recoil change in momentum. Each laser phase is given by

$$\phi_i = \mathbf{k}_{\text{eff}} \cdot \mathbf{x}_i \quad (3.40)$$

$$= 2n\mathbf{k} \cdot \mathbf{x}_i \quad (3.41)$$

This is a different way to state the same result as in Ref. [187], but simpler as we are dealing with Bragg and not Raman transitions and so do not have to deal with changes in internal state. Also, the laser phase as stated here only applies to a two-path interferometer configuration. To generalize to more paths it must be stated in terms of the direction of each kick as in Ref. [187], as opposed to w.r.t the space-time area \mathcal{A} .

3.3 Extensions

3.3.1 Constant energy offset

If one of the trajectories experiences a spatially constant potential energy offset $V_0(t)$, for example due to a state-dependent Stark shift, this will cause a phase offset in the interferometer of $\frac{1}{\hbar} \int V_0(t) dt$. In the case where this shift is cancelled by an equal shift in the opposite direction later in time, there is zero net phase shift. This cancellation occurs in particular in the Constant-Acceleration Bloch (CAB) interferometer configuration, because the un-accelerated arm of the interferometer experiences a Stark shift due to the average optical lattice intensity.

3.3.2 Vibrations and time-varying \mathbf{g}

There is nothing in the derivation above preventing \mathbf{g} being considered an arbitrary function of time. In this case it must say within the integral

$$\Delta\Phi_{\text{inertial}} = \frac{m}{\hbar} \int_{-T}^T \mathbf{g} \cdot \Delta\mathbf{x} dt. \quad (3.42)$$

A symmetric variation of the form $\mathbf{g}(t) = \mathbf{g}(-t)$ is used in measurements of the fine structure constant, e.g. Refs [32, 39]. After a Ramsey-Bordé configuration interferometer has had its paths separated, *both* arms are loaded into the same Bloch lattice and accelerated, then decelerated again, effectively changing \mathbf{g} symmetrically in a way proportional to the recoil frequency $\omega_{\text{rec}} = \frac{\hbar k^2}{2m}$.

We can also consider the effect of a vibration and how this will couple in to our interferometer signal. We can write a sinusoidal acceleration with frequency ω as

$$\mathbf{g} = \mathbf{a}_c \cos(\omega t) + \mathbf{a}_s \sin(\omega t) \quad (3.43)$$

which will cause a phase shift in the interferometer output of

$$\Delta\Phi_{\text{inertial}} = \frac{m}{\hbar} \int_{-T}^T [\mathbf{a}_c \cos(\omega t) + \mathbf{a}_s \sin(\omega t)] \cdot \Delta\tilde{\mathbf{x}} dt \quad (3.44)$$

$$= \frac{m}{\hbar} \left[\mathbf{a}_c \cdot \int_{-T}^T \cos(\omega t) \Delta\tilde{\mathbf{x}} dt + \mathbf{a}_s \cdot \int_{-T}^T \sin(\omega t) \Delta\tilde{\mathbf{x}} dt \right] \quad (3.45)$$

$$= \frac{m}{\hbar} [\mathbf{a}_c \cdot \mathcal{A}_c(\omega) + \mathbf{a}_s \cdot \mathcal{A}_s(\omega)] \quad (3.46)$$

where on the last line we have defined the effective space-time areas $\mathcal{A}_c(\omega)$ and $\mathcal{A}_s(\omega)$ for a given frequency of vibration ω . Note that the space-time area as defined before is $\mathcal{A} = \mathcal{A}_c(0)$.

If the path separation is symmetric about $t = 0$, i.e. $\Delta\tilde{\mathbf{x}}(t) = \Delta\tilde{\mathbf{x}}(-t)$ then the sine term cancels $\mathcal{A}_s(\omega) = 0$, leaving only the cosine term $\mathcal{A}_c(\omega)$. A useful measure of vibration sensitivity when this symmetry is present is the relative acceleration sensitivity as a function of frequency, normalised to the sensitivity at $\omega = 0$. This is given by $\mathcal{R}(\omega) \equiv \frac{|\mathcal{A}_c(\omega)|}{|\mathcal{A}|}$. From this unitless ratio we can deduce the phase response to an acceleration with frequency ω via

$$\Delta\Phi_{\text{inertial}} = \frac{m\mathcal{R}(\omega)}{\hbar} \mathbf{a}_c \cdot \mathcal{A} \quad (3.47)$$

If the path separation is antisymmetric about $t = 0$, i.e. $\Delta\tilde{x}(t) = -\Delta\tilde{x}(-t)$ then the cosine term cancels $\mathcal{A}_c(\omega) = 0$, leaving only the sine term $\mathcal{A}_s(\omega)$. Therefore, these types of interferometer are insensitive to a constant acceleration. A useful measure of vibration sensitivity when this symmetry is present is the relative acceleration sensitivity as a function of frequency, normalised to the sensitivity to a constant acceleration of the corresponding symmetrized interferometer, i.e. $\mathcal{A}^* \equiv \int_{-T}^T |\Delta\tilde{x}| dt$ at $\omega = 0$. This is given by $\mathcal{R}^*(\omega) \equiv \frac{|\mathcal{A}_s(\omega)|}{|\mathcal{A}^*|}$. From this unitless ratio we can deduce the phase response to an acceleration with frequency ω via

$$\Delta\Phi_{\text{inertial}} = \frac{m\mathcal{R}^*(\omega)}{\hbar} \mathbf{a}_s \cdot \mathcal{A}^* \quad (3.48)$$

3.3.2.1 Fourier series decomposition

If $\mathbf{g}(t)$ can be considered an arbitrary piecewise continuous function of time between $-T \leq t \leq T$, then it can be written as a Fourier series

$$\mathbf{g}(t) = \sum_{j=0}^{\infty} \left[\mathbf{a}_{c,j} \cos\left(\frac{j\pi t}{T}\right) + \mathbf{a}_{s,j} \sin\left(\frac{j\pi t}{T}\right) \right] \quad (3.49)$$

for the Fourier coefficients

$$\mathbf{a}_{c,j} = \frac{1}{T} \int_{-T}^T \cos\left(\frac{j\pi t}{T}\right) \mathbf{a}(t) dt \quad (3.50)$$

and

$$\mathbf{a}_{s,j} = \frac{1}{T} \int_{-T}^T \sin\left(\frac{j\pi t}{T}\right) \mathbf{a}(t) dt. \quad (3.51)$$

We can see that the effect of such an arbitrary acceleration will be a phase shift of

$$\Delta\Phi_{\text{inertial}} = \frac{m}{\hbar} \sum_{j=0}^{\infty} \left[\mathbf{a}_{c,j} \cdot \mathcal{A}_c\left(\frac{j\pi}{T}\right) + \mathbf{a}_{s,j} \cdot \mathcal{A}_s\left(\frac{j\pi}{T}\right) \right]. \quad (3.52)$$

3.3.3 Coriolis Effect

Similarly to the previous section the common inertial acceleration \mathbf{g} should be kept inside the integral

$$\Delta\Phi = \frac{m}{\hbar} \int_{-T}^T \mathbf{g} \cdot \Delta\mathbf{x} dt \quad (3.53)$$

whereupon the substitution $\mathbf{g} \rightarrow \mathbf{g} + \Omega \times \mathbf{v}$ can be used to perturbatively incorporate the effect of rotation on the interferometer for small constant Ω , e.g. the rotation of the earth¹. Thus

$$\Delta\Phi_{\text{inertial}} = \frac{m}{\hbar} \int_{-T}^T (\mathbf{g} + \Omega \times \mathbf{v}) \cdot \Delta\mathbf{x} dt \quad (3.54)$$

$$= \frac{m}{\hbar} \left(\mathbf{g} \cdot \mathcal{A} - \int_{-T}^T \Omega \cdot \Delta\mathbf{x} \times \mathbf{v} dt \right) \quad (3.55)$$

$$= \frac{m}{\hbar} \left(\mathbf{g} \cdot \mathcal{A} - \Omega \cdot \int_{-T}^T \Delta\mathbf{x} \times d\mathbf{x} \right) \quad (3.56)$$

$$= \frac{m}{\hbar} \left(\mathbf{g} \cdot \mathcal{A} - \Omega \cdot \oint \mathbf{x} \times d\mathbf{x} \right) \quad (3.57)$$

$$= \frac{m}{\hbar} (\mathbf{g} \cdot \mathcal{A} - 2\Omega \cdot \mathbf{A}) \quad (3.58)$$

which reproduces the well-known Sagnac phase shift as the term on the right, where \mathbf{A} is the vector-area enclosed by the interferometer paths. Under the assumption that all the \mathbf{k} -vectors are parallel, the area arises both from an initial velocity \mathbf{v}_i and the mean velocity of the accelerating atoms \mathbf{g} , the area \mathbf{A} is given by

$$\mathbf{A} = -\mathbf{v}_i \times \mathcal{A} - \mathbf{g} \times \int_{-T}^T t \Delta\mathbf{x} dt \quad (3.59)$$

where the second term (which goes as a higher power of interferometer time T than the first term) will disappear if $\mathbf{g} \times \mathbf{k} = 0$, or if the separation $\Delta\mathbf{x}$ is symmetric about $t = 0$. In this case the interferometer phase becomes

¹Technically, this is evaluating a perturbative Lagrangian $\mathcal{L} \approx m\Omega \cdot \mathbf{r} \times \mathbf{v}$ along the unperturbed path, as in Ref. [189], and ignoring the term proportional to Ω^2 .

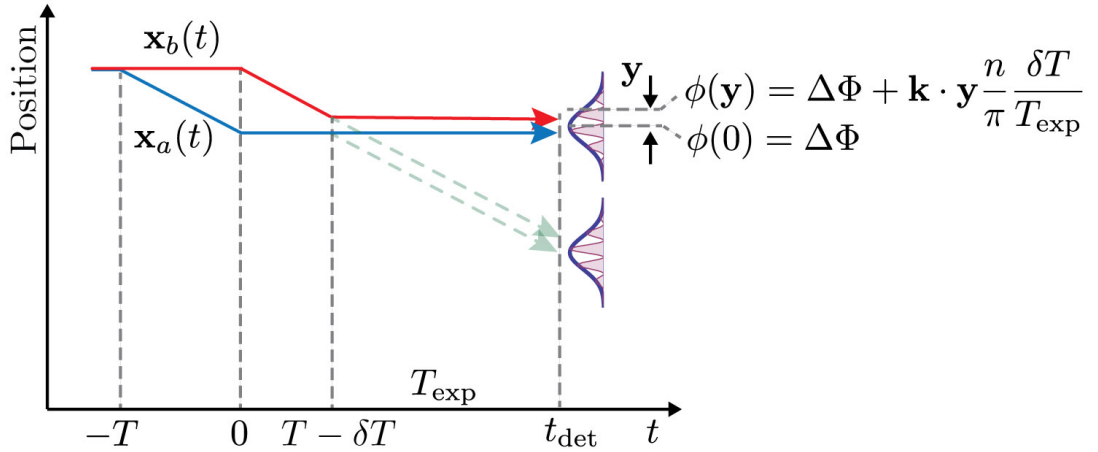


Figure 3.3: An interferometer in which the paths do not match up exactly at the final beamsplitter is analogous to a double slit experiment [175]. In this case, the upper output will be a fringe pattern like $\frac{\nu}{2} \cos(\phi(\mathbf{y}) + \phi_L) + c$ where ϕ_L is the laser phase and $\phi(\mathbf{y})$ determines the spatial fringes, but not the envelope. The lower output will of course be π out of phase with the top output.

$$\Delta\Phi = \frac{m}{\hbar} (\mathbf{g} - 2\Omega \times \mathbf{v}_i) \cdot \mathcal{A} \quad (3.60)$$

3.3.4 Separation Phase

The results above all apply to a closed-loop interferometer configuration. If for some reason, the parts of each state which overlap at the end of the interferometer did not originate from the same place at the beginning of the interferometer (for example due to a slight timing offset of the last pulse, as shown in Fig. 3.3), then the separation phase is non-zero and we have

$$\Delta\Phi_{\text{sep}} = \mathbf{k}_e \cdot \Delta\mathbf{x}_f \quad (3.61)$$

where $\Delta\mathbf{x}_f$ is the separation of the two wavepackets at the recombination pulse, and $\mathbf{k}_e = 2n\mathbf{k}$ is the momentum separation of the last Bragg kick. If this is due to a timing

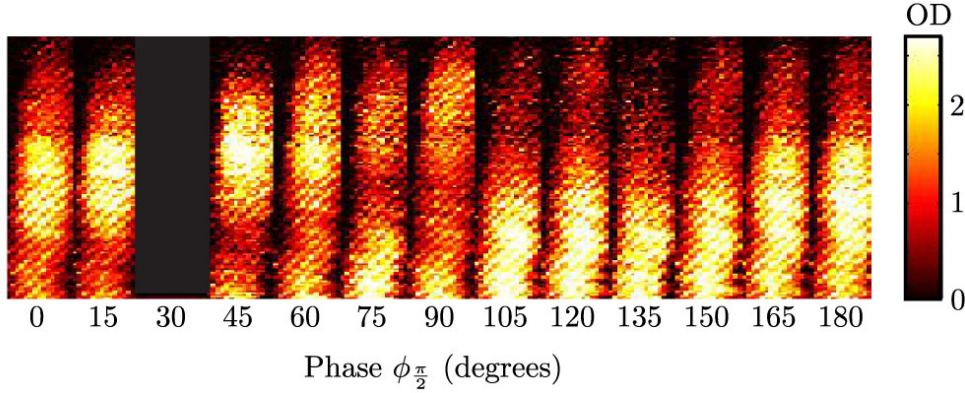


Figure 3.4: Demonstration of spatial fringes due to a timing offset δT , performed in our lab. In a Mach-Zehnder interferometer with a small time offset δT on the last pulse, this is the $4\hbar k$ output state only, as the interferometric phase $\phi_{\frac{\pi}{2}}$ of the recombination $\frac{\pi}{2}$ pulse is varied. In the image for $\phi_{\frac{\pi}{2}} = 30^\circ$ the DDS generated the pulse sequence incorrectly so this image is not shown.

offset δT then the separation phase is given by

$$\Delta\Phi_{\text{sep}} = \mathbf{k}_e \cdot \frac{\hbar\mathbf{k}_e}{m} \delta T \quad (3.62)$$

$$= 8n^2\omega_{\text{rec}} \delta T \quad (3.63)$$

where $\omega_{\text{rec}} = \frac{\hbar k^2}{2m}$ is the single-photon recoil frequency.

In this case a spatial interference pattern can develop in the far field which is analogous to a double slit experiment [175]. The analogous double slit experiment would have a slit spacing equal to the separation of the two wavepackets at the final beam-splitter Δx_f . If \mathbf{y} is the position vector away from the centre of the envelope of the top output port in Fig. 3.3, then the spatial fringe in this output port will be given by a fraction N_{rel} of the envelope,

$$N_{\text{rel}} = \frac{\mathcal{V}}{2} \cos(\phi(\mathbf{y}) + \phi_L) + c \quad (3.64)$$

$$= \frac{\mathcal{V}}{2} \cos\left(\Delta\Phi + \mathbf{k} \cdot \mathbf{y} \frac{n}{\pi} \frac{\delta T}{T_{\text{exp}}} + n\phi_{\frac{\pi}{2}}\right) + c \quad (3.65)$$

This is experimentally demonstrated in Fig. 3.4, for one output port of a $4\hbar k$ interferometer.

3.4 Example Interferometer Configurations

3.4.1 Mach-Zehnder (MZ)

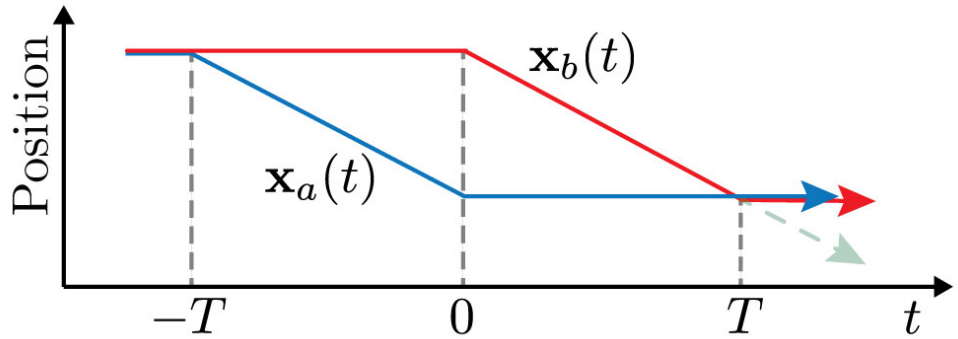


Figure 3.5: Diagram illustrating the paths in a Mach-Zehnder interferometer.

First consider the case of a $\frac{\pi}{2} - \pi - \frac{\pi}{2}$ Bragg-based Mach-Zehnder interferometer, in the absence of rotation. In this case the acceleration on each path is given by

$$\begin{aligned}\ddot{\mathbf{a}}_a(t) &= \frac{2n\hbar\mathbf{k}}{m} [\delta(t+T) - \delta(t)] \\ \ddot{\mathbf{a}}_b(t) &= \frac{2n\hbar\mathbf{k}}{m} [\delta(t) - \delta(t-T)]\end{aligned}\quad (3.66)$$

and it can be seen that these satisfy our time symmetry requirement Eq. 3.33. The space-time area is easy to calculate in this case:

$$\mathcal{A} = \frac{2n\hbar\mathbf{k}T^2}{m} \quad (3.67)$$

so the interferometer phase becomes

$$\Delta\Phi = \frac{mg}{\hbar} \cdot \frac{2n\hbar\mathbf{k}T^2}{m} \quad (3.68)$$

$$= 2n\mathbf{k} \cdot \mathbf{g}T^2 \quad (3.69)$$

while the laser phase is

$$\phi_L = \underbrace{(n\phi_1 - n\phi_2)}_{\text{from path 1}} + \underbrace{(-n\phi_2 + n\phi_3)}_{\text{from path 2}} \quad (3.70)$$

$$= n(\phi_1 - 2\phi_2 + \phi_3). \quad (3.71)$$

With the inclusion of the Coriolis effect, and under the assumption that \mathbf{g} and \mathbf{k} are parallel, the interferometric phase becomes

$$\Delta\Phi = 2n\mathbf{k} \cdot (\mathbf{g} - 2\boldsymbol{\Omega} \times \mathbf{v}_i) T^2. \quad (3.72)$$

A Mach-Zehnder is sensitive to vibrations according to Eq. (3.47). In this case the relative sensitivity to acceleration is given by

$$\mathcal{R}(\omega) = \frac{4 \sin^2(\frac{\omega T}{2})}{(\omega T)^2} \quad (3.73)$$

which is plotted in Fig. 3.7 (a), and so the phase shift due to an acceleration $\mathbf{a} = \mathbf{a}_c \cos(\omega t)$ is given by

$$\delta\Phi = \frac{m\mathcal{R}(\omega)}{\hbar} \mathbf{a}_c \cdot \mathcal{A} \quad (3.74)$$

$$= 2n\mathbf{k} \cdot \mathbf{a}_c \frac{4 \sin^2(\frac{\omega T}{2})}{\omega^2} \quad (3.75)$$

$$= 8n\mathbf{k} \cdot \mathbf{x}_c \sin^2\left(\frac{\omega T}{2}\right) \quad (3.76)$$

which on the last line has been rewritten in terms of the distance amplitude of the vibration, $\mathbf{x}_c = \mathbf{a}_c / \omega^2$.

3.4.2 Continuous-Acceleration Bloch (CAB) sequence

In this case the acceleration along each path is given by Eq. 3.95 with the addition of a constant Bloch acceleration along one arm at a time, during each half of the interferometer,

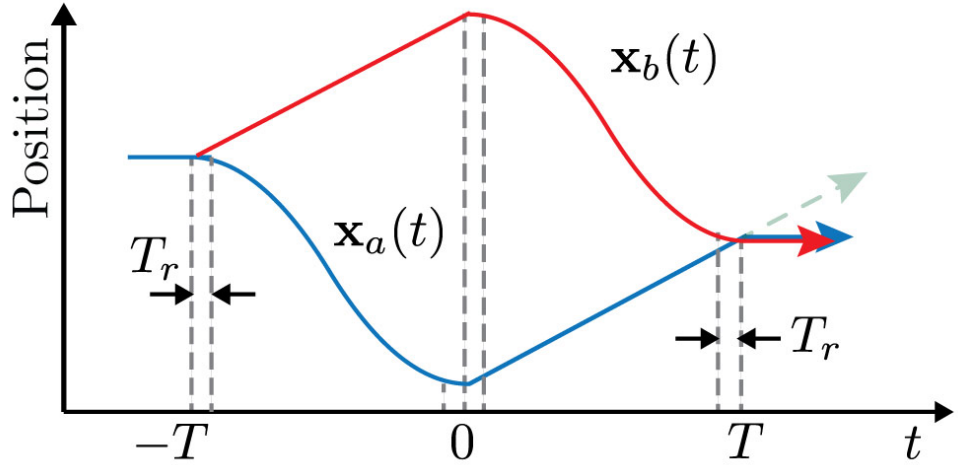


Figure 3.6: Diagram illustrating the paths in a CAB interferometer sequence. The Bloch lattice is increasing (decreasing) in intensity for a time T_r after (before) each Bragg kick. In the example here, the lattice is not unloaded and reloaded at $t \approx \pm T/2$, unlike in the experimental configuration discussed in chapter 6

$$\begin{aligned}\tilde{\mathbf{a}}_a(t) &= \underbrace{\frac{2n\hbar\mathbf{k}}{m} [\delta(t) - \delta(t-T)]}_{\text{Bragg Kicks}} + \underbrace{\frac{2n_b\hbar\mathbf{k}}{m\tau_b} \cdot (T_r - T < t < -T_r) \cdot (-1)^{(t>-T/2)}}_{\text{Bloch Oscillations}} \\ \tilde{\mathbf{a}}_b(t) &= \underbrace{\frac{2n\hbar\mathbf{k}}{m} [\delta(t+T) - \delta(t)]}_{\text{Bragg Kicks}} + \underbrace{\frac{2n_b\hbar\mathbf{k}}{m\tau_b} \cdot (T_r < t < T - T_r) \cdot (-1)^{(t>T/2)}}_{\text{Bloch Oscillations}}\end{aligned}\quad (3.77)$$

where n_b is the number of Bloch oscillations, τ_b is the period for one Bloch oscillation, and T_r is small time in which the atoms are loaded into the lattice and there is no acceleration. In this expression I have used the notation $(x < y)$ to mean a boolean function which is 1 if the condition $x < y$ is satisfied and 0 if it is not. The space-time area in this case is calculated to be

$$\begin{aligned}\mathcal{A} &= \left[\frac{2n\hbar\mathbf{k}T}{m} + \frac{2n_b\hbar\mathbf{k}(T - 4T_r)}{2m} \right] \cdot T \\ &= \frac{2\hbar\mathbf{k}T^2}{m} \left[n + n_b \left(\frac{1}{2} - \frac{2T_r}{T} \right) \right]\end{aligned}\quad (3.78)$$

so the interferometer phase becomes (in the absence of rotation)

$$\Delta\Phi = \frac{m\mathbf{g}}{\hbar} \cdot \frac{2\hbar\mathbf{k}T}{m} \left[n + n_b \left(\frac{1}{2} - \frac{2T_r}{T} \right) \right] \quad (3.79)$$

$$= 2 \left[n + n_b \left(\frac{1}{2} - \frac{2T_r}{T} \right) \right] \mathbf{k} \cdot \mathbf{g} T^2 \quad (3.80)$$

while the laser phase is

$$\phi_L = \underbrace{(n\phi_1 - n\phi_2 - n_b\phi_{b3} + n_b\phi_{b4})}_{\text{from path 1}} + \underbrace{(n_b\phi_{b1} - n_b\phi_{b2} - n\phi_2 + n\phi_3)}_{\text{from path 2}} \quad (3.81)$$

$$= n(\phi_1 - 2\phi_2 + \phi_3) + n_b(\phi_{b1} - \phi_{b2} - \phi_{b3} + \phi_{b4}). \quad (3.82)$$

which implies that an interferometric fringe can be scanned out by changing the phase of the Bloch lattices, as well as the Bragg pulses.

Since the Bloch acceleration is constant, we can write the number of Bloch oscillations as $n_b = \frac{T-4T_r}{2\tau}$, so the interferometric phase in Eq. (3.80) becomes

$$\Delta\Phi = \frac{m\mathbf{g}}{\hbar} \cdot \frac{2\hbar\mathbf{k}T}{m} \left[n + n_b \left(\frac{1}{2} - \frac{2T_r}{T} \right) \right] \quad (3.83)$$

$$= 2 \left[n + \frac{T-4T_r}{2\tau} \left(\frac{1}{2} - \frac{2T_r}{T} \right) \right] \mathbf{k} \cdot \mathbf{g} T^2 \quad (3.84)$$

$$= 2 \left[n + \frac{T}{\tau} \left(\frac{1}{2} - \frac{2T_r}{T} \right)^2 \right] \mathbf{k} \cdot \mathbf{g} T^2. \quad (3.85)$$

and when $T \gg T_r$ we have

$$\Delta\Phi = 2 \left[n + \frac{T}{4\tau} \right] \mathbf{k} \cdot \mathbf{g} T^2 \quad (3.86)$$

$$= 2n\mathbf{k} \cdot \mathbf{g} T^2 + \frac{\mathbf{k} \cdot \mathbf{g} T^3}{2\tau} \quad (3.87)$$

which shows the T^3 sensitivity to acceleration \mathbf{g} clearly. This can of course also be written as

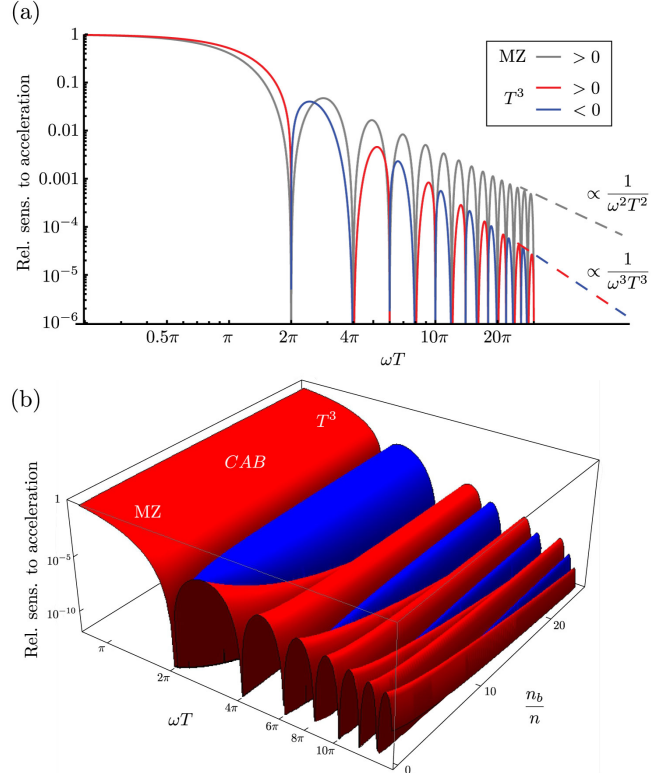


Figure 3.7: (a) The relative sensitivity \mathcal{R} to an oscillating acceleration with frequency ω is plotted for the two extreme cases: a Mach-Zehnder configuration, which exhibits a ω^2 roll-off, and the T^3 case, which exhibits a ω^3 roll-off. (b) The CAB configuration has an intermediate sensitivity to vibrations, which can look like either of the two extremes depending upon the ratio of Bloch oscillations to Bragg diffraction recoils, $\frac{n_b}{n}$. Note that the CAB configuration has double the number of vibration frequencies to which it is completely insensitive, as compared to either of the extreme cases.

$$\Delta\Phi = \left(2nT^2 + \frac{T^3}{2\tau}\right) \mathbf{k} \cdot \mathbf{g} \quad (3.88)$$

The inclusion of the Coriolis effect (again under the assumption that $\mathbf{g} \times \mathbf{k} = 0$) then changes the interferometric phase to

$$\Delta\Phi = \left(2nT^2 + \frac{T^3}{2\tau}\right) \mathbf{k} \cdot (\mathbf{g} - 2\boldsymbol{\Omega} \times \mathbf{v}_i) . \quad (3.89)$$

The CAB scheme is sensitive to vibrations, again according to Eq. (3.47). In the limit of $T \gg T_r$ the relative sensitivity to acceleration is given by

$$\mathcal{R}_{CAB}(\omega) = \frac{1}{1+\epsilon} \frac{4 \sin^2(\frac{\omega T}{2})}{(\omega T)^2} + \frac{1}{1+\frac{1}{\epsilon}} \frac{64 \cos(\frac{\omega T}{4}) \sin^3(\frac{\omega T}{4})}{(\omega T)^3} \quad (3.90)$$

$$= \frac{1}{1+\epsilon} \mathcal{R}_{MZ}(\omega) + \frac{1}{1+\frac{1}{\epsilon}} \mathcal{R}_{T^3}(\omega) \quad (3.91)$$

for $\epsilon = \frac{n_b}{2n}$. Thus as ϵ approaches zero, the noise sensitivity is that of a Mach-Zehnder, whereas when ϵ is large, the noise sensitivity approaches that of a pure acceleration separation between the arms of the interferometer, i.e. T^3 sensitivity. All three cases are illustrated in Figure 3.7.

The phase shift due to an acceleration $\mathbf{a} = \mathbf{a}_c \cos(\omega t)$ is given by

$$\delta\Phi = \frac{m\mathcal{R}_{CAB}(\omega)}{\hbar} \mathbf{a}_c \cdot \mathcal{A} \quad (3.92)$$

which for large ϵ is that of a T^3 interferometer,

$$\delta\Phi = \frac{m\mathcal{R}_{T^3}(\omega)}{\hbar} \mathbf{a}_c \cdot \mathcal{A} \quad (3.93)$$

$$= \frac{64 \cos(\frac{\omega T}{4}) \sin^3(\frac{\omega T}{4})}{\omega^3} \frac{\mathbf{k} \cdot \mathbf{g}}{2\tau}. \quad (3.94)$$

3.4.3 Butterfly configuration

A butterfly configuration is a $\frac{\pi}{2} - \pi - \pi - \frac{\pi}{2}$ Bragg-based interferometer. In this case the acceleration on each path is given by

$$\begin{aligned} \tilde{\mathbf{a}}_a(t) &= \frac{2n\hbar\mathbf{k}}{m} \left[\delta(t + \frac{T}{2}) - \delta(t - \frac{T}{2}) + \delta(t - T) \right] \\ \tilde{\mathbf{a}}_b(t) &= \frac{2n\hbar\mathbf{k}}{m} \left[\delta(t + T) - \delta(t + \frac{T}{2}) + \delta(t - \frac{T}{2}) \right] \end{aligned} \quad (3.95)$$

The space-time area is easy to calculate in this case - it is zero, as one parallelogram cancels the other. So this is a constant-acceleration-insensitive configuration, useful for testing the effect of vibration noise in a system, as in Sec. 5.6. Due to the anti-

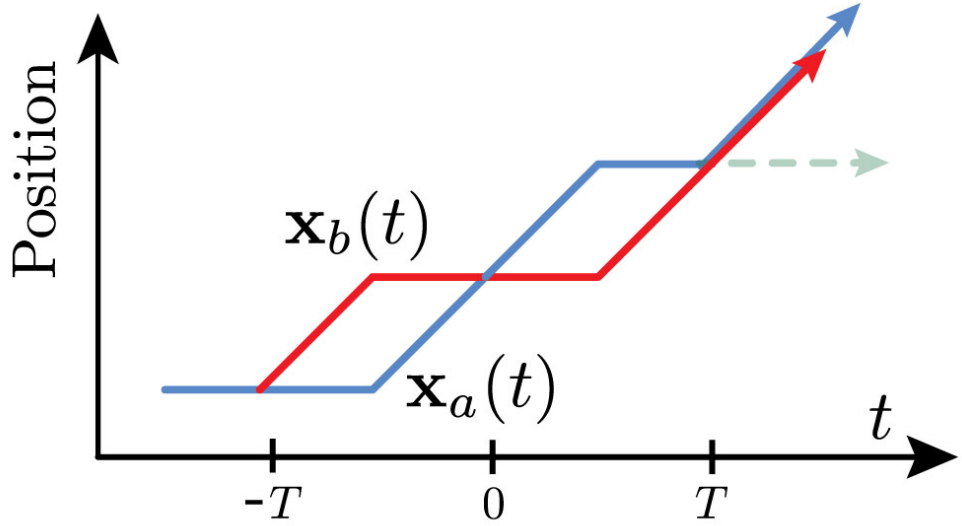


Figure 3.8: Diagram illustrating the paths in a Butterfly interferometer sequence, which is insensitive to constant accelerations.

symmetric nature of this configuration, the sine terms of a vibration now contribute, while the cosine terms do not. Thus the relative acceleration sensitivity becomes

$$\mathcal{R}^*(\omega) = \frac{|\mathcal{A}_s(\omega)|}{|\mathcal{A}^*|} \quad (3.96)$$

$$= \frac{32 \sin^3\left(\frac{\omega T}{4}\right) \cos\left(\frac{\omega T}{4}\right)}{\omega T^2} \quad (3.97)$$

$$(3.98)$$

which is plotted in Fig. 3.9. So the phase shift due to an acceleration $\mathbf{a} = \mathbf{a}_s \sin(\omega t)$ is given by

$$\delta\Phi = \frac{m\mathcal{R}^*(\omega)}{\hbar} \mathbf{a}_s \cdot \mathcal{A}^* \quad (3.99)$$

$$= 2n\mathbf{k} \cdot \mathbf{a}_s \frac{16 \cos\left(\frac{\omega T}{4}\right) \sin^3\left(\frac{\omega T}{4}\right)}{\omega^2} \quad (3.100)$$

$$\approx \frac{n\mathbf{k} \cdot \mathbf{a}_s \omega T^3}{2} \quad (3.101)$$

for small ωT .

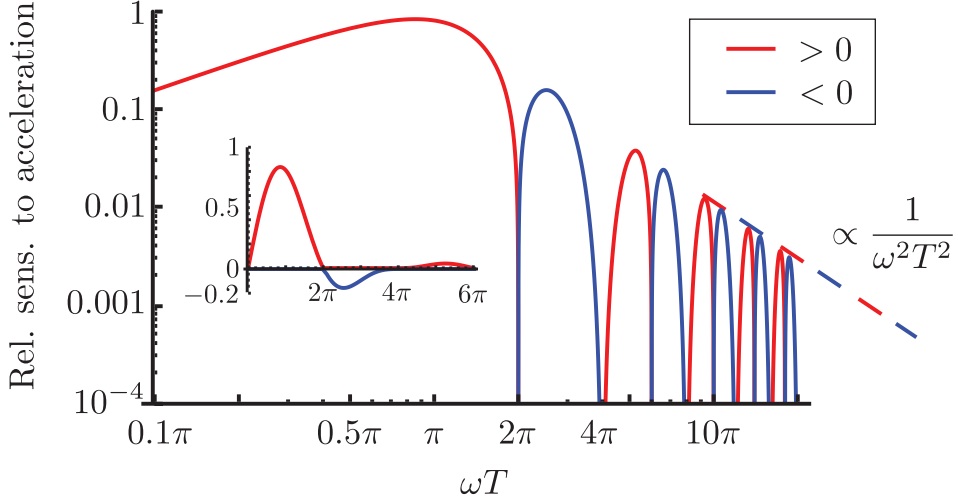


Figure 3.9: Diagram illustrating \mathcal{R}^* , the relative sensitivity of the butterfly configuration to vibrations. This configuration is insensitive to constant acceleration, and at higher frequencies its sensitivity rolls off as ω^2 . Inset: Same plot on a linear-linear scale to show that the sensitivity goes to zero for a constant acceleration.

3.4.4 Recoil sensitive interferometers

Interferometer configurations in which $\Delta\Phi_{\text{kin}} \neq 0$ are in general also sensitive to the recoil frequency $\omega_{\text{rec}} = \frac{\hbar k^2}{2m}$, since

$$\Delta\Phi_{\text{kin}} = \int_{-T}^T \tilde{\omega}_b - \tilde{\omega}_a dt \quad (3.102)$$

$$= \omega_{\text{rec}} \int_{-T}^T \tilde{n}_b^2(t) - \tilde{n}_a^2(t) dt \quad (3.103)$$

where $\tilde{n}_i(t)$ is the number of photon recoils in the velocity along path i at a given time t .

Consider the triangular configuration depicted in Figure 3.10. We assume that the velocity along path a is zero in the inertial frame $\tilde{\mathbf{v}}_a = 0$, and the velocity along path b is $\tilde{\mathbf{v}}_b = \pm \mathbf{v} = \pm \frac{2n\hbar\mathbf{k}}{m}$ as shown in Fig. 3.10. Then the phase is given by

$$\Delta\Phi = \Delta\Phi_{\text{kin}} + \Delta\Phi_{\text{inertial}} \quad (3.104)$$

$$= \omega_{\text{rec}} \int_{-T}^T \tilde{n}_b^2(t) - \tilde{n}_a^2(t) dt + \frac{m}{\hbar} \int_{-T}^T \mathbf{g} \cdot \Delta\tilde{\mathbf{x}} dt \quad (3.105)$$

$$= 8n^2 \omega_{\text{rec}} T - 2n\mathbf{k} \cdot \mathbf{g} T^2 \quad (3.106)$$

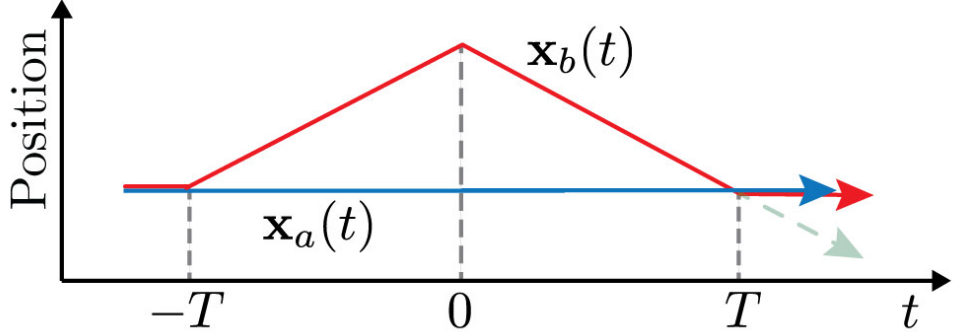


Figure 3.10: Diagram illustrating the paths in an asymmetric, recoil frequency sensitive interferometer sequence.

If we instead choose a constant acceleration separation between the two states, i.e. the velocity goes as

$$\tilde{\mathbf{v}}(t) = \begin{cases} (t + T) \mathbf{a} & \text{for } t < -\frac{T}{2} \\ -(t) \mathbf{a} & \text{for } -\frac{T}{2} < t < \frac{T}{2} \\ (t - T) \mathbf{a} & \text{for } t > \frac{T}{2} \end{cases}$$

then we have the interferometric phase

$$\Delta\Phi = \frac{m}{\hbar} \left(\int_{-T}^T |\mathbf{v}|^2 ds + \mathbf{g} \cdot \mathcal{A} \right) \quad (3.107)$$

$$= \frac{m}{\hbar} \left(4 \int_0^{T/2} |\mathbf{a}|^2 s^2 ds - \frac{\mathbf{g} \cdot \mathbf{a}}{4} \right) T^3 \quad (3.108)$$

$$= \frac{m}{\hbar} \left(\frac{|\mathbf{a}|^2}{6} - \frac{\mathbf{g} \cdot \mathbf{a}}{4} \right) T^3 \quad (3.109)$$

$$(3.110)$$

and so our sensitivity to the recoil frequency (which is now buried in $|\mathbf{a}|^2$) goes as T^3 . For instance if the constant acceleration is due to n_b $2\hbar\mathbf{k}$ -Bloch oscillations over each time $T/2$, then $\mathbf{a} = \frac{4n_b\hbar\mathbf{k}}{mT}$, and the phase becomes

$$\Delta\Phi = \frac{8}{3} n_b^2 \omega_{rec} T - n_b \mathbf{k} \cdot \mathbf{g} T^2 \quad (3.111)$$

$$= \left(\frac{2}{3} \frac{\omega_{rec}}{\tau_b^2} - \frac{\mathbf{k} \cdot \mathbf{g}}{2\tau_b} \right) T^3 \quad (3.112)$$

where on the last line we have substituted $n_b = \frac{T}{2\tau_b}$ for a constant time τ_b for each Bloch oscillation. As we keep higher derivatives of position (let's say the p -th derivative) constant, the space-time area will increase as T^{p+1} , whereas the recoil-dependant term will increase as T^{2p-1} .

To build an acceleration-insensitive configuration you can put two of these back to back in such a way as to cancel the acceleration signal as in Ref. [106]. It is also possible to put them together in such a way as to cancel the recoil phase shift instead, and this is equivalent to a Mach-Zehnder with twice the momentum splitting.

Dual-Species $^{87}\text{Rb}/^{85}\text{Rb}$ BEC Machine

Atom interferometry requires a source of atoms. In our experiments, the two naturally abundant isotopes of Rubidium are our atoms of choice. One reason for this choice is the availability of cheap laser diodes (produced en-mass for CD drives) at the correct wavelength for the D_2 transition at 780 nm in both isotopes [2]. Rubidium-87 also has favourable scattering properties for thermalisation during evaporative cooling, with an s -wave scattering length of $\approx 100 a_0$ [75, 167], and a low three-body recombination rate which would cause an unwanted loss of atoms at high density. These properties make ^{87}Rb one of the most common species of atom for Bose-Einstein condensation.

Rubidium-85 is more difficult to evaporatively cool, with a background s -wave scattering length of $-443 a_0$ and a higher three body recombination rate. Having a BEC of ^{85}Rb is advantageous as its scattering length is variable through the use of a Feshbach resonance at a magnetic field of 155 G. This has many advantages for atom interferometry which will be explored in Chapter 7. A difficulty in the evaporative cooling of ^{85}Rb is that the s -wave contribution to the scattering length disappears at a temperature of $\approx 350 \mu\text{K}$ [37], which precludes efficient self-evaporative cooling through this temperature. One option for condensation of ^{85}Rb would be to tune the Feshbach resonance so that it can evaporatively cool itself [56, 160]. Since the three-body recombination rate is much higher, this leads to larger losses at the densities required for condensation.

We choose instead to use a sympathetic cooling process [182, 9, 27] whereby Rubidium-87 atoms cool the Rubidium-85 atoms via inter-species interactions which occur with an s -wave scattering length of $213 a_0$ [38]. This method has the advantage that during radio-frequency forced evaporative cooling the Rubidium-87 atoms are preferentially removed from the trap, ensuring no loss of the ^{85}Rb while ^{87}Rb is still present. If the process is sufficiently efficient, we can stop the evaporation with a condensate

Property	^{85}Rb	^{87}Rb
Mass m (amu)	84.911789732(14) [34]	86.909180520(15) [34]
Mass m (kg)	1.410×10^{-25}	1.443×10^{-25}
D_2 Transition Wavelength λ_0		780.241 nm [248]
D_2 Transition Linewidth Γ		$2\pi \times 6.067$ MHz [241, 109]

Table 4.1: Important properties of the D2 line in Rubidium [226].

Function	^{85}Rb	^{87}Rb	Detuning from resonance
2D Trapping	30 mW	120 mW	-20 MHz
3D Trapping	50 mW	100 mW	-22 MHz
2D Repump	30 mW	60 mW	0 MHz
3D Repump	20 mW	50 mW	0 MHz
Push beam	$200 \mu\text{W}$	$500 \mu\text{W}$	-15 MHz ^{85}Rb -20 MHz ^{87}Rb
Imaging	1 mW	1 mW	-12 MHz to +12 MHz

Table 4.2: Laser power available on the Science table and the frequencies used during the MOT loading stage, reported as detuning from the relevant closed cycling transition in that isotope.

of each isotope co-existing in the trap. The use of this combination of isotopes for common-mode noise cancellation and precision measurement will be investigated in Chapter 8.

4.1 Laser System

The laser system we use to make BEC requires two sets of frequencies, one for ^{85}Rb and one for ^{87}Rb . For each isotope, imaging, trapping and push beam light are all generated from the master laser. These are all near-resonant to the closed cycling transition for that isotope. In ^{87}Rb the closed cycling transition is $|F = 2, m_F = 2\rangle \rightarrow |F' = 3, m'_F = 3\rangle$ and in ^{85}Rb it is $|F = 3, m_F = 3\rangle \rightarrow |F' = 4, m'_F = 4\rangle$. We generate both sets at the same time, by detuning the ^{85}Rb light before locking it so that it is the same $\Delta f = -212$ MHz away from where it needs to be as the ^{87}Rb (See Table 4.2).

The ^{87}Rb Master laser is locked to the cross-over peak halfway between the $|F = 2\rangle \rightarrow |F' = 1\rangle$ and $|F = 2\rangle \rightarrow |F' = 3\rangle$ transition in ^{87}Rb [See Fig. 4.1 (b)], which is 212 MHz below the latter transition. The ^{85}Rb master laser has a double-pass Acousto-Optic Modulator (AOM) detuning the light by 151 MHz to the blue before it is locked to the cross-over peak halfway between the $|F = 3\rangle \rightarrow |F' = 3\rangle$ and $|F = 3\rangle \rightarrow |F' = 4\rangle$ transition [Fig. 4.1 (c)], leaving the master ^{85}Rb also locked 212 MHz away from its

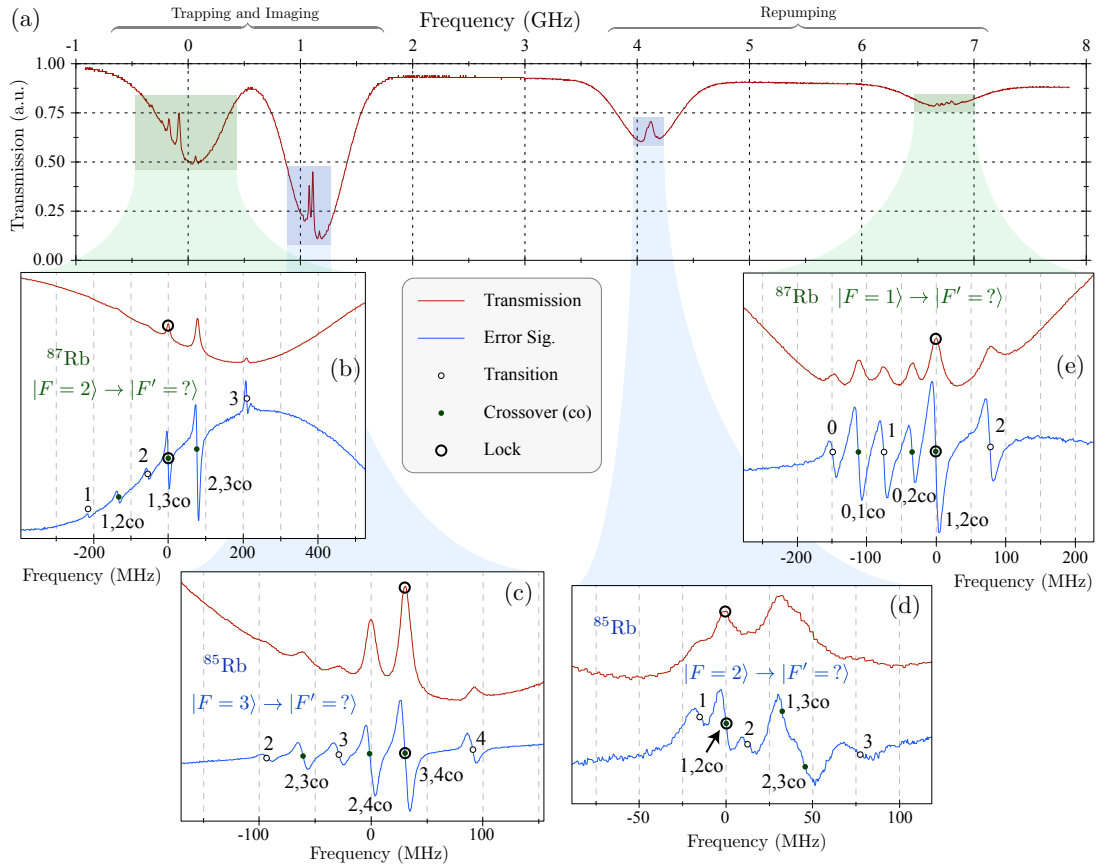


Figure 4.1: (a) This is a scan of the D2 line at 780 nm in a natural abundance mixture of Rubidium gas in a vapour cell. The use of saturated absorption spectroscopy (SAS) means that an individual transition turns up as a narrow peak which is a lack of absorption, against the background of the Doppler-broadened absorption profile. (b-e) Zoomed insets with transitions labelled. Crossovers (co) are artefacts of SAS and they occur halfway between two actual transitions. Error signals [blue, lower lines in (b-e)] are approximately the derivative of the transmission signal. We lock to the peaks by staying at the negative-slope zero crossings of the error signal.

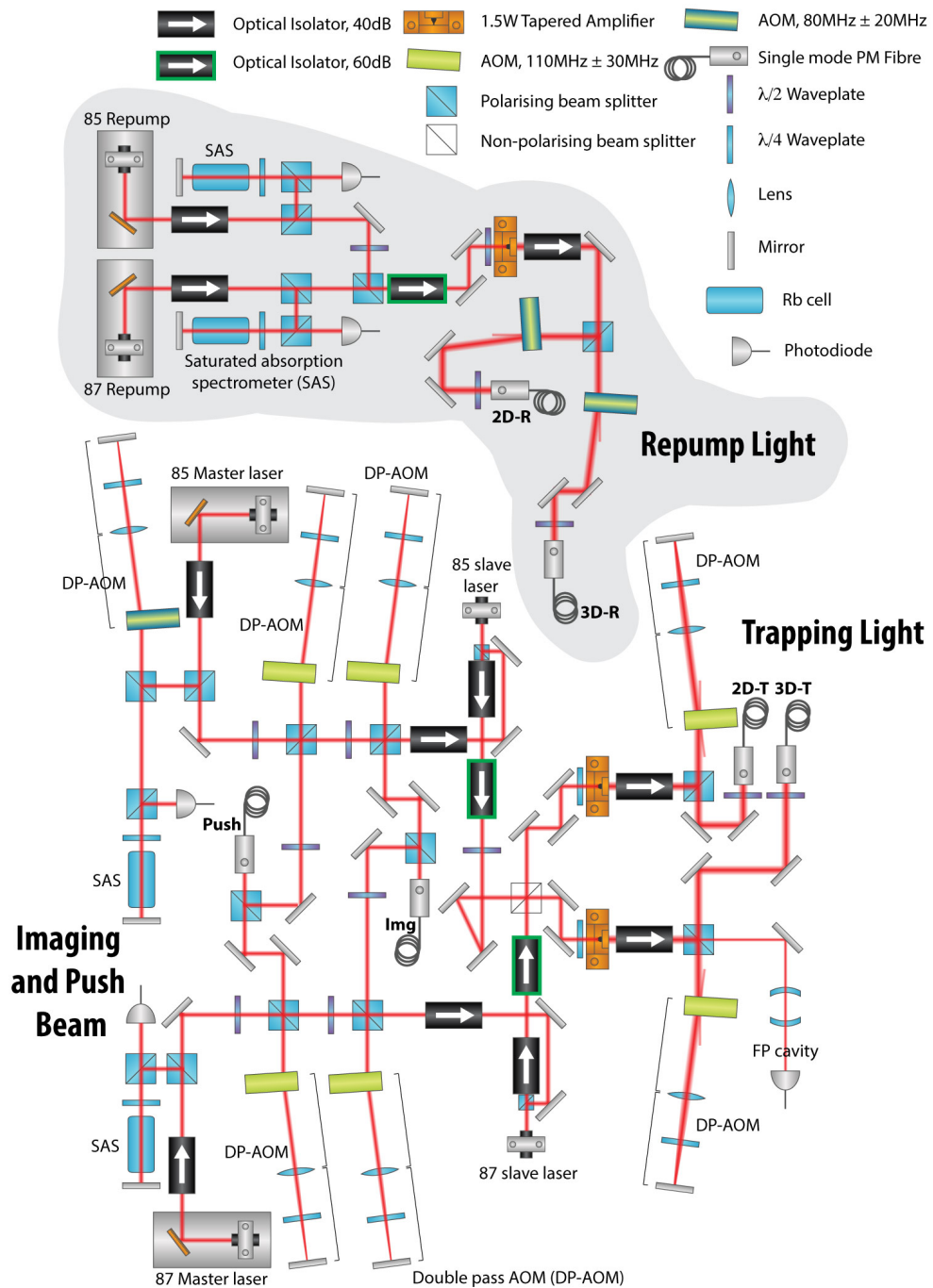


Figure 4.2: This schematic shows the laser system developed for the dual-isotope Rubidium BEC machine. One repumping laser is used for each isotope. Each isotope also has one master laser which is split between trapping, imaging and push beams. The repump and trapping beams go through a tapered amplifier in order to generate a larger amount of power to enable a larger trapping volume for the MOTs. All generated laser frequencies are fibre-coupled to the science table. The Fabry-Perot cavity is used to check that the slave laser diodes are each operating in a single mode.

cycling transition, $|F = 3\rangle \rightarrow |F' = 4\rangle$. Each master diode laser has around 40 mW of light available after the isolator. For each push beam (which sends the atoms from the 2D into the 3D MOT) ≈ 1 mW is picked off from the master laser and tuned appropriately (detunings shown in Table 4.2) through a double-pass AOM setup. For each imaging beam ≈ 5 mW is picked off and sent through a double-pass AOM to set the frequency to be anywhere between 0-12 MHz (0-2 linewidths) detuned either side of the cycling transition, depending upon the imaging requirements. The remaining part of each master laser beam is used to injection-lock a free-standing laser diode to the same frequency. These “slave” beams for ^{85}Rb and ^{87}Rb are then combined on a non-polarising beam-splitter to produce two combined outputs. Each of these outputs goes through a separate tapered amplifier producing around 1 W of each, before being detuned through a double-pass AOM setup. One of these amplified beams is then used for the 2D MOT trapping light, while the other is used for the 3D MOT trapping light. The light from each isotope can be detuned by the same amount due to the AOM in the locking loop of ^{85}Rb which was described earlier.

The repumping laser for ^{87}Rb is locked to the cross-over peak halfway between the $|F = 1\rangle \rightarrow |F' = 1\rangle$ and $|F = 1\rangle \rightarrow |F' = 2\rangle$ transition [See Fig. 4.1 (e)], which is detuned by 78.5 MHz from the $|F = 1\rangle \rightarrow |F' = 2\rangle$ repumping transition in ^{87}Rb . The repumping laser for ^{85}Rb is locked to the cross-over peak halfway between the $|F = 2\rangle \rightarrow |F' = 1\rangle$ and $|F = 2\rangle \rightarrow |F' = 2\rangle$ transition in ^{85}Rb [Fig. 4.1 (d)], which is conveniently 78.1 MHz away from its $|F = 2\rangle \rightarrow |F' = 3\rangle$ repumping transition. As the two detunings are much the same, we then combine the light and pass it through a single tapered amplifier. After this the light is split into two separate beams, one for the 2D MOT and one for the 3D MOT. Each beam is modified in frequency by ~ 78 MHz when it goes through a single-pass AOM to bring it back to resonance and control its amplitude.

All the light generated on the optics table is fibre-coupled to the Science table in single-mode polarisation-maintaining optical fibres. The amount and detuning of each beam which is available on the Science table is given in Table 4.2. See also the schematic of the optics layout in Figure 4.2.

4.2 Science Table

The experiments described in this thesis were performed in a vacuum system (shown in Figure 4.3) which was designed by P. A. Altin, and is well described in his thesis [5]. It has a high pressure end ($\approx 10^{-7}$ torr) where the rubidium is sourced in a 2D Magneto-Optical Trap (2D MOT), and a low pressure end ($\approx 10^{-10}$ torr) where it is collected in a 3D MOT and subsequently cooled to BEC. The rubidium is obtained from an alkali metal dispenser [1] which, when a current of ≈ 3 A is run through it,

sublimes rubidium vapour with the natural abundance ratio of $2/3$ ^{85}Rb to $1/3$ ^{87}Rb .

In the 2D MOT, the magnetic coils are wrapped in a racetrack configuration around the glass cell as shown in Fig. 4.3 (a). Running 10 A through these coils generates a quadrupole field radially and an elongated region of zero field axially down the centre line. Trapping and repump beams for each isotope are retro-reflected along the x and z axes over a long region of the y axis. The red-detuned push beam (also 2-frequencies) encourages the atoms to move down the axis of the 2D MOT, through an impedance, and into the 3D MOT chamber.

The 3D MOT is formed from three retro-reflected beams directed along x-y, y-x and z respectively, as shown in Fig. 4.3 (b). The coils are electrically connected in series in an anti-helmholtz configuration in order to generate a quadrupole magnetic field, and are run with 4.5 A current with only passive air cooling. We load atoms into the 3D MOT for approximately 10 s to achieve a load of approximately 5×10^8 ^{87}Rb atoms and 3×10^6 ^{85}Rb atoms. As the ^{85}Rb is a heat load on the sympathetic coolant of ^{87}Rb , it is important to ensure that there is much less ^{85}Rb present in the 3D MOT. This is done by only turning on the ^{85}Rb push beam late in the 3D MOT loading process, about 0.5 s before the end of the load.

At the end of our MOT loading stage we perform Polarisation Gradient Cooling (PGC) [60]. Over 25 ms we smoothly detune the 3D MOT trapping light from -22 MHz to -95 MHz, while simultaneously ramping off the quadrupole magnetic field, and the amplitude of the repump and trapping light. Immediately thereafter we catch the cooled atoms again in the quadrupole magnetic field by switching it on to 10 A and compress them by ramping it up over 10 ms up to its maximum current of 15 A which produces a gradient of $\approx 300\text{G/cm}$. We also ramp on the crossed-beam optical dipole trap over a second. The crossed-beam optical dipole trap is formed from two laser beams intersecting at a 30° angle. The waveguide beam has 16 W of power at 1064 nm with a linewidth of 1 MHz and a waist of $60\ \mu\text{m}$. The cross beam has 12 W of power at 1090 nm with a linewidth of 2 nm and waist $100\ \mu\text{m}$. The hybrid magnetic-quadrupole/optical-dipole trap provides a potential minimum slightly below the quadrupole trap's magnetic field zero [155] which somewhat avoids loss due to spin-flips at the bottom of the trap. Approximately 1/2 of the MOT atoms are caught here in the target states of $|F = 1, m_F = -1\rangle$ for ^{87}Rb and $|F = 2, m_F = -2\rangle$ for ^{85}Rb . The remainder are either magnetically repelled from the trap or simply untrapped as they are in the wrong m_F state. We now apply radio-frequency evaporative cooling to further cool the mixture of atoms. Because of the magnetic moments of each isotope, ^{87}Rb is selectively evaporated and so ^{85}Rb (which is confined more tightly in the magnetic potential) is sympathetically cooled without loss in this stage. This process, which takes ≈ 9.5 s, is described in depth in the thesis of P. A. Altin [5]. We slowly ramp off the quadrupole trap, leaving the atoms in the crossed-beam optical dipole trap. Now we have around 3×10^6 ^{87}Rb atoms, and 4×10^5 ^{85}Rb atoms loaded into the crossed-beam dipole trap at a temperature of around a micro-Kelvin.

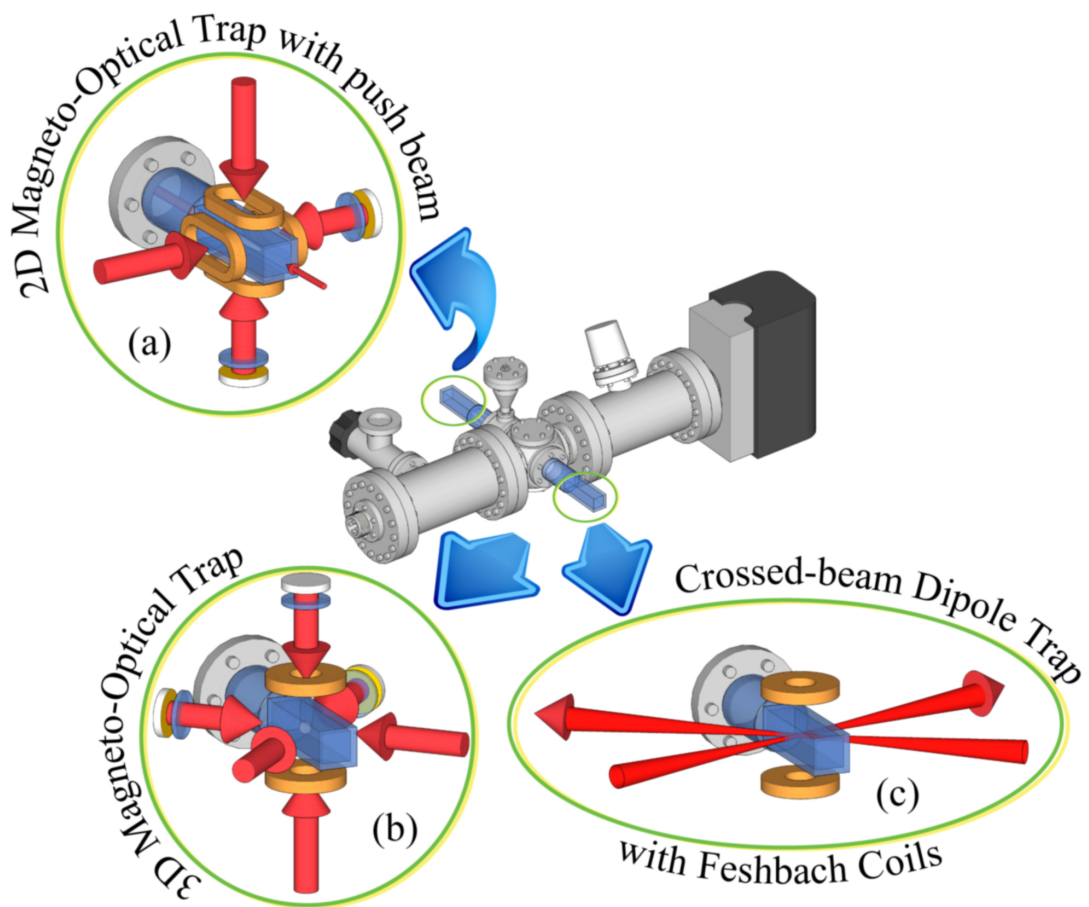


Figure 4.3: Centre: The vacuum system with some key components shown. (a) The source of Rubidium is an alkali vapour dispenser in the 2D MOT cell. The 2D MOT collects the atoms in a line down the centre of the cell from where they are pushed through the vacuum impedance by a push beam into the science cell, which is held at a lower pressure. (b) Here, the atoms are collected and cooled in a 3D MOT. After the 3D MOT is fully loaded with atoms, polarisation gradient cooling is applied, followed by radio-frequency evaporative cooling in the quadrupole magnetic trap. (c) Finally the atoms are transferred to a crossed-beam optical dipole trap. Lowering the intensity of this optical trap provides a final stage of evaporative cooling. After the atoms are held in the optical dipole trap, the direction of current in one of the quadrupole coils can be flipped, so that the coils now produce a near-uniform magnetic field at the location of the atoms. This allows manipulation of the ^{85}Rb Feshbach resonance.

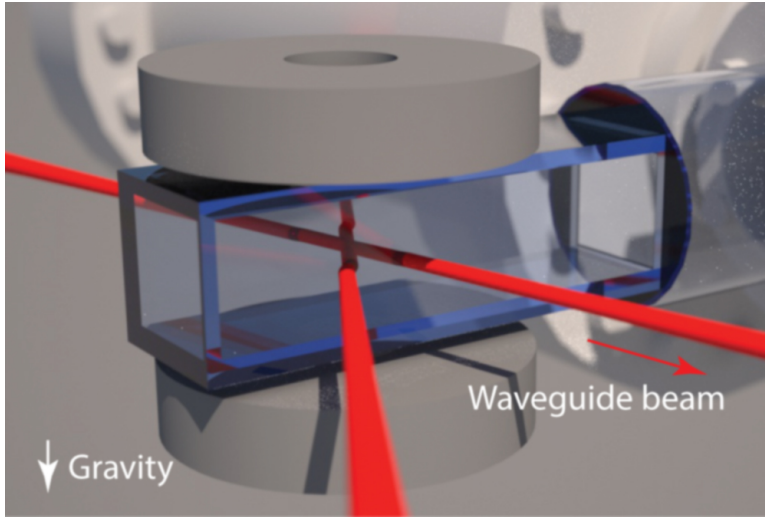


Figure 4.4: This figure shows the orientation of the crossed-dipole trapping beams with respect to the glass cell and Quadrupole/Feshbach coils.

At this point in the run, with the primary magnetic field coils off, we switch the primary coils from an anti-helmholtz to a helmholtz configuration using a H-bridge solid state relay array. This helmholtz configuration now provides a (near) constant magnetic field bias¹ across the whole cloud, which we use to tune the scattering length of ^{85}Rb throughout its Feshbach resonance at $B=155\text{ G}$. This stage is depicted in Fig. 4.3 (c). Now we slowly lower the intensity of the cross-beam optical dipole trap to provide a further stage of evaporative cooling. In the case that we have loaded both species into the trap, the ^{85}Rb is again sympathetically cooled, this time less selectively but due to the difference in mass (and hence gravitational sag) between the two species.

Depending upon the ratio of isotopes that we started with, we now have either a condensate of ^{85}Rb , a condensate of ^{87}Rb , or a mixture of both. We can also adjust the final ratio inefficiently by changing the stop of the r.f. evaporation sweep. We find the largest ^{85}Rb condensates are formed by holding the scattering length of ^{85}Rb at $300 a_0$ for most of the 2.5 s dipole evaporative cooling, and then at $100 a_0$ for the last 0.5 s. This indicates that in this stage, the ^{85}Rb is acting as its own coolant and is no longer being significantly sympathetically cooled. The final cross-beam dipole trap has an axial trapping frequency of $3\text{ Hz} < f_z < 9\text{ Hz}$ depending upon the chosen parameters, and a radial trapping frequency of around $f_z \approx 70\text{ Hz}$. The largest pure ^{85}Rb BEC we have formed at this stage has 2×10^4 atoms, and the largest pure ^{87}Rb BEC we have formed in this configuration has 2×10^6 atoms. Mixtures of the two isotopes will tend to have less of each.

¹As the coils were designed for a quadrupole trap, the “constant” field actually has a small repulsive curvature, as measured in Section 7.1, with the results displayed in Fig. 7.3.

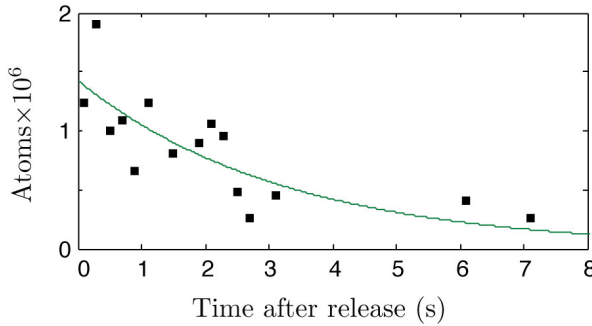


Figure 4.5: This plot shows the number of ^{87}Rb atoms remaining in the optical waveguide over time, indicating an exponential decay with a lifetime of $\approx 3\text{ s}$.

Next the atoms are loaded into the waveguide. Our waveguide is formed from one of the crossed dipole trap beams. To load, we ramp up the waveguide beam's intensity, while ramping down the cross beam's intensity such that the waveguide is sufficient to hold the atoms against gravity by itself. Simultaneously, the scattering length of ^{85}Rb can be ramped to a desired value, for example to zero. In the case of a pure ^{87}Rb condensate, the Feshbach coils are not required and remain off. In Fig. 4.5, the number of ^{87}Rb atoms remaining in the waveguide as function of time is plotted. This data shows an exponential decay in the number of atoms remaining with a decay constant of around 3 seconds.

We can fine-tune the tilt of our waveguide at this stage by adjusting the tilt of the optics table upon which the experiment rests. The table is supported by four air-filled sacs to absorb vibrations, and we can pump these up to varying degrees using a hand-held bicycle pump. Using this technique we adjust the level of the table so that the atoms do not slide to one side or the other when they are held in the waveguide for various lengths of time.

4.3 Optical Lattice Beams

Our optical lattice beams are brought in to the condensate along the same path as the waveguide trapping beam, with the use of dichroic mirrors which reflect 780 nm light but allow 1064 nm light to pass. This is shown schematically in Figures 4.6 and 4.7.

We have up to 60mW of optical lattice light in each of two counter-propagating beams. These are aligned collinear with the waveguide in a two-step process. First, the small fraction of waveguide light which reflects off the dichroic mirror (see Fig. 4.7) is back coupled into the optical fibre which one of the lattice beams comes

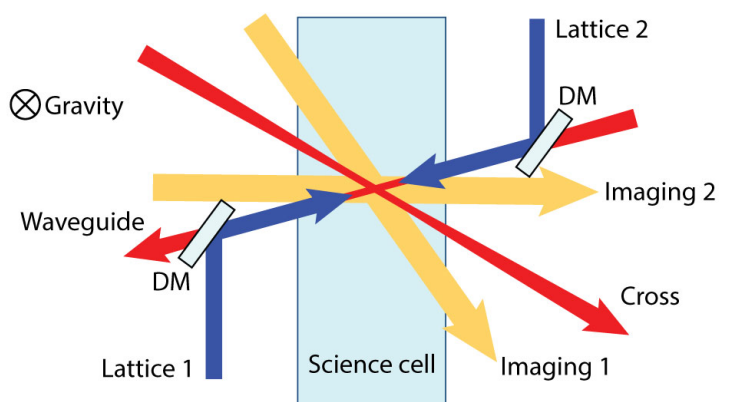


Figure 4.6: The laser beams used to generate optical lattices are brought in along the same path as the waveguide by using dichroic mirrors (DM). To image the results of our experiment, we have two imaging beams which pass through the location of the atoms, and are focussed upon separate cameras (not shown).

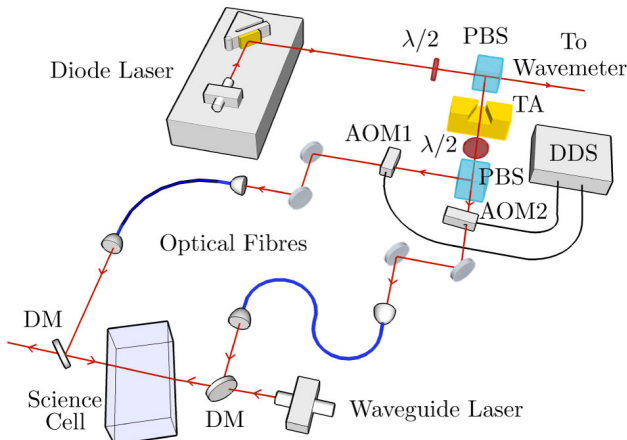


Figure 4.7: Our Bragg laser system consists of two counter-propagating 780nm beams aligned co-linear with the waveguide and detuned from one another on the order of tens of kHz. The beam from an external cavity diode laser detuned by $\sim 130\text{GHz}$ from the D_2 line of ^{87}Rb (as measured using a HighFinesse WSU Wavemeter) is used to seed a tapered amplifier (TA). The output from the TA is split between two acousto-optic modulators (AOM) by a polarising beam splitter (PBS) with a half-wave plate ($\lambda/2$) for frequency and amplitude control. Each AOM is driven near 80MHz by one of two amplified, phase-locked channels from a direct digital synthesiser (DDS, Spincore PulseBlaster). The modulated beams are coupled into separate optical fibres which bring the beams near to the atoms. Dichroic mirrors (DM) are then used to align these Bragg beams counter-propagating and co-linear with the waveguide.

from. Secondly, the other lattice beam is coupled into the same optical fibre. The lattice beams are collimated with a full $\frac{1}{e^2}$ width of 1.85mm and detuned 105 GHz to the blue from the $|F = 1\rangle \rightarrow |F' = 2\rangle$ transition of the D_2 line in ^{87}Rb , which keeps the number of spontaneous emissions below 1% of our total atom number during our interferometric sequence. Arbitrary, independent control of the frequency detuning and amplitude of each beam is achieved using a direct digital synthesizer.

After ballistic expansion of the cold atom cloud, we look at atom density using absorption imaging, as described in Section 2.8.2. In the case that we are taking a series of data for an interferometry run, we will make use of the following Fourier decomposition algorithm to analyse the series of images collected for each interference fringe.

4.4 Fourier Decomposition Algorithm

We process the data we take for an interferometric sequence in the following way. For each run, an interferometric pulse sequence is applied to the atoms, and a picture is taken which shows the spatial distribution of atoms after the interferometric sequence and an expansion.

A simple method to count the atoms in each state is to draw a box around the area where each state is expected and count the atoms in each box for each phase ϕ_3 . To avoid counting non-contributing pixels in our image, which would add unnecessary noise, we use a Fourier phase decomposition algorithm to select which pixels we attribute to each momentum state. For each pixel i in our absorption image we calculate the number of atoms it contains as a function of recombination phase at the end of the interferometer, $n_i(\phi_3)$. We then take the inner product with sinusoids of the expected periodicity

$$\begin{aligned}\alpha_i &= \int_0^{2\pi} n_i(\phi_3) \cdot \sin(m\phi_3) d\phi_3 \\ \beta_i &= \int_0^{2\pi} n_i(\phi_3) \cdot \cos(m\phi_3) d\phi_3\end{aligned}\tag{4.1}$$

where, for example, m is 2 for a $4\hbar k$ transition. Any oscillatory signal in $n_i(\phi_3)$ of the correct frequency such as $n_i(\phi_3) = A_i \cos(m\phi_3 + \Phi_i)$ can be extracted by the relations

$$\begin{aligned}A_i &= 2\sqrt{\alpha_i^2 + \beta_i^2} \\ \Phi_i &= \tan^{-1}\left(\frac{\alpha_i}{\beta_i}\right)\end{aligned}\tag{4.2}$$

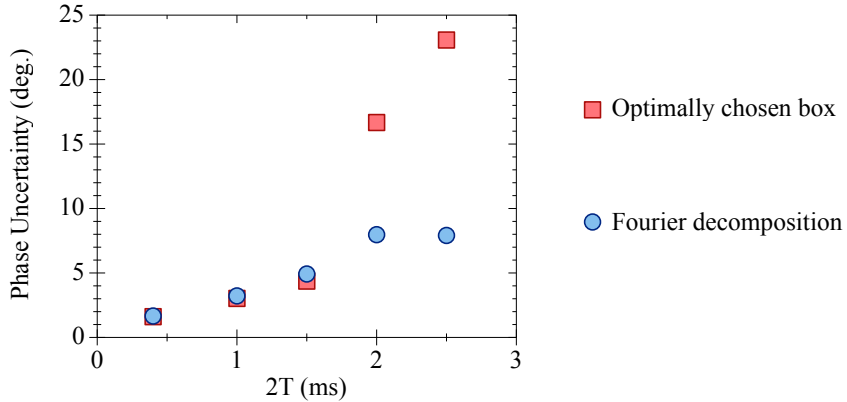


Figure 4.8: Improvement in phase uncertainty by using the Fourier decomposition algorithm.

For a small phase offset ($\Phi_i \approx 0$ for the $0\hbar k$ state) it is sufficient to simply plot β_i , as $|\beta_i| \approx A_i$ and $\text{sign}(\beta_i) \approx \cos(\Phi_i)$, and this has been done in Fig. 5.3. Ideally, two identifiable components will be visible in an image, the $0\hbar k$ momentum state with $\Phi \approx 0$ (with positive amplitude, shown in red) and the $4\hbar k$ momentum state with $\Phi \approx \pi$ (negative amplitude, blue). From this image we select which pixels to include in our regular counting of $N_{0\hbar k}$ and $N_{4\hbar k}$ for all ϕ_3 by setting a tolerance on β_i . The optimal tolerance will depend upon the background noise in the image.

The resulting images are shown in Figure 5.3. Comparing this Fourier decomposition method to an optimally chosen box, for the results discussed in Section 5.4 we find a 56% increase in visibility and a 65% reduction in phase uncertainty at $2T = 2.5\text{ms}$, with the best improvement at longer T and higher phase noise, demonstrating the utility of this method. This is illustrated in Figure 4.8.

Part II

A selection of interferometers

Optically Guided Interferometry

Some of the work in this chapter has been published in:

Optically guided linear Mach-Zehnder atom interferometer

G. D. McDonald*, H. Keal, P. A. Altin, J. E. Debs, S. Bennetts, C. C. N. Kuhn, K. S. Hardman, M. T. Johnsson, J. D. Close, and N. P. Robins.
Phys. Rev. A **87**, 013632 (2013).

Atom Interferometry in an Optical Waveguide,

Honours Thesis by Hannah Keal, October 2012, Australian National University.

5.1 Why guided interferometry?

Guided interferometers have the advantage of being able to constrain the atom's motion in two dimensions while being able to conduct a freely-propagating interferometer in the remaining dimension. This is an example of a defined-axis sensor. For example, one could construct a gravitationally sensitive interferometer in the horizontal plane, suspended against the Earth's gravity, to measure the tidal influence of the sun and moon in the horizontal direction. Alternatively one could measure the difference between the gravitational acceleration with and without a well-calibrated mass present [201], to determine the gravitational constant G in the expression

$$F_{\text{grav}} = \frac{Gm_1m_2}{r^2}. \quad (5.1)$$

An acceleration-sensitive configuration could measure the horizontal acceleration for the purposes of dead-reckoning (e.g. submarine navigation) in a smaller package as compared with a free-fall geometry which requires a vertical height equivalent to the

fall time.

A disadvantage of this configuration is, ironically, the strong coupling to the environment provided by the transverse confinement of the waveguide. This will allow excess vibrational noise to couple in to the interferometer itself.

5.2 Magnetic Waveguides

Over the past decade there has been significant interest in the application of Bose-Einstein condensates (BEC) to the development of compact inertial sensors based on magnetically guided ultra-cold atoms [87, 80]. Trapped atom systems offer the possibility of the ultra-high precision sensing demonstrated by free-space atom interferometry [209, 239] in a more compact package. Atoms can now be Bose-condensed [210, 181, 113, 120], guided [137, 151], split [65, 43, 118], switched [171], recombined [237] and imaged [125, 220] in reconfigurable magnetic potentials which support the atoms against gravity. Typical geometries for magnetically trapped atom interferometers use either atoms bound to a trap which is adiabatically deformed [216, 217, 128, 214] or a magnetic guide in which atoms are manipulated using a standing wave [90, 245, 242, 246, 232].

Precision in these schemes is usually limited by both the roughness of the magnetic waveguide potential which causes decoherence and fragmentation of the condensate [213, 130, 152, 86], as well as interaction induced dephasing due to the tight trapping potentials used in magnetic guiding [47, 121, 147]. Methods used to address these problems have included a Michelson configuration which is only sensitive to relative acceleration between the two arms [242, 132], a constant displacement scheme with an inherently reduced scaling in sensitivity to absolute acceleration [232], or trapping currents oscillating in the kHz range which smooths the potential but causes unwanted heating [238, 33]. The impact of these problems has been highlighted in Ref. [161].

5.3 Optical Waveguide

An alternative solution using optical trapping and manipulation of ultra cold atoms has the advantage of being inherently smooth. Optical elements have been con-

structed which guide [29, 105, 91, 61], reflect [79, 46] and split [123, 92, 73] atom clouds. Recently, a ring interferometer has been constructed to measure rotation [161]. Additionally, relatively large BECs can be quickly produced in optical traps (10^5 atoms in 500 ms [53]) and the atoms in an optical trap can be confined in any internal state, allowing the trapping of magnetically insensitive ensembles [8].

In this chapter we present the first linear, optically guided atom interferometer in an inertially sensitive configuration. A BEC of ^{87}Rb is loaded into an atomic waveguide constructed from a far-detuned optical dipole beam (Fig. 5.1). The atoms are then transferred into the first-order magnetically insensitive $|F = 1, m_F = 0\rangle$ spin state. A Mach-Zehnder (MZ) atom interferometer with $4\hbar k$ momentum splitting is constructed using counter-propagating Bragg beams aligned co-linear with the waveguide.

The first version of the optical waveguide beam had transverse and axial frequencies of 114Hz (measured by exciting a trap oscillation) and 1Hz (calculated from the beam properties) respectively, and is on a tilt of less than 1° with respect to gravity. Consequently the atoms slowly accelerate out of the field of view of our vertical imaging system ($\approx 3\text{mm}$) after around 100ms. We observed the condensate expanding along the waveguide for times on the order of 0.5s (Fig. 5.1) by using a $6\hbar k$ Bloch lattice acceleration up the slight incline and observing the atom cloud as it falls back down the waveguide. The structure visible on the images in Figure 5.1 is largely due to classical noise on our imaging system.

After the BEC is released into the waveguide, we allow it to expand axially for 20ms to reduce any mean-field effects which may be present due to inter-particle interactions at higher density [63]. After expansion we measure the momentum width in the directions axial and transverse to the waveguide to be $0.8\hbar k$ and $0.2\hbar k$ respectively. Using time of flight observations we have determined that the majority of the atoms occupy the transverse ground state of the waveguide [135].

While the BEC expands along the waveguide a constant magnetic field of 30 Gauss is applied by a pair of Helmholtz coils to define the spin axis. During this time the atoms are transferred into the first-order magnetically insensitive $|m_F = 0\rangle$ state using a Landau-Zener radio frequency sweep. We can verify that the atoms are in the $|m_F = 0\rangle$ state by hitting the cloud with a short magnetic pulse, knocking them out of the waveguide if they are in the $|m_F = -1\rangle$ state but leaving them trapped if they are in the $|m_F = 0\rangle$ state.

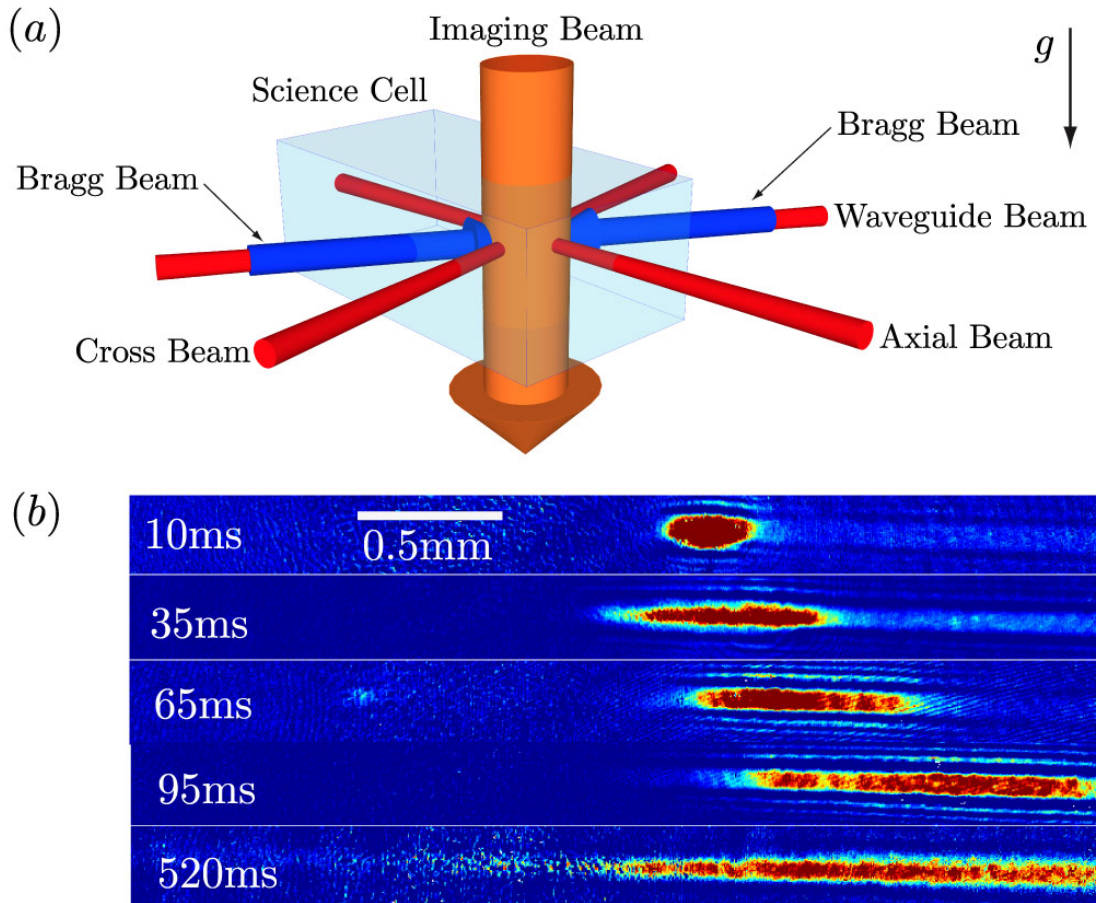


Figure 5.1: (a) The geometry of the first iteration of the optically guided atom interferometer. A BEC is formed in an optical dipole “triple trap” at the intersection of three far-detuned beams. Two of these are switched off to release the atoms into the third beam, the waveguide. A MZ atom interferometer is constructed using Bragg transitions from counter-propagating beams aligned along the waveguide. We image the resulting momentum states using a vertical absorption imaging system. A second absorption imaging system, not shown in this diagram, has its axis in the horizontal plane between the cross and waveguide dipole beams. (b) Images showing expansion of the condensate in the waveguide after different expansion times. Because gravity slowly pulls the atoms out of the field of view of our imaging system, the image after 520ms expansion is of a condensate thrown ‘up hill’ by a $6\hbar k$ Bloch acceleration, and then allowed to fall back into the field of view.

5.4 Optically Waveguided Interferometer

We use Bragg transitions to coherently split, reflect and recombine our atomic wavepacket in momentum along the waveguide to construct a Mach Zehnder (MZ) interferometer. Our Bragg setup is shown schematically in Figure 4.7. For counter-propagating beams, an n th order Bragg pulse which imparts $2n\hbar k$ momentum to the kicked atoms, has a resonance condition (see Section 2.7.6.1) given by $\Delta f = n\hbar k^2/m\pi$, where k is the wavenumber of the light and m is the mass of the atoms. We use $\Delta f = 30.3\text{kHz}$ to effect second order Bragg transitions. We use gaussian laser pulses to achieve optimal momentum state coupling efficiencies [233, 172]. It is important that the waveguide beam and the Bragg beams are perfectly collinear. If not, the atoms which have been kicked by a Bragg transition will develop a helical wiggle as shown in Fig. 5.2, which will cause mismatch at the output of the interferometer. For this reason we align the Bragg beams in a two-step process. First, one Bragg beam is aligned by coupling the small fraction of the waveguide beam going the wrong way on the dichroic mirror back into the Bragg fibre outcoupler. Then, the other Bragg beam is adjusted so as to couple it into the same fibre outcoupler.

Using these Bragg transitions we build a Mach-Zehnder atom interferometer, which is schematically illustrated in Figure 3.5. First a $\pi/2$ pulse is applied to coherently split the atoms into two momentum states, one initially stationary at $0\hbar k$, the other travelling at $4\hbar k$. After a time T we apply a π pulse to invert the two momentum states. After another period T , the two halves of the atomic wave packet are overlapped again and we apply a second $\pi/2$ pulse to interfere the two states. This completes the interferometer sequence.

To measure the acquired interferometric phase, we allow these final states to separate along the waveguide for $(35 - 2T)\text{ms}$, then switch off the waveguide. Another 5 ms of ballistic expansion allows us to avoid lensing of the imaging light by the narrow, dense cloud of atoms. Using absorption imaging we count the number of atoms in each momentum state. To remove the effect of run-to-run fluctuations in total atom

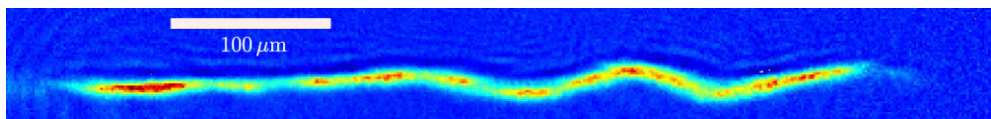


Figure 5.2: Overlaid images after a $2\hbar k$ Bragg kick and various propagation times in the waveguide up to 40 ms, to show the effect poor alignment can have on waveguide propagation. A helical oscillation in the waveguide becomes visible after it has rotated to be in the plane of the imaging system after a few hundred micrometers of propagation. This data was taken in version two of the waveguided interferometer setup. As the oscillation has a period of roughly 13 ms, this means that the transverse oscillation frequency in the waveguide (at this particular intensity level) is $\approx 77\text{Hz}$.

number, we look at the relative atom number in the $0\hbar k$ state

$$N_{\text{rel}} = \frac{N_{0\hbar k}}{N_{0\hbar k} + N_{4\hbar k}} \quad (5.2)$$

This should be an oscillatory function of phase, of the form

$$N_{\text{rel}} = \frac{\mathcal{V}}{2} \cos(\Phi) + \text{offset} \quad (5.3)$$

where the visibility \mathcal{V} of the fringe is the amplitude of the sinusoidal fit, and the offset is ideally $\frac{1}{2}$. The phase Φ of the MZ atom interferometer can be found by combining equations (3.69) and (3.82), and is given by

$$\Phi = 2n\mathbf{k} \cdot \mathbf{a}T^2 + n(\phi_1 - 2\phi_2 + \phi_3) \quad (5.4)$$

where \mathbf{k} is the wavevector of the light used in the n th order Bragg transitions, \mathbf{a} is the acceleration experienced by the atoms from external forces, T is the time between pulses in the interferometer of total length $2T$ and ϕ_j is the phase of the j th Bragg laser pulse. Running the interferometer with constant frequency difference between the two Bragg beams will have two drawbacks. Firstly, the interferometer will quickly acquire a phase shift of many multiples of 2π , and secondly, the Bragg beams will become non-resonant with the desired momentum kick as the atoms fall faster and faster under gravity. To compensate this, the laser frequency difference is swept at a rate $\alpha = \frac{d\omega}{dt} = \frac{d^2\phi}{dt^2}$ which couples in via the laser phase to finally give the expression

$$\Phi = n(2\mathbf{k} \cdot \mathbf{a} - \alpha)T^2 + n(\phi_1 - 2\phi_2 + \phi_3) \quad (5.5)$$

Tuning the interferometer phase Φ to near zero using α , we can measure the component of acceleration along \mathbf{k} . We will demonstrate this by measuring the small residual component of gravity along the near-horizontal waveguide. Measured by time-of-flight imaging, this small residual acceleration is approximately 0.10m/s^2 in this instance. One of the Bragg beams is then swept by $\alpha = 2\pi \times 258\text{Hz/ms}$ in the laboratory frame so as to remain resonant, with no Doppler shift, in the frame of the atoms.

By scanning the relative phase ϕ_3 of the final $\pi/2$ pulse, we obtain fringes in N_{rel} , and these are shown in Fig. 5.3. We obtain a visibility \mathcal{V} of 38% at $2T = 1\text{ms}$ and 15% at $2T = 2.5\text{ms}$. By $2T = 3\text{ms}$, phase noise effectively randomises the final phase of the interferometer, but interference is still seen in the contrast of the interferometer, which is defined as the spread of data in N_{rel} . Even at $2T = 7\text{ms}$ we still have interference with contrast of $\approx 37\%$, albeit with random phase and hence

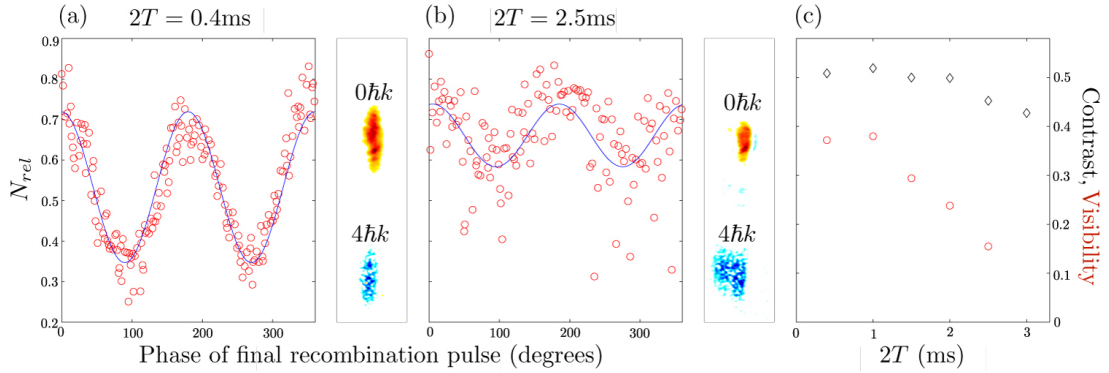


Figure 5.3: We obtained fringes in Mach-Zehnder configuration with $4\hbar k$ momentum splitting. Measured fringes (red circles) and a sinusoidal fit (blue line) of the form $N_{rel} = \frac{\mathcal{V}}{2} \cos(2\phi_3 + \Phi) + c$ for (a) $2T = 400\mu\text{s}$ and (b) $2T = 2.5\text{ms}$. The density plot next to each fringe is a Fourier component of our absorption images for all recombination phases ϕ_3 (see text), and shows the sections of our absorption images which contribute to each state of the interferometer. The $0\hbar k$ (red atom cloud) and $4\hbar k$ state (blue atom cloud) are separated by $870\mu\text{m}$. (c) Visibility \mathcal{V} (red circles) as measured by the sinusoidal fit to each fringe set. Contrast (black diamonds) as measured by range of data N_{rel} from the 2nd percentile to the 98th percentile, is shown for comparison to indicate possible gains in fringe visibility after the elimination of phase noise.

no possibility of an acceleration measurement.

5.4.1 Phase Noise

The phase instability observed at longer interferometer times is likely due to acoustic vibrations affecting the optical fibre out-couplers which bring the Bragg beams to the table. By looking at the beat between our Bragg beams on a low-frequency spectrum analyser we see a significant noise peak between 130Hz and 200Hz in our laboratory. We can consider the effect of vibrations by using the formalism developed in Chapter 3. The phase shift caused by vibrations (those which are even in time with respect to the space-time area of the interferometer) is given by Eq. (3.76),

$$\delta\Phi = 8n\mathbf{k} \cdot \mathbf{x}_c \sin^2\left(\frac{\omega T}{2}\right) \quad (5.6)$$

For a vibration frequency of 170 Hz, and an interferometer time of $T = 2\text{ms}$, a possible 2π phase shift will be caused by a fluctuation in the distance between the two

Bragg fibre couplers of as little as 60 nm.

We calculate the fluctuations in Bragg beam intensity to contribute 1/300th of the measured uncertainty in acceleration, so this was not yet limiting our sensitivity. Run-to-run fluctuations in atom number would not be expected to greatly affect the sensitivity, however the loss of contrast seen in Fig. 5.3 (c) may be due to residual inter-particle interactions [180].

The highest sensitivity to acceleration along the guide that we obtained in the first iteration of the interferometer is $\Delta a = 7 \times 10^{-4} \text{m/s}^2$ at $2T = 2.5\text{ms}$ over 136 runs ($9 \times 10^{-2} / \sqrt{\text{Hz}}$), and we obtain an acceleration of $a = 0.0997(7) \text{m/s}^2$. For comparison, a free space gravimeter run in the same lab [63] had an acceleration sensitivity of $5 \times 10^{-4} \text{m/s}^2$ at $2T = 6\text{ms}$ over 30 runs ($3 \times 10^{-2} / \sqrt{\text{Hz}}$).

The similar results obtained for both the free space and guided interferometer indicated that it was likely that by vibrationally isolating the sensor and Bragg laser system from the mechanical noise present in our laboratory we could achieve significantly higher sensitivity. Thus, one of the changes we made in the second iteration of the machine is that we vibrationally isolated the optical benches the experiment is constructed upon, as well as removing all sources of acoustic and electronic noise from the room in which the experiment was conducted. This achieved significant gains in sensitivity, as will be seen in subsequent chapters.

The quantum projection noise limit on acceleration sensitivity for this type of system is given by $\Delta a = 1 / \sqrt{NkT^2}$ where N is the total number of atoms involved in several runs of the experiment [8], and the visibility is assumed to be $\mathcal{V} = 1$. For our longest waveguide propagation time of $2T = 520\text{ms}$ this limit is an enticing $\Delta a = 4 \times 10^{-11} \text{m/s}^2$ ($2 \times 10^{-9} / \sqrt{\text{Hz}}$). In this hypothetical interferometer we would have a maximum displacement between the atom clouds of 3.6mm, or 10% of the Rayleigh length in either direction and the resulting change in waveguide intensity experienced by the atoms will be less than 1%.

5.4.2 Summary

In summary we have demonstrated a proof-of-principle acceleration sensor based upon Bragg interferometry in an optical waveguide. Our Mach-Zender configuration atom interferometer is sensitive to acceleration along the waveguide axis. As the atoms are optically trapped we are able to operate the interferometer with atoms in the first-order magnetically insensitive $|F = 1, m_F = 0\rangle$ internal state. We have demonstrated clean propagation in the optical waveguide without fragmentation for more than half a second. In the future, this single axis system could be readily adapted to produce a multi-axis inertial sensor by including two additional orthogo-

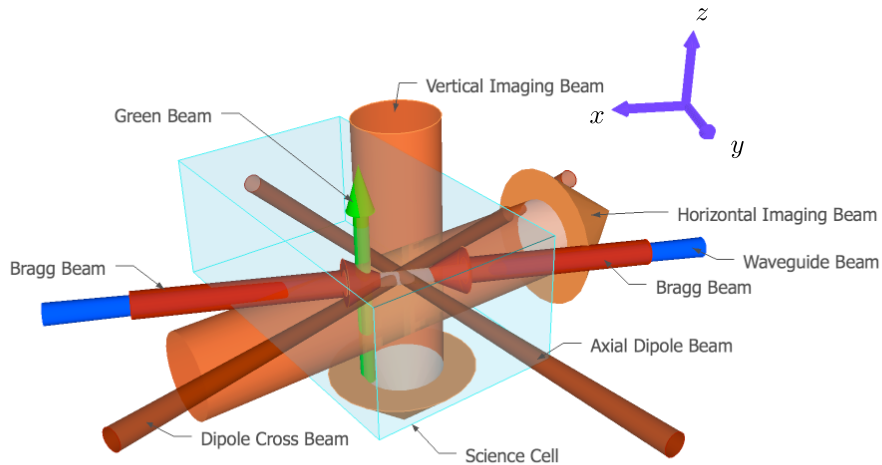


Figure 5.4: The arrangement of optical beams allowing the green potential barrier and waveguide into the science chamber. Gravity lies along the negative z -axis in this figure.

nal waveguide atom interferometers.

5.5 Repulsive optical barrier as a horizontal mirror

The blue-detuned repulsive optical barrier in Sec. 2.7.1 was reimplemented as a horizontal mirror in our optical waveguide as shown in Fig. 5.4 and Fig 5.5. This time a lens with a focal length of 5 cm was used to bring the green $\lambda = 532$ nm beam to a tight focus at the position of the waveguide, but not on top of the position BEC. The beam was brought into the cell along the vertical imaging path in the opposite direction, through the use of a dichroic mirror.

This allowed a simple alignment technique, described as follows. First, a picture of the waveguide's position would be taken by allowing the atoms to expand in the waveguide. This line would be marked on screen with a whiteboard marker. Then, a picture of the MOT with the green beam applied would be taken, in which a small dot with no atom density is seen, at the location of the green beam. The alignment mirrors would be adjusted to bring this spot in line with the waveguide (as seen by the line drawn on the screen). The imaging light was refocussed by an $f=10$ cm lens as shown in Fig. 5.5, in a telescope configuration, before hitting the imaging camera.

By replacing the Bragg mirror with the repulsive optical barrier blue detuned light sheet at 532nm we have constructed a hybrid interferometer similar to the triangular configuration in Fig. 3.10. The space-time diagram for this interferometer is shown in Figure 5.6 (a). First, half the BEC is kicked 'uphill' in the waveguide with a $4\hbar k$

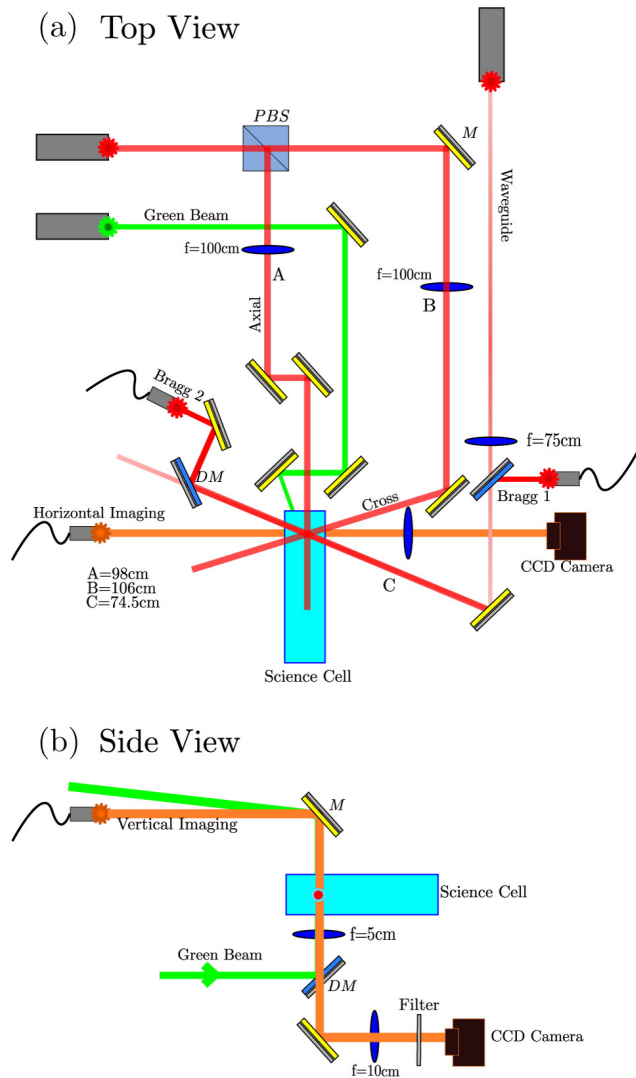


Figure 5.5: The arrangement of optical beams allowing the green potential barrier and waveguide into the science chamber, shown as a top-down diagram in (a) and a side-on view in (b). The Dichroic Mirror and $f=5\text{cm}$ lens shown in (b) were attached to the same, custom made mount to allow both to fit in the limited space available and allow the placement of the lens as close to the atoms as possible.

Bragg $\pi/2$ pulse. The kicked cloud of atoms slows as it slides uphill, then bounces off the repulsive optical barrier, conserving energy and reflecting momentum along the waveguide. It then speeds up as it slides downhill. During this time, the cloud which was not Bragg kicked begins to slide downhill. When the two clouds are overlapped again, slightly further downhill than where they started, we apply a final $4\hbar k \pi/2$ Bragg pulse to recombine the atoms. As before, we then allow the two momentum states to separate along the waveguide, ballistically expand to avoid lensing by the dense cloud, and count the relative number of atoms N_{rel} in the $|0\hbar k\rangle$ momentum state. By adjusting the laser phase $\phi_{\frac{\pi}{2}}$ of the final $\pi/2$ Bragg pulse we can scan an interference fringe. This is shown in Fig. 5.6 (b) for an interferometer time $T = 30.5$ ms. We must be careful to scan the laser frequency difference to compensate for the Doppler shift on the atoms as they accelerate. We must also be sure to calculate the time T_f at which the atoms will overlap again precisely. The phase of the triangle configuration is both velocity and acceleration sensitive. It is given by Eq. (3.106),

$$\Delta\Phi = 8n^2\omega_{\text{rec}}T - 2n\mathbf{k} \cdot \mathbf{g}T^2 \quad (5.7)$$

in the approximation that the repulsive barrier is stationary in the inertial frame, i.e. accelerating along the waveguide at the same rate as the atoms. In our configuration, the repulsive barrier is stationary in the lab frame. Calculating explicitly the result for the repulsive barrier being stationary in the lab frame we find that

$$\Delta\Phi = \Delta\Phi_{\text{kin}} + \Delta\Phi_{\text{inertial}} + \Delta\Phi_{\text{sep}} \quad (5.8)$$

$$= \overbrace{4n^2\omega_{\text{rec}}T_f + 2n\mathbf{k} \cdot \mathbf{v}_0 T_f}^{} - \overbrace{n\mathbf{k} \cdot \mathbf{g}T_m T_f}^{} + \overbrace{2n\mathbf{k} \cdot \mathbf{x}_f \left(1 - \frac{1}{\frac{T_f}{T_m} - 1}\right)}^{} \quad (5.9)$$

where \mathbf{v}_0 is the initial velocity of the cloud w.r.t the lab before the interferometer begins, \mathbf{x}_f is the final position of the cloud w.r.t. the initial position, T_m is the time at which the kicked cloud hits the mirror, and T_f is the time at which the two clouds are overlapped again ready for the final beamsplitter pulse. This final time T_f is given by

$$T_f = T_m \left(1 + \frac{1}{1 + m \frac{v_0 - gT_m/2}{n\hbar k}}\right). \quad (5.10)$$

Simplifying the expression in Eq. (5.9) is possible if we make the trajectories symmetric about T_m by setting $\mathbf{v}_0 = \mathbf{g}T_m/2$. In this case $T_f = 2T_m = 2T$, the separation phase is zero, and the Doppler shift part of the kinetic phase cancels the inertial phase exactly, leaving just the recoil sensitivity

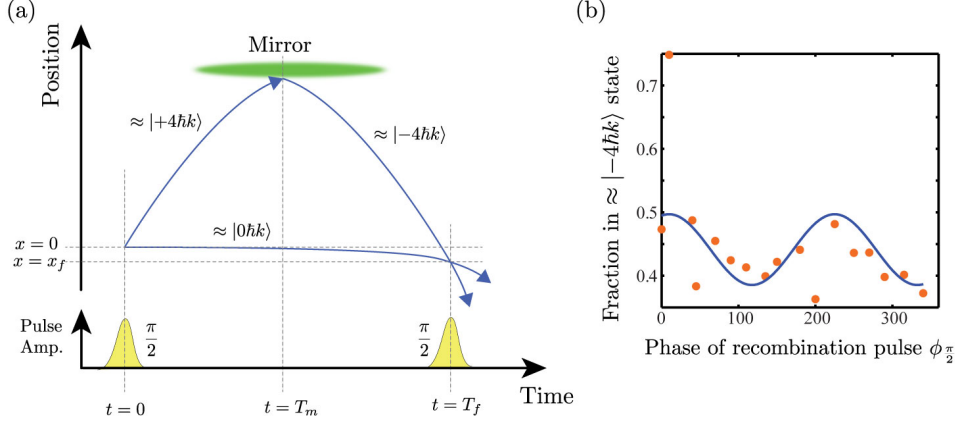


Figure 5.6: (a) Space-time area diagram of a velocity-sensitive interferometer configuration involving reflection from a blue-detuned repulsive optical barrier, similar to Fig. 3.10. (b) Interferometric fringe recorded in this configuration for $T_f = 61\text{ms}$.

$$\Delta\Phi = 8n^2\omega_{rec}T. \quad (5.11)$$

Unfortunately the experiment itself was pulled apart before the expected phase shift was understood properly, so an extensive experimental verification of the phase shift dependence has not yet been performed.

5.6 Butterfly configuration

One way to investigate the effect of vibrational noise on an interferometer is to build an acceleration-insensitive configuration, which vibrations will not degrade as readily. One such configuration is the “butterfly” configuration depicted in Fig. 5.7 (a). This configuration begins like a normal Mach-Zehnder interferometer with a $\pi/2$ pulse then a π pulse separated by a time T . Then, we wait a time $2T$ for the two clouds to pass through one another and reach the same displacement on the other side of each other. At this point, another π pulse is applied, and after a time T the clouds have overlapped a third time and we apply the recombination $\pi/2$ pulse. The theory of this configuration has been explored in Section 3.4.3. Its symmetry makes it insensitive to recoil frequency, and insensitive to any constant acceleration such as gravity. It is sensitive to accelerations which change between the first and second half of the interferometer, for example a vibration of the experiment table during the interferometer. This sensitivity is given by Eq. (3.100), here rewritten for a total interferometer time of $4T$,

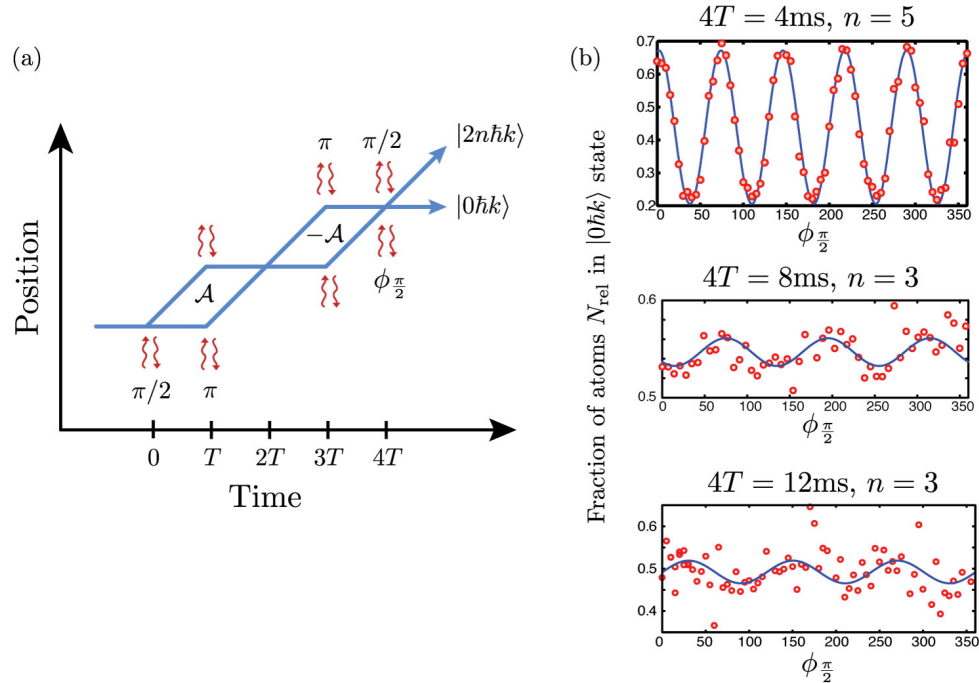


Figure 5.7: (a) The butterfly configuration, which can be sensitive to rotations but not to constant accelerations. (b) Some interference fringes generated by this configuration.

$$\delta\Phi = 2n\mathbf{k} \cdot \mathbf{a}_s \frac{16 \cos(\omega T) \sin^3(\omega T)}{\omega^2} \quad (5.12)$$

where \mathbf{a}_s refers to the component of the vibration amplitude which is in phase with the relative path displacement Δx in the interferometer, i.e. odd w.r.t. the centre of the interferometer.

In Fig. 5.7 (b) we show some interference fringes with this interferometer configuration which were taken on the second iteration of the machine, after some vibration isolation had been put in place. They show coherent interference for longer times than comparable MZ interference fringes, showing that further vibration isolation of the table will yield improvement in the longest interferometer times and largest sensitivities achievable in future versions of the experiment.

Large Momentum Transfer in Atom Interferometry

The work discussed in this chapter is published as

80 $\hbar k$ momentum separation with Bloch oscillations in an optically guided atom interferometer
G. D. McDonald,* C. C. N. Kuhn, S. Bennetts, J. E. Debs, K. S. Hardman, M. Johnsson,
J. D. Close, and N. P. Robins.
Phys. Rev. A **88**, 053620 (2013).

A faster scaling in acceleration-sensitive atom interferometers
G. D. McDonald,* C. C. N. Kuhn, S. Bennetts, J. E. Debs, K. S. Hardman, J. D. Close,
and N. P. Robins.
Europhysics Letters **105**, 63001 (2014).

The interferometer in the previous section in which atoms reflected off a repulsive barrier in the middle of the interferometer is an example of a Large Momentum Transfer (LMT) interferometer. These kinds of interferometer are desirable as the output signal of an atom interferometer generally increases with the momentum splitting of the two states which form the arms of the interferometer.

In this chapter we explore the Coherently Accelerated Bloch (CAB) configuration which allows LMT, based upon momentum transfer of up to 80 photon recoils to and from optical lattices via Bloch oscillations. We measure the interferometric phase in this configuration and show that phase sensitivity to an external acceleration in this configuration scales as T^3 , faster than both the T^2 of a Mach-Zehnder configuration and the T -scaling of a Ramsey-Bordé interferometer. We propose extensions to T^4 scalings and beyond. We characterize the longitudinal curvature of our optical waveguide by constructing a gradiometer in the guide. We also demonstrate a single beamsplitter with $\Delta\mathbf{p} = 510\hbar\mathbf{k}$, indicating the scalability of this approach to LMT.

6.1 Some history of Large Momentum Transfer (LMT)

What is Large Momentum Transfer? In a Mach-Zehnder atom interferometer the interferometric phase scales with acceleration \mathbf{a} as [from Eq. (3.69)]

$$\Phi = \mathbf{k}_e \cdot \mathbf{a} T^2 \quad (6.1)$$

where $\hbar\mathbf{k}_e$ is the total effective momentum separation between the two arms of the atom interferometer. In this form it is plain to see that it is possible to increase the sensitivity to acceleration $\frac{d\Phi}{da}$ by using a larger transfer of momentum, i.e. a larger \mathbf{k}_e . It is also possible in this form to see that the acceleration sensitivity does not depend upon the mass of the atom used.

So given a standard Mach-Zehnder atom interferometer utilising bragg transitions as a starting point, how should one go about increasing momentum transfer, or the space-time area of our interferometer? Here are several methods which have been proposed and/or explored.

Use higher-frequency light

By switching the optical lattice from using light coupling to the D2 transition in ^{87}Rb at 780 nm, to a different transition at ≈ 420 nm, we can approximately double the momentum transferred per photon. This has the disadvantage of requiring a new set of optics which work at UV frequencies. In the absence of an atomic transition, an ionisation grating can be used [115]. Here, 157 nm light gives a fourfold improvement over a $2\hbar\mathbf{k}$ transition employing 780 nm light. This technique has the advantage that it can be applied to any atomic or molecular species. A disadvantage is that as it imprints the diffraction grating via ionisation, it requires a certain fraction of the flux to be lost.

Use an ‘atomic mirror’ to reflect the atoms

Using a stationary sheet of blue-detuned light as a reflecting barrier for the atoms allows the momentum of the atoms to be completely reversed, and was used in Section 5.5 to form a velocity-sensitive interferometer. A disadvantage of this technique is that it is limited to reflecting a momentum which the atoms already have w.r.t the laboratory frame. To overcome this difficulty you could create a moving optical barrier for the atoms using e.g. a rastered AOM setup [199].

Higher-order Bragg transitions: Kick the atoms many times in one go

By coherently coupling two momentum states $\Delta\mathbf{p} = 2n\hbar\mathbf{k}$ apart, it is possible to create a LMT beam-splitter from a single pulse. This has been used to make

atom-interferometers with $6\hbar\mathbf{k}$ [98, 7], $10\hbar\mathbf{k}$ [150, 144] and even up to $24\hbar\mathbf{k}$ momentum separation in a Ramsey-Bordè configuration with 4% visibility [174]. The disadvantage to this technique is that the laser power required to coherently drive this transition scales quadratically with the momentum transfer desired. However, high-power laser systems are being developed with exactly this in mind [204].

Sequential Bragg: Kick the atoms more than once

This technique is known as Sequential-Bragg interferometry. It has been used to demonstrate a momentum transfer of up to $24\hbar\mathbf{k}$ in an acceleration-sensitive configuration. A momentum transfer of $102\hbar\mathbf{k}$ from sequential $6\hbar\mathbf{k}$ Bragg kicks has been used in a system which demonstrated interference [49], however this system was overwhelmed by random noise and therefore could not make any acceleration measurement.

A disadvantage of this technique is that you are limited to an exponential decrease in atom flux as the momentum transfer is increased. Say each Bragg kick imparts $\Delta\mathbf{p}$ momentum to the atoms. On top of the standard MZ configuration, you sequentially stack m of these Bragg kicks together on each arm of the interferometer at each beam-splitter, to reach a total momentum separation of $\Delta\mathbf{p}_{tot} = (2m + 1)\Delta\mathbf{p}$ between the arms of your interferometer. Assuming each Bragg kick has an efficiency (fraction of atoms coherently transferred as desired) $0 \leq E \leq 1$, then the efficiency of the interferometer will be given by $E_{tot} = E^{3+4m} \propto E^{2\Delta p_{tot}}$. Thus the total efficiency of the interferometer exponentially decays as the total momentum separation of the arms is increased, leading the experiment in Ref. [49] to have only ≈ 150 atoms remaining at the end of each interferometer run.

Bloch Lattice Acceleration: Accelerate the atoms on a conveyer belt

This technique is known as Bloch Lattice Acceleration [194]. By loading atoms into an optical lattice, many tens [51], hundreds [39, 250, 45] and even thousands [32, 190, 82] of photon recoils of coherent momentum transfer have been demonstrated in interferometers in which both arms are in the *same* momentum state. Prior to the work described in this chapter, the application of this technique to interferometers in which the arms are *separated* in momentum had achieved $6\hbar\mathbf{k}$ (15% visibility) [63], $10\hbar\mathbf{k}$ ($\approx 2\%$ visibility) [50, 52] and $24\hbar\mathbf{k}$ with $\approx 15\%$ visibility [173].

The difficulty in this technique lies both in the *momentum-state-selective* loading of atoms into the Bloch lattice so that only one of the arms of the interferometer is accelerated, and in accelerating the atoms in such a way that the coherence is maintained, and interference can be generated.

Kapitza-Dirac scattering

By diffracting the atoms from a standing wave (stationary w.r.t. the motion of the atoms) an equal fraction of the total number of atoms will be diffracted into the $\pm 2n\hbar\mathbf{k}$ diffraction orders. This is used to measure the photon recoil frequency $\omega = \frac{\hbar k^2}{2m}$ in Ref. [106] to achieve a $\pm 2\hbar\mathbf{k}$ splitting which is then enlarged to $\pm 4\hbar\mathbf{k}$ by a sequential Bragg transition, for a total momentum separation of $8\hbar\mathbf{k}$.

Other techniques

Double-diffraction Raman techniques [153, 158] have reached $\Delta p = 8\hbar\mathbf{k}$ with 5% fringe visibility, and an extension to double-diffraction Bragg transitions has been proposed [97]. Second-order sequential Raman transitions have been used for rotation sensing [21]. Quasi-Bragg diffraction in the presence of a small magnetic field ($\approx 1G$) has reached $\Delta p = 24\hbar\mathbf{k}$ beam-splitting [70] and been theoretically predicted to be able to achieve much larger momentum splitting [249] but has not as yet been incorporated into an interferometer. Stern-Gerlach magnetic splitting has been used to construct an interferometer with a splitting equivalent to a few $\hbar\mathbf{k}$, and can create beamsplitters in the hundreds of $\hbar\mathbf{k}$ [157]. Another possible technique once the two clouds are spatially separated, is to grab each cloud in the interferometer with a rastered dipole trap [199] and throw them in opposite directions. This is discussed later in Section 6.8.

An important consideration in making an LMT atom interferometer work is the momentum-width of the atom source-cloud used, as this impacts upon the efficiency and coherence of each step [233]. This results in a narrower momentum width source directly translating into a larger achievable coherent momentum transfer.

6.2 Space-time Area and LMT

Following the theory of Section 3.1, the phase shift in a general acceleration-sensitive atom interferometer is given by Eq. (3.30),

$$\Phi = \frac{m}{\hbar} \mathcal{A} \cdot \mathbf{a} \quad (6.2)$$

In this form it is obvious that when talking about Large Momentum Transfer, what is really meant is large space-time area $\mathcal{A} = \int \Delta\mathbf{x} dt$, and, in the case of a Mach-Zehnder atom-interferometer Eqs. (6.2) and (6.1) are equivalent. Space-time area increases monotonically as the momentum transfer is increased, although the exact functional dependence is specific to each implementation. The disadvantage of the form of Eq. (6.2) is that the space-time area \mathcal{A} contains a factor of \hbar/m which cancels

its inverse in Eq. (6.2), and so this form clouds the invariance of the interferometric phase to the mass of the atom used.

Two acceleration sensitive configurations are in common use. The Ramsey-Bordé configuration [31, 45, 50, 173, 23, 14, 174] is constructed from two trajectories which stay a constant distance Δx apart for the duration T of the interferometer¹. It therefore has a space-time area $\mathcal{A} = \Delta x T$ and so its acceleration sensitivity scales linearly with T . The Mach-Zehnder (MZ) configuration [136, 174, 153, 7, 63, 165, 164, 207] is constructed from two paths that have a constant velocity difference $|\Delta \mathbf{v}|$, which is reversed after the interferometer time T . The MZ space-time area is given by $\mathcal{A} = |\Delta \mathbf{v}| T^2$ and so the sensitivity to acceleration will scale with T^2 , as in Eq. (6.1).

In this chapter we also present the logical extension: an interferometer configuration in which the two paths are separated by a constant acceleration $|\Delta \mathbf{a}_b|$ with respect to one another. In this configuration, the space-time area is given by $\mathcal{A} = \frac{|\Delta \mathbf{a}_b|}{4} T^3$ and so the sensitivity to the common, external acceleration \mathbf{a} will scale as T^3 . This technique will allow greater sensitivity for a given interferometer time T , thereby increasing the sensitivity to accelerations at all frequencies to which the interferometer is unambiguously² sensitive $f \lesssim 1/T$. We demonstrate an increase in sensitivity given by this technique, as compared with a standard MZ configuration. A straight forward extension of the technique to a T^4 scaling is also discussed.

6.3 Experimental set-up

Our interferometric source is a ^{87}Rb condensate of 2×10^6 atoms, formed as discussed in Chapter 4, with a repetition rate of 2.5/min. We measure the axial trap frequency just before release into the waveguide to be 9 Hz, by measuring the momentum oscillations after a $2\hbar\mathbf{k}$ Bloch acceleration. Similarly, by misaligning the Bragg beams and giving a kick after release into the waveguide we measure the transverse (radial) frequency to be 60 Hz.

6.4 Delta-kick cooling for a narrow momentum width source

As the cross beam is adiabatically ramped off, the waveguide intensity is increased back to 4.5 W so as to hold the atoms against gravity. We then wait a time t_f for the

¹Neglecting the quick accelerations required to initially separate and finally recombine the two trajectories.

²The interferometer is of course sensitive to higher frequencies as described in Section 3.3.2, but due to aliasing it is not easy to determine which of the possible frequencies caused the signal.

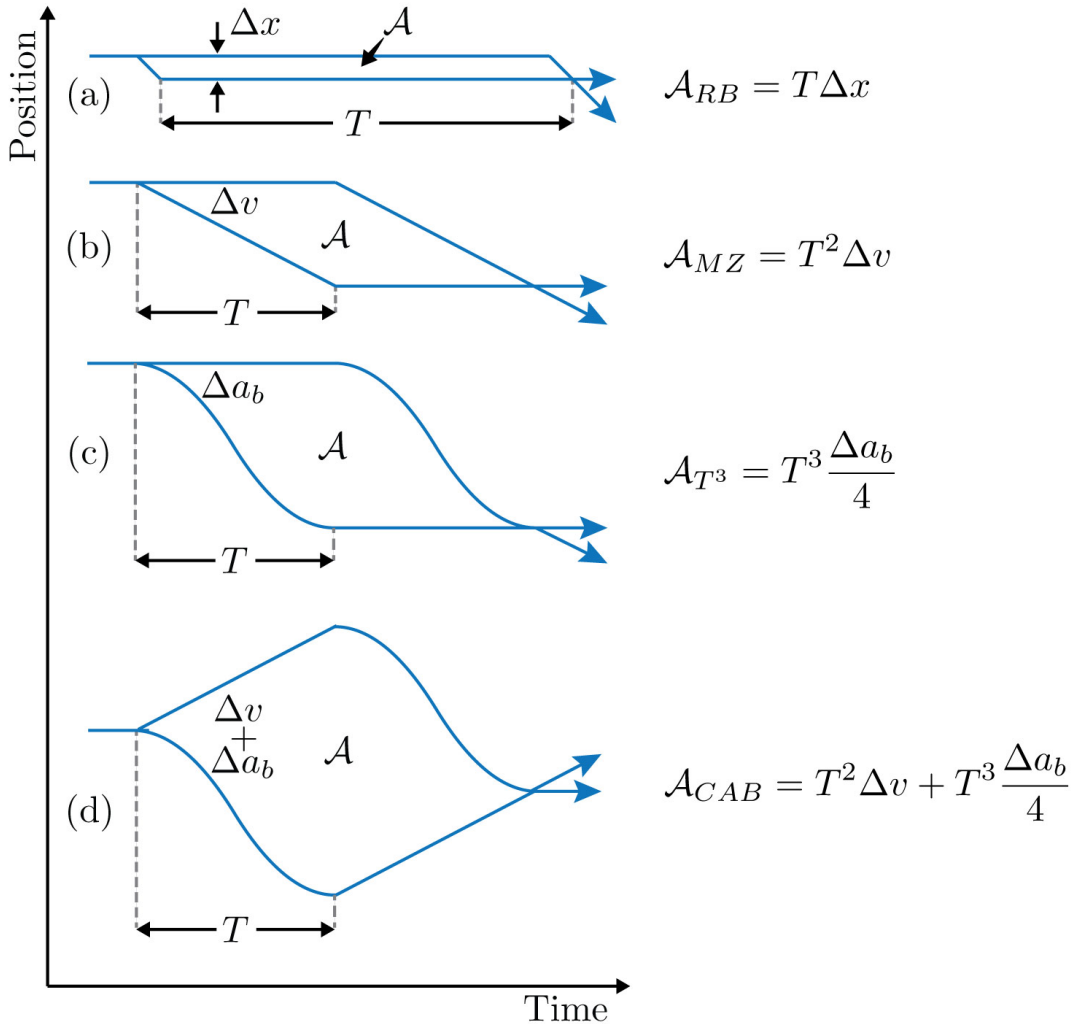


Figure 6.1: The space time area $\mathcal{A} = \int \Delta x dt$ is illustrated for several acceleration-sensitive interferometer configurations. For clarity, the common inertial acceleration a is zero in this diagram. (a) In a Ramsey-Bordé configuration, the two particle trajectories are separated by a constant displacement Δx for the duration of the interferometer. (b) A Mach-Zehnder configuration separates the two trajectories by a constant velocity difference $|\Delta v|$. Halfway through the interferometer, this velocity difference reverses sign. (c) This paper introduces the configuration in which the two trajectories are separated by a constant acceleration $|\Delta a_b|$. (d) In practice, an initial velocity difference between the two arms is required before the acceleration can be accomplished state-selectively, so the CAB interferometer configuration we investigate experimentally is a combination of both (b) and (c).

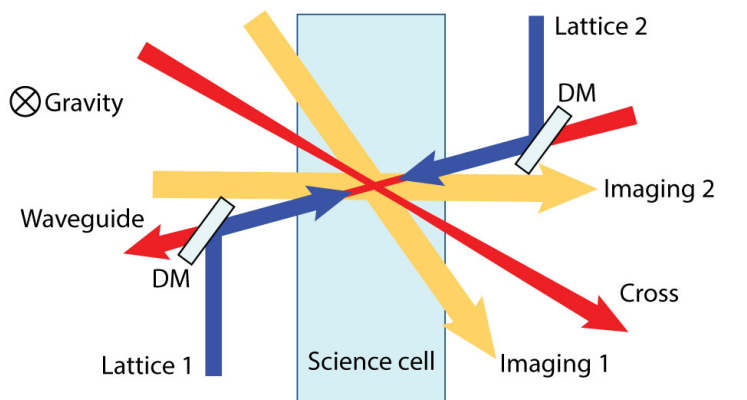


Figure 6.2: We form a BEC in a cross beam dipole trap, before releasing it into the waveguide. After it has expanded for 125ms, we flash on the cross beam again to apply delta-kick cooling to the atoms. Our interferometer is formed by Bragg and Bloch pulses from counter-propagating lattice beams aligned collinear with the waveguide beam. The collinearity is achieved through the use of Dichroic Mirrors (DM).

atoms to expand in the guide, during which time they convert their mean-field energy into the kinetic energy of their velocity spread [63, 164] and then expand further until the position of each atom along the guide is well correlated with its momentum [See Fig. 6.3 (a) and (b)]. Now the dipole cross beam is flashed on again for 2ms, providing an approximately harmonic potential which decelerates the faster atoms. This is an example of delta-kick cooling [12], which has been employed previously using Quadrupole-Ioffe magnetic traps [175, 12], but had not yet been reported for an optically generated harmonic potential. Subsequently this optical delta-kick cooling technique has been used in combination with magnetic techniques to demonstrate temperatures as low as 50 pK [146] (equivalent to a momentum width of $0.012\hbar k$), and is proposed to be used in future space-based missions. Delta-kick cooling effectively rotates the ellipse describing position-momentum correlation along the waveguide so as to have minimal spread in momenta across the cloud [See Fig. 6.3 (c)].

For the case of a point source of atoms the process can be considered equivalent collimation of an expanding laser beam through a thin lens, and the thin lens equation (with position variables appropriately transformed to time) applies;

$$\frac{1}{t_f} = \frac{1}{t_i} + \frac{1}{t_o} \quad (6.3)$$

where t_f is the focal time of a specific lensing (delta-kick cooling) pulse which occurred a time t_o after the point source was released and began to expand, and t_i is the time before the focussed image of the original source cloud will appear. To collimate the atoms into a narrow momentum width requires expanding them for a large time t_o and then applying a focussing pulse with $t_f = t_o$ such that t_i is as large as possible

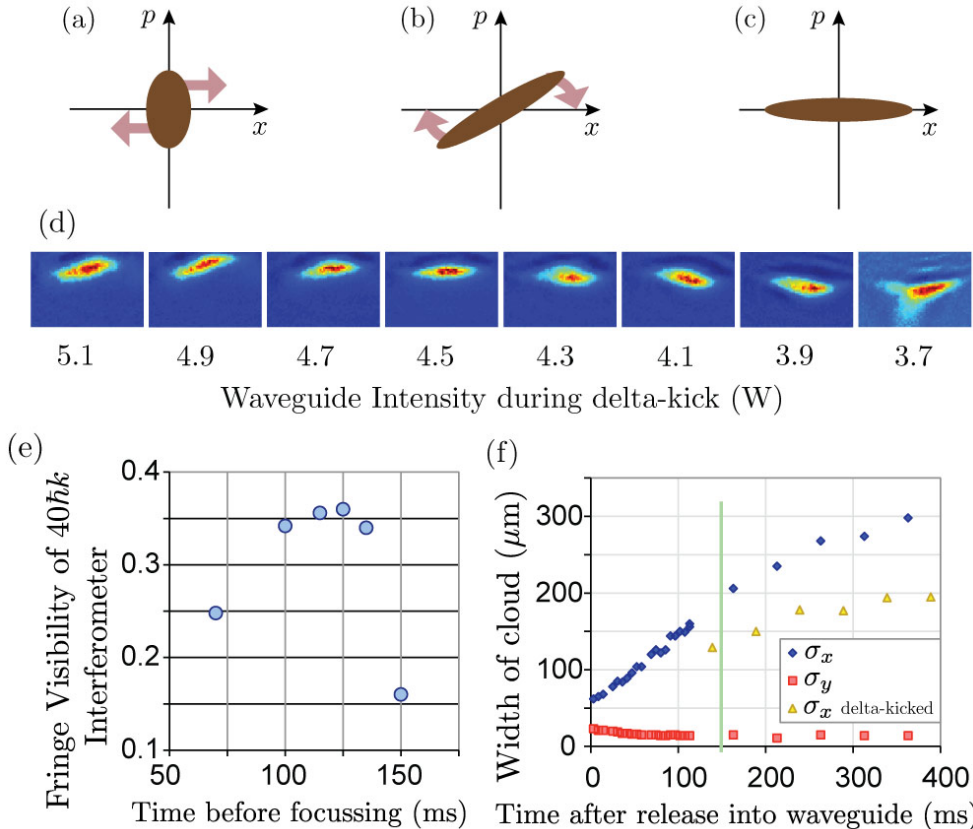


Figure 6.3: (a) Immediately after the condensate is released into the waveguide, it has a minimal spread in spatial extent and in momentum width. (b) Over time, the cloud expands ballistically until momentum is well correlated with position along the guide. (c) Application of a harmonic potential for a short time (the delta-kick) reduces the momentum spread of the cloud, which now has a larger spatial extent. (d) It is important to adjust the waveguide intensity so that the delta-kick cross-beam pulse is applied symmetrically over the cold cloud, otherwise transverse oscillations will occur in the guide. Here we show this adjustment process, in which the cloud is photographed a certain time after delta-kick cooling. The cloud is observed to oscillate if the waveguide power is either side of 4.5 W. At 3.7 W we can see atoms falling out of the guide as they oscillate. (e) We optimize our delta-kick cooling by looking at the fringe visibility (as measured by a sinusoidal fit) of a $40\hbar k$ interferometer. We find our best visibility when our cross-beam flashes on 125ms after the atoms are released into the waveguide. (f) Of course, this collimation is imperfect; here we show the longitudinal width σ_x of the cloud expanding after release as measured by the standard deviation of a gaussian fit, both with (yellow triangles) and without (blue diamonds) the cross beam flash at 125ms. Also shown is the transverse width σ_y (red squares). All widths are measured after an extra 22ms of ballistic expansion after the waveguide expansion time shown in (f).

and the matter-wave is collimated.

In the case of a BEC in trap we do not have a point source of atoms. A non-interacting BEC sourced from a harmonic potential will initially be at the Heisenberg limit of $\sigma_x \sigma_{p_x} = \hbar/2$. As the BEC expands σ_x will increase while σ_{p_x} will stay constant, so the uncertainty product will no longer be at this limit. However, either at the point of refocussing (t_i) or after collimation, the cloud will return to the Heisenberg limit but with a different σ'_x and σ'_{p_x} . Because of this, delta-kick cooling (or matter-wave focussing) is a form of quantum-mechanical squeezing³. In a BEC with interactions, the untrapped momentum width will increase after release as the mean-field energy converts to kinetic energy, which is an additional imperfection on the delta-kick cooling process.

Due to the finite-size σ_x , the mean-field energy conversion and the anharmonicity of our dipole cross beam potential our delta-kick cooling is not ideal, so in practice we calibrate the process by measuring the fringe visibility of a $40\hbar k$ CAB interferometer performed after various configurations of pulse strength ($\propto 1/t_f$) and object times t_o . We find $t_f = t_o = 125$ ms for our optimal delta-kick cooling configuration. Figure 6.3 (e) shows this calibration and demonstrates that a narrow-momentum-width atom source is critical for reasonable fringe visibility in an LMT interferometer. By extracting the gradient of a linear fit to the expanding delta-kick-cooled cloud width (Figure 6.3 (f), yellow triangles) we see that our interferometric atom source now has a momentum width of $0.05\hbar k$, equivalent to a temperature of around 900 pK.

Also, as shown in Figure 6.3 (d) it is important to adjust the intensity of the waveguide through this process, in order that the cloud of atoms is not set in motion transversally by the delta-kick cooling pulse. This motion occurs if the dipole cross-beam is not aligned vertically with the position of the atoms when the delta-kick cooling pulse is applied. Adjusting the waveguide intensity corrects this missalignment though gravitational sag as discussed in Section 2.7.3.

6.5 Interferometer Pulse Sequences

Our optical lattice laser setup is described in Section 4.3. Prior to our interferometer, a velocity selection Bragg pulse of $10\hbar k$ is used to isolate the portion of atoms ($\approx 80\%$)

³In general, squeezing results from some kind of (usually quadratic) non-linearity. In the case of the free-space expansion here, the nonlinearity is trivial — it is the kinetic energy term $\frac{\hat{p}^2}{2m}$ in the Schrödinger equation. At the time of the delta-kick cooling pulse itself, the harmonic potential $\frac{m\omega^2}{2}$ plays this role.

with a narrow momentum width σ_p from those not properly cooled by our delta-kick process. For clarity, the following interferometry sequences will be described in the frame of these velocity selected atoms, which are themselves moving at $10\hbar\mathbf{k}$ with respect to the laboratory frame. Each part of each sequence is labeled with roman numerals corresponding to its depiction in Figure 6.4.

6.5.1 Mach-Zehnder sequence

A standard MZ interferometer sequence is constructed as follows, as depicted in Fig 6.4 (a). **i.** An optical standing wave formed from two counter-propagating beams each of wavevector $\pm\mathbf{k}$ is used as a matter-wave diffraction grating, beam-splitting the atoms along two trajectories which are separated in momenta by the Bragg condition, $\Delta\mathbf{p}_x = 2n\hbar\mathbf{k}$, where n is the diffraction order. **v.** After a time T , another Bragg-diffraction pulse is applied which diffracts the stationary state to $2n\hbar\mathbf{k}$ at the same time as diffracting the $2n\hbar\mathbf{k}$ state to be stationary. This effectively swaps the momenta of each state, so it is the atom-optical equivalent of a mirror. **vii.** When a total time $2T$ has elapsed and both trajectories are overlapping once again, a final Bragg-diffraction beam-splitter pulse is applied which recombines the two momentum states.

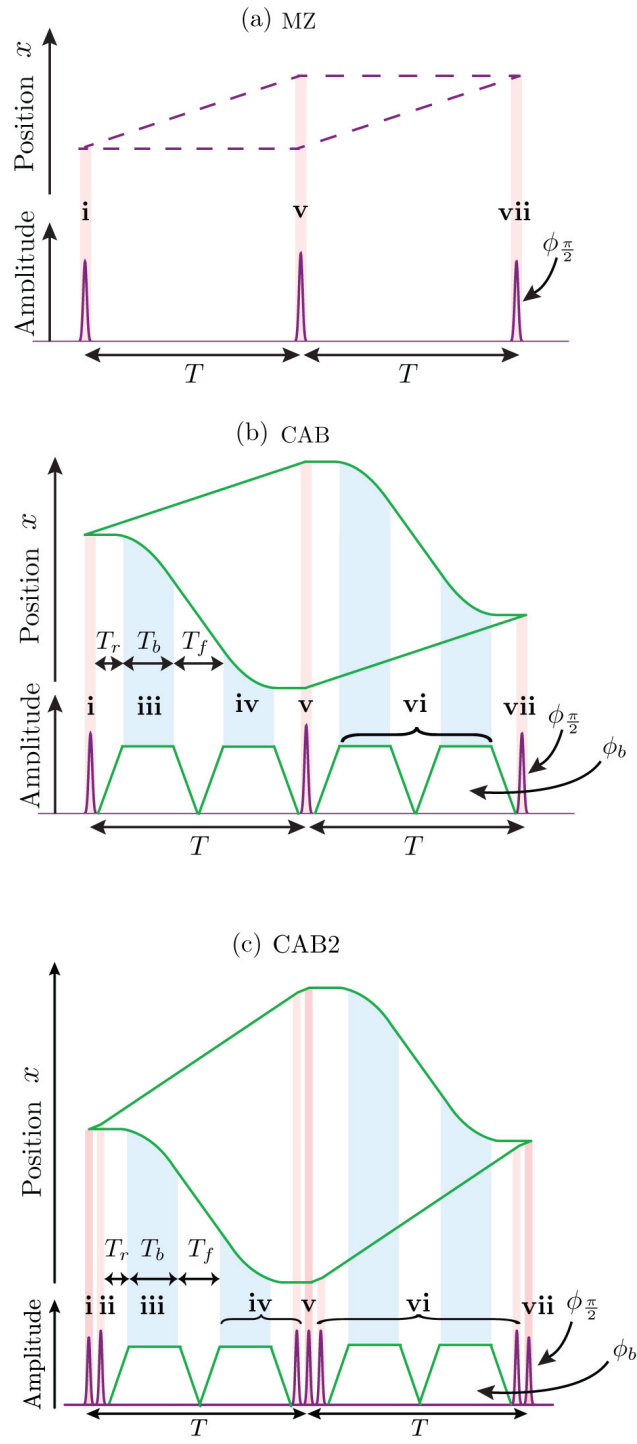
6.5.2 CAB sequence

Our CAB interferometer sequence, illustrated in Fig. 6.4 (b), is built upon this standard MZ configuration. **i.** After the first Bragg-diffraction beam-splitter there are two momentum states in the waveguide, one stationary and one with momentum $\mathbf{p}_x = 2n\hbar\mathbf{k}$ in the positive- x direction. **iii.** Over a time T_r we selectively load the stationary momentum state into a stationary optical lattice with a potential energy depth of $15E_r$, where the photon recoil energy is given by $E_r = (\hbar k)^2/2m$. We accelerate the lattice in the negative- x direction via n_b Bloch oscillations [184] over a time T_b , each of which imparts $2\hbar\mathbf{k}$ momentum. This amounts to a constant acceleration rate of $\Delta\mathbf{a}_b = \frac{2n_b\hbar\mathbf{k}}{mT_b}$ applied to the state loaded into the lattice. The state selectivity is accomplished because the optical lattice is moving fast enough with respect to the $\mathbf{p} = 2n\hbar\mathbf{k}$ momentum state that this state experiences just the time-averaged lattice potential, which imparts no acceleration [see Fig. 2.10 (a)]. **iv.** After a negligible time T_f we decelerate the state until it is stationary again. **v.** The Bragg-diffraction mirror pulse is applied a time T after the beginning of the interferometer, which swaps the momenta of each state. **vi.** The Bloch lattice acceleration and deceleration sequence is now applied to the other arm of the interferometer. **vii.** The two momentum states are recombined by a final Bragg-diffraction beam-splitter.

Figure 6.4: The space-time trajectories of the three interferometer configurations considered in this chapter are shown here in the freely-falling frame, along with the pulse sequence required to generate each one. (a) A $10\hbar\mathbf{k}$ Mach-Zehnder interferometer is constructed from three Bragg pulses in a $\pi/2 - \pi - \pi/2$ configuration. A fringe can be scanned out by adjusting the phase $\phi_{\frac{\pi}{2}}$ of the final beam-splitter pulse.

(b) The CAB scheme builds upon the $10\hbar\mathbf{k}$ MZ by selectively accelerating one arm of the interferometer at a time by up to $60\hbar\mathbf{k}$ using a Bloch lattice. In this case the interferometric fringe can be scanned out by adjusting either the phase $\phi_{\frac{\pi}{2}}$ of the final Bragg beam-splitter pulse, or the phase ϕ_b of the last Bloch acceleration lattice applied. (The choice of which pulse to use for adjusting the phase is of course completely arbitrary)

(c) Faster acceleration in the Bloch lattice requires a larger initial velocity separation in order to maintain the velocity-state selectivity. The CAB2 sequence increases this separation by making each beam-splitter from sequential Bragg pulses.



6.5.3 CAB2 sequence

i. The CAB2 sequence [shown in Fig. 6.4 (c)] begins with a $2n\hbar\mathbf{k}$ $\frac{\pi}{2}$ Bragg pulse with $n = 5$ applied to the atoms to coherently split them into two momentum states, one in the initial $0\hbar\mathbf{k}$ state, the other traveling at $10\hbar\mathbf{k}$ ii. followed by an extra $10\hbar\mathbf{k}$ Bragg kick which is given to the faster $10\hbar\mathbf{k}$ atoms, taking them to $20\hbar\mathbf{k}$. iii. The $0\hbar\mathbf{k}$ atoms are then loaded into a Bloch lattice of 10-20 recoil energies over a rise time of $T_r = 110\mu\text{s}$ which is accelerated in the other direction up to $2n_b\hbar\mathbf{k} = -60\hbar\mathbf{k}$ depending upon the final momentum separation desired, over a time $T_b = 150\mu\text{s}$. iv. After a free evolution time of T_f , these accelerations are reversed, to bring the atoms in the lower arm back to the $0\hbar\mathbf{k}$ and the upper arm back to $10\hbar\mathbf{k}$. v. A time T after the initial $\frac{\pi}{2}$ pulse we apply a π Bragg pulse to invert the two momentum states before vi. repeating the acceleration and deceleration sequence, which now acts upon the opposite arm of the interferometer. vii. After another period T , the two halves of the atomic wave packet are overlapped again and we apply a second $\frac{\pi}{2}$ pulse to interfere the two states.

6.5.4 Calibration of Bloch Lattice

Adjusting the Bloch lattice intensity, load rate and acceleration rate for the CAB and CAB2 sequences requires careful decomposition and inspection of the interferometer sequence, and the process is illustrated in the flowchart of Fig. 6.5.

6.5.5 Detection

The final optical standing wave (vii, the recombination $\pi/2$ pulse beam-splitter) can have an arbitrary phase offset $\phi_{\frac{\pi}{2}}$ from the initial optical standing wave i, which amounts to an x -displacement of the peaks and troughs in optical intensity⁴.

We allow these final states to separate, then switch off the waveguide to allow ballistic expansion for 8ms to avoid lensing of the imaging light by the narrow, optically dense cloud of atoms. Using absorption imaging we count the number of atoms in each spatially separated momentum state. To remove the effect of run-to-run fluctuations in total atom number, the relative atom number in the $0\hbar\mathbf{k}$ state $N_{rel} = N_{0\hbar\mathbf{k}} / (N_{0\hbar\mathbf{k}} + N_{10\hbar\mathbf{k}})$ is used. The final images are analyzed with a Fourier decomposition algorithm described in Section 4.4 to determine which parts of our final atomic density distribution are contributing to the interference. By scanning the

⁴Of course all of the pulses can have arbitrary phase offsets, but this is an unnecessary complication. This generalisation is dealt with in Section 3.2.3.

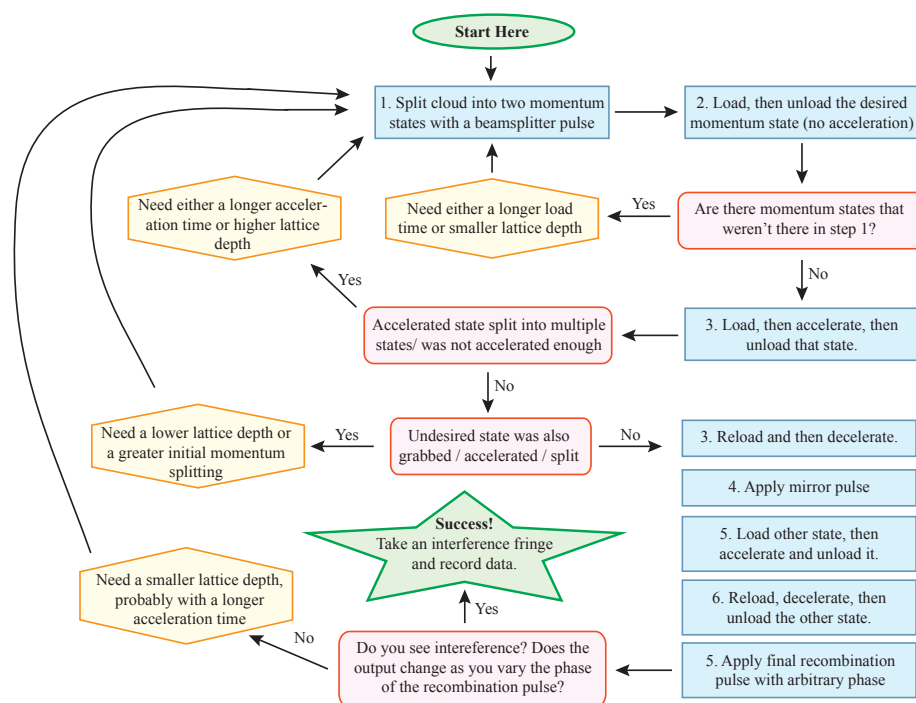


Figure 6.5: Flowchart illustrating the calibration process for Bloch lattice intensity and acceleration rate in the Bloch lattice, so as to maintain coherence throughout the interferometer sequences.

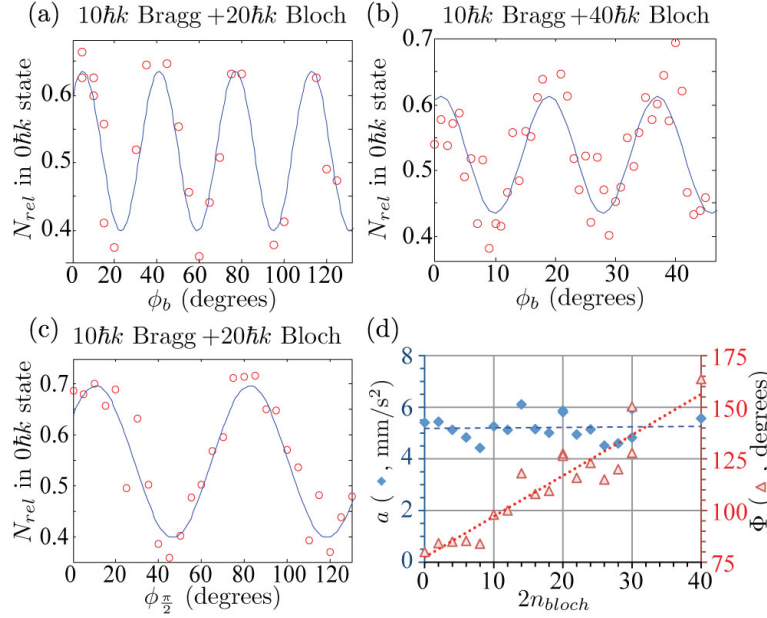


Figure 6.6: Interferometric fringes are displayed for a \$30\hbar k\$ interferometer with \$n_b = 10, n = 5\$ while scanning (a) \$\phi_b\$ or (c) \$\phi_{\pi/2}\$, and (b) a \$50\hbar k\$ interferometer with \$n_b = 20, n = 5\$ while scanning \$\phi_b\$. Red circles are data points and the blue line is a sinusoidal fit to the data. (d) The phase shift \$\Phi_0\$ of fringes taken using the CAB interferometer sequence (red triangles) increases linearly with \$n_b\$. We use Equation (6.5) to calculate the acceleration (blue diamonds) from each fringe set (with the addition of a systematic offset due to imperfect beam alignment for this data set). The blue dashed horizontal line indicates the average of the measurements of acceleration, and the red dotted line is a line of best fit to the phase shift data.

laser phase \$\phi_{\pi/2}\$ of the final \$\frac{\pi}{2}\$ Bragg pulse, we obtain fringes in \$N_{rel}\$ which oscillate according to Eq. (5.3) which in this case is equivalent to

$$N_{rel} = \frac{\mathcal{V}}{2} \cos(\Phi_0 + n\phi_{\pi/2} + n_b\phi_b) + c \quad (6.4)$$

where \$\Phi_0\$, the phase shift which is sensitive to an external constant acceleration \$a\$, is given by Eq. (3.80) from Section 3.4.2 (after including an additional acceleration-free period \$T_f\$ in each half of the interferometer)

$$\Phi_0 = 2 \left(n + n_b \cdot \frac{T_b + T_f}{T} \right) \cdot kaT^2. \quad (6.5)$$

As can be seen from Eq. (6.4), an interferometer fringe can be scanned out by changing the relative phase of any of the pulses in the sequence. Shown in Figure 6.6 (a)-(c), are the fringes obtained by scanning either the phase of the final recombination Bragg

pulse $\phi_{\frac{\pi}{2}}$ or the phase of the last Bloch acceleration lattice ϕ_b in a CAB sequence. The choice of which phase to vary is arbitrary and does not affect the measurement of the signal Φ_0 . The linear dependence of Φ_0 on the number of Bloch oscillations n_b with all other variables in Eq. (6.5) held constant is verified in Figure 6.6 (d) (red triangles), all the way from a $10\hbar k$ through to a $50\hbar k$ CAB interferometer. As all the data in Figure 6.6 (d) was taken sequentially on the same day with no adjustment to the waveguide tilt, the calculated acceleration from each interferometric fringe should be the same, and it can be seen (blue diamonds) that this is indeed the case.

The Bloch lattice acceleration rate $|\Delta \mathbf{a}_b|$ implicitly appears in T_b in Eq. (6.5), because $|\Delta \mathbf{a}_b| = 2n_b\hbar k / m_{Rb}T_b$. As per the discussion in Section 2.7.7.2, for small lattice depths $U_0 \lesssim 10E_r$ the maximum adiabatic acceleration rate $|\Delta \mathbf{a}_b|$ increases quadratically with lattice depth (see also Ref. [184]), and therefore also increases quadratically with available laser power. For larger lattice depths, $U_0 \gtrsim 10E_r$, the maximum adiabatic acceleration rate $|\Delta \mathbf{a}_b|$ increases linearly with lattice depth and therefore also increases linearly with available laser power. This means that a Bloch-based configuration such as the CAB sequence can achieve a larger sensitivity for a given laser power than an equivalent sequential-Bragg configuration [49], in which the momentum transferrable in each Bragg diffraction pulse increases as the square root of the available laser power [233]. In practice the lattice depth is limited because it must not bind the other “non-resonant” arm of the interferometer [50], which means that the other arm must be in the top-left part of Fig. 2.10. By using additional sequential $10\hbar k$ Bragg π pulses, it is possible to increase each Bragg splitting to an effective $\Delta p = 20\hbar k$ split for our CAB2 sequence, as opposed to a $\Delta p = 10\hbar k$ Bragg split in our CAB sequence. In this way it is possible to avoid unintentionally binding the other arm of the interferometer while the lattice depth is increased, so as to achieve a higher Bloch lattice acceleration rate and a higher total momentum separation.

In Fig. 6.8, we show the fringe visibility we have observed for various interferometer configurations: a standard $\Delta \mathbf{p} = 10\hbar k$ MZ with 98% visibility, our CAB sequence with the total momentum separation up to $\Delta \mathbf{p} = 70\hbar k$, and our CAB2 sequence with $\Delta \mathbf{p}$ up to $80\hbar k$. We see that the CAB sequence, with its initial $10\hbar k$ Bragg splitting before the Bloch lattice is applied, decays to zero fringe visibility at a lower $\Delta \mathbf{p}$ than our CAB2 sequence, which has an initial $20\hbar k$ sequential Bragg splitting. This result is in agreement with our earlier discussion about $|\Delta \mathbf{a}_b|$ and lattice depth.

The maximum momentum separation we have achieved (while still being directly sensitive to phase) is $\Delta \mathbf{p} = 80\hbar k$, with a visibility of 7% at $2T = 2.6$ ms as seen in Fig. 6.7 (h). The acceleration measured from this data is $a = 3.1(1) \times 10^{-3} \text{ m/s}^2$ from 146 runs of the experiment, which corresponds to that part of the waveguide being tilted 0.31(1) mrad away from horizontal. Our best acceleration sensitivity of $7 \times 10^{-3} \text{ m/s}^2 \text{ Hz}^{-1/2}$ is achieved at $\Delta \mathbf{p} = 70\hbar k$, also shown in Fig. 6.7 (g).

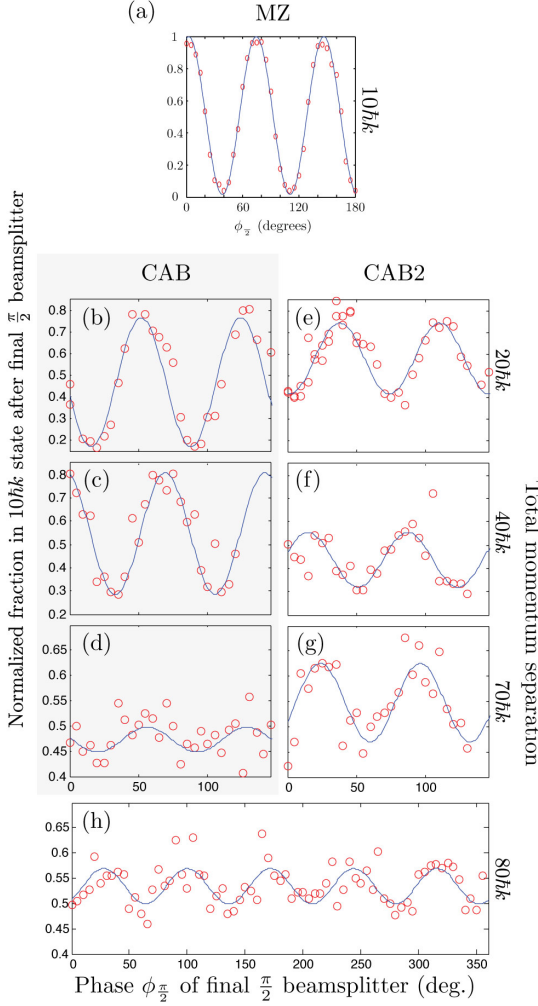


Figure 6.7: Interferometric fringes recorded by scanning the laser phase $\phi_{\frac{\pi}{2}}$ of the final recombination $10\hbar k \frac{\pi}{2}$ pulse. Each realisation of the experiment is shown as a red circle, and a sinusoidal fit of the form $N_{rel} = \frac{V}{2} \cos(n\phi_{\frac{\pi}{2}} + \Phi) + c$ is shown as a blue line. (a) $10\hbar k$ MZ with $T = 0.2$ ms, shows a visibility V of 98%. This is the starting configuration for the other pulse sequences. (b)-(d) CAB with $2T = 2$ ms and the highest momentum separation being $20, 40$ and $70\hbar k$, with visibilities V of 60%, 52% and 5% respectively. (e)-(h) CAB2 with $2T = 2.6$ ms and momentum separation of $20, 40, 70$ and $80\hbar k$, with visibilities V of 33%, 23%, 16% and 7% respectively. CAB performs better at low momentum separation, while CAB2 performs better at high momentum separation, as can be seen in Fig. 6.8. In (h) we have used averaging of three runs of the experiment at each $\phi_{\frac{\pi}{2}}$ to combat phase noise.

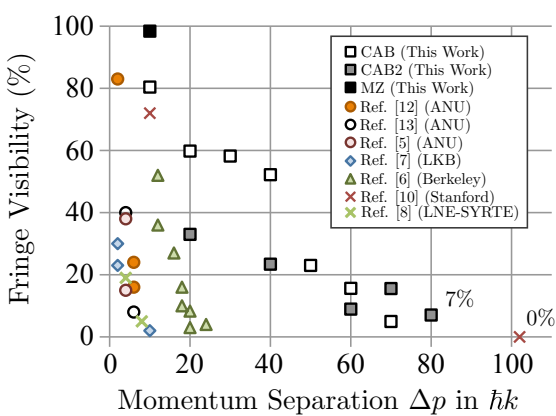


Figure 6.8: Fringe visibility for various LMT accelerometer experiments [164, 174, 50, 153, 173, 49, 144, 63, 7] as measured by the peak-to-peak amplitude of a sinusoidal fit to each fringe set. A standard $10\hbar k$ Mach-Zehnder and both the CAB and CAB2 pulse sequences used in this work (see text) are displayed for comparison. It should be noted that the fringe visibility of the interferometer with $\Delta p = 102\hbar k$ in Ref. [49] is zero, as phase noise prevented any phase measurement from being performed.

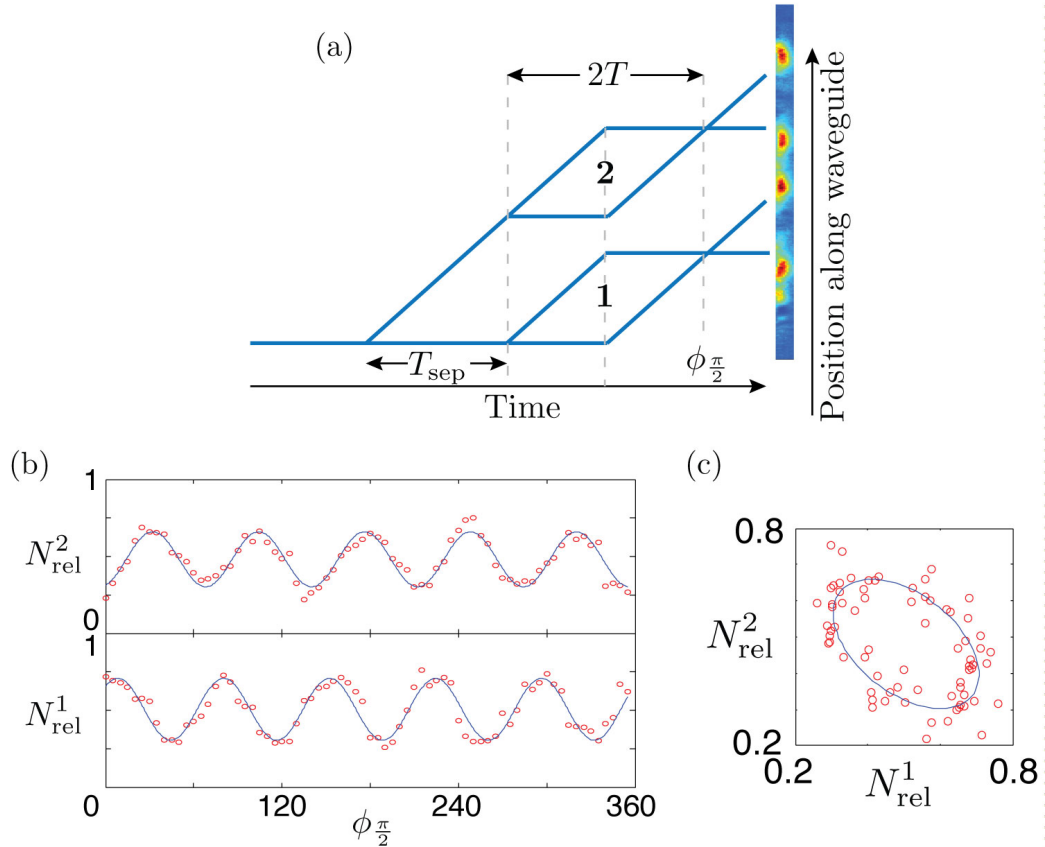


Figure 6.9: (a) The atomic trajectories (not to scale) which make up the gradiometer. Four distinct states are seen which are derived from two spatially separate interferometers. (b) The relative atom number N_{rel}^i in the $0\hbar\mathbf{k}$ state from the i th interferometer is plotted while scanning the common phase $\phi \frac{\pi}{2}$ of the last $\frac{\pi}{2}$ pulse. A fit to each sinusoid gives the acceleration-sensitive phase of each interferometer. (c) When the two fringes are plotted parametrically against one another, an ellipse is generated from which the phase difference of the two interferometers can also be determined.

6.6 Gradiometer to measure waveguide curvature

Because the optical waveguide is formed at the shallow focus of a gaussian laser beam, it will have some curvature over the scale of the Rayleigh length (see Section 2.7.3). To measure the trapping frequency in the longitudinal direction (which is ideally zero), we construct a $\Delta\mathbf{p} = 10\hbar\mathbf{k} = m_{Rb}\mathbf{v}_{\text{rec}}$ gradiometer from two interferometers with a spatial extent $T\mathbf{v}_{\text{rec}} = 0.1\text{mm}$ which are separated by a distance $x_2 - x_1 = T_{\text{sep}}\mathbf{v}_{\text{rec}} = 1\text{mm}$, as shown in Fig. 6.9. Since the difference between the measured accelerations in each interferometer can be related to the trapping frequency ω of the waveguide curvature by $a_2 - a_1 = \omega^2(x_2 - x_1)$, using Eq. (3.69) we can relate the phase difference $\Phi_2 - \Phi_1$ between the two interferometers to the trapping

frequency by

$$\omega = \frac{1}{2nkT} \sqrt{\frac{m_{Rb}(\Phi_2 - \Phi_1)}{\hbar T_{sep}}}. \quad (6.6)$$

We calculate the longitudinal waveguide frequency by this method to be $\omega = 2\pi \cdot 0.22(2) \text{ rad/s}$, using the data shown in Figure 6.9. This compares well with a calculated estimate based upon the waveguide beam characteristics of $\omega = 2\pi \cdot 0.18 \text{ rad/s}$.

6.7 A faster sensitivity scaling

One application of this system to high-sensitivity inertial sensing is in creating an accelerometer in which the acceleration sensitive phase scales as T^3 , as opposed to a typical MZ which scales with T^2 , or a Ramsey-Bordé configuration in which sensitivity scales with T . The acceleration dependence of this phase offset is given by the space-time area $\mathcal{A}_{CAB} = \int \Delta\mathbf{x} dt$ of our interferometer,

$$\begin{aligned} \Phi_{CAB} &= \frac{m}{\hbar} \mathbf{a} \cdot \mathcal{A}_{CAB} \\ &= 2 \left(n + n_b \cdot \frac{T_b + T_f}{T} \right) \mathbf{k} \cdot \mathbf{a} T^2 \end{aligned} \quad (6.7)$$

which reduces to the phase offset of an MZ configuration $\Phi_{MZ} = 2n\mathbf{k} \cdot \mathbf{a} T^2$ when $n_b = 0$.

In order to obtain the T^3 scaling, we must look at what happens when the interferometer time T is increased, keeping constant the relative acceleration $\Delta\mathbf{a}_b$ which we apply via the Bloch lattice. In this case $n_b = T_b/\tau$, where the constant $\tau = \frac{2\hbar k}{m|\Delta\mathbf{a}_b|}$ is the period for one Bloch oscillation. Assuming T_r and T_f are much smaller than T_b , then we have $T_b \rightarrow \frac{T}{2}$, and Eq. (6.7) becomes

$$\begin{aligned} \Phi_{CAB} &= 2n\mathbf{k} \cdot \mathbf{a} T^2 + \frac{\mathbf{k} \cdot \mathbf{a} T^3}{2\tau} \\ &= \Phi_{MZ} + \frac{\mathbf{k} \cdot \mathbf{a} T^3}{2\tau} \end{aligned} \quad (6.8)$$

which explicitly shows the extra T^3 scaling in acceleration sensitivity achievable with this configuration.

We experimentally test Eq. (6.7) by first measuring Φ_{MZ} for a standard MZ configuration with $n = 5$, $n_b = 0$ (blue triangles on Fig. 6.10) in order to extract the external acceleration a due to a tilt in the waveguide. From this we calculate via Eq. (6.7) what Φ_{CAB} will be for the CAB sequence (red dashed line). We then measure Φ_{CAB} for $T = 0.642$ ms, $n_b = 1$ through to $T = 1.042$ ms, $n_b = 21$ (red circles) and our experimental parameters were set such that $T = 2n_b\tau + 0.622$ ms with a Bloch oscillation period of $\tau = 10 \mu\text{s}$. The excellent agreement shown in Fig. 6.10 between the predicted phase for the CAB sequence which was deduced from the MZ measurements, and the measurements of Φ_{CAB} validate Equation (6.7) and demonstrate a T^3 scaling in phase sensitivity to acceleration.

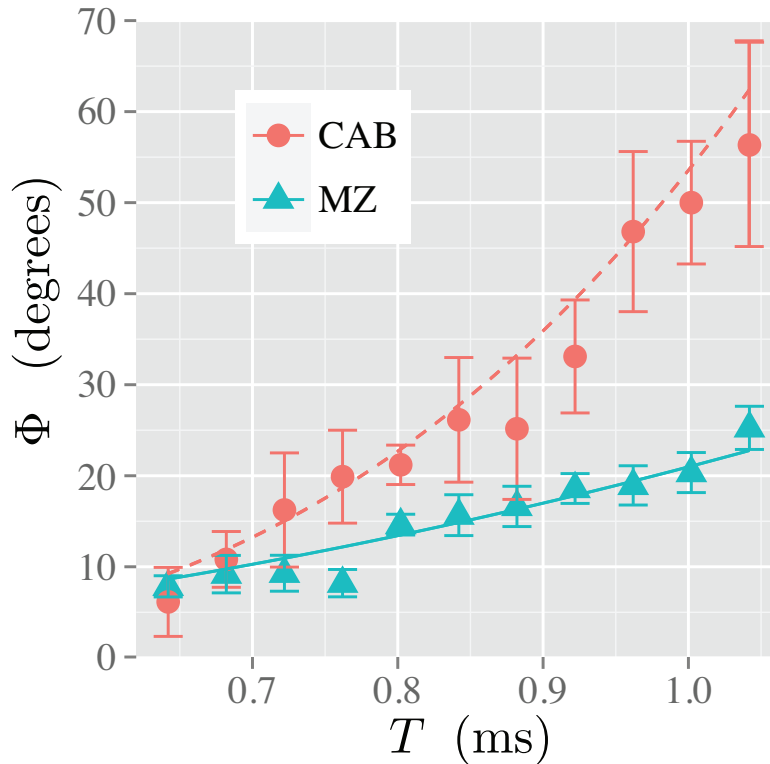


Figure 6.10: Here we experimentally demonstrate the faster sensitivity scaling. The interferometric phase offset Φ is measured for each fringe as the interferometer time T is increased. The blue solid line is a fit to the MZ phase Φ_{MZ} (blue triangles) of the form $\Phi_{MZ} = 2nk \cdot aT^2$ to extract the acceleration a along the waveguide (due to a slight tilt) for the day the data was taken. This acceleration is then used to predict Φ_{CAB} for the CAB sequence by equation (6.7) (red dashed line). Experimental measurement of Φ_{CAB} for the CAB sequence (red circles) increases faster than T^2 , as predicted by Eq. (6.7). Uncertainties in Φ extracted from each fringe are one standard deviation confidence intervals.

6.8 Extension to T^n scaling

We now turn to yet higher scalings with respect to T . The maximum adiabatic acceleration rate $\Delta\mathbf{a}_b$ using a Bloch lattice increases quadratically with lattice depth until $U_0 \approx 10E_r$ and then linearly thereafter (see Sec. 2.7.7.2). However, in the CAB scheme both lattice depth and acceleration rate are limited by the instantaneous velocity separation of the two clouds. This is because if the lattice is too deep it will also bind the other momentum state, and thus our acceleration will no longer be state selective. Therefore, the best possible use of available laser power would require the application of a constantly increasing relative acceleration $\Delta\frac{d\mathbf{a}_b}{dt}$ (known as constant jerk) between the two states, while commensurately increasing the optical lattice depth. This would give a space-time area of $\mathcal{A}_{T^4} = \frac{1}{24}\Delta\frac{d\mathbf{a}_b}{dt}T^4$, producing an interferometer with phase $\Phi = \Phi_{MZ} + \frac{m}{\hbar}\mathbf{a} \cdot \mathcal{A}_{T^4}$. At the point at which lattice depth is limited by available laser power, the maximum acceleration rate will become constant again, and so the scaling will revert to T^3 . Generalising to arbitrary scalings in T would be possible if an interferometer were developed with a constant n -th derivative of displacement (for $n \geq 1$). It would have a space time area of

$$\mathcal{A}_{T^{n+1}} = \frac{1}{n!2^{n-1}} \left[\left(\frac{d}{dt} \right)^n \Delta\mathbf{x} \right] T^{n+1} \quad (6.9)$$

and therefore a T^{n+1} scaling in acceleration sensitivity. Although there is no practical advantage in the present system beyond constant jerk, it is possible that an analogous scheme will be developed in the future which is not limited by laser power, and could practically take advantage of these higher scalings. For instance, one can envisage positionally dependent trapping potentials (e.g. dipole traps [199]) accelerating each cloud in opposite directions once they are separated in space.

6.9 Future Directions

In an attempt to explore the boundaries of these kinds of LMT interferometer, we have constructed a $\Delta\mathbf{p} = 510\hbar\mathbf{k}$ beamsplitter according to the CAB sequence, limited only by the size of the absorption image, and this is displayed in Fig. 6.11. In fact, Bloch lattices have been used to accelerate cold clouds by up to several thousand photon recoils [45, 32, 39, 14, 82] but these configurations have no momentum separation between interferometric states, $\Delta\mathbf{p} = 0$.

In the future, optical-lattice intensity-noise reduction in this system is possible by using multiple overlaid Bloch lattices to address both momentum states separately,



Figure 6.11: An absorption image of a BEC which has been split by $\Delta p = 510\hbar k$ by the CAB beamsplitter. This was limited only by the size of the absorption image, as the clouds are separated by ≈ 8 mm at the time of the image.

and accelerate them in opposite directions at the same time [173]. This will cancel the a.c. Stark shift due to Bloch laser intensity noise, as each arm simultaneously experiences the Bloch lattice. In the present CAB sequence the a.c. Stark shift is only cancelled at a later time in the interferometer, so with this improvement the interferometer will become less sensitive to such fluctuations. However, as each arm of the interferometer only experiences half the laser intensity, this technique will lower the maximum acceleration rate of each state. This results in a lowering of the signal Φ . Other noise reductions in order to enhance signal-to-noise can be achieved by reducing mechanical vibrations [165], evacuating the optical path and locking-out optical-lattice-laser frequency fluctuations [25].

There are numerous avenues for future research in this system. By imaging a cold atom interferometer at the quantum-projection-noise limit [72, 222] we can investigate large-atom-number squeezing directly via spatial overlap of the two states [129, 110, 77]. An important follow-on experiment will be to repeat the experiments described in this chapter, using an interactionless condensate. The ability to hold all magnetic sub-states in the same waveguide spatial mode with an arbitrary, constant magnetic field allows us to completely remove the self-interaction in such a system by setting the scattering length to zero [9, 6]. This is described in detail in the next chapter. This could allow Heisenberg-limited delta-kick cooling of our atomic source, reaching even narrower momentum widths for interferometry. An interactionless cloud may also reduce decoherence in the Bloch lattice, allowing larger momentum separation or longer coherence times. The system offers the possibility of superimposing multidimensional lattices onto the propagating atoms to investigate universality in a 1D Bose gas [148, 149], or create the atom-optic equivalent of photonic crystals [78].

6.10 Discussion

In summary we have shown a MZ interferometer based upon a CAB2 sequence with a momentum separation of up to $80\hbar k$. We have achieved an acceleration sensitivity of $7 \times 10^{-3} m/s^2/\sqrt{Hz}$ and a tilt sensitivity of $18 \text{ mrad}/\sqrt{Hz}$. We speculate that it is our use of an optical waveguide which allows us to achieve high Bloch accelera-

tions without a drastic loss of coherence. There are three mechanisms we propose for this. First, since the atoms are transversely confined, they sample only a small segment of the comparatively much larger optical lattice beams so any spatial wavefront distortion due to an imperfect lattice beam mode is common to the whole interferometer. Secondly, the transverse confinement during Bloch acceleration allows for better mode matching at the final recombination pulse as compared with the use of a Bloch lattice in free space. Lastly, our use of an optical waveguide to support against gravity allows us to reduce the longitudinal velocity width via our optical delta-kick cooling.

A single beamsplitter of $\Delta\mathbf{p} = 510\hbar\mathbf{k}$ was constructed to demonstrate the scalability of this method. We also constructed a gradiometer which was used to measure the curvature of our optical waveguide with a sensitivity $\sigma_\omega = 0.1 \text{ rad/s}$. As an indication of the possible sensitivity this device is capable of, we can look at the quantum-projection-noise-limited sensitivity of a single run of an acceleration sensor with this architecture. Taking a momentum separation of $500\hbar\mathbf{k}$, an interrogation time of $T = 50 \text{ ms}$ (limited by a vacuum system of length 10 cm), and using 2×10^6 atoms, the shot noise limited sensitivity is $1.3 \times 10^{-10} \text{ m/s}^2$. This is the same sensitivity as could be achieved with a $2\hbar\mathbf{k}$ interferometer with $T = 580 \text{ ms}$ in the same vacuum system.

We have also demonstrated a novel configuration for a cold-atom interferometer in which acceleration sensitivity scales as T^3 . This CAB configuration is realised using an optical Bloch lattice to subject one arm of the interferometer at a time to an additional constant acceleration. The additional T^3 scaling in sensitivity to the external inertial acceleration \mathbf{a} allows this CAB configuration to have increased sensitivity to accelerations measured with a given interferometer time T as compared with a Mach-Zehnder configuration. This CAB configuration will therefore be useful in increasing the phase sensitivity to accelerations at any given frequency, without requiring any increase in available laser power. This technique can therefore be immediately applied in navigation and inertial sensors which are currently under development, and in proposed schemes for gravitational wave detection.

The choice of Bragg [165] and not Raman [50] beamsplitters in this CAB configuration allows both momentum states to be in the same magnetic internal state throughout the interferometer, eliminating this particular systematic phase shift. The use of a BEC source cloud presents its own systematic phase shift, the density-dependent mean-field shift [63]. However, this shift can be reduced arbitrarily by lowering the cloud's density via the delta-kick-cooling process, or removed entirely by turning off mean-field interactions through the use of a Feshbach resonance as we will describe in Chapters 7 and 8. To separate the effects of acceleration due to gravity, the optical potential and the magnetic field gradients possibly present in the experiment, one could use a magnetically insensitive internal state as we did in Chapter 5 or compare the phase shift across different isotopes simultaneously, which is discussed in Chapter 8.

Variable Scattering Length Interferometry

Scattering length is a low-energy description of inter-atomic collisions [48]. As will be demonstrated in this chapter and the following chapter, a condensate with a variable scattering length is a versatile tool for interferometry. By setting the scattering length to zero [81, 108] it is possible to eliminate mean-field phase-shifts, a common perturbation in interferometers using condensed sources. Removing interactions also allows the condensate to disperse only at the Heisenberg limit $\Delta x \Delta p \approx \hbar$. Even more tantalisingly, the interactions can be made attractive, just enough to cancel out the Heisenberg limited dispersion, creating a cloud with *no dispersion at all*. This solitary non-dispersive propagating wave is known as a soliton.

The work discussed in this chapter is published as

A Bright solitonic matter-wave interferometer

G. D. McDonald,* C. C. N. Kuhn, K. S. Hardman, S. Bennetts, P. J. Everitt, P. A. Altin, J. E. Debs, J. D. Close, and N. P. Robins.

Phys. Rev. Lett. **113**, 013002 (2014).

A Bose-condensed, simultaneous dual species Mach-Zehnder atom interferometer

C. C. N. Kuhn, G. D. McDonald, K. S. Hardman, S. Bennetts, P. J. Everitt, P. A. Altin, J. E. Debs, J. D. Close, and N. P. Robins.

New J. Phys. **16**, 073035 (2014).

7.1 Feshbach resonance

The Feshbach resonance used to manipulate the *s*-wave scattering length of the $|F = 2, m_F = -2\rangle$ state in ^{85}Rb is controlled by an external magnetic bias field. The

resonance is well characterised by the equation

$$a = a_{bg} \left(1 - \frac{\Delta}{B - B_0} \right), \quad (7.1)$$

relating the *s*-wave scattering length, a , to the magnetic field, B , through the background scattering length, $a_{bg} = -443 a_0$, the width of the Feshbach resonance, $\Delta = 10.71$ G, and the centre of the resonance, $B_0 = 155.041$ G [198, 10]. This relation is depicted in Figure 7.1.

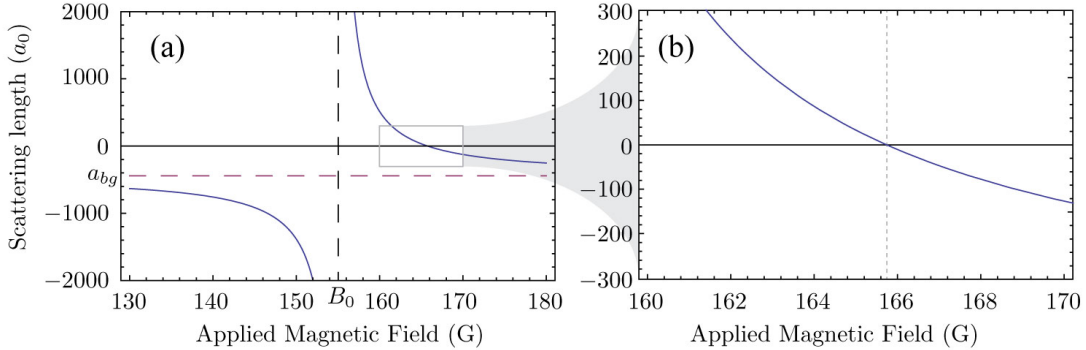


Figure 7.1: (a) Scattering length as a function of Magnetic field near the Feshbach resonance in the $|F = 2, m_F = -2\rangle$ state of ^{85}Rb , as per Equation (7.1). The dashed vertical line indicates the resonance itself at $B_0 = 155.041$ G, and the dashed horizontal line indicates the background scattering length a_{bg} near the resonance. Most of our experiments are conducted on the high-field side of the resonance, near the scattering-length zero at $B = 165.75$ G. This section is enlarged in (b), and the scattering-length zero is marked with a dotted vertical line.

To begin we must verify that we have a ^{85}Rb condensate and have control over its scattering length via the Feshbach resonance at $B = 155$ G. This was done by looking at the expansion of the BEC at different magnetic field strengths, both expanding in free space and in the waveguide. The dependence of this expansion upon scattering length is much easier to detect using a BEC source than an ultra-cold thermal cloud, due to the higher density and collision rate. This expansion data is shown in Figure 7.2 for the free-space expansion (a) and the guided expansion (b). At large positive scattering lengths, the BEC should expand rapidly as the large in-trap mean-field energy is converted to kinetic energy in the untrapped directions. At large negative scattering lengths, the BEC should implode [6, 202, 71, 203] and either lose atoms to three-body recombination due to the high density as the condensate collapses, or expand outwards again after implosion, again with the mean-field energy now converted to kinetic energy. All of these effects lead to the Optical Depth (OD, see Section 2.8.2) of the expanded condensate being a maximum near the zero of scattering length, and dropping either side of zero. The width of the expanded

condensate will be a minimum for a near-non-interacting cloud ($a \approx 0$) and get wider for $|a| > 0$. Of course the minimum in expansion will not be at exactly $a = 0$, but at a slightly attractive (negative) scattering length to cancel out the Heisenberg-limited dispersion of the BEC. The exact value will depend upon the density of the cloud and the shape of the trapping potential. This will be explored further in the next section.

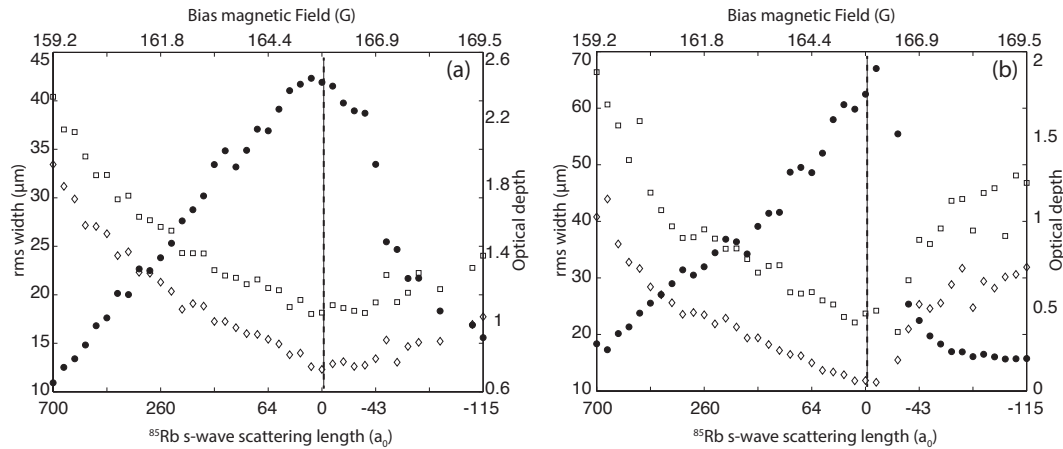


Figure 7.2: (a) Expansion of the ^{85}Rb condensate from the crossed dipole trap as a function of scattering length after the trap has turned off. Filled circles - OD, squares - σ_x radial width, diamonds - σ_y axial width. Vertical dashed line indicates zero scattering length on the horizontal axis. (b) Expansion along the waveguide as a function of Feshbach magnetic field. Filled circles - OD, squares - σ_x radial width, diamonds - σ_y axial width. Both sets of data represent a single set of runs sweeping through the magnetic field values.

Because the waveguide is extended in space, it is critically important to precisely characterise the bias field change along the waveguide. Radio-frequency (r.f.) transitions on an extended matter wave source are used to achieve this. A $1\,\mu\text{K}$ sample of ^{87}Rb atoms is released into the waveguide and allowed to expand over a second. A $10\,\text{ms}$ burst of r.f. couples the $|F = 1, m_F = -1\rangle$ and $|F = 1, m_F = 0\rangle$ internal Zeeman states over a narrow frequency range according to the relation $\hbar\omega_{\text{r.f.}} = \mu_B\Delta m_F g_F B$, where μ_B is the Bohr magneton, g_F is the Landé g -factor for ^{87}Rb and the magnetic bias field is held at $B = 165.776\,\text{G}$ at the trap center. The bias field is then turned off and the resulting magnetic species are separated by a $2\,\text{ms}$ Stern-Gerlach pulse from the quadrupole coils. The locations at which each frequency couples the two internal states maps to our magnetic field along the waveguide, and this is shown in Figure 7.3. A parabolic fit to this data yields a magnetic field curvature of $\frac{\partial^2 B}{\partial z^2} = -103(1)\,\text{mG/mm}^2$. This curvature provides the dominant longitudinal potential for our ^{85}Rb atoms which, according to the relation $\omega_z^2 = \frac{\mu_B g_F m_F}{m_{^{85}\text{Rb}}} \frac{\partial^2 B}{\partial z^2}$ (where $m_{^{85}\text{Rb}}$ is the mass of ^{85}Rb) gives an inverted harmonic potential along the waveguide with

(anti) trapping frequency $\omega_z = 2\pi i \times 3 \text{ Hz}$ where $i = \sqrt{-1}$. It is important to note that the change in magnetic field due to this curvature along the waveguide corresponds to a few percent of a Bohr radius a_0 across the condensate, so the scattering length of the cloud is spatially constant to a good approximation.

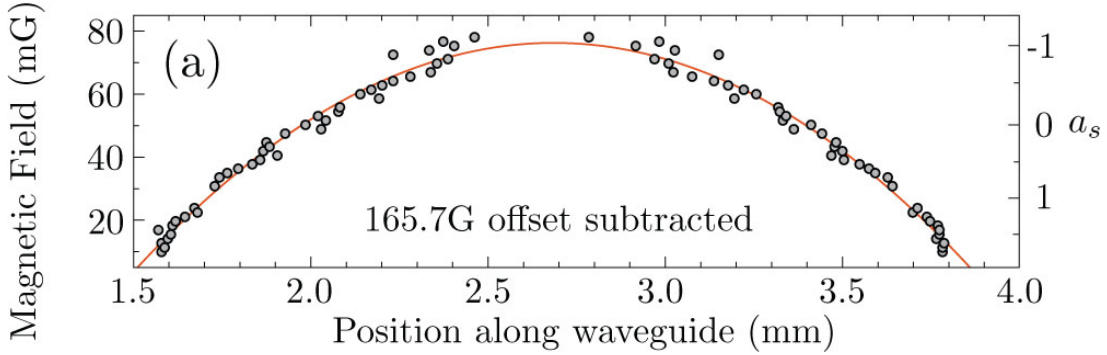


Figure 7.3: (Color online) Measurement of the magnetic field curvature in the waveguide via r.f. spectroscopy. The magnetic field at each position is determined from the frequency required to drive inter- m_F transitions on an extended cloud of atoms in the guide. The red line is a parabolic fit to the data, indicating a repulsive harmonic potential with frequency $\omega_z = 2\pi i \times 3 \text{ Hz}$ along the waveguide.

7.2 Soliton Formation

Solitons can arise in any system which is described by a weakly nonlinear dispersive partial differential equation, and in our case this equation is the Gross-Pitaevski equation, which describes the mean-field evolution of a BEC:

$$i\hbar \frac{d}{dt} \Psi = \frac{\hbar^2}{2m} \nabla^2 \Psi + V\Psi + U|\Psi|^2\Psi \quad (7.2)$$

where $V(x)$ is the trapping potential at a given point in space, and $U = \frac{4\pi\hbar^2 a}{m}$ is the interaction parameter for two-body, s-wave collisions.

Soliton formation, stability and dynamics forms an enormous field of rich and diverse study which is well reviewed in Ref. [141]. Solitons appear in non-linear optical systems [133], in which the analog equation to Eq. (7.2) is that of the electric field propagating in, for example, an optical fibre with non-linear permittivity [83],

$$-i\hbar \frac{d}{dz} \hat{a} = \frac{1}{2} \frac{d^2}{dt^2} \hat{a} + N^2 |\hat{a}|^2 \hat{a} \quad (7.3)$$

where \hat{a} is the annihilation operator for a photon in the fibre at position z , analogous

to the annihilation operator of an atom $\hat{\Psi}$ which has been averaged to the mean-field $\langle \hat{\Psi} \rangle = \Psi$ in Eq. (7.2) above. Solitons also feature in oceanography [126], magnetic materials [143, 236], financial markets [156], and biological systems [117] among others. Depending upon whether the solitary propagating wave is a crest or a trough, it is known as a bright or a dark soliton respectively. So a light pulse propagating dispersionlessly through either vacuum or a non-linear optical material, or a condensate propagating dispersionlessly through time would both be called bright solitons, as would a water-wave propagating dispersionlessly along a channel. An example of a dark soliton might be a dip in the density profile of an elongated condensate which propagates along the condensate [88], a dip in the density of water propagating along a channel [44], or a dark shadow propagating dispersionlessly in an otherwise-bright non-linear optical fibre [76, 140].

Let us examine Eq. (7.2) in more detail. Say, for simplicity, that the condensate is in free space so that there is no trapping potential, $V = 0$; and there are no interactions so $U = 0$ also. Then the dispersion is simply that of a wave function in free space

$$i\hbar \frac{d}{dt} \Psi = \frac{\hbar^2}{2m} \nabla^2 \Psi. \quad (7.4)$$

If we instead set the interaction constant U to some negative value, and set the shape of the condensate density $|\Psi|^2$ such that the interaction term and the kinetic dispersion term cancel out each other's positional dependence, and look for stationary solutions $\Psi(\mathbf{r}, t) = \psi(\mathbf{r}) e^{\frac{i\mu t}{\hbar}}$ we find

$$\mu\psi = \frac{\hbar^2}{2m} \nabla^2 \psi + U|\psi|^2\psi \quad (7.5)$$

and we thus have our solitary propagating wave - a soliton. Equation (7.5) has the following exact soliton solution in 1D:

$$\psi(z) = \frac{1}{\sqrt{l_z}} \operatorname{sech} \left(\frac{z}{l_z} \right). \quad (7.6)$$

In 3D however, solitons are inherently unstable. Nevertheless, following Ref. [42], and motivated by the 1D solution above we can look for elongated solitonic solutions to the 3D GP equation with a transverse harmonic confining potential. We assume a stationary trial wave function of the form

$$\psi(\rho, z) = \frac{1}{\sqrt{2\pi l_\rho^2 l_z}} \exp \left(-\frac{\rho^2}{2l_\rho^2} \right) \operatorname{sech} \left(\frac{z}{l_z} \right) \quad (7.7)$$

which allows a gaussian radial profile, with a longitudinal shape given by the solu-

tion in one dimension shown in Eq. (7.6).

Substituting this into the Gross-Pitaevski energy functional

$$E_{GP} = \int d^3r \left\{ \frac{\hbar^2}{2m} |\nabla\psi|^2 + \frac{gN}{2} |\psi|^4 + \frac{m}{2} [\omega_\rho^2(x^2 + y^2) + \omega_z^2 z^2] |\psi|^2 \right\} \quad (7.8)$$

allows us to obtain the following energy surface with respect to both the axial and radial size of the condensate,

$$\epsilon = \frac{1}{2\gamma_\rho^2} + \frac{\gamma_\rho^2}{2} + \frac{1}{6\gamma_z^2} + \frac{\pi^2}{24} \lambda^2 \gamma_z^2 + \frac{\alpha}{3\gamma_\rho^2 \gamma_z} \quad (7.9)$$

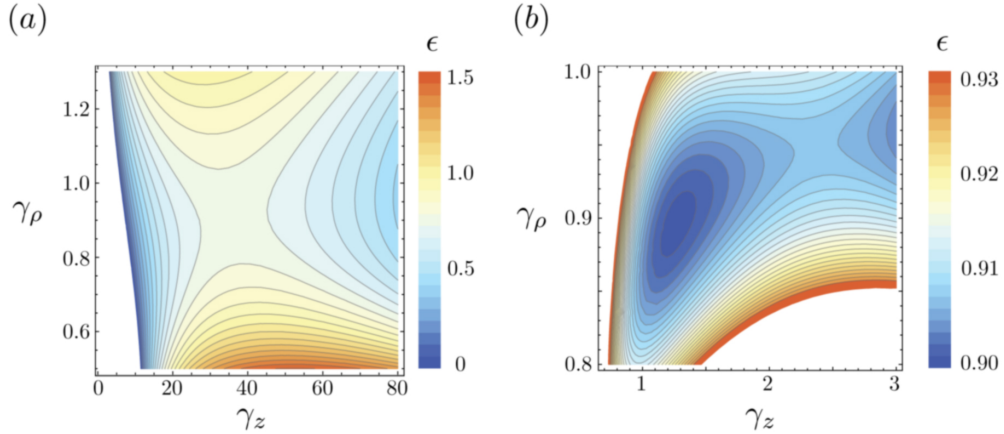


Figure 7.4: The energy surface defined by Equation (7.9) in dimensionless units. (a) Parameters similar to our experiment with $\omega_\rho = 2\pi \times 70 \text{ Hz}$, $\omega_z = 2\pi i \times 1 \text{ Hz}$, $N = 1.5 \times 10^4$ atoms, $a = -30a_0$, showing a saddle point at $\gamma_\rho = l_\rho \sqrt{\frac{m\omega_\rho}{\hbar}} \approx 0.9$ and $\gamma_z = l_z \sqrt{\frac{m\omega_\rho}{\hbar}} \approx 40$, corresponding to $l_z \approx 50 \mu\text{m}$, the longitudinal width of our soliton. (b) Parameters near those of the ${}^7\text{Li}$ soliton experiment of Ref. [138], as shown in Fig 3. of Ref. [42].

where all the variables have been rescaled to the radial harmonic oscillator frequency ω_ρ or harmonic oscillator length $\sigma_\rho = \sqrt{\frac{\hbar}{m\omega_\rho}}$, i.e. energy $\epsilon = \frac{E}{\hbar\omega_\rho}$, radial width $\gamma_\rho = \frac{l_\rho}{\sigma_\rho}$, axial width $\gamma_z = \frac{l_z}{\sigma_\rho}$, trap aspect ratio $\lambda = \frac{\omega_z}{\omega_\rho} = \frac{i|\omega_z|}{\omega_\rho}$ and interaction parameter $\alpha = \frac{Na}{\sigma_\rho}$.

Soliton solutions are found at stationary points ($\nabla\epsilon = 0$) on this energy surface. Ref. [42] focussed upon the stable stationary point found at a minima of the energy surface, which only exists for a very limited parameter range (see Fig. 1 of that

paper). Our experiment has a much larger interaction parameter $|\alpha| \approx 12$ than anything in this region of stability (which is bounded by $|\alpha| \lesssim 0.8$). In fact, by looking at the energy surface of Eq. (7.9) for parameters similar to those used in this experiment, we see that we are at a different stationary point, a saddle point, shown in the centre of Fig. 7.4 below (c.f. Fig. 2 of Ref. [42]).

Experimental studies have previously been done on both bright and dark solitons. In cold atom experiments, dark solitons are a dip in the density profile of a Bose-Einstein condensate [66, 36, 88]. Systems of dark-bright soliton pairs have also been shown in experiments [20, 247]. On the contrary, studies of bright matter wave solitons have been relatively few, despite offering similarly nuanced and interesting physics to dark solitons. Early work observed the break-up of attractive ^7Li and ^{85}Rb condensates into soliton trains [229, 230, 57]. A single 6000-atom ^7Li bright soliton in an optical waveguide was created in 2002 [138] and recently, a pair of neighbouring 100-atom ^7Li bright solitons were formed in a magnetic waveguide [166]. A 2000-atom ^{85}Rb soliton has been studied while colliding with a repulsive barrier [159]. Among many possible applications, a bright-soliton-based matter-wave interferometer has been proposed as a method to test the fine details of atom surface interactions [68], and soliton collisions have been suggested as a mechanism for creating Bell-type entangled states [95]. As a tantalising precursor to detecting these entangled states, phase-dependent collisions at low velocity between two 28,000-atom ^7Li solitons has been studied using minimally destructive imaging, showing the effect of phase on the collision dynamics [178]. Additionally, bright-solitonic atom interferometers hold great promise for precision measurements [191, 177], including measurements of gravity [7, 187], rotations and magnetic field gradients [240, 59], and tests of the weak equivalence principle [235, 223, 211, 3].

How do we experimentally find the soliton point $a = a_s$ in our BEC of 10,000 atoms of ^{85}Rb ? The condensate is adiabatically loaded into the waveguide at $a = 5a_0$, before the scattering length is instantaneously changed to a given value a . We take pictures after varying lengths of time, as the BEC expands in the waveguide. In Fig. 7.5 (a), the width of the cloud after 90 ms of expansion time is plotted, showing that for our parameters, the minimum expansion is achieved at $a_s = -30a_0$. Fig. 7.5 (b) shows that at this scattering length, the condensate maintains a constant width for up to 50 ms of expansion. Thus $a_s = -30a_0$ is the soliton point for the parameters of this system. This optimal value will of course depend upon density and the dimensions of the cloud, and the geometry of the (anti-)trapping potential.

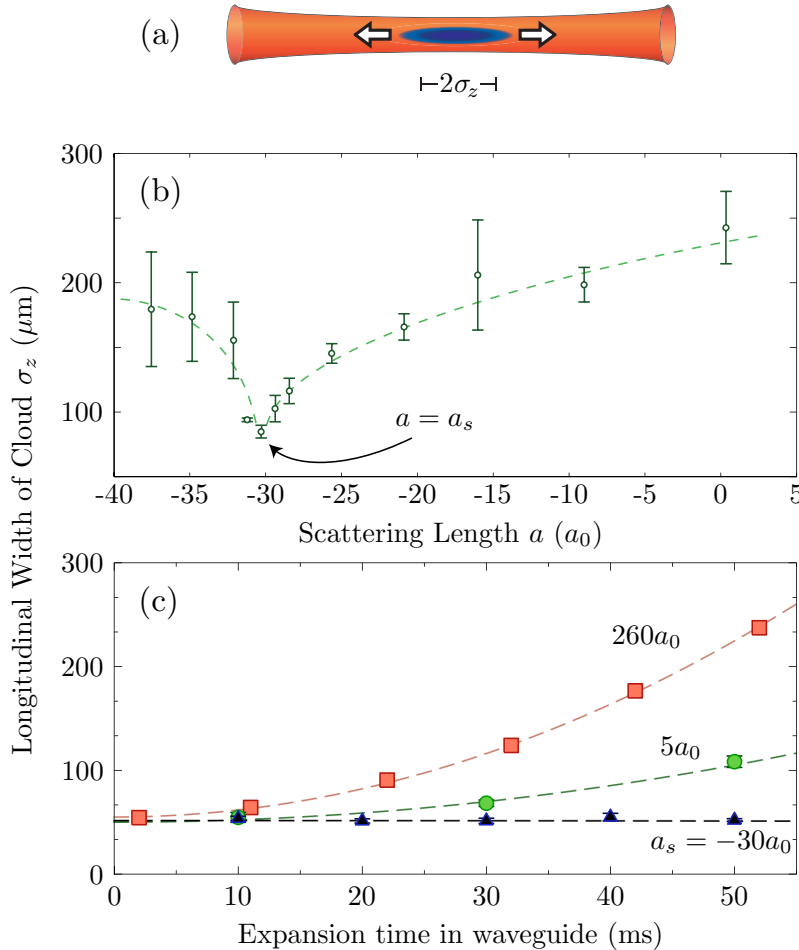


Figure 7.5: (a) Diagram illustrating the condensate's expansion along the waveguide. The width σ_z is the standard deviation of a gaussian fit to the ballistic expansion image. (b) Longitudinal width of a matter wave as a function of scattering length, measured after 90 ms of free expansion in the guide. Green dashed lines are to guide the eye. The soliton parameter of $a_s = -30a_0$ is seen to minimise this expansion. (c) Comparison of longitudinal expansion along the guide for three different scattering lengths: the repulsive self-interaction of $a = 260a_0$, the low interaction case of $a = 5a_0$ and the soliton parameter of $a_s = -30a_0$. The dashed lines are parabolic fits to extract the acceleration of cloud width. For $a = a_s$ this acceleration is consistent with zero.

Error bars shown in both (a) and (b) are statistical.

7.3 Soliton Interferometry

To investigate the properties of the soliton, we now construct a Mach-Zehnder interferometer along the waveguide using two-photon ($2\hbar k$) Bragg transitions. The scattering length was abruptly changed from $a = 0, 0.4\text{ ms}$ before the first $\pi/2$ pulse and back to $a = 0, 0.4\text{ ms}$ after the last $\pi/2$ pulse. Of course for long interferometer times, the two arms of the interferometer will separate, so that the density will be halved in each cloud. This means that neither cloud will have sufficient attractive interaction to remain solitonic, and in a future scheme this should be corrected for by making the scattering length more negative as the clouds separate to compensate. However, in our experiment the two clouds do not have enough time to fully separate. The separation of the peaks of the two clouds is given by

$$d = vT \quad (7.10)$$

$$= \frac{2\hbar k}{m_{^{85}\text{Rb}}} T \quad (7.11)$$

$$= 12\text{ }\mu\text{m/ms} \times T \quad (7.12)$$

At the longest interferometer time reported here, $T = 3.5\text{ms}$, the clouds separate by $42\text{ }\mu\text{m}$, about the width of each cloud (as shown in Fig. 7.5 (c)). For the shorter interferometer times the clouds are mostly overlapped throughout the interferometer sequence, maintaining the density required to keep the soliton point consistent. No significant systematic loss of atoms is measured over the range of s -wave scattering length observed. In Figure 7.6 is shown an example interference fringe in N_{rel} at $a_s = -30a_0$ scattering length, together with the raw absorption images below. Each fringe is fit with a function

$$N_{\text{rel}} = \frac{\mathcal{V}}{2} \cos \left(\Phi + \phi_{\frac{\pi}{2}} \right) + c \quad (7.13)$$

where \mathcal{V} is the fringe visibility, Φ is the interferometric phase, $\phi_{\frac{\pi}{2}}$ is the applied phase of the final beamsplitter, and c is the fringe offset.

Figure 7.7 (a) shows the fringe visibility \mathcal{V} of a $T = 1\text{ ms}$ and a $T = 2.7\text{ ms}$ Mach-Zehnder interferometer as a function of the s -wave scattering length a during the interferometer sequence. The sharp peak in the interferometer visibility \mathcal{V} occurs exactly at $a_s = -30a_0$, the ‘soliton parameter’ identified from the expansion data in Figure 7.5, which therefore shows a solitonic matter wave very clearly outperforming a non-interacting cloud. We attribute the increase in fringe visibility seen around $a = a_s$ to the lack of spatial dispersion as seen in Fig. 7.5 (b). Reduced longitudinal

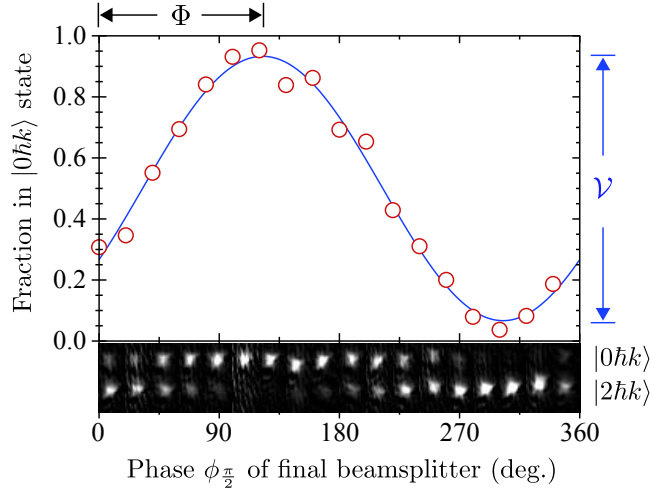


Figure 7.6: An example fringe taken at the soliton point $a = a_s$ for an interferometer time of $T = 1$ ms. As the phase $\phi_{\pi/2}$ of the last beamsplitter is varied, the relative number of atoms in the $|0\hbar k\rangle$ state traces out a fringe. Also indicated are the important parameters extracted from the fit, the fringe visibility V and the interferometric phase Φ . At the bottom the raw absorption images after each run are shown.

momentum width has been shown to increase visibility in atom interferometers in general due to the frequency dependence of the Bragg transition [233] and in our system in particular, reduced spatial dispersion has also been shown to increase mode-matching and therefore fringe visibility in the context of delta-kick cooling (Fig. 6.3(e) in Section 6.4 of this thesis). Here, a more striking visibility peak due to the jump in scattering length from zero to the s-wave soliton parameter is also due to effectively freezing out the matter wave dispersion during the interferometer, increasing mode-matching in both position and momentum by conserving the phase-space density of each atom cloud. We hypothesise that this causes the interference to be more robust against visibility degradation due to any spatial inhomogeneity of the confining potential. Fringe visibility enhancement is also predicted for a solitonic interferometer due to collisional many-body entanglement [94], which has already been demonstrated for the case of an optical soliton interferometer [83]. However we do not expect to see this here as our Bragg beamsplitters should not cause any entanglement.

The interferometric phase Φ for $T = 1$ ms as measured in Fig. 7.7 (b) is interesting as it seems to show a constant phase shift for scattering lengths below $a = 0$, implying there is negligible mean field shift in this case. The data in the inset of the same figure, which shows Φ for a $T = 2.7$ ms interferometer as a function of scattering length, would seem to contradict this theory as the phase abruptly drops by around 200 degrees above $a = -20a_0$. However, comparing to the inset of Fig. 7.7 (a) we see that these are fringes with quite small visibilities of $V < 0.05$ and so perhaps the phase of these particular points should not be trusted. It would be instructive

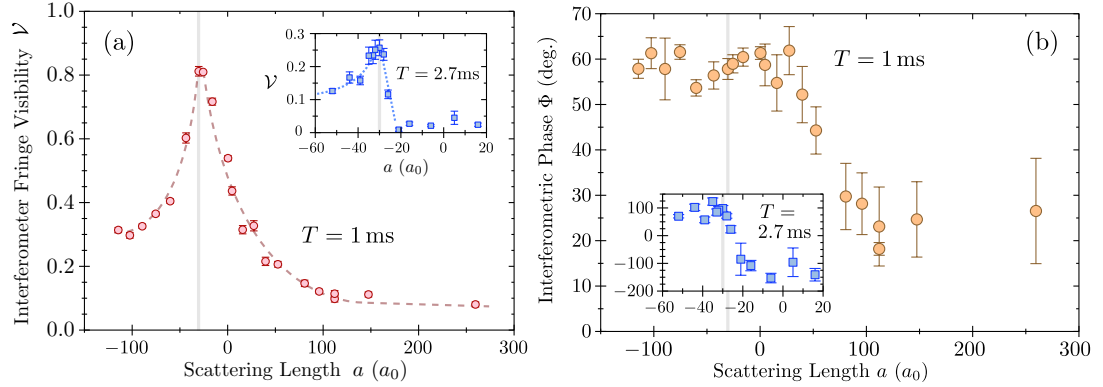


Figure 7.7: Fringe visibility (a) and interferometer phase Φ (b) as a function of scattering length a during the interferometer. The main plots are for interferometer time $T = 1 \text{ ms}$, and the insets are data taken on a different day with interferometer time $T = 2.7 \text{ ms}$. The grey vertical lines mark the soliton point of $a_s = -30a_0$ in each graph. The dashed lines in (a) are a guide to the eye. Error bars in both (a) and (b) are 1 s.d. confidence intervals on that parameter from the fit to each fringe.

therefore to look at how the interferometer behaves as a function of time T for a given scattering length, and this is the data presented in Figure 7.8.

In Figure 7.8 (a), the fringe visibility as a function of T is plotted for both a non-interacting BEC with $a = 0$ and a soliton with $a = a_s$. The coherence time τ of the interferometer is measured by a gaussian fit (see Refs [176, 114]) of the form

$$\mathcal{V} = \mathcal{V}_0 \exp\left(-\ln 2 \frac{T^2}{\tau^2}\right) \quad (7.14)$$

$$= \mathcal{V}_0 2^{-\frac{T^2}{\tau^2}} \quad (7.15)$$

which is defined such that τ is the half-maximum decay time of the visibility \mathcal{V} . The coherence time τ of the soliton interferometer has a half-maximum decay time of $2.3(1) \text{ ms}$. This is ~ 2.5 times as long as the non-interacting interferometer, with a coherence time of $\tau = 0.9(1) \text{ ms}$. This again shows the clear advantage afforded by the solitonic matter wave. Figure 7.8 (b) shows the interferometric phase measured as a function of interferometer time T for the solitonic and non-interacting interferometers. Again the phase shift appears to agree for small T , but diverges around 1.5 to 2 ms as the visibility of the non-interacting interferometer decays.

The repulsion observed previously [229, 230, 4] between solitons with a phase difference of π is not seen here. Ref. [183] suggests that this behaviour is only ob-

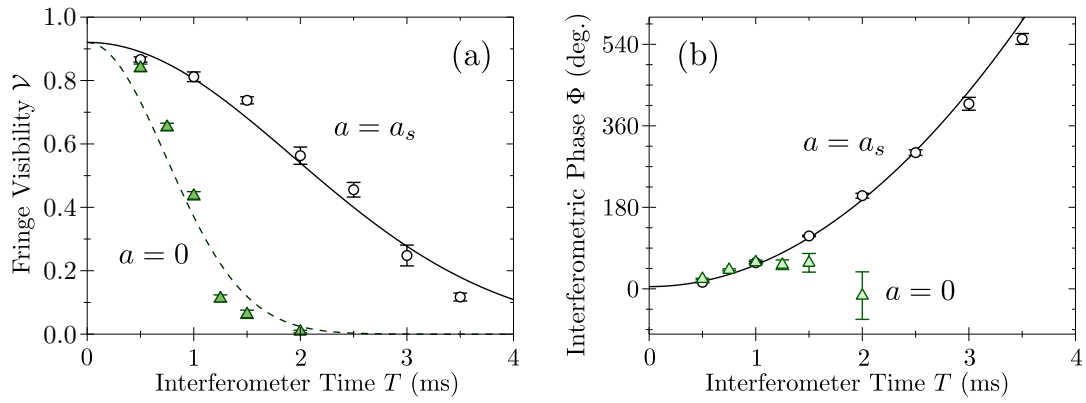


Figure 7.8: (a) Fringe visibility as a function of interferometer time T for the soliton point of $a = a_s$ (circles, solid line) and the non-interacting cloud at $a = 0$ (triangles, dashed line). The lines are gaussian fits to the coherence time τ at each scattering length (measured by the half-maximum decay in visibility) with $\tau = 2.3(1)$ ms and $\tau = 0.9(1)$ ms for the soliton and the non-interacting cloud respectively. (b) Measured interferometric phase Φ for the soliton interferometer (open circles, solid line) and the non-interacting cloud (triangles) as a function of interferometer time. The non-interacting phase measurement at $T = 2$ ms should probably not have too much weight attached to it as the visibility for that fringe is very low, at 0.8%. Error bars in both (a) and (b) are 1 s.d. confidence intervals on that parameter from the fit to each fringe.

served for low relative velocities ($\Delta v < 1 \text{ mm/s}$) whereas in our interferometer $\Delta v = 2\hbar k/m_{^{85}\text{Rb}} = 12 \text{ mm/s}$. This conclusion is supported by a recent experimental result on soliton collisions at $\Delta v \approx 4 \text{ mm/s}$ [178], which did not see a repulsion.

A quadratic fit to the phase data for the soliton is consistent with the cloud accelerating at $|\mathbf{a}| = 5.2(1) \times 10^{-2} \text{ m/s}^2$ due to both a slight tilt in the optical waveguide potential and the magnetic field gradient at the position of the atoms. The phase shift is quadratic because a Mach-Zehnder atom interferometer with $2\hbar\mathbf{k}$ momentum separation is sensitive to external acceleration \mathbf{a} according to $\Phi = 2\mathbf{k} \cdot \mathbf{a}T^2$ (see chapters 3 and 6). As the interferometer only samples a small region of the potential in Fig. 7.3 (b), the center-of-mass acceleration is to a good approximation constant. This is equivalent to a first-order Taylor series approximation to the potential, around the point at which the BEC is located.

7.4 Summary and Future Directions

We have demonstrated that a solitonic matter-wave optimises the choice of scattering length to give the highest visibility and the longest coherence time for a Mach Zehnder atom interferometer. Of course this technique is only practically applicable to clouds starting at sufficient density so that the collisional interactions play a significant role. The use of a soliton in an atom interferometer is another example of dispersion management, much like the expansion and delta-kick cooling shown in Chapter 6 maximises the visibility of a large momentum transfer atom interferometer.

This new system offers an intriguing array of both fundamental and applied future research directions. Studies of soliton collision dynamics [178] in a system with an interferometric probe offer the possibility to look for many-body entanglement [94]. A time varying scattering length could also allow investigation of squeezing enhanced interferometry [129, 110, 77]. It will also be possible to look for breather solitons [162] and yet more complicated soliton-like oscillations [40]. Applications to precision measurement will require an in-depth study of the phase evolution of the solitons as a function of density and scattering length, especially for the interesting domain highlighted in this chapter of phase evolution at negative scattering lengths.

Dual Isotope Interferometry

The work discussed in this chapter is published as

A Bose-condensed, simultaneous dual species Mach-Zehnder atom interferometer
 C. C. N. Kuhn, G. D. McDonald, K. S. Hardman, S. Bennetts, P. J. Everitt, P. A. Altin,
 J. E. Debs, J. D. Close, and N. P. Robins.
New J. Phys. **16**, 073035 (2014).

8.1 Equivalence Principle Measurements

There are many theories which attempt to unify General Relativity with the rest of modern physics [111, 139, 154, 99]. These theories typically imply some kind of violation of the assumptions underpinning General Relativity. One goal of a dual-isotope interferometer may be to check for any violations of the Weak Equivalence Principle (WEP). This principle states that all small test masses will experience the same acceleration due to a given gravitational field, or equivalently, that gravitational mass is equal to inertial mass. In the case that this principle is violated and the acceleration for each small test mass differs, this violation is quantified by the Eötvos parameter η , which is the difference in acceleration $\Delta\mathbf{a} = \mathbf{a}_1 - \mathbf{a}_2$ divided by the average acceleration of the two masses $\langle \mathbf{a} \rangle = (\mathbf{a}_1 + \mathbf{a}_2) / 2$,

$$\begin{aligned}\eta &= \frac{\Delta\mathbf{a}}{\langle \mathbf{a} \rangle} \\ &= 2 \frac{\mathbf{a}_1 - \mathbf{a}_2}{\mathbf{a}_1 + \mathbf{a}_2}.\end{aligned}\tag{8.1}$$

A violation of the WEP, $\eta \neq 0$, is expected at the $\eta \approx 10^{-12} - 10^{-17}$ level [99].

The best measurements of η so far are a torsion balance experiment comparing the acceleration of test masses consisting of Titanium and Beryllium due to the earth's gravity [206], and a lunar laser ranging experiment looking at the relative acceleration of the earth and moon due to the gravitational pull of the sun [243]. Both these experiments measure down to the $\eta \approx 10^{-13}$ level. Atom-interferometric experiments have compared the acceleration due to gravity of different atomic species down to the $\eta \approx 10^{-7}$ level by comparing the isotopes ^{85}Rb and ^{87}Rb [89, 30], ^{87}Sr and ^{88}Sr [234], or ^{87}Rb and ^{39}K [208]. A comparison between an atom interferometric gravimeter using ^{133}Cs and a falling corner-cube gravimeter reached the level of $\eta \approx 10^{-8}$ [186]. Ground-based experiments are in development for measurements comparing ^6Li and ^7Li to the level of $\eta \approx 10^{-14}$ [112, 119], and for comparing ^{85}Rb and ^{87}Rb for much longer drop times, aiming for an accuracy of $\eta \approx 10^{-15}$ [69].

Proposed microgravity and space-based missions include STE-QUEST [212, 3, 211] and QUANTUS [175, 195]. The QUANTUS-II project will use a $^{41}\text{K}/^{87}\text{Rb}$ dual-species BEC combination with a maximum micro-gravity interferometer time of 6 seconds, while the entire apparatus is on a parabolic trajectory in a drop tower. Closely related is the MAIUS project which aims to run an atom interferometer on the same two species on a sounding rocket. The STE-QUEST proposal plans to use the $^{85}\text{Rb}/^{87}\text{Rb}$ combination in microgravity to eliminate vibrational effects and prolong the drop time. They also plan to use BEC sources of each isotope and multi-stage delta-kick cooling (see Section 6.4) to prepare their source clouds for the interferometer. They are aiming for a sensitivity of $\eta \approx 10^{-15}$ over four years of data collection.

As these microgravity and space-based missions will rely on simultaneous interferometers performed upon each of two overlapping condensates, it is worthwhile to examine experimentally some of the difficulties which may be faced by this particular combination.

8.2 Dual Species condensate

Only minimal modification of our experimental procedure is required to produce dual species $^{87}\text{Rb}/^{85}\text{Rb}$ condensates. If the final stage of evaporation in the crossed dipole trap is tuned so that not all of the ^{87}Rb is lost, we can form a dual condensate, as discussed in Chapter 4. In this case we have a BEC of both ^{85}Rb and ^{87}Rb coexisting in the trap at the same time, and we can simultaneously perform interferometry on both condensates. As each isotope has a different mass, the Bragg resonance is slightly shifted. The recoil frequency ω_r for either isotope is given by

$$\omega_r \equiv \frac{\hbar|\mathbf{k}|^2}{2m} \quad (8.2)$$

and since their mass differs by 2.3%, the resonant Bragg transition frequency does as well. For low Bragg order this is no problem for driving a transition in both isotopes simultaneously. However, this will introduce a relative phase shift between the isotopes which increases linearly in time, in proportion to the isotopic detuning which will be shown in Equation (8.6).

8.3 Simultaneous Interference Fringes

By running an interferometer with both isotopes present, driven by the same optical lattice at the same time, we can generate simultaneous fringes as shown in Figure 8.1 (a) and (c). We can represent these fringes mathematically by

$${}^{87}N_{\text{rel}} = \frac{\mathcal{V}_{87}}{2} \cos \left(\Phi_{87} + n\phi_{\frac{\pi}{2}} + \delta_{87} \right) + c_{87} \quad (8.3)$$

$${}^{85}N_{\text{rel}} = \frac{\mathcal{V}_{85}}{2} \cos \left(\Phi_{85} + n\phi_{\frac{\pi}{2}} + \delta_{85} \right) + c_{85} \quad (8.4)$$

where ${}^iN_{\text{rel}}$ is the relative number of atoms in the $0\hbar k$ state, \mathcal{V}_i is the visibility, Φ_i is the interferometric phase and c_i is the fringe offset for the ${}^i\text{Rb}$ isotope. The applied laser phase on the last pulse $n\phi_{\frac{\pi}{2}}$ depends upon the Bragg order n but is common to both interferometers, whereas the phase noise on each fringe, δ_i , can be correlated in various different ways or completely uncorrelated depending upon what causes it. In general it is possible in such simultaneous experiments to get greater precision on the relative phase between the two interferometers. This is done by plotting one fringe against the other to form an ellipse, as in Figure 8.1 (b). In this case the curve is parametrised by the phase $\phi_{\frac{\pi}{2}}$. Common mode noise such as a vibration of the optical lattice is removed in such a scheme as both isotopes will experience the same phase shift, i.e. $\delta_{87} = \delta_{85}$. As this amounts to relabelling the implicit parameter $\phi_{\frac{\pi}{2}}$, this results in the data point moving further around the ellipse, but not moving off it, despite not lying on either sinusoidal fringe. As we do not see much less noise plotting the ellipse, this means our dominant noise sources are affecting the phase of each isotope differently. A more general model might say that instead of one-to-one phase noise on each isotope there might be some more general correlation $\delta_{87} = b\delta_{85}$ for some ratio $b \in \mathbb{R}$. In this case the ellipse plot would still look quite noisy, despite a perfect correlation between the phase noise of each isotope. If instead the data is plotted in 3D as in Fig. 8.1 (d), noiseless data would turn up on an elliptical helix, and the general correlated noise described above would fan out the data points onto a surface in which the elliptical helix is embedded. This is illustrated in Fig. 8.2 with simulated data. Of course if δ_{85} and δ_{87} are uncorrelated then no fancy analysis

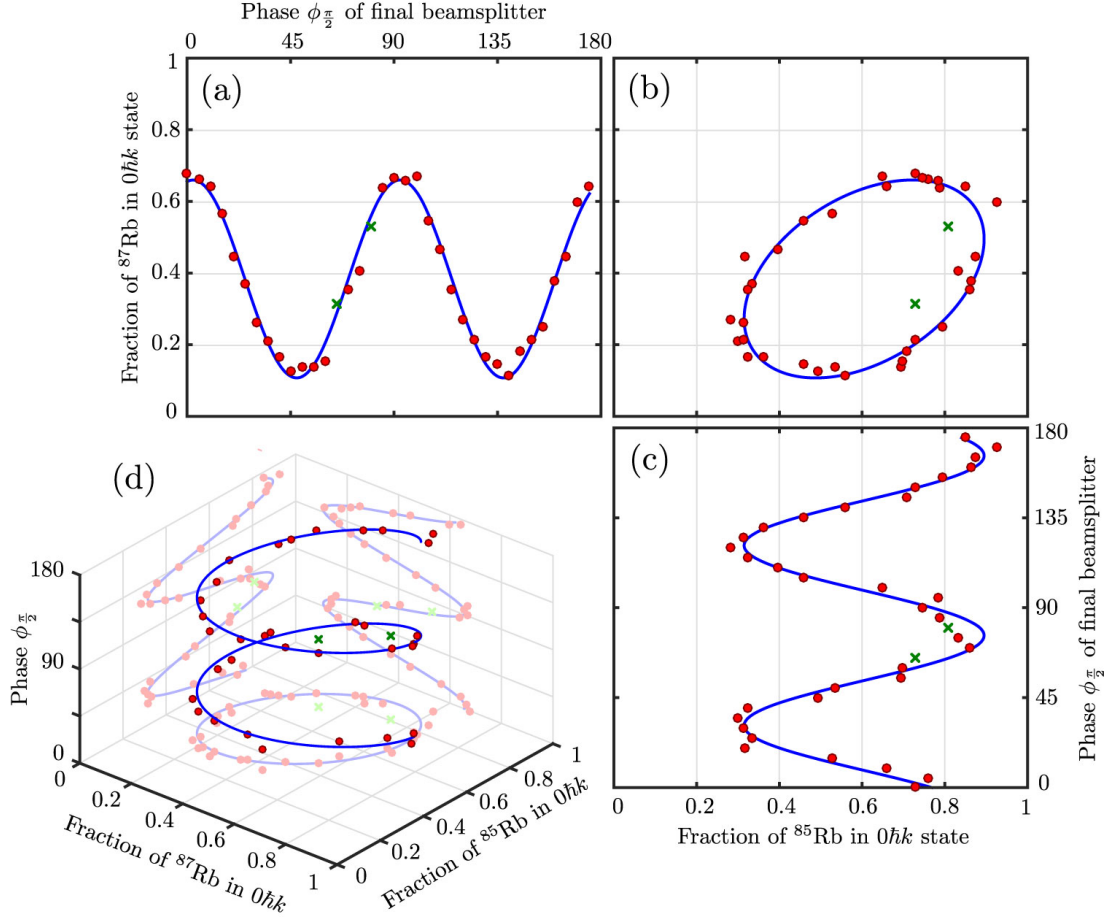


Figure 8.1: The simultaneous interferometer fringes acquired from a $T = 0.4\text{ ms}$ interferometer for ^{87}Rb and ^{85}Rb are shown in (a) and (c) respectively. Shown in (b) is the ellipse generated by plotting the data in (a) and (c) parametrically in terms of the phase $\phi_{\frac{\pi}{2}}$ we apply to the final beamsplitter. This ellipse plot should eliminate the effect of common-mode phase noise which causes a 1-to-1 phase shift in each interferometer. In (d) the data is shown in all three dimensions, with the projections (a), (b) and (c) shown on the “walls” of the plot. In the case of more general correlated phase noise, e.g. anti-correlated phase noise, the data will lie upon a complicated 3D surface in (d). Red dots are experimental data points, and the blue line is from the fit to each sinusoid in (a) and (c). The green crosses are experimental data points rejected as outliers by our ellipse fitting algorithm, which excludes those points with a distance to the nearest point on the ellipse which is 3 standard deviations or more higher than the mean distance to the ellipse.

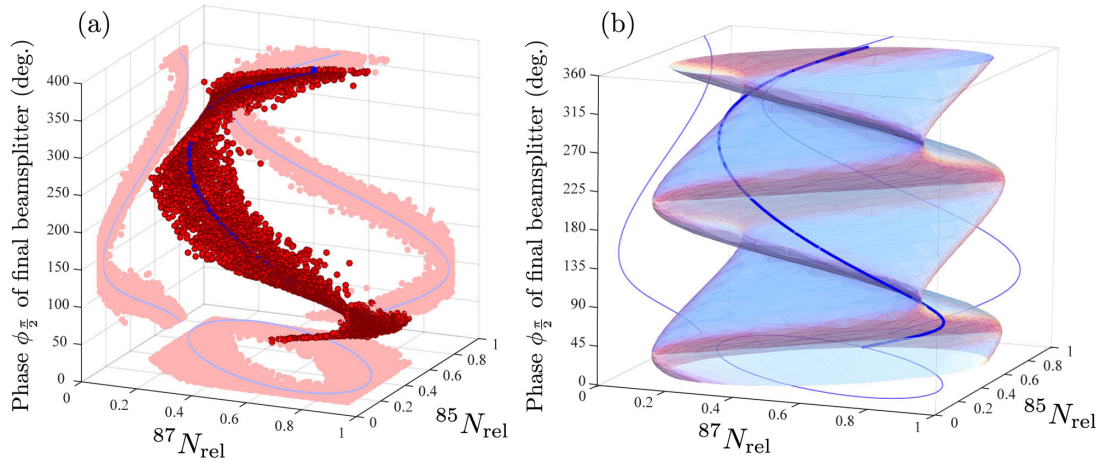


Figure 8.2: (a) Simulated data for simultaneous $2\hbar k$ interferometers with perfectly anti-correlated phase noise on each fringe, i.e. $\delta_{85} = -\delta_{87}$. This simulated data is plotted the same as the experimental data in Fig. 8.1 (d). It can be seen that the ellipse plot (on the ‘floor’) does not remove *anti*-corellated noise from the data. (b) The elliptical helix (along which the data would lie if there were no noise) is embedded in a 3D surface which has been parametrically plotted here. The shape of the 3D surface depends upon the coefficient b which specifies the relationship between phase noise on one interferometer and phase noise on the other. Thus a fit to the shape of the 3D surface can yield both the removal of unwanted noise for a general correlation b , and the value of b itself. This plot is for $b = -1$, i.e. perfectly anti-correlated phase noise.

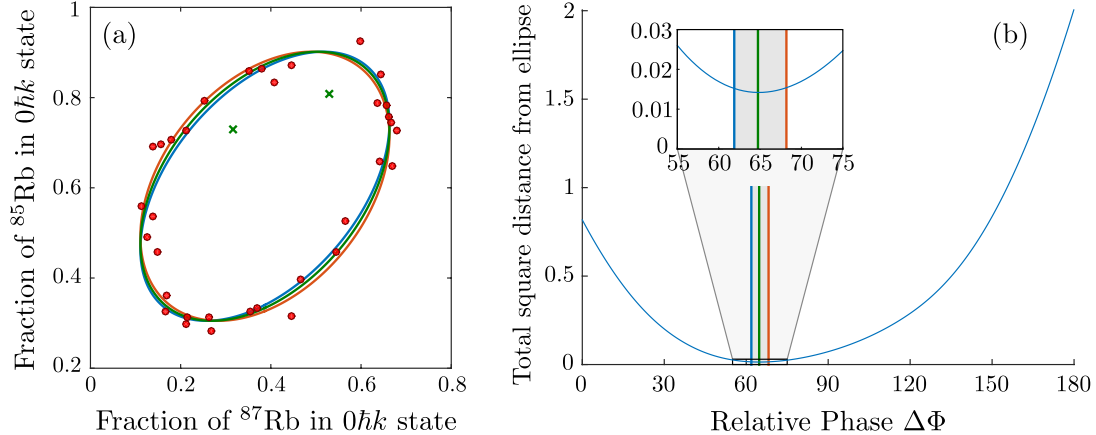


Figure 8.3: (a) The ellipse for $T = 0.4\text{ ms}$ with relative phase $\Delta\Phi = 65 \pm 3$ degrees. Red dots are experimental data, while green crosses have been excluded by the outlier detection algorithm. The blue, green and oranges ellipses have respectively the minimum, best and maximum estimates of relative phase $\Delta\Phi$. (b) The relative phase $\Delta\Phi = \Phi_{85} - \Phi_{87}$ is adjusted and we calculate the sum of square distances of each point to the ellipse, $\sum d_i^2$. Inset: The minimum in $\sum d_i^2$ is our choice of the best relative phase. The uncertainty is generated by finding the angles $\Delta\Phi$ for which the total square distance from the ellipse $\sum d_i^2$ is 10% larger than the minimum.

technique can reduce the noise beyond the improvement due to simple statistics as increasing amounts of data is taken.

Our ellipse fitting technique (illustrated in Fig. 8.3) is a multi-step algorithm.

1. *Algebraic Fit.* First we perform an algebraic fit to the ellipse from the data points using a direct least-squares fit [84, 54]. Although this is computationally efficient, it does not reject outliers, and does not provide an estimate of the uncertainty of the relative phase $\Delta\Phi$.
2. *Scan Relative Phase.* We then scan the relative phase estimator $\hat{\Delta}\Phi$ over all possible values in the range $\hat{\Delta}\Phi \in [0, \pi]$. For each value of $\hat{\Delta}\Phi$ we compute numerically the distance d_i of each data point to the nearest point on the ellipse. Plotted in Figure 8.3 (b) is the sum of the squared distances from each point to the ellipse $\sum d_i^2$, as a function of the relative phase estimator $\hat{\Delta}\Phi$. We take the value of $\hat{\Delta}\Phi$ which minimizes $\sum d_i^2$ as the best estimate of $\Delta\Phi$. We also take the values of $\hat{\Delta}\Phi$ above and below the optimum, which produce a $\sum d_i^2$ which is 10% higher than the minimum value, as an estimate of the uncertainty in $\Delta\Phi$ using the ellipse fitting technique.
3. *Reject Outliers.* From the list of distances d_i of each data point i from the ellipse

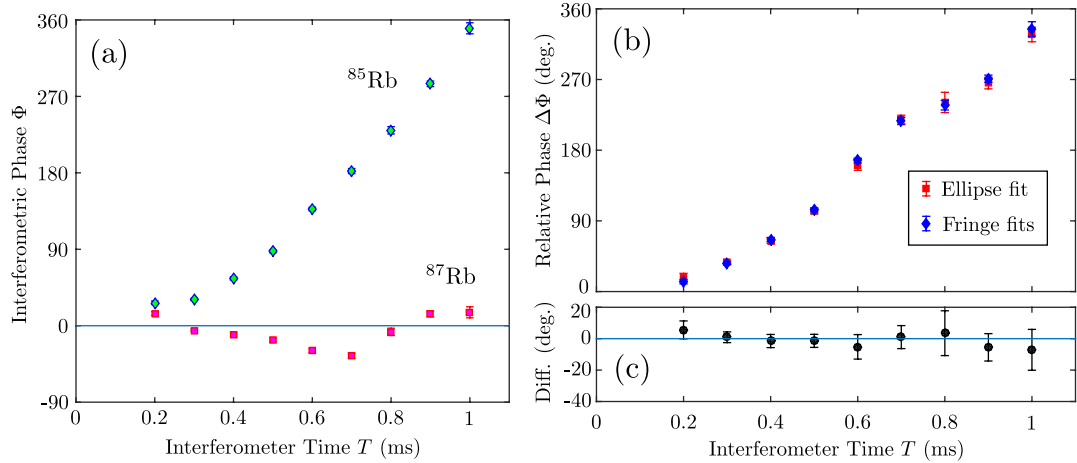


Figure 8.4: (a) The interferometric phase Φ of each isotope's interferometer is measured as a function of interferometer time T by a simple sinusoidal fit. (b) The relative phase $\Delta\Phi = \Phi_{85} - \Phi_{87}$ is computed for each T by two methods; subtraction of the interferometric phases recorded in (a), or by a fit to the ellipse as shown in Fig. 8.3 (a). (c) The difference between the relative phase $\Delta\Phi$ as computed using each of the two methods shows that they agree within uncertainty.

with our optimal choice of relative phase $\Delta\Phi$ we reject all data points for which d_i is more than 3 standard deviations away from the mean. Rejected data points are kept and plotted but not fitted to in the remaining steps.

4. Iterate. Steps 1 and 2 are repeated, now that the outliers have been rejected.

The result of this fitting technique is shown in Figure 8.3 (a) for a $T = 0.4$ ms, $8\hbar\mathbf{k}$ interferometer on both isotopes. The red dots are the data points, while green crosses are the rejected outliers. The green ellipse is the optimal fit, and the uncertainty in relative phase is represented by the orange and blue ellipses which have a relative phase of (optimal+uncertainty) and (optimal-uncertainty) respectively. It should be noted that our fitting algorithm is a post-processing technique, and is not computationally efficient for real-time processing. Others have used a Bayesian technique for the purpose of real-time processing [228].

A comparison between the relative phase as computed using this ellipse fitting technique, and that calculated from a simple sinusoidal fit to each isotope's interference fringe directly is shown in Figure 8.4 (b). Both methods calculate the same relative phase to within uncertainty, as shown in Fig. 8.4 (c) where the difference between the two is plotted.

8.4 Systematic phase shifts between isotopes

It is perhaps interesting that the relative phase between the two isotopes' interference fringes [in Figure 8.4 (b)] evolves roughly linearly in time. What could explain this behaviour? Here I present some possible simple explanations.

Because the recoil frequency for each isotope differs by $\Delta\omega_{\text{rec}} = \frac{\hbar k^2}{2} \left(\frac{1}{m_{85}} - \frac{1}{m_{87}} \right)$, the isotopic detuning between the $2n$ -photon Bragg resonance of ^{85}Rb and ^{87}Rb is given by

$$\Delta_{\text{iso}} = 4n\Delta\omega_{\text{rec}} \quad (8.5)$$

$$= 2n\hbar k^2 \left(\frac{1}{m_{85}} - \frac{1}{m_{87}} \right) \quad (8.6)$$

This will lead to a differential phase shift between the isotopes which will increase linearly in time as $\Delta\Phi_{\text{iso}} = \Delta_{\text{iso}}T$. For an $8\hbar k$ interferometer this works out to be $\Delta_{\text{iso}} = 558 \text{ rad/s}$, which is the same order of magnitude as the measured differential phase shift [shown in figure 8.4 (b)] which is approximately linear, increasing at 434 rad/s .

Another possible explanation is a difference in initial velocity of the two isotopic BECs at the beginning of the interferometer. This could arise due to e.g. the different response to magnetic field gradients present as the BECs are released into the waveguide, before the beginning of the interferometer. This will cause a Doppler shift between the relative frequencies of each cloud as $\Delta_{\Delta v} = \mathbf{k} \cdot \Delta \mathbf{v}$, and thus a relative phase shift of $\Delta\Phi_{\Delta v} = \mathbf{k}T \cdot \Delta \mathbf{v}$, again linear in interferometer time.

Of course, there are other complicating factors such as the mean-field interactions between ^{87}Rb atoms, and the inter-isotope mean field interactions between ^{87}Rb and ^{85}Rb atoms. The phase shift due to these effects will be density dependent. One way to investigate these shifts is to look at the phase of just the ^{85}Rb interferometer, with its self-interaction turned off ($a_{85} = 0$), while varying the number of co-incident ^{87}Rb atoms. This measurement is shown in Figure 8.5 for a $2\hbar k$ interferometer. For these short interferometer times we can approximate that the clouds with different momentum states stay largely overlapped. The GPE for ^{85}Rb becomes

$$-i\hbar \frac{\partial}{\partial t} \Psi_{85} = \left(-\frac{\hbar^2}{2m_{85}} \nabla^2 + V + U_{\text{int}} \right) \Psi_{85} \quad (8.7)$$

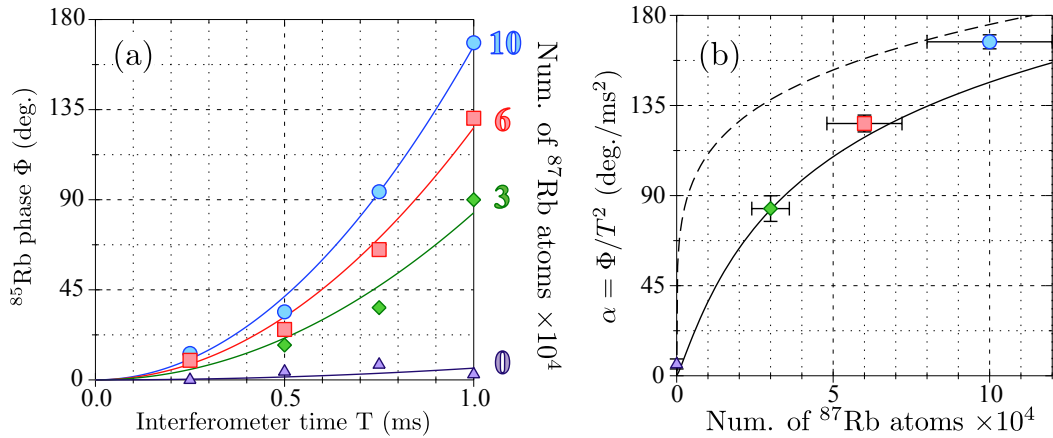


Figure 8.5: (a) We found we were able to measure the density of ^{87}Rb in a dual-species MZ interferometer by looking at the phase of the ^{85}Rb interferometer. Phase shift on ^{85}Rb ($a_s \sim 0$) fringes as a function of interferometer time, T , in the waveguide, for a varying number N_{87} of ^{87}Rb atoms co-incident. The lines are a fit of the form $\Phi = \alpha T^2$ to each set with constant N_{87} . (b) The value of α from the fits in (a) as a function of N_{87} . The dashed and solid lines are two simple models developed in the text, with no free parameters, and no fitting involved.

In the axial direction z the external potential V is roughly zero, so the main potential felt by the ^{85}Rb atoms comes from the interaction with ^{87}Rb , in the term U_{int} [192]

$$U_{\text{int}} = \frac{4\pi\hbar^2 a_{85/87}}{m_{86}} |\Psi_{87}|^2 \quad (8.8)$$

where m_{86} is just a shorthand for the reduced mass

$$m_{86} = 2 \frac{m_{85} m_{87}}{m_{85} + m_{87}} \quad (8.9)$$

As there are $\approx 2 \times 10^4$ ^{85}Rb atoms and up to 10^5 ^{87}Rb atoms, let us assume first that the ^{85}Rb has no impact on the density profile of the ^{87}Rb condensate in trap. In that case the density profile will be approximately Thomas-Fermi (TF),

$$|\Psi_{87}|^2 = \frac{m_{87}}{4\pi\hbar^2 a_{87}} (\mu_{87} - V_{\text{trap}}) \quad (8.10)$$

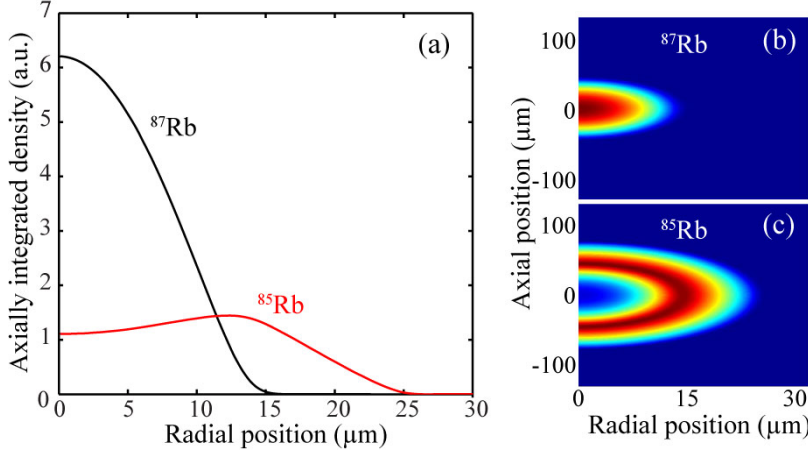


Figure 8.6: A ‘miscible’ initial condition in our trap, with $a_{85} = 1000a_0$, $a_{87} = 100a_0$ and $a_{85/87} = 212a_0$ and therefore $\mu_{\text{misc}} = 2.2$. Computed with no asymmetry due to gravity or magnetic response of the two isotopes, using a 3D cylindrically symmetric grid. The density of ^{87}Rb , $|\Psi_{87}(r,z)|^2$, is shown in (b) as a function of the radial coordinate r and axial coordinate z . Likewise the density of ^{85}Rb , $|\Psi_{85}(r,z)|^2$, is shown in (c). In (a), both densities have been integrated along z and plotted as a function of r . It can be seen that the ^{87}Rb condensate is at the bottom of the harmonic trap, as it has both the heavier mass and the smaller self-scattering length, making it more dense than the ^{85}Rb .

for the in-trap potential

$$V_{\text{trap}} = \frac{m_{87}}{2} (\omega_r^2 r^2 + \omega_z^2 z^2) \quad (8.11)$$

and chemical potential

$$\mu_{87} = \frac{1}{2} \left(15N_{87}a_{87}\hbar^2\omega_z\omega_r^2\sqrt{m_{87}} \right)^{2/5} \quad (8.12)$$

This density profile is a paraboloid with a spatial extent in each direction of the TF radius

$$r_{\text{tf}} = \frac{1}{\omega_r} \sqrt{\frac{2\mu_{87}}{m_{87}}} \quad (8.13)$$

$$z_{\text{tf}} = \frac{1}{\omega_z} \sqrt{\frac{2\mu_{87}}{m_{87}}} \quad (8.14)$$

The miscibility criterion μ_{misc} for the two condensates is given by

$$\mu_{\text{misc}}^2 = \frac{a_{85}a_{87}}{a_{85/87}^2} \quad (8.15)$$

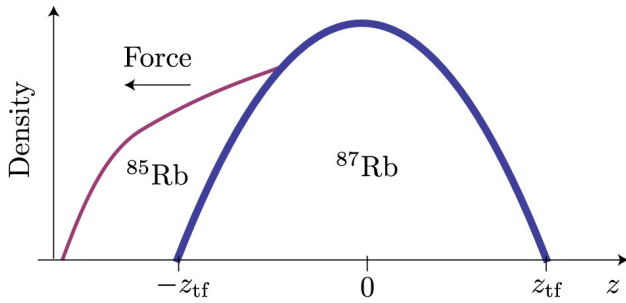


Figure 8.7: A simple model is to assume that the ^{87}Rb condensate has roughly a Thomas-Fermi distribution. Due to some asymmetry (such as different gravitational sag, or different magnetic responses of each isotope) the smaller ^{85}Rb condensate is resting on one side of the ^{87}Rb condensate, and so when the two are released into the waveguide, the ^{85}Rb experiences a force dependent upon the density gradient of ^{87}Rb .

When this is less than one, then the condensates are said to be immiscible. Roughly speaking, they are repelled from one another more than they are repelled from themselves. In our case with $a_{85} = 0$, $a_{87} = 100a_0$ and $a_{85/87} = 212a_0$ then $\mu_{\text{misc}} = 0$ and the clouds will not be overlapped in equilibrium. If the miscibility criterion μ_{misc} is less than one (i.e. when $a_{85} > 450a_0$), the condensates will be found to be overlapping in places. For example, with $a_{85} = 1000a_0$, $a_{87} = 100a_0$ and $a_{85/87} = 212a_0$ then $\mu_{\text{misc}} = 2.2$ and the two condensates should be overlapped in some places. This ‘miscible’ choice of scattering length is shown in Figure 8.6 as the equilibrium density profiles of the two condensates in our trap, which was numerically computed using a cylindrically symmetric 3D GPE simulation [13]. It can be seen despite the miscibility parameter, there is only minimal overlap between the two condensates due to the large difference between the scattering lengths of each.

If there is some asymmetry, for example a slight difference in the equilibrium position of ^{85}Rb and ^{87}Rb due to the combined optical, magnetic and gravitational potential, then the two condensates will not be perfectly concentric. We will assume the ^{85}Rb condensate is sitting on one side of the ^{87}Rb condensate we have described, as shown in Fig. 8.7. Now if we treat the ^{85}Rb condensate as a point particle, being affected by the potential energy generated by the density of ^{87}Rb , U_{int} , and located at the Thomas-Fermi length in the axial z direction, it will experience an acceleration away from the ^{87}Rb condensate at the rate

$$\mathbf{a} = -\frac{1}{m_{85}} \nabla U_{\text{int}} \Big|_{r=0, z=z_{tf}} \quad (8.16)$$

$$= -\frac{4\pi\hbar^2 a_{85/87}}{m_{85}m_{86}} \nabla |\Psi_{87}|^2 \Big|_{r=0, z=z_{tf}} \quad (8.17)$$

$$= \frac{m_{87}}{m_{85}m_{86}} \frac{a_{85/87}}{a_{87}} \frac{d}{dz} V_{\text{trap}} \Big|_{z=z_{tf}} \hat{\mathbf{z}} \quad (8.18)$$

$$= \frac{m_{87}^2}{m_{85}m_{86}} \frac{a_{85/87}}{a_{87}} \omega_z^2 z_{tf} \quad (8.19)$$

$$= \frac{m_{87}}{m_{85}} \frac{\frac{m_{87}}{m_{85}} + 1}{2} \frac{a_{85/87}}{a_{87}} \omega_z^2 z_{tf} \hat{\mathbf{z}} \quad (8.20)$$

This acceleration will be measured by the interferometer as a phase shift

$$\Phi = 2n\mathbf{k} \cdot \mathbf{a} T^2 \quad (8.21)$$

$$= n\mathbf{k} \cdot \hat{\mathbf{z}} T^2 \frac{m_{87}}{m_{85}} \left(\frac{m_{87}}{m_{85}} + 1 \right) \frac{a_{85/87}}{a_{87}} \omega_z^2 z_{tf} \quad (8.22)$$

and so the quadratic phase coefficient is

$$\alpha = \frac{\Phi}{T^2} \quad (8.23)$$

$$= 2n\mathbf{k} \cdot \hat{\mathbf{z}} \frac{m_{87}}{m_{85}} \left(\frac{m_{87}}{m_{85}} + 1 \right) \frac{a_{85/87}}{a_{87}} \omega_z^2 z_{tf} \quad (8.24)$$

This is the dashed curve plotted in Fig. 8.5 (b) for our parameters, and it scales as $\propto N_{87}^{1/5}$, the same as z_{tf} . Of course the ^{85}Rb cloud is not always much smaller than the ^{87}Rb cloud. When they have roughly the same number of atoms, we could perhaps treat the ^{85}Rb cloud as a point particle further up on the TF profile of the ^{87}Rb BEC. To account for this we can say that it is located at a point

$$z = \frac{N_{87}}{N_{85} + N_{87}} z_{tf} \quad (8.25)$$

along the z-axis. This results in a quadratic phase coefficient of

$$\alpha = \frac{\Phi}{T^2} \quad (8.26)$$

$$= n\mathbf{k} \cdot \hat{\mathbf{z}} \frac{m_{87}}{m_{85}} \left(\frac{m_{87}}{m_{85}} + 1 \right) \frac{a_{85/87}}{a_{87}} \frac{N_{87}}{N_{85} + N_{87}} \omega_z^2 z_{tf} \quad (8.27)$$

which is the solid curve plotted in Fig. 8.5 (b). It can be seen that the experimental data lies between these two simple models. To confirm that this is the exact cause

of the phase shift would require a full 3D GPE simulation involving the particular asymmetry which offset the two condensates in the first place.

8.5 Summary

We have experimentally investigated some of the issues involved in simultaneous dual-species interferometry. In particular with the $^{85}\text{Rb}/^{87}\text{Rb}$ combination, it is difficult to get a good spatial overlap between the two clouds. We have seen that the effect of this spatial mismatch can be a density dependent mean-field phase shift caused as the two clouds repel one another.

We have also seen that using the same optical lattice to Bragg diffract both isotopes simultaneously can cause a phase shift which is linear in time. This phase shift could be used to make a measurement of the difference in recoil frequency between the two isotopes, i.e. a precision measurement of their mass difference. These effects will need to be considered in any future space mission aiming to make precision measurements using this simultaneous lattice on dual-condensate configuration.

Conclusion and Outlook

This thesis has demonstrated the utility of an axial optical confinement for condensed-atom interferometry (Chapter 5). This configuration will prove useful in defined-axis acceleration sensors and compact, long-time interferometry. Two of the engineering challenges which will be necessary for this to come to fruition are improved vibration isolation and a flatter optical waveguide potential, perhaps through the use of a Bessel beam, or a hexagonal optical lattice [78] as the wave-guiding potential.

This thesis has introduced two dispersion management techniques to BEC interferometry, optical delta-kick cooling and the use of interactions to form a self-trapping cloud known as a soliton. Optical Delta-Kick Cooling (Section 6.4) consisted of the brief application of a harmonic optical potential after expansion of the atom cloud in order to remove kinetic energy from the cloud. This technique was used to create a low momentum-width source, which was critical in achieving Large Momentum Transfer (LMT) of up to 80 photon recoils in an acceleration-measuring atom interferometer. Indeed without delta-kick cooling, the LMT result would not have been possible as illustrated well in Figure 6.3 (e). The self-trapped soliton of Chapter 7 provided the curious result that it had higher visibility than all other choices of two-body collisional interaction strength in an atom interferometer, illustrated in Figure 7.7 (a). This was due to the constant phase-space density throughout the interferometer. Both of these techniques will no doubt become common source preparation techniques for atom interferometry in the future.

Having developed a large momentum transfer technique, it was employed to generate a new configuration of atom interferometer with a constant acceleration separation between the two interfering arms (Section 6.7). This configuration allows the acceleration sensitivity to scale as the cube of the interferometer time, allowing faster measurements at the same sensitivity level (increasing bandwidth), or more sensitive measurements with the same interferometer time. In the future, this could be improved upon yet again through the use of rastered dipole traps to allow scalings of T^4 or even higher, as detailed in Section 6.8.

Finally, this thesis looked at some of the confounding factors involved in simultaneous dual-isotope BEC interferometry in Chapter 8. An extension to the commonly used ellipse-fitting technique to find the inter-isotope phase shift was proposed which allows the removal of more general correlated noise than in the ellipse fit. Also, a mean-field inter-isotope repulsion model was used to explain the measured phase shift difference between ^{87}Rb and ^{85}Rb . Such issues will need to be considered when planning for space-based experiments to test the Weak Equivalence Principle such as STE-QUEST.

Promising directions for future study in ^{85}Rb include looking for soliton breathing modes, in which the self-trapped cloud undergoes axial width oscillations. It is possible that these could allow improved atom interferometers [74]. Another future direction would be to look at the phase difference as a function of time between neighbouring solitons in a soliton train [178]. It has been predicted that their relative phase should become uncorrelated over time due to beyond-mean-field effects [231]. A Ramsey-type atom interferometer ($\pi/2 - T - \pi/2$) would be ideal for measuring the relative phase between the neighbouring solitons in the train.

Bibliography

1. Alvatec alkali metal dispensers. <http://www.alvatec.com/files/9013/3760/9166/alvasources-web-high.pdf>. (cited on page 71)
2. Roithner laser diodes, adl-78901tx. http://www.roithner-laser.com/ld_diverse.html. (cited on page 67)
3. AGUILERA, D. N.; AHLERS, H.; BATELIER, B.; BAWAMIA, A.; BERTOLDI, A.; BONDARESCU, R.; BONGS, K.; BOUYER, P.; BRAXMAIER, C.; CACCIAPUOTI, L.; CHALONER, C.; CHWALLA, M.; ERTMER, W.; FRANZ, M.; GAALOUL, N.; GEHLER, M.; GERARDI, D.; GESA, L.; GÜRLEBECK, N.; HARTWIG, J.; HAUTH, M.; HELLMIG, O.; HERR, W.; HERRMANN, S.; HESKE, A.; HINTON, A.; IRELAND, P.; JETZER, P.; JOHANN, U.; KRUTZIK, M.; KUBELKA, A.; LÄMMERZAHN, C.; LANDRAGIN, A.; LLORO, I.; MASSONNET, D.; MATEOS, I.; MILKE, A.; NOFRARIAS, M.; OSWALD, M.; PETERS, A.; POSSO-TRUJILLO, K.; RASEL, E.; ROCCO, E.; ROURA, A.; RUDOLPH, J.; SCHLEICH, W.; SCHUBERT, C.; SCHULDIT, T.; SEIDEL, S.; SENGSTOCK, K.; SOPUERTA, C. F.; SORRENTINO, F.; SUMMERS, D.; TINO, G. M.; TRENKEL, C.; UZUNOGLU, N.; VON KLITZING, W.; WALSER, R.; WENDRICH, T.; WENZLAWSKI, A.; WEßELS, P.; WICHT, A.; WILLE, E.; WILLIAMS, M.; WINDPASSINGER, P.; AND ZAHZAM, N., 2014. STE-QUEST - test of the universality of free fall using cold atom interferometry. *Classical and Quantum Gravity*, 31, 11 (2014), 115010. <http://stacks.iop.org/0264-9381/31/i=11/a=115010>. (cited on pages 123 and 132)
4. AL KHAWAJA, U.; STOOF, H. T. C.; HULET, R. G.; STRECKER, K. E.; AND PARTRIDGE, G. B., 2002. Bright soliton trains of trapped Bose-Einstein condensates. *Phys. Rev. Lett.*, 89 (Oct 2002), 200404. doi:10.1103/PhysRevLett.89.200404. <http://link.aps.org/doi/10.1103/PhysRevLett.89.200404>. (cited on page 127)
5. ALTIN, P. A., 2012. The role of interactions in atom interferometry with Bose-condensed atoms. *PhD thesis, Australian National University*, (2012). <http://atomlaser.anu.edu.au/publications/altin.pdf>. (cited on pages 7, 8, 28, 71, and 72)
6. ALTIN, P. A.; DENNIS, G. R.; McDONALD, G. D.; DÖRING, D.; DEBS, J. E.; CLOSE, J. D.; SAVAGE, C. M.; AND ROBINS, N. P., 2011. Collapse and three-body loss in a ^{85}Rb Bose-Einstein condensate. *Phys. Rev. A*, 84 (Sep 2011), 033632. doi:10.1103/PhysRevA.84.033632. <http://link.aps.org/doi/10.1103/PhysRevA.84.033632>. (cited on pages 115 and 118)

7. ALTIN, P. A.; JOHNSSON, M. T.; NEGNEVITSKY, V.; DENNIS, G. R.; ANDERSON, R. P.; DEBS, J. E.; SZIGETI, S. S.; HARDMAN, K. S.; BENNETTS, S.; McDONALD, G. D.; TURNER, L. D.; CLOSE, J. D.; AND ROBINS, N. P., 2013. Precision atomic gravimeter based on Bragg diffraction. *New Journal of Physics*, 15, 2 (2013), 023009. <http://stacks.iop.org/1367-2630/15/i=2/a=023009>. (cited on pages 3, 97, 99, 110, and 123)
8. ALTIN, P. A.; McDONALD, G.; DÖRING, D.; DEBS, J. E.; BARTER, T. H.; CLOSE, J. D.; ROBINS, N. P.; HAINE, S. A.; HANNA, T. M.; AND ANDERSON, R. P., 2011. Optically trapped atom interferometry using the clock transition of large ^{87}Rb Bose–Einstein condensates. *New Journal of Physics*, 13, 6 (2011), 065020. <http://stacks.iop.org/1367-2630/13/i=6/a=065020>. (cited on pages 83 and 88)
9. ALTIN, P. A.; ROBINS, N. P.; DORING, D.; DEBS, J. E.; POLDY, R.; FIGL, C.; AND CLOSE, J. D., 2010. ^{85}Rb tunable-interaction bose–einstein condensate machine. *Review of Scientific Instruments*, 81, 6 (2010), 063103. doi:10.1063/1.3430538. <http://link.aip.org/link/?RSI/81/063103/1>. (cited on pages 67 and 115)
10. ALTIN, P. A.; ROBINS, N. P.; POLDY, R.; DEBS, J. E.; DÖRING, D.; FIGL, C.; AND CLOSE, J. D., 2010. Measurement of inelastic losses in a sample of ultracold ^{85}Rb . *Phys. Rev. A*, 81 (Jan 2010), 012713. doi:10.1103/PhysRevA.81.012713. <http://link.aps.org/doi/10.1103/PhysRevA.81.012713>. (cited on page 118)
11. AMINOFF, C. G.; STEANE, A. M.; BOUYER, P.; DESBIOLLES, P.; DALIBARD, J.; AND COHEN-TANNOUDJI, C., 1993. Cesium atoms bouncing in a stable gravitational cavity. *Phys. Rev. Lett.*, 71 (Nov 1993), 3083–3086. doi:10.1103/PhysRevLett.71.3083. <http://link.aps.org/doi/10.1103/PhysRevLett.71.3083>. (cited on page 23)
12. AMMANN, H. AND CHRISTENSEN, N., 1997. Delta kick cooling: A new method for cooling atoms. *Phys. Rev. Lett.*, 78 (Mar 1997), 2088–2091. doi:10.1103/PhysRevLett.78.2088. <http://link.aps.org/doi/10.1103/PhysRevLett.78.2088>. (cited on page 101)
13. ANDERSON, R. P., 2010. Nonequilibrium dynamics and relative phase evolution of two-component Bose-Einstein condensates. *PhD thesis, Swinburne University*, (2010). http://bec.physics.monash.edu.au/docs/RPA_Thesis_Digital.pdf. (cited on page 141)
14. ANDIA, M.; JANNIN, R.; NEZ, F. M. C.; BIRABEN, F. M. C.; GUELLATI-KHÉLIFA, S.; AND CLADÉ, P., 2013. Compact atomic gravimeter based on a pulsed and accelerated optical lattice. *Phys. Rev. A*, 88 (Sep 2013), 031605. doi:10.1103/PhysRevA.88.031605. <http://link.aps.org/doi/10.1103/PhysRevA.88.031605>. (cited on pages 99 and 114)
15. ANDREWS, M. R.; TOWNSEND, C. G.; MIESNER, H.-J.; DURFEE, D. S.; KURN, D. M.; AND KETTERLE, W., 1997. Observation of interference between two bose condensates. *Science*, 275, 5300 (1997), 637–641. doi:10.1126/science.275.5300.637. <http://www.sciencemag.org/content/275/5300/637.abstract>. (cited on page 1)

-
16. ARNOLD, A. S.; MACCORMICK, C.; AND BOSHIER, M. G., 2002. Adaptive inelastic magnetic mirror for Bose-Einstein condensates. *Phys. Rev. A*, 65 (Jan 2002), 031601. doi:10.1103/PhysRevA.65.031601. <http://link.aps.org/doi/10.1103/PhysRevA.65.031601>. (cited on page 23)
 17. BAGNATO, V. S.; FRANTZESKAKIS, D. J.; KEVREKIDIS, P. G.; MALOMED, B. A.; AND MIHALACHE, D., 2015. Bose-Einstein condensation: Twenty years after. *Romanian Reports in Physics*, 67, 1 (2015), 5–50. (cited on page 7)
 18. BARRETT, B.; CHAN, I.; AND KUMARAKRISHNAN, A., 2011. Atom-interferometric techniques for measuring uniform magnetic field gradients and gravitational acceleration. *Phys. Rev. A*, 84 (Dec 2011), 063623. doi:10.1103/PhysRevA.84.063623. <http://link.aps.org/doi/10.1103/PhysRevA.84.063623>. (cited on page 3)
 19. BARRETT, B.; GEIGER, R.; DUTTA, I.; MEUNIER, M.; CANUEL, B.; GAUGUET, A.; BOUYER, P.; AND LANDRAGIN, A., 2014. The Sagnac effect: 20 years of development in matter-wave interferometry. *Comptes Rendus Physique*, 15, 10 (2014), 875 – 883. doi:<http://dx.doi.org/10.1016/j.crhy.2014.10.009>. <http://www.sciencedirect.com/science/article/pii/S1631070514001467>. The Sagnac effect: 100 years later / L'effet Sagnac : 100 ans après. (cited on page 3)
 20. BECKER, C.; SENGSTOCK, K.; SCHMELCHER, P.; KEVREKIDIS, P. G.; AND CARRETERO-GONZÁLEZ, R., 2013. Inelastic collisions of solitary waves in anisotropic Bose Einstein condensates: sling-shot events and expanding collision bubbles. *New Journal of Physics*, 15, 11 (2013), 113028. <http://stacks.iop.org/1367-2630/15/i=11/a=113028>. (cited on page 123)
 21. BERG, P.; ABEND, S.; TACKMANN, G.; SCHUBERT, C.; GIESE, E.; SCHLEICH, W. P.; NARDUCCI, F. A.; ERTMER, W.; AND RASEL, E. M., 2015. Composite-light-pulse technique for high-precision atom interferometry. *Phys. Rev. Lett.*, 114 (Feb 2015), 063002. doi:10.1103/PhysRevLett.114.063002. <http://link.aps.org/doi/10.1103/PhysRevLett.114.063002>. (cited on page 98)
 22. BERMAN, P. R. (Ed.), 1997. *Atom Interferometry*. Academic Press, San Diego. ISBN 978-0-12-092460-8. doi:<http://dx.doi.org/10.1016/B978-012092460-8/50000-X>. <http://www.sciencedirect.com/science/article/pii/B978012092460850000X>. (cited on page 1)
 23. BERRADA, T.; VAN FRANK, S.; BÜCKER, R.; SCHUMM, T.; SCHAFF, J. F.; AND SCHMIEDMAYER, J., 2013. Integrated Mach-Zehnder interferometer for Bose-Einstein condensates. *Nat. Commun.*, 4 (Jun 2013). <http://dx.doi.org/10.1038/ncomms3077>. (cited on pages 5 and 99)
 24. BERRY, M. V. AND BALAZS, N. L., 1979. Nonspreadng wave packets. *American Journal of Physics*, 47, 3 (1979), 264–267. doi:<http://dx.doi.org/10.1119/1.11855>. <http://scitation.aip.org/content/aapt/journal/ajp/47/3/10.1119/1.11855>. (cited on page 23)

25. BIEDERMANN, G., 2008. Gravity tests, differential accelerometry and interleaved clocks with cold atom interferometers. *PhD thesis, Stanford University*, (2008). <http://web.stanford.edu/group/kasevich/cgi-bin/wordpress/wp-content/uploads/2012/09/Gb-thesis.pdf>. (cited on page 115)
26. BILLAM, T. P.; BLACKLEY, C. L.; GERTJERENKEN, B.; CORNISH, S. L.; AND WEISS, C., 2014. Entangling two distinguishable quantum bright solitons via collisions. *Journal of Physics: Conference Series*, 497, 1 (2014), 012033. <http://stacks.iop.org/1742-6596/497/i=1/a=012033>. (cited on page 26)
27. BLOCH, I.; GREINER, M.; MANDEL, O.; HÄNSCH, T. W.; AND ESSLINGER, T., 2001. Sympathetic cooling of ^{85}Rb and ^{87}Rb . *Phys. Rev. A*, 64 (Jul 2001), 021402. doi:10.1103/PhysRevA.64.021402. <http://link.aps.org/doi/10.1103/PhysRevA.64.021402>. (cited on page 67)
28. BONGS, K.; BURGER, S.; BIRKL, G.; SENGSTOCK, K.; ERTMER, W.; RZĄŻEWSKI, K.; SANPERA, A.; AND LEWENSTEIN, M., 1999. Coherent evolution of bouncing Bose-Einstein condensates. *Phys. Rev. Lett.*, 83 (Nov 1999), 3577–3580. doi:10.1103/PhysRevLett.83.3577. <http://link.aps.org/doi/10.1103/PhysRevLett.83.3577>. (cited on page 23)
29. BONGS, K.; BURGER, S.; DETTMER, S.; HELLWEG, D.; ARLT, J.; ERTMER, W.; AND SENGSTOCK, K., 2001. Waveguide for Bose-Einstein condensates. *Phys. Rev. A*, 63 (Feb 2001), 031602. doi:10.1103/PhysRevA.63.031602. <http://link.aps.org/doi/10.1103/PhysRevA.63.031602>. (cited on page 83)
30. BONNIN, A.; ZAHZAM, N.; BIDEL, Y.; AND BRESSON, A., 2013. Simultaneous dual-species matter-wave accelerometer. *Phys. Rev. A*, 88 (Oct 2013), 043615. doi:10.1103/PhysRevA.88.043615. <http://link.aps.org/doi/10.1103/PhysRevA.88.043615>. (cited on page 132)
31. BORDÉ, C., 1989. Atomic interferometry with internal state labelling. *Physics Letters A*, 140, 1–2 (1989), 10 – 12. doi:[http://dx.doi.org/10.1016/0375-9601\(89\)90537-9](http://dx.doi.org/10.1016/0375-9601(89)90537-9). <http://www.sciencedirect.com/science/article/pii/0375960189905379>. (cited on page 99)
32. BOUCHENDIRA, R.; CLADÉ, P.; GUELLATI-KHÉLIFA, S.; NEZ, F.; AND BIRABEN, F., 2011. New determination of the fine structure constant and test of the quantum electrodynamics. *Phys. Rev. Lett.*, 106 (Feb 2011), 080801. doi:10.1103/PhysRevLett.106.080801. <http://link.aps.org/doi/10.1103/PhysRevLett.106.080801>. (cited on pages 4, 52, 97, and 114)
33. BOUCHOULE, I.; TREBBIA, J.-B.; AND GARRIDO ALZAR, C. L., 2008. Limitations of the modulation method to smooth wire-guide roughness. *Phys. Rev. A*, 77 (Feb 2008), 023624. doi:10.1103/PhysRevA.77.023624. <http://link.aps.org/doi/10.1103/PhysRevA.77.023624>. (cited on page 82)

34. BRADLEY, M. P.; PORTO, J. V.; RAINVILLE, S.; THOMPSON, J. K.; AND PRITCHARD, D. E., 1999. Penning trap measurements of the masses of ^{133}Cs , $^{87,85}\text{Rb}$, and ^{23}Na with uncertainties ≤ 0.2 ppb. *Phys. Rev. Lett.*, 83 (Nov 1999), 4510–4513. doi:10.1103/PhysRevLett.83.4510. <http://link.aps.org/doi/10.1103/PhysRevLett.83.4510>. (cited on page 68)
35. BRAJE, D.; DESAVAGE, S.; ADLER, C.; DAVIS, J.; AND NARDUCCI, F., 2014. A frequency selective atom interferometer magnetometer. *Journal of Modern Optics*, 61, 1 (2014), 61–71. doi:10.1080/09500340.2013.850776. <http://dx.doi.org/10.1080/09500340.2013.850776>. (cited on page 3)
36. BURGER, S.; BONGS, K.; DETTMER, S.; ERTMER, W.; SENGSTOCK, K.; SANPERA, A.; SHLYAPNIKOV, G. V.; AND LEWENSTEIN, M., 1999. Dark solitons in Bose-Einstein condensates. *Phys. Rev. Lett.*, 83 (Dec 1999), 5198–5201. doi:10.1103/PhysRevLett.83.5198. <http://link.aps.org/doi/10.1103/PhysRevLett.83.5198>. (cited on page 123)
37. BURKE, J. P., 1999. Theoretical investigation of cold alkali atom collisions. *PhD thesis, University of Colorado*, (1999). https://jila.colorado.edu/sites/default/files/assets/files/publications/burke_thesis.pdf. (cited on page 67)
38. BURKE, J. P. AND BOHN, J. L., 1999. Ultracold scattering properties of the short-lived Rb isotopes. *Phys. Rev. A*, 59 (Feb 1999), 1303–1308. doi:10.1103/PhysRevA.59.1303. <http://link.aps.org/doi/10.1103/PhysRevA.59.1303>. (cited on page 67)
39. CADORET, M.; DE MIRANDES, E.; CLADÉ, P.; GUELLATI-KHÉLIFA, S.; SCHWOB, C.; NEZ, F.; JULIEN, L.; AND BIRABEN, F., 2008. Combination of Bloch oscillations with a Ramsey-Bordé interferometer: New determination of the fine structure constant. *Phys. Rev. Lett.*, 101 (Dec 2008), 230801. doi:10.1103/PhysRevLett.101.230801. <http://link.aps.org/doi/10.1103/PhysRevLett.101.230801>. (cited on pages 52, 97, and 114)
40. CARDOSO, W.; AVELAR, A.; AND BAZEIA, D., 2010. Modulation of breathers in cigar-shaped Bose-Einstein condensates. *Physics Letters A*, 374, 26 (2010), 2640 – 2645. doi:<http://dx.doi.org/10.1016/j.physleta.2010.04.050>. <http://www.sciencedirect.com/science/article/pii/S0375960110004895>. (cited on page 129)
41. CARNAL, O. AND MLYNEK, J., 1991. Young's double-slit experiment with atoms: A simple atom interferometer. *Phys. Rev. Lett.*, 66 (May 1991), 2689–2692. doi:10.1103/PhysRevLett.66.2689. <http://link.aps.org/doi/10.1103/PhysRevLett.66.2689>. (cited on page 4)
42. CARR, L. D. AND CASTIN, Y., 2002. Dynamics of a matter-wave bright soliton in an expulsive potential. *Phys. Rev. A*, 66 (Dec 2002), 063602. doi:10.1103/PhysRevA.66.063602. <http://link.aps.org/doi/10.1103/PhysRevA.66.063602>. (cited on pages 121, 122, and 123)

43. CASSETTARI, D.; HESSMO, B.; FOLMAN, R.; MAIER, T.; AND SCHMIEDMAYER, J., 2000. Beam splitter for guided atoms. *Phys. Rev. Lett.*, 85 (Dec 2000), 5483–5487. doi:10.1103/PhysRevLett.85.5483. <http://link.aps.org/doi/10.1103/PhysRevLett.85.5483>. (cited on page 82)
44. CHABCHOUB, A.; KIMMOUN, O.; BRANGER, H.; HOFFMANN, N.; PROMENT, D.; ONORATO, M.; AND AKHMEDIEV, N., 2013. Experimental observation of dark solitons on the surface of water. *Phys. Rev. Lett.*, 110 (Mar 2013), 124101. doi:10.1103/PhysRevLett.110.124101. <http://link.aps.org/doi/10.1103/PhysRevLett.110.124101>. (cited on page 121)
45. CHARRIÈRE, R.; CADORET, M.; ZAHZAM, N.; BIDEL, Y.; AND BRESSON, A., 2012. Local gravity measurement with the combination of atom interferometry and Bloch oscillations. *Phys. Rev. A*, 85 (Jan 2012), 013639. doi:10.1103/PhysRevA.85.013639. <http://link.aps.org/doi/10.1103/PhysRevA.85.013639>. (cited on pages 97, 99, and 114)
46. CHEINEY, P.; FABRE, C. M.; VERMERSCH, F.; GATTOBIGIO, G. L.; MATHEVET, R.; LAHAYE, T.; AND GUÉRY-ODELIN, D., 2013. Matter-wave scattering on an amplitude-modulated optical lattice. *Phys. Rev. A*, 87 (Jan 2013), 013623. doi:10.1103/PhysRevA.87.013623. <http://link.aps.org/doi/10.1103/PhysRevA.87.013623>. (cited on page 83)
47. CHEN, S. AND EGGER, R., 2003. Destruction of interference by many-body interactions in cold atomic Bose gases. *Phys. Rev. A*, 68 (Dec 2003), 063605. doi:10.1103/PhysRevA.68.063605. <http://link.aps.org/doi/10.1103/PhysRevA.68.063605>. (cited on page 82)
48. CHIN, C.; GRIMM, R.; JULIENNE, P.; AND TIESINGA, E., 2010. Feshbach resonances in ultracold gases. *Rev. Mod. Phys.*, 82 (Apr 2010), 1225–1286. doi:10.1103/RevModPhys.82.1225. <http://link.aps.org/doi/10.1103/RevModPhys.82.1225>. (cited on page 117)
49. CHIOW, S.-w.; KOVACHY, T.; CHIEN, H.-C.; AND KASEVICH, M. A., 2011. $102\hbar k$ large area atom interferometers. *Phys. Rev. Lett.*, 107 (Sep 2011), 130403. doi:10.1103/PhysRevLett.107.130403. <http://link.aps.org/doi/10.1103/PhysRevLett.107.130403>. (cited on pages 97, 109, and 110)
50. CLADÉ, P.; GUELLATI-KHÉLIFA, S.; NEZ, F.; AND BIRABEN, F., 2009. Large momentum beam splitter using Bloch oscillations. *Phys. Rev. Lett.*, 102 (Jun 2009), 240402. doi:10.1103/PhysRevLett.102.240402. <http://link.aps.org/doi/10.1103/PhysRevLett.102.240402>. (cited on pages 97, 99, 109, 110, and 116)
51. CLADÉ, P.; GUELLATI-KHÉLIFA, S.; SCHWOB, C.; NEZ, F.; JULIEN, L.; AND BIRABEN, F., 2005. A promising method for the measurement of the local acceleration of gravity using Bloch oscillations of ultracold atoms in a vertical standing wave. *EPL (Europhysics Letters)*, 71, 5 (2005), 730. <http://stacks.iop.org/0295-5075/71/i=5/a=730>. (cited on page 97)

-
52. CLADÉ, P.; PLISSON, T.; GUELLATI-KHÉLIFA, S.; NEZ, F.; AND BIRABEN, F., 2010. Theoretical analysis of a large momentum beamsplitter using Bloch oscillations. *The European Physical Journal D*, 59, 3 (2010), 349–360. doi:10.1140/epjd/e2010-00198-0. <http://dx.doi.org/10.1140/epjd/e2010-00198-0>. (cited on pages 35 and 97)
53. CLÉMENT, J.-F.; BRANTUT, J.-P.; ROBERT-DE SAINT-VINCENT, M.; NYMAN, R. A.; ASPECT, A.; BOURDEL, T.; AND BOUYER, P., 2009. All-optical runaway evaporation to Bose-Einstein condensation. *Phys. Rev. A*, 79 (Jun 2009), 061406. doi:10.1103/PhysRevA.79.061406. <http://link.aps.org/doi/10.1103/PhysRevA.79.061406>. (cited on page 83)
54. COLLETT, M. J. AND TEE, G. J., 2014. Ellipse fitting for interferometry. Part 1: static methods. *J. Opt. Soc. Am. A*, 31, 12 (Dec 2014), 2573–2583. doi:10.1364/JOSAA.31.002573. <http://josaa.osa.org/abstract.cfm?URI=josaa-31-12-2573>. (cited on page 136)
55. COLOMBE, Y.; MERCIER, B.; PERRIN, H.; AND LORENT, V., 2005. Diffraction of a Bose-Einstein condensate in the time domain. *Phys. Rev. A*, 72 (Dec 2005), 061601. doi:10.1103/PhysRevA.72.061601. <http://link.aps.org/doi/10.1103/PhysRevA.72.061601>. (cited on page 23)
56. CURNISH, S. L.; CLAUSSEN, N. R.; ROBERTS, J. L.; CORNELL, E. A.; AND WIEMAN, C. E., 2000. Stable ^{85}Rb Bose-Einstein condensates with widely tunable interactions. *Phys. Rev. Lett.*, 85 (Aug 2000), 1795–1798. doi:10.1103/PhysRevLett.85.1795. <http://link.aps.org/doi/10.1103/PhysRevLett.85.1795>. (cited on page 67)
57. CURNISH, S. L.; THOMPSON, S. T.; AND WIEMAN, C. E., 2006. Formation of bright matter-wave solitons during the collapse of attractive Bose-Einstein condensates. *Phys. Rev. Lett.*, 96 (May 2006), 170401. doi:10.1103/PhysRevLett.96.170401. <http://link.aps.org/doi/10.1103/PhysRevLett.96.170401>. (cited on page 123)
58. CRONIN, A. D.; SCHMIEDMAYER, J.; AND PRITCHARD, D. E., 2009. Optics and interferometry with atoms and molecules. *Rev. Mod. Phys.*, 81 (Jul 2009), 1051–1129. doi:10.1103/RevModPhys.81.1051. <http://link.aps.org/doi/10.1103/RevModPhys.81.1051>. (cited on page 1)
59. CUEVAS, J.; KEVREKIDIS, P. G.; MALOMED, B. A.; DYKE, P.; AND HULET, R. G., 2013. Interactions of solitons with a gaussian barrier: splitting and recombination in quasi-one-dimensional and three-dimensional settings. *New Journal of Physics*, 15, 6 (2013), 063006. <http://stacks.iop.org/1367-2630/15/i=6/a=063006>. (cited on page 123)
60. DALIBARD, J. AND COHEN-TANNOUDJI, C., 1989. Laser cooling below the Doppler limit by polarization gradients: simple theoretical models. *J. Opt. Soc. Am. B*, 6, 11 (Nov 1989), 2023–2045. doi:10.1364/JOSAB.6.002023. <http://josab.osa.org/abstract.cfm?URI=josab-6-11-2023>. (cited on page 72)

61. DALL, R. G.; HODGMAN, S. S.; JOHNSSON, M. T.; BALDWIN, K. G. H.; AND TRUSCOTT, A. G., 2010. Transverse mode imaging of guided matter waves. *Phys. Rev. A*, 81 (Jan 2010), 011602. doi:10.1103/PhysRevA.81.011602. <http://link.aps.org/doi/10.1103/PhysRevA.81.011602>. (cited on page 83)
62. DEBS, J. E., 2012. The application of Bose-Einstein condensates to inertial sensing. *PhD thesis, Australian National University*, (2012). http://atomlaser.anu.edu.au/publications/jed_thesis.pdf. (cited on pages 8 and 28)
63. DEBS, J. E.; ALTIN, P. A.; BARTER, T. H.; DÖRING, D.; DENNIS, G. R.; McDONALD, G.; ANDERSON, R. P.; CLOSE, J. D.; AND ROBINS, N. P., 2011. Cold-atom gravimetry with a Bose-Einstein condensate. *Phys. Rev. A*, 84 (Sep 2011), 033610. doi:10.1103/PhysRevA.84.033610. <http://link.aps.org/doi/10.1103/PhysRevA.84.033610>. (cited on pages 45, 83, 88, 97, 99, 101, 110, and 116)
64. DELLA VALLE, G.; SAVOINI, M.; ORNIGOTTI, M.; LAPORTA, P.; FOGLIETTI, V.; FINAZZI, M.; DUÒ, L.; AND LONGHI, S., 2009. Experimental observation of a photon bouncing ball. *Phys. Rev. Lett.*, 102 (May 2009), 180402. doi:10.1103/PhysRevLett.102.180402. <http://link.aps.org/doi/10.1103/PhysRevLett.102.180402>. (cited on page 23)
65. DENSCHLAG, J.; CASSETTARI, D.; CHENET, A.; SCHNEIDER, S.; AND SCHMIEDMAYER, J., 1999. A neutral atom and a wire: towards mesoscopic atom optics. *Applied Physics B: Lasers and Optics*, 69 (1999), 291–301. <http://dx.doi.org/10.1007/s003400050809>. 10.1007/s003400050809. (cited on page 82)
66. DENSCHLAG, J.; SIMSARIAN, J. E.; FEDER, D. L.; CLARK, C. W.; COLLINS, L. A.; CUBIZOLLES, J.; DENG, L.; HAGLEY, E. W.; HELMERSON, K.; REINHARDT, W. P.; ROLSTON, S. L.; SCHNEIDER, B. I.; AND PHILLIPS, W. D., 2000. Generating solitons by phase engineering of a Bose-Einstein condensate. *Science*, 287, 5450 (2000), 97–101. doi:10.1126/science.287.5450.97. <http://www.sciencemag.org/content/287/5450/97.abstract>. (cited on page 123)
67. DENSCHLAG, J. H.; SIMSARIAN, J. E.; HÄFFNER, H.; MCKENZIE, C.; BROWAEYS, A.; CHO, D.; HELMERSON, K.; ROLSTON, S. L.; AND PHILLIPS, W. D., 2002. A Bose-Einstein condensate in an optical lattice. *Journal of Physics B: Atomic, Molecular and Optical Physics*, 35, 14 (2002), 3095. <http://stacks.iop.org/0953-4075/35/i=14/a=307>. (cited on page 37)
68. DIMOPOULOS, S. AND GERACI, A. A., 2003. Probing submicron forces by interferometry of Bose-Einstein condensed atoms. *Phys. Rev. D*, 68 (Dec 2003), 124021. doi:10.1103/PhysRevD.68.124021. <http://link.aps.org/doi/10.1103/PhysRevD.68.124021>. (cited on page 123)
69. DIMOPOULOS, S.; GRAHAM, P. W.; HOGAN, J. M.; AND KASEVICH, M. A., 2007. Testing general relativity with atom interferometry. *Phys. Rev. Lett.*, 98 (Mar 2007), 111102. doi:10.1103/PhysRevLett.98.111102. <http://link.aps.org/doi/10.1103/PhysRevLett.98.111102>. (cited on page 132)

70. DOMEN, K. F. E. M.; JANSEN, M. A. H. M.; VAN DIJK, W.; AND VAN LEEUWEN, K. A. H., 2009. Atomic quasi-Bragg-diffraction in a magnetic field. *Phys. Rev. A*, 79 (Apr 2009), 043605. doi:10.1103/PhysRevA.79.043605. <http://link.aps.org/doi/10.1103/PhysRevA.79.043605>. (cited on page 98)
71. DONLEY, E. A.; CLAUSSEN, N. R.; CORNISH, S. L.; ROBERTS, J. L.; CORNELL, E. A.; AND WIEMAN, C. E., 2001. Dynamics of collapsing and exploding Bose-Einstein condensates. *Nature*, 412, 6844 (07 2001), 295–299. (cited on page 118)
72. DÖRING, D.; McDONALD, G.; DEBS, J. E.; FIGL, C.; ALTIN, P. A.; BACHOR, H.-A.; ROBINS, N. P.; AND CLOSE, J. D., 2010. Quantum-projection-noise-limited interferometry with coherent atoms in a Ramsey-type setup. *Phys. Rev. A*, 81 (Apr 2010), 043633. doi:10.1103/PhysRevA.81.043633. <http://link.aps.org/doi/10.1103/PhysRevA.81.043633>. (cited on page 115)
73. DUMKE, R.; MÜTHER, T.; VOLK, M.; ERTMER, W.; AND BIRKL, G., 2002. Interferometer-type structures for guided atoms. *Phys. Rev. Lett.*, 89 (Nov 2002), 220402. doi:10.1103/PhysRevLett.89.220402. <http://link.aps.org/doi/10.1103/PhysRevLett.89.220402>. (cited on page 83)
74. DUNJKO, V. AND OLSHANII, M., 2015. Superheated integrability and multisoliton survival through scattering off barriers. *arXiv:1501.00075*, (Dec. 2015). <http://arxiv.org/abs/1501.00075>. (cited on page 146)
75. EGOROV, M.; OPANCHUK, B.; DRUMMOND, P.; HALL, B. V.; HANNAFORD, P.; AND SIDOROV, A. I., 2013. Measurement of *s*-wave scattering lengths in a two-component Bose-Einstein condensate. *Phys. Rev. A*, 87 (May 2013), 053614. doi:10.1103/PhysRevA.87.053614. <http://link.aps.org/doi/10.1103/PhysRevA.87.053614>. (cited on page 67)
76. EMPLIT, P.; HAMAIDE, J.; REYNAUD, F.; FROEHLY, C.; AND BARTHELEMY, A., 1987. Picosecond steps and dark pulses through nonlinear single mode fibers. *Optics Communications*, 62, 6 (1987), 374 – 379. doi:[http://dx.doi.org/10.1016/0030-4018\(87\)90003-4](http://dx.doi.org/10.1016/0030-4018(87)90003-4). <http://www.sciencedirect.com/science/article/pii/0030401887900034>. (cited on page 121)
77. ESTEVE, J.; GROSS, C.; WELLER, A.; GIOVANAZZI, S.; AND OBERTHALER, M. K., 2008. Squeezing and entanglement in a Bose-Einstein condensate. *Nature*, 455, 7217 (10 2008), 1216–1219. <http://dx.doi.org/10.1038/nature07332>. (cited on pages 5, 115, and 129)
78. EVERITT, P. J., 2014. Matter wave meta-materials. *Honours thesis, Australian National University*, (2014). (cited on pages 115 and 145)
79. FABRE, C. M.; CHEINEY, P.; GATTOBIGIO, G. L.; VERMERSCH, F.; FAURE, S.; MATHEVET, R.; LAHAYE, T.; AND GUÉRY-ODELIN, D., 2011. Realization of a distributed Bragg reflector for propagating guided matter waves. *Phys. Rev. Lett.*, 107 (Nov 2011), 213901. doi:10.1103/PhysRevLett.107.213901. <http://link.aps.org/doi/10.1103/PhysRevLett.107.213901>. (cited on page 115)

- 2011), 230401. doi:10.1103/PhysRevLett.107.230401. <http://link.aps.org/doi/10.1103/PhysRevLett.107.230401>. (cited on page 83)
80. FARKAS, D. M.; HUDEK, K. M.; SALIM, E. A.; SEGAL, S. R.; SQUIRES, M. B.; AND ANDERSON, D. Z., 2010. A compact, transportable, microchip-based system for high repetition rate production of Bose–Einstein condensates. *Applied Physics Letters*, 96, 9 (2010), 093102. doi:10.1063/1.3327812. <http://link.aip.org/link/?APL/96/093102/1>. (cited on page 82)
81. FATTORI, M.; D'ERRICO, C.; ROATI, G.; ZACCANTI, M.; JONA-LASINIO, M.; MODUGNO, M.; INGUSCIO, M.; AND MODUGNO, G., 2008. Atom interferometry with a weakly interacting Bose-Einstein condensate. *Phys. Rev. Lett.*, 100 (Feb 2008), 080405. doi:10.1103/PhysRevLett.100.080405. <http://link.aps.org/doi/10.1103/PhysRevLett.100.080405>. (cited on page 117)
82. FERRARI, G.; POLI, N.; SORRENTINO, F.; AND TINO, G. M., 2006. Long-lived Bloch oscillations with bosonic Sr atoms and application to gravity measurement at the micrometer scale. *Phys. Rev. Lett.*, 97 (Aug 2006), 060402. doi:10.1103/PhysRevLett.97.060402. <http://link.aps.org/doi/10.1103/PhysRevLett.97.060402>. (cited on pages 97 and 114)
83. FIORENTINO, M.; SHARPING, J. E.; KUMAR, P.; LEVANDOVSKY, D.; AND VASILYEV, M., 2001. Soliton squeezing in a Mach-Zehnder fiber interferometer. *Phys. Rev. A*, 64 (Aug 2001), 031801. doi:10.1103/PhysRevA.64.031801. <http://link.aps.org/doi/10.1103/PhysRevA.64.031801>. (cited on pages 120 and 126)
84. FITZGIBBON, M., A. W. AND PILU AND FISHER, R. B., 1999. Direct least-squares fitting of ellipses. *IEEE Transactions on Pattern Analysis and Machine Intelligence*, 21, 5 (May 1999), 476–480. <http://research.microsoft.com/en-us/um/people/awf/ellipse/>. (cited on page 136)
85. FOOT, C., 2005. *Atomic physics*. Oxford master series in physics. Oxford University Press. ISBN 9780198506966. <http://books.google.com.au/books?id=kXYpAQAAQAAJ>. (cited on page 42)
86. FORTÁGH, J.; OTT, H.; KRAFT, S.; GÜNTHER, A.; AND ZIMMERMANN, C., 2002. Surface effects in magnetic microtraps. *Phys. Rev. A*, 66 (Oct 2002), 041604. doi:10.1103/PhysRevA.66.041604. <http://link.aps.org/doi/10.1103/PhysRevA.66.041604>. (cited on page 82)
87. FORTÁGH, J. AND ZIMMERMANN, C., 2007. Magnetic microtraps for ultracold atoms. *Rev. Mod. Phys.*, 79 (Feb 2007), 235–289. doi:10.1103/RevModPhys.79.235. <http://link.aps.org/doi/10.1103/RevModPhys.79.235>. (cited on page 82)
88. FRANTZESKAKIS, D. J., 2010. Dark solitons in atomic Bose-Einstein condensates: from theory to experiments. *Journal of Physics A: Mathematical and Theoretical*, 43, 21 (2010), 213001. <http://stacks.iop.org/1751-8121/43/i=21/a=213001>. (cited on pages 121 and 123)

89. FRAY, S.; DIEZ, C. A.; HÄNSCH, T. W.; AND WEITZ, M., 2004. Atomic interferometer with amplitude gratings of light and its applications to atom based tests of the equivalence principle. *Phys. Rev. Lett.*, 93 (Dec 2004), 240404. doi:10.1103/PhysRevLett.93.240404. <http://link.aps.org/doi/10.1103/PhysRevLett.93.240404>. (cited on page 132)
90. GARCIA, O.; DEISSLER, B.; HUGHES, K. J.; REEVES, J. M.; AND SACKETT, C. A., 2006. Bose-Einstein-condensate interferometer with macroscopic arm separation. *Phys. Rev. A*, 74 (Sep 2006), 031601. doi:10.1103/PhysRevA.74.031601. <http://link.aps.org/doi/10.1103/PhysRevA.74.031601>. (cited on page 82)
91. GATTOBIGIO, G. L.; COUVERT, A.; JEPPESEN, M.; MATHEVET, R.; AND GUÉRYODELIN, D., 2009. Multimode-to-monomode guided-atom lasers: An entropic analysis. *Phys. Rev. A*, 80 (Oct 2009), 041605. doi:10.1103/PhysRevA.80.041605. <http://link.aps.org/doi/10.1103/PhysRevA.80.041605>. (cited on page 83)
92. GATTOBIGIO, G. L.; COUVERT, A.; REINAUDI, G.; GEORGEOT, B.; AND GUÉRYODELIN, D., 2012. Optically guided beam splitter for propagating matter waves. *Phys. Rev. Lett.*, 109 (Jul 2012), 030403. doi:10.1103/PhysRevLett.109.030403. <http://link.aps.org/doi/10.1103/PhysRevLett.109.030403>. (cited on page 83)
93. GEA-BANACLOCHE, J., 1999. A quantum bouncing ball. *American Journal of Physics*, 67, 9 (1999), 776–782. doi:<http://dx.doi.org/10.1119/1.19124>. <http://scitation.aip.org/content/aapt/journal/ajp/67/9/10.1119/1.19124>. (cited on page 24)
94. GERTJERENKEN, B., 2013. Bright-soliton quantum superpositions: Signatures of high- and low-fidelity states. *Phys. Rev. A*, 88 (Nov 2013), 053623. doi:10.1103/PhysRevA.88.053623. <http://link.aps.org/doi/10.1103/PhysRevA.88.053623>. (cited on pages 26, 126, and 129)
95. GERTJERENKEN, B.; BILLAM, T. P.; BLACKLEY, C. L.; LE SUEUR, C. R.; KHAYKOVICH, L.; CORNISH, S. L.; AND WEISS, C., 2013. Generating mesoscopic Bell states via collisions of distinguishable quantum bright solitons. *Phys. Rev. Lett.*, 111 (Sep 2013), 100406. doi:10.1103/PhysRevLett.111.100406. <http://link.aps.org/doi/10.1103/PhysRevLett.111.100406>. (cited on page 123)
96. GIBBS, R. L., 1975. The quantum bouncer. *American Journal of Physics*, 43, 1 (1975), 25–28. doi:<http://dx.doi.org/10.1119/1.10024>. <http://scitation.aip.org/content/aapt/journal/ajp/43/1/10.1119/1.10024>. (cited on page 23)
97. GIESE, E.; ROURA, A.; TACKMANN, G.; RASEL, E. M.; AND SCHLEICH, W. P., 2013. Double Bragg diffraction: A tool for atom optics. *Phys. Rev. A*, 88 (Nov 2013), 053608. doi:10.1103/PhysRevA.88.053608. <http://link.aps.org/doi/10.1103/PhysRevA.88.053608>. (cited on page 98)
98. GILTNER, D. M.; McGOWAN, R. W.; AND LEE, S. A., 1995. Atom interferometer based on Bragg scattering from standing light waves. *Phys. Rev. Lett.*, 75 (Oct

- 1995), 2638–2641. doi:10.1103/PhysRevLett.75.2638. <http://link.aps.org/doi/10.1103/PhysRevLett.75.2638>. (cited on page 97)
99. GÖKLÜ, E. AND LÄMMERZAH, C., 2008. Metric fluctuations and the weak equivalence principle. *Classical and Quantum Gravity*, 25, 10 (2008), 105012. <http://stacks.iop.org/0264-9381/25/i=10/a=105012>. (cited on page 131)
100. GRAHAM, P. W.; HOGAN, J. M.; KASEVICH, M. A.; AND RAJENDRAN, S., 2013. New method for gravitational wave detection with atomic sensors. *Phys. Rev. Lett.*, 110 (Apr 2013), 171102. doi:10.1103/PhysRevLett.110.171102. <http://link.aps.org/doi/10.1103/PhysRevLett.110.171102>. (cited on page 4)
101. GREENBERGER, D. M., 1983. The neutron interferometer as a device for illustrating the strange behavior of quantum systems. *Rev. Mod. Phys.*, 55 (Oct 1983), 875–905. doi:10.1103/RevModPhys.55.875. <http://link.aps.org/doi/10.1103/RevModPhys.55.875>. (cited on page 1)
102. GREENBERGER, D. M.; SCHLEICH, W. P.; AND RASEL, E. M., 2012. Relativistic effects in atom and neutron interferometry and the differences between them. *Phys. Rev. A*, 86 (Dec 2012), 063622. doi:10.1103/PhysRevA.86.063622. <http://link.aps.org/doi/10.1103/PhysRevA.86.063622>. (cited on page 1)
103. GREENE, G. L., 2011. Ultracold neutrons: Quantum bouncing ball resonates. *Nat Phys*, 7, 6 (06 2011), 447–448. <http://dx.doi.org/10.1038/nphys1990>. (cited on page 23)
104. GREINER, M., 2003. Ultracold quantum gases in three-dimensional lattice potentials. *PhD thesis, Ludwig Maximilians Universitaet München, Germany*, (2003). http://greiner.physics.harvard.edu/PDFFiles/PhD_greiner.pdf. (cited on pages 35 and 36)
105. GUERIN, W.; RIOU, J.-F.; GAEBLER, J. P.; JOSSE, V.; BOUYER, P.; AND ASPECT, A., 2006. Guided quasicontinuous atom laser. *Phys. Rev. Lett.*, 97 (Nov 2006), 200402. doi:10.1103/PhysRevLett.97.200402. <http://link.aps.org/doi/10.1103/PhysRevLett.97.200402>. (cited on page 83)
106. GUPTA, S.; DIECKMANN, K.; HADZIBABIC, Z.; AND PRITCHARD, D. E., 2002. Contrast interferometry using Bose-Einstein condensates to measure h/m and α . *Phys. Rev. Lett.*, 89 (Sep 2002), 140401. doi:10.1103/PhysRevLett.89.140401. <http://link.aps.org/doi/10.1103/PhysRevLett.89.140401>. (cited on pages 66 and 98)
107. GUSTAVSON, T. L.; LANDRAGIN, A.; AND KASEVICH, M. A., 2000. Rotation sensing with a dual atom-interferometer Sagnac gyroscope. *Classical and Quantum Gravity*, 17, 12 (2000), 2385. <http://stacks.iop.org/0264-9381/17/i=12/a=311>. (cited on page 4)
108. GUSTAVSSON, M.; HALLER, E.; MARK, M. J.; DANZL, J. G.; ROJAS-KOPEINIG, G.; AND NÄGERL, H.-C., 2008. Control of interaction-induced dephasing of Bloch

- oscillations. *Phys. Rev. Lett.*, 100 (Feb 2008), 080404. doi:10.1103/PhysRevLett.100.080404. <http://link.aps.org/doi/10.1103/PhysRevLett.100.080404>. (cited on page 117)
109. GUTTERRES, R. F.; AMIOT, C.; FIORETTI, A.; GABBANINI, C.; MAZZONI, M.; AND DULIEU, O., 2002. Determination of the ^{87}Rb 5p state dipole matrix element and radiative lifetime from the photoassociation spectroscopy of the Rb_2 0 $_g^-$ (P $_{3/2}$) long-range state. *Phys. Rev. A*, 66 (Aug 2002), 024502. doi:10.1103/PhysRevA.66.024502. <http://link.aps.org/doi/10.1103/PhysRevA.66.024502>. (cited on page 68)
110. HAINES, S. A. AND JOHNSSON, M. T., 2009. Dynamic scheme for generating number squeezing in Bose-Einstein condensates through nonlinear interactions. *Phys. Rev. A*, 80 (Aug 2009), 023611. doi:10.1103/PhysRevA.80.023611. <http://link.aps.org/doi/10.1103/PhysRevA.80.023611>. (cited on pages 115 and 129)
111. HALL, M. J. W.; REGINATTO, M.; AND SAVAGE, C. M., 2012. Nonlocal signaling in the configuration space model of quantum-classical interactions. *Phys. Rev. A*, 86 (Nov 2012), 054101. doi:10.1103/PhysRevA.86.054101. <http://link.aps.org/doi/10.1103/PhysRevA.86.054101>. (cited on page 131)
112. HAMILTON, P.; BARTER, T.; KIM, G.; MUKHERJEE, B.; AND MÜLLER, H., 2012. Progress towards a test of the universality of free fall using a ^6Li - ^7Li atom interferometer. In *Bull. Am. Phys. Soc.*, vol. 57, T5.00004. (cited on page 132)
113. HÄNSEL, W.; HOMMELHOFF, T.; HÄNSCH, T.; AND REICHEL, J., 2001. Bose-Einstein condensation on a microelectronic chip. *Nature*, 413 (Oct 2001), 498. doi:10.1038/35097032. <http://www.nature.com/nature/journal/v413/n6855/abs/413498a0.html>. (cited on page 82)
114. HARDMAN, K. S.; KUHN, C. C. N.; McDONALD, G. D.; DEBS, J. E.; BENNETTS, S.; CLOSE, J. D.; AND ROBINS, N. P., 2014. Role of source coherence in atom interferometry. *Phys. Rev. A*, 89 (Feb 2014), 023626. doi:10.1103/PhysRevA.89.023626. <http://link.aps.org/doi/10.1103/PhysRevA.89.023626>. (cited on pages 7, 8, and 127)
115. HASLINGER, P.; DORRE, N.; GEYER, P.; RODEWALD, J.; NIMMRICHTER, S.; AND ARNDT, M., 2013. A universal matter-wave interferometer with optical ionization gratings in the time domain. *Nat Phys*, 9, 3 (03 2013), 144–148. <http://dx.doi.org/10.1038/nphys2542>. (cited on pages 1 and 96)
116. HASSELBACH, F., 2010. Progress in electron- and ion-interferometry. *Reports on Progress in Physics*, 73, 1 (2010), 016101. <http://stacks.iop.org/0034-4885/73/i=1/a=016101>. (cited on page 1)
117. HEIMBURG, T. AND JACKSON, A. D., 2005. On soliton propagation in biomembranes and nerves. *Proceedings of the National Academy of Sciences of the United*

- States of America*, 102, 28 (2005), 9790–9795. doi:10.1073/pnas.0503823102. <http://www.pnas.org/content/102/28/9790.abstract>. (cited on page 121)
118. HINDS, E. A.; VALE, C. J.; AND BOSHIER, M. G., 2001. Two-wire waveguide and interferometer for cold atoms. *Phys. Rev. Lett.*, 86 (Feb 2001), 1462–1465. doi:10.1103/PhysRevLett.86.1462. <http://link.aps.org/doi/10.1103/PhysRevLett.86.1462>. (cited on page 82)
119. HOHENSEE, M. A. AND MÜLLER, H., 2011. Precision tests of general relativity with matter waves. *Journal of Modern Optics*, 58, 21 (2011), 2021–2027. doi:10.1080/09500340.2011.606376. <http://dx.doi.org/10.1080/09500340.2011.606376>. (cited on page 132)
120. HORIKOSHI, M. AND NAKAGAWA, K., 2006. Atom chip based fast production of Bose-Einstein condensate. *Applied Physics B*, 82 (2006), 363–366. doi:10.1007/s00340-005-2083-z. <http://dx.doi.org/10.1007/s00340-005-2083-z>. (cited on page 82)
121. HORIKOSHI, M. AND NAKAGAWA, K., 2006. Dephasing due to atom-atom interaction in a waveguide interferometer using a Bose-Einstein condensate. *Phys. Rev. A*, 74 (Sep 2006), 031602. doi:10.1103/PhysRevA.74.031602. <http://link.aps.org/doi/10.1103/PhysRevA.74.031602>. (cited on page 82)
122. HOSKINSON, E.; SATO, Y.; AND PACKARD, R., 2006. Superfluid ^4He interferometer operating near 2 K. *Phys. Rev. B*, 74 (Sep 2006), 100509. doi:10.1103/PhysRevB.74.100509. <http://link.aps.org/doi/10.1103/PhysRevB.74.100509>. (cited on page 1)
123. HOUDE, O.; KADIO, D.; AND PRUVOST, L., 2000. Cold atom beam splitter realized with two crossing dipole guides. *Phys. Rev. Lett.*, 85 (Dec 2000), 5543–5546. doi:10.1103/PhysRevLett.85.5543. <http://link.aps.org/doi/10.1103/PhysRevLett.85.5543>. (cited on page 83)
124. HU, Z.-K.; SUN, B.-L.; DUAN, X.-C.; ZHOU, M.-K.; CHEN, L.-L.; ZHAN, S.; ZHANG, Q.-Z.; AND LUO, J., 2013. Demonstration of an ultrahigh-sensitivity atom-interferometry absolute gravimeter. *Phys. Rev. A*, 88 (Oct 2013), 043610. doi:10.1103/PhysRevA.88.043610. <http://link.aps.org/doi/10.1103/PhysRevA.88.043610>. (cited on pages 3 and 4)
125. HUET, L.; AMMAR, M.; MORVAN, E.; SARAZIN, N.; POCHOLLE, J.-P.; REICHEL, J.; GUERLIN, C.; AND SCHWARTZ, S., 2012. Experimental investigation of transparent silicon carbide for atom chips. *Applied Physics Letters*, 100, 12 (2012), 121114. doi:10.1063/1.3689777. <http://link.aip.org/link/?APL/100/121114/1>. (cited on page 82)
126. JACKSON, C. R., 2004. *An atlas of internal solitary-like waves and their properties*. Office of Naval Research, 2nd edn. (cited on page 121)

-
127. JENKE, T.; GELTENBORT, P.; LEMMEL, H.; AND ABELE, H., 2011. Realization of a gravity-resonance-spectroscopy technique. *Nat Phys*, 7, 6 (06 2011), 468–472. <http://dx.doi.org/10.1038/nphys1970>. (cited on page 23)
128. JO, G.-B.; SHIN, Y.; WILL, S.; PASQUINI, T. A.; SABA, M.; KETTERLE, W.; PRITCHARD, D. E.; VENGALATTORE, M.; AND PRENTISS, M., 2007. Long phase coherence time and number squeezing of two Bose-Einstein condensates on an atom chip. *Phys. Rev. Lett.*, 98 (Jan 2007), 030407. doi:10.1103/PhysRevLett.98.030407. <http://link.aps.org/doi/10.1103/PhysRevLett.98.030407>. (cited on page 82)
129. JOHNSSON, M. T. AND HAINE, S. A., 2007. Generating quadrature squeezing in an atom laser through self-interaction. *Phys. Rev. Lett.*, 99 (Jul 2007), 010401. doi:10.1103/PhysRevLett.99.010401. <http://link.aps.org/doi/10.1103/PhysRevLett.99.010401>. (cited on pages 115 and 129)
130. JONES, M. P. A.; VALE, C. J.; SAHAGUN, D.; HALL, B. V.; AND HINDS, E. A., 2003. Spin coupling between cold atoms and the thermal fluctuations of a metal surface. *Phys. Rev. Lett.*, 91 (Aug 2003), 080401. doi:10.1103/PhysRevLett.91.080401. <http://link.aps.org/doi/10.1103/PhysRevLett.91.080401>. (cited on page 82)
131. JOSHI, A. AND PACKARD, R., 2013. A continuously operating, flux locked, superfluid interferometer. *Journal of Low Temperature Physics*, 172, 1-2 (2013), 162–174. doi:10.1007/s10909-013-0857-y. <http://dx.doi.org/10.1007/s10909-013-0857-y>. (cited on page 1)
132. KAFLE, R. P.; ANDERSON, D. Z.; AND ZOZULYA, A. A., 2011. Analysis of a free oscillation atom interferometer. *Phys. Rev. A*, 84 (Sep 2011), 033639. doi:10.1103/PhysRevA.84.033639. <http://link.aps.org/doi/10.1103/PhysRevA.84.033639>. (cited on page 82)
133. KARTASHOV, Y. V.; MALOMED, B. A.; AND TORNER, L., 2011. Solitons in nonlinear lattices. *Rev. Mod. Phys.*, 83 (Apr 2011), 247–305. doi:10.1103/RevModPhys.83.247. <http://link.aps.org/doi/10.1103/RevModPhys.83.247>. (cited on page 120)
134. KASEVICH, M. AND CHU, S., 1991. Atomic interferometry using stimulated raman transitions. *Phys. Rev. Lett.*, 67 (Jul 1991), 181–184. doi:10.1103/PhysRevLett.67.181. <http://link.aps.org/doi/10.1103/PhysRevLett.67.181>. (cited on page 4)
135. KEAL, H., 2012. Atom interferometry in an optical waveguide. *Honours thesis, Australian National University*, (2012). (cited on page 83)
136. KEITH, D. W.; EKSTROM, C. R.; TURCHETTE, Q. A.; AND PRITCHARD, D. E., 1991. An interferometer for atoms. *Phys. Rev. Lett.*, 66 (May 1991), 2693–2696. doi:10.1103/PhysRevLett.66.2693. <http://link.aps.org/doi/10.1103/PhysRevLett.66.2693>. (cited on pages 1, 4, and 99)

137. KEY, M.; HUGHES, I. G.; ROOIJAKKERS, W.; SAUER, B. E.; HINDS, E. A.; RICHARDSON, D. J.; AND KAZANSKY, P. G., 2000. Propagation of cold atoms along a miniature magnetic guide. *Phys. Rev. Lett.*, 84 (Feb 2000), 1371–1373. doi:10.1103/PhysRevLett.84.1371. <http://link.aps.org/doi/10.1103/PhysRevLett.84.1371>. (cited on page 82)
138. KHAYKOVICH, L.; SCHRECK, F.; FERRARI, G.; BOURDEL, T.; CUBIZOLLES, J.; CARR, L. D.; CASTIN, Y.; AND SALOMON, C., 2002. Formation of a matter-wave bright soliton. *Science*, 296, 5571 (2002), 1290–1293. doi:10.1126/science.1071021. <http://www.sciencemag.org/content/296/5571/1290.abstract>. (cited on pages 122 and 123)
139. KIEFER, C., 2012. *Quantum Gravity, 3rd Edition*. Oxford University Press. (cited on page 131)
140. KIVSHAR, Y. AND AGRAWAL, G., 2003. *Optical Solitons: From Fibers to Photonic Crystals*. Elsevier Science. ISBN 9780080538099. <http://books.google.com.au/books?id=zzWgibj4ypsC>. (cited on page 121)
141. KIVSHAR, Y. S. AND MALOMED, B. A., 1989. Dynamics of solitons in nearly integrable systems. *Rev. Mod. Phys.*, 61 (Oct 1989), 763–915. doi:10.1103/RevModPhys.61.763. <http://link.aps.org/doi/10.1103/RevModPhys.61.763>. (cited on page 120)
142. KLEPP, J.; SPONAR, S.; AND HASEGAWA, Y., 2014. Fundamental phenomena of quantum mechanics explored with neutron interferometers. *Progress of Theoretical and Experimental Physics*, 2014, 8 (2014). doi:10.1093/ptep/ptu085. <http://ptep.oxfordjournals.org/content/2014/8/082A01.abstract>. (cited on page 1)
143. KOSEVICH, A.; GANN, V.; ZHUKOV, A.; AND VORONOV, V., 1998. Magnetic soliton motion in a nonuniform magnetic field. *Journal of Experimental and Theoretical Physics*, 87, 2 (1998), 401–407. doi:10.1134/1.558674. <http://dx.doi.org/10.1134/1.558674>. (cited on page 121)
144. KOVACHY, T.; CHIOW, S.-w.; AND KASEVICH, M. A., 2012. Adiabatic-rapid-passage multiphoton bragg atom optics. *Phys. Rev. A*, 86 (Jul 2012), 011606. doi:10.1103/PhysRevA.86.011606. <http://link.aps.org/doi/10.1103/PhysRevA.86.011606>. (cited on pages 97 and 110)
145. KOVACHY, T.; HOGAN, J. M.; JOHNSON, D. M. S.; AND KASEVICH, M. A., 2010. Optical lattices as waveguides and beam splitters for atom interferometry: An analytical treatment and proposal of applications. *Phys. Rev. A*, 82 (Jul 2010), 013638. doi:10.1103/PhysRevA.82.013638. <http://link.aps.org/doi/10.1103/PhysRevA.82.013638>. (cited on pages 37 and 46)
146. KOVACHY, T.; HOGAN, J. M.; SUGARBAKER, A.; DICKERSON, S. M.; DONNELLY, C. A.; OVERSTREET, C.; AND KASEVICH, M. A., 2015. Matter wave lensing to picokelvin

- temperatures. *Phys. Rev. Lett.*, 114 (Apr 2015), 143004. doi:10.1103/PhysRevLett.114.143004. <http://link.aps.org/doi/10.1103/PhysRevLett.114.143004>. (cited on page 101)
147. KREUTZMANN, H.; POULSEN, U. V.; LEWENSTEIN, M.; DUMKE, R.; ERTMER, W.; BIRKL, G.; AND SANPERA, A., 2004. Coherence properties of guided-atom interferometers. *Phys. Rev. Lett.*, 92 (Apr 2004), 163201. doi:10.1103/PhysRevLett.92.163201. <http://link.aps.org/doi/10.1103/PhysRevLett.92.163201>. (cited on page 82)
148. KUHN, C. C. N.; GUAN, X. W.; FOERSTER, A.; AND BATCHELOR, M. T., 2012. Quantum criticality of spin-1 bosons in a one-dimensional harmonic trap. *Phys. Rev. A*, 86 (Jul 2012), 011605. doi:10.1103/PhysRevA.86.011605. <http://link.aps.org/doi/10.1103/PhysRevA.86.011605>. (cited on page 115)
149. KUHN, C. C. N.; GUAN, X. W.; FOERSTER, A.; AND BATCHELOR, M. T., 2012. Universality class of quantum criticality for strongly repulsive spin-1 bosons with antiferromagnetic spin-exchange interaction. *Phys. Rev. A*, 85 (Apr 2012), 043606. doi:10.1103/PhysRevA.85.043606. <http://link.aps.org/doi/10.1103/PhysRevA.85.043606>. (cited on page 115)
150. LAN, S.-Y.; KUAN, P.-C.; ESTEY, B.; HASLINGER, P.; AND MÜLLER, H., 2012. Influence of the Coriolis force in atom interferometry. *Phys. Rev. Lett.*, 108 (Feb 2012), 090402. doi:10.1103/PhysRevLett.108.090402. <http://link.aps.org/doi/10.1103/PhysRevLett.108.090402>. (cited on pages 45 and 97)
151. LEANHARDT, A. E.; CHIKKATUR, A. P.; KIELPINSKI, D.; SHIN, Y.; GUSTAVSON, T. L.; KETTERLE, W.; AND PRITCHARD, D. E., 2002. Propagation of Bose-Einstein condensates in a magnetic waveguide. *Phys. Rev. Lett.*, 89 (Jul 2002), 040401. doi:10.1103/PhysRevLett.89.040401. <http://link.aps.org/doi/10.1103/PhysRevLett.89.040401>. (cited on page 82)
152. LEANHARDT, A. E.; SHIN, Y.; CHIKKATUR, A. P.; KIELPINSKI, D.; KETTERLE, W.; AND PRITCHARD, D. E., 2003. Bose-Einstein condensates near a microfabricated surface. *Phys. Rev. Lett.*, 90 (Mar 2003), 100404. doi:10.1103/PhysRevLett.90.100404. <http://link.aps.org/doi/10.1103/PhysRevLett.90.100404>. (cited on page 82)
153. LÉVÈQUE, T.; GAUGUET, A.; MICHAUD, F.; PEREIRA DOS SANTOS, F.; AND LANDRAGIN, A., 2009. Enhancing the area of a Raman atom interferometer using a versatile double-diffraction technique. *Phys. Rev. Lett.*, 103 (Aug 2009), 080405. doi:10.1103/PhysRevLett.103.080405. <http://link.aps.org/doi/10.1103/PhysRevLett.103.080405>. (cited on pages 98, 99, and 110)
154. LIBERATI, S., 2013. Tests of Lorentz invariance: a 2013 update. *Classical and Quantum Gravity*, 30, 13 (2013), 133001. <http://stacks.iop.org/0264-9381/30/i=13/a=133001>. (cited on page 131)

155. LIN, Y.-J.; PERRY, A. R.; COMPTON, R. L.; SPIELMAN, I. B.; AND PORTO, J. V., 2009. Rapid production of ^{87}Rb Bose-Einstein condensates in a combined magnetic and optical potential. *Phys. Rev. A*, 79 (Jun 2009), 063631. doi:10.1103/PhysRevA.79.063631. <http://link.aps.org/doi/10.1103/PhysRevA.79.063631>. (cited on page 72)
156. MA, J.-L. AND MA, F.-T., 2007. Solitary wave solutions of nonlinear financial markets: data-modeling-concept-practicing. *Frontiers of Physics in China*, 2, 3 (2007), 368–374. doi:10.1007/s11467-007-0047-y. <http://dx.doi.org/10.1007/s11467-007-0047-y>. (cited on page 121)
157. MACHLUF, S.; JAPHA, Y.; AND FOLMAN, R., 2013. Coherent Stern-Gerlach momentum splitting on an atom chip. *Nat Commun*, 4 (09 2013). <http://dx.doi.org/10.1038/ncomms3424>. (cited on page 98)
158. MALOSSI, N.; BODART, Q.; MERLET, S.; LÉVÈQUE, T.; LANDRAGIN, A.; AND SANTOS, F. P. D., 2010. Double diffraction in an atomic gravimeter. *Phys. Rev. A*, 81 (Jan 2010), 013617. doi:10.1103/PhysRevA.81.013617. <http://link.aps.org/doi/10.1103/PhysRevA.81.013617>. (cited on page 98)
159. MARCHANT, A. L.; BILLAM, T. P.; WILES, T. P.; YU, M. M. H.; GARDINER, S. A.; AND CORNISH, S. L., 2013. Controlled formation and reflection of a bright solitary matter-wave. *Nat Commun*, 4 (2013), 1865. doi:10.1038/ncomms2893. <http://dx.doi.org/10.1038/ncomms2893>. (cited on page 123)
160. MARCHANT, A. L.; HÄNDL, S.; HOPKINS, S. A.; WILES, T. P.; AND CORNISH, S. L., 2012. Bose-Einstein condensation of ^{85}Rb by direct evaporation in an optical dipole trap. *Phys. Rev. A*, 85 (May 2012), 053647. doi:10.1103/PhysRevA.85.053647. <http://link.aps.org/doi/10.1103/PhysRevA.85.053647>. (cited on page 67)
161. MARTI, G. E.; OLF, R.; AND STAMPER-KURN, D. M., 2015. Collective excitation interferometry with a toroidal Bose-Einstein condensate. *Phys. Rev. A*, 91 (Jan 2015), 013602. doi:10.1103/PhysRevA.91.013602. <http://link.aps.org/doi/10.1103/PhysRevA.91.013602>. (cited on pages 82 and 83)
162. MATUSZEWSKI, M.; INFELD, E.; ROWLANDS, G.; AND TRIPPENBACH, M., 2005. Stability analysis of three-dimensional breather solitons in a Bose-Einstein condensate. *Proceedings of the Royal Society A: Mathematical, Physical and Engineering Science*, 461, 2063 (2005), 3561–3574. doi:10.1098/rspa.2005.1531. <http://rspa.royalsocietypublishing.org/content/461/2063/3561.abstract>. (cited on page 129)
163. McDONALD, G. D., 2009. *Detecting Atomic Shot Noise On Ultra-cold Atom Clouds*. Honours thesis, Australian National University. <http://atomlaser.anu.edu.au/publications/gordon-honours-thesis.pdf>. (cited on page 44)
164. McDONALD, G. D.; KEAL, H.; ALTIN, P. A.; DEBS, J. E.; BENNETTS, S.; KUHN, C. C. N.; HARDMAN, K. S.; JOHNSSON, M. T.; CLOSE, J. D.; AND ROBINS, N. P.,

2013. Optically guided linear Mach-Zehnder atom interferometer. *Phys. Rev. A*, 87 (Jan 2013), 013632. doi:10.1103/PhysRevA.87.013632. <http://link.aps.org/doi/10.1103/PhysRevA.87.013632>. (cited on pages 3, 99, 101, and 110)
165. McDONALD, G. D.; KUHN, C. C. N.; BENNETTS, S.; DEBS, J. E.; HARDMAN, K. S.; JOHNSON, M.; CLOSE, J. D.; AND ROBINS, N. P., 2013. $80\hbar k$ momentum separation with Bloch oscillations in an optically guided atom interferometer. *Phys. Rev. A*, 88 (Nov 2013), 053620. doi:10.1103/PhysRevA.88.053620. <http://link.aps.org/doi/10.1103/PhysRevA.88.053620>. (cited on pages 99, 115, and 116)
166. MEDLEY, P.; MINAR, M. A.; CIZEK, N. C.; BERRYRIESER, D.; AND KASEVICH, M. A., 2014. Evaporative production of bright atomic solitons. *Phys. Rev. Lett.*, 112 (Feb 2014), 060401. doi:10.1103/PhysRevLett.112.060401. <http://link.aps.org/doi/10.1103/PhysRevLett.112.060401>. (cited on page 123)
167. MERTES, K. M.; MERRILL, J. W.; CARRETERO-GONZÁLEZ, R.; FRANTZESKAKIS, D. J.; KEVREKIDIS, P. G.; AND HALL, D. S., 2007. Nonequilibrium dynamics and superfluid ring excitations in binary Bose-Einstein condensates. *Phys. Rev. Lett.*, 99 (Nov 2007), 190402. doi:10.1103/PhysRevLett.99.190402. <http://link.aps.org/doi/10.1103/PhysRevLett.99.190402>. (cited on page 67)
168. METCALF, H. AND VAN DER STRATEN, P., 1999. *Laser Cooling and Trapping*. Graduate Texts in Contemporary Physics. Springer New York. ISBN 9780387987286. <https://books.google.com.au/books?id=i-40VaXqrj0C>. (cited on page 42)
169. MICHELSON, A. A., 1881. The relative motion of the earth and the luminiferous ether. *American Journal of Science*, 22 (1881), 120–129. (cited on page 1)
170. MICHELSON, A. A. AND MORLEY, E., 1887. On the relative motion of the earth and the luminiferous ether. *American Journal of Science*, 34, 203 (1887), 333–345. http://en.wikisource.org/wiki/On_the_Relative_Motion_of_the_Earth_and_the_Luminiferous_Ether. (cited on page 1)
171. MÜLLER, D.; CORNELL, E. A.; PREVEDELLI, M.; SCHWINDT, P. D. D.; WANG, Y.-J.; AND ANDERSON, D. Z., 2001. Magnetic switch for integrated atom optics. *Phys. Rev. A*, 63 (Mar 2001), 041602. doi:10.1103/PhysRevA.63.041602. <http://link.aps.org/doi/10.1103/PhysRevA.63.041602>. (cited on page 82)
172. MÜLLER, H.; CHIOW, S.-W.; AND CHU, S., 2008. Atom-wave diffraction between the Raman-Nath and the Bragg regime: Effective Rabi frequency, losses, and phase shifts. *Phys. Rev. A*, 77 (Feb 2008), 023609. doi:10.1103/PhysRevA.77.023609. <http://link.aps.org/doi/10.1103/PhysRevA.77.023609>. (cited on page 85)
173. MÜLLER, H.; CHIOW, S.-W.; HERRMANN, S.; AND CHU, S., 2009. Atom interferometers with scalable enclosed area. *Phys. Rev. Lett.*, 102 (Jun 2009), 240403. doi:10.1103/PhysRevLett.102.240403. <http://link.aps.org/doi/10.1103/PhysRevLett.102.240403>. (cited on pages 97, 99, 110, and 115)

174. MÜLLER, H.; CHIOW, S.-w.; LONG, Q.; HERRMANN, S.; AND CHU, S., 2008. Atom interferometry with up to 24-photon-momentum-transfer beam splitters. *Phys. Rev. Lett.*, 100 (May 2008), 180405. doi:10.1103/PhysRevLett.100.180405. <http://link.aps.org/doi/10.1103/PhysRevLett.100.180405>. (cited on pages 97, 99, and 110)
175. MÜNTINGA, H.; AHLERS, H.; KRUTZIK, M.; WENZLAWSKI, A.; ARNOLD, S.; BECKER, D.; BONGS, K.; DITTUS, H.; DUNCKER, H.; GAALOUL, N.; GHERASIM, C.; GIESE, E.; GRZESCHIK, C.; HÄNSCH, T. W.; HELLMIG, O.; HERR, W.; HERRMANN, S.; KAJARI, E.; KLEINERT, S.; LÄMMERZAH, C.; LEWOCZKO-ADAMCZYK, W.; MALCOLM, J.; MEYER, N.; NOLTE, R.; PETERS, A.; POPP, M.; REICHEL, J.; ROURA, A.; RUDOLPH, J.; SCHIEMANGK, M.; SCHNEIDER, M.; SEIDEL, S. T.; SENGSTOCK, K.; TAMMA, V.; VALENZUELA, T.; VOGEL, A.; WALSER, R.; WENDRICH, T.; WINDPASSINGER, P.; ZELLER, W.; VAN ZOEST, T.; ERTMER, W.; SCHLEICH, W. P.; AND RASEL, E. M., 2013. Interferometry with Bose-Einstein condensates in microgravity. *Phys. Rev. Lett.*, 110 (Feb 2013), 093602. doi:10.1103/PhysRevLett.110.093602. <http://link.aps.org/doi/10.1103/PhysRevLett.110.093602>. (cited on pages 55, 56, 101, and 132)
176. NARASCHEWSKI, M. AND GLAUBER, R. J., 1999. Spatial coherence and density correlations of trapped Bose gases. *Phys. Rev. A*, 59 (Jun 1999), 4595–4607. doi:10.1103/PhysRevA.59.4595. <http://link.aps.org/doi/10.1103/PhysRevA.59.4595>. (cited on page 127)
177. NEGRETTI, A. AND HENKEL, C., 2004. Enhanced phase sensitivity and soliton formation in an integrated BEC interferometer. *Journal of Physics B: Atomic, Molecular and Optical Physics*, 37, 23 (2004), L385. <http://stacks.iop.org/0953-4075/37/i=23/a=L02>. (cited on page 123)
178. NGUYEN, J. H. V.; DYKE, P.; LUO, D.; MALOMED, B. A.; AND HULET, R. G., 2014. Collisions of matter-wave solitons. *Nat Phys*, 10, 12 (12 2014), 918–922. <http://dx.doi.org/10.1038/nphys3135>. (cited on pages 123, 129, and 146)
179. OCKELOEN, C. F.; SCHMIED, R.; RIEDEL, M. F.; AND TREUTLEIN, P., 2013. Quantum metrology with a scanning probe atom interferometer. *Phys. Rev. Lett.*, 111 (Oct 2013), 143001. doi:10.1103/PhysRevLett.111.143001. <http://link.aps.org/doi/10.1103/PhysRevLett.111.143001>. (cited on pages 3 and 5)
180. OLSHANII, M. AND DUNJKO, V., 2005. Interferometry in dense nonlinear media and interaction-induced loss of contrast in microfabricated atom interferometers. *arXiv:cond-mat/0505358*, (2005). <http://arxiv.org/abs/cond-mat/0505358>. (cited on page 88)
181. OTT, H.; FORTAGH, J.; SCHLOTTERBECK, G.; GROSSMANN, A.; AND ZIMMERMANN, C., 2001. Bose-Einstein condensation in a surface microtrap. *Phys. Rev. Lett.*, 87 (Nov 2001), 230401. doi:10.1103/PhysRevLett.87.230401. <http://link.aps.org/doi/10.1103/PhysRevLett.87.230401>. (cited on page 82)

-
182. PAPP, S. B.; PINO, J. M.; AND WIEMAN, C. E., 2008. Tunable miscibility in a dual-species Bose-Einstein condensate. *Phys. Rev. Lett.*, 101 (Jul 2008), 040402. doi: 10.1103/PhysRevLett.101.040402. <http://link.aps.org/doi/10.1103/PhysRevLett.101.040402>. (cited on page 67)
183. PARKER, N. G.; MARTIN, A. M.; CORNISH, S. L.; AND ADAMS, C. S., 2008. Collisions of bright solitary matter waves. *Journal of Physics B: Atomic, Molecular and Optical Physics*, 41, 4 (2008), 045303. <http://stacks.iop.org/0953-4075/41/i=4/a=045303>. (cited on page 127)
184. PEIK, E.; BEN DAHAN, M.; BOUCHOULE, I.; CASTIN, Y.; AND SALOMON, C., 1997. Bloch oscillations of atoms, adiabatic rapid passage, and monokinetic atomic beams. *Phys. Rev. A*, 55 (Apr 1997), 2989–3001. doi:10.1103/PhysRevA.55.2989. <http://link.aps.org/doi/10.1103/PhysRevA.55.2989>. (cited on pages 40, 104, and 109)
185. PERRIN, H.; COLOMBE, Y.; MERCIER, B.; LORENT, V.; AND HENKEL, C., 2005. A Bose-Einstein condensate bouncing off a rough mirror. *Journal of Physics: Conference Series*, 19, 1 (2005), 151. <http://stacks.iop.org/1742-6596/19/i=1/a=025>. (cited on page 23)
186. PETERS, A.; CHUNG, K.; AND CHU, S., 1999. Measurement of gravitational acceleration by dropping atoms. *Nature*, 400 (Aug 1999), 849–852. doi:10.1038/23655. <http://www.nature.com/nature/journal/v400/n6747/abs/400849a0.html>. (cited on page 132)
187. PETERS, A.; CHUNG, K. Y.; AND CHU, S., 2001. High-precision gravity measurements using atom interferometry. *Metrologia*, 38, 1 (2001), 25. <http://stacks.iop.org/0026-1394/38/i=1/a=4>. (cited on pages 3, 4, 51, and 123)
188. PETHICK, C. AND SMITH, H., 2002. *Bose-Einstein Condensation in Dilute Gases*. Cambridge University Press. ISBN 9780521665803. http://books.google.com.au/books?id=iBk0G3_5iIQC. (cited on page 7)
189. PIPPA STOREY AND CLAUDE COHEN-TANNOUDJI, 1994. The Feynman path integral approach to atomic interferometry. A tutorial. *J. Phys. II France*, 4, 11 (1994), 1999–2027. doi:10.1051/jp2:1994103. <http://dx.doi.org/10.1051/jp2:1994103>. (cited on pages 45 and 54)
190. POLI, N.; WANG, F.-Y.; TARALLO, M. G.; ALBERTI, A.; PREVEDELLI, M.; AND TINO, G. M., 2011. Precision measurement of gravity with cold atoms in an optical lattice and comparison with a classical gravimeter. *Phys. Rev. Lett.*, 106 (Jan 2011), 038501. doi:10.1103/PhysRevLett.106.038501. <http://link.aps.org/doi/10.1103/PhysRevLett.106.038501>. (cited on page 97)
191. POLO, J. AND AHUFINGER, V., 2013. Soliton-based matter-wave interferometer. *Phys. Rev. A*, 88 (Nov 2013), 053628. doi:10.1103/PhysRevA.88.053628. <http://link.aps.org/doi/10.1103/PhysRevA.88.053628>. (cited on page 123)

192. PU, H. AND BIGELOW, N., 1998. Properties of two-species Bose condensates. *Phys. Rev. Lett.*, 80 (Feb 1998), 1130–1133. doi:10.1103/PhysRevLett.80.1130. <http://link.aps.org/doi/10.1103/PhysRevLett.80.1130>. (cited on page 139)
193. RAAB, E. L.; PRENTISS, M.; CABLE, A.; CHU, S.; AND PRITCHARD, D. E., 1987. Trapping of neutral sodium atoms with radiation pressure. *Phys. Rev. Lett.*, 59 (Dec 1987), 2631–2634. doi:10.1103/PhysRevLett.59.2631. <http://link.aps.org/doi/10.1103/PhysRevLett.59.2631>. (cited on page 42)
194. RAIZEN, M.; SALOMON, C.; AND NIU, Q., 1997. New light on quantum transport. *Physics Today*, 50, 7 (July 1997), 30. http://george.ph.utexas.edu/papers/new_light.pdf. (cited on page 97)
195. RASEL, E., 2014. Interferometry with Bose-Einstein condensates in space: MAIUS. <https://artemis.oca.eu/IMG/file/8-Rasel.pdf>. (cited on page 132)
196. RAUCH, H., 1979. *Scope of neutron interferometry*. Clarendon Press, United Kingdom. (cited on page 1)
197. RIEHLE, F.; KISTERS, T.; WITTE, A.; HELMCKE, J.; AND BORDÉ, C. J., 1991. Optical Ramsey spectroscopy in a rotating frame: Sagnac effect in a matter-wave interferometer. *Phys. Rev. Lett.*, 67 (Jul 1991), 177–180. doi:10.1103/PhysRevLett.67.177. <http://link.aps.org/doi/10.1103/PhysRevLett.67.177>. (cited on page 4)
198. ROBERTS, J. L.; CLAUSSEN, N. R.; CORNISH, S. L.; AND WIEMAN, C. E., 2000. Magnetic field dependence of ultracold inelastic collisions near a Feshbach resonance. *Phys. Rev. Lett.*, 85 (Jul 2000), 728–731. doi:10.1103/PhysRevLett.85.728. <http://link.aps.org/doi/10.1103/PhysRevLett.85.728>. (cited on page 118)
199. ROBERTS, K. O.; MCKELLAR, T.; FEKETE, J.; RAKONJAC, A.; DEB, A. B.; AND KJÆRGAARD, N., 2014. Steerable optical tweezers for ultracold atom studies. *Opt. Lett.*, 39, 7 (Apr 2014), 2012–2015. doi:10.1364/OL.39.002012. <http://ol.osa.org/abstract.cfm?URI=ol-39-7-2012>. (cited on pages 96, 98, and 114)
200. ROSI, G.; CACCIAPUOTI, L.; SORRENTINO, F.; MENCHETTI, M.; PREVEDELLI, M.; AND TINO, G. M., 2015. Measurement of the gravity-field curvature by atom interferometry. *Phys. Rev. Lett.*, 114 (Jan 2015), 013001. doi:10.1103/PhysRevLett.114.013001. <http://link.aps.org/doi/10.1103/PhysRevLett.114.013001>. (cited on page 3)
201. ROSI, G.; SORRENTINO, F.; CACCIAPUOTI, L.; PREVEDELLI, M.; AND TINO, G. M., 2014. Precision measurement of the Newtonian gravitational constant using cold atoms. *Nature*, 510, 7506 (06 2014), 518–521. <http://dx.doi.org/10.1038/nature13433>. (cited on pages 3 and 81)
202. SACKETT, C. A.; GERTON, J. M.; WELLING, M.; AND HULET, R. G., 1999. Measurements of collective collapse in a Bose-Einstein condensate with attractive interactions. *Phys. Rev. Lett.*, 82 (Feb 1999), 876–879. doi:10.1103/PhysRevLett.82.876. <http://link.aps.org/doi/10.1103/PhysRevLett.82.876>. (cited on page 118)

203. SAITO, H. AND UEDA, M., 2001. Intermittent implosion and pattern formation of trapped Bose-Einstein condensates with an attractive interaction. *Phys. Rev. Lett.*, 86 (Feb 2001), 1406–1409. doi:10.1103/PhysRevLett.86.1406. <http://link.aps.org/doi/10.1103/PhysRevLett.86.1406>. (cited on page 118)
204. SANÉ, S. S.; BENNETTS, S.; DEBS, J. E.; KUHN, C. C. N.; McDONALD, G. D.; ALTIN, P. A.; CLOSE, J. D.; AND ROBINS, N. P., 2012. 11 W narrow linewidth laser source at 780nm for laser cooling and manipulation of rubidium. *Opt. Express*, 20, 8 (Apr 2012), 8915–8919. doi:10.1364/OE.20.008915. <http://www.opticsexpress.org/abstract.cfm?URI=oe-20-8-8915>. (cited on page 97)
205. SATO, Y. AND PACKARD, R. E., 2012. Superfluid helium quantum interference devices: physics and applications. *Reports on Progress in Physics*, 75, 1 (2012), 016401. <http://stacks.iop.org/0034-4885/75/i=1/a=016401>. (cited on page 1)
206. SCHLAMMINGER, S.; CHOI, K.-Y.; WAGNER, T. A.; GUNDLACH, J. H.; AND ADELBERGER, E. G., 2008. Test of the equivalence principle using a rotating torsion balance. *Phys. Rev. Lett.*, 100 (Jan 2008), 041101. doi:10.1103/PhysRevLett.100.041101. <http://link.aps.org/doi/10.1103/PhysRevLett.100.041101>. (cited on page 132)
207. SCHLEICH, W. P.; GREENBERGER, D. M.; AND RASEL, E. M., 2013. A representation-free description of the Kasevich-Chu interferometer: a resolution of the redshift controversy. *New Journal of Physics*, 15, 1 (2013), 013007. <http://stacks.iop.org/1367-2630/15/i=1/a=013007>. (cited on page 99)
208. SCHLIPPERT, D.; HARTWIG, J.; ALBERS, H.; RICHARDSON, L. L.; SCHUBERT, C.; ROURA, A.; SCHLEICH, W. P.; ERTMER, W.; AND RASEL, E. M., 2014. Quantum test of the universality of free fall. *Phys. Rev. Lett.*, 112 (May 2014), 203002. doi:10.1103/PhysRevLett.112.203002. <http://link.aps.org/doi/10.1103/PhysRevLett.112.203002>. (cited on page 132)
209. SCHMIDT, M.; SENGER, A.; HAUTH, M.; FREIER, C.; SCHKOLNIK, V.; AND PETERS, A., 2011. A mobile high-precision absolute gravimeter based on atom interferometry. *Gyroscopy and Navigation*, 2, 3 (2011), 170–177. doi:10.1134/S2075108711030102. <http://dx.doi.org/10.1134/S2075108711030102>. (cited on page 82)
210. SCHNEIDER, J. AND SCHENZLE, A., 1999. Output from an atom laser: theory vs. experiment. *Applied Physics B*, 69 (1999), 353–356. (cited on page 82)
211. SCHUBERT, C.; HARTWIG, J.; AHLERS, H.; POSSO-TRUJILLO, K.; GAALOUL, N.; VELTE, U.; LANDRAGIN, A.; BERTOLDI, A.; BATTELIER, B.; BOUYER, P.; SORRENTINO, F.; TINO, G. M.; KRUTZIK, M.; PETERS, A.; HERRMANN, S.; LÄMMERZAH, C.; CACCIAPOUTI, L.; ROCCO, E.; BONGS, K.; ERTMER, W.; AND RASEL, E. M., 2013. Differential atom interferometry with ^{87}Rb and ^{85}Rb for testing the UFF in STEQUEST. *arXiv:1312.5963*, (Dec. 2013). <http://arxiv.org/abs/1312.5963>. (cited on pages 123 and 132)

212. SCHULDT, T.; SCHUBERT, C.; KRUTZIK, M.; BOTE, L.; GAALOUL, N.; HARTWIG, J.; AHLERS, H.; HERR, W.; POSSO-TRUJILLO, K.; RUDOLPH, J.; SEIDEL, S.; WENDRICH, T.; ERTMER, W.; HERRMANN, S.; KUBELKA-LANGE, A.; MILKE, A.; RIEVERS, B.; ROCCO, E.; HINTON, A.; BONGS, K.; OSWALD, M.; FRANZ, M.; HAUTH, M.; PETERS, A.; BAWAMIA, A.; WICHT, A.; BATTELIER, B.; BERTOLDI, A.; BOUYER, P.; LANDRAGIN, A.; MASSONNET, D.; LÉVÈQUE, T.; WENZLAWSKI, A.; HELLMIG, O.; WINDPASSINGER, P.; SENGSTOCK, K.; VON KLITZING, W.; CHALONER, C.; SUMMERS, D.; IRELAND, P.; MATEOS, I.; SOPUERTA, C.; SORRENTINO, F.; TINO, G.; WILLIAMS, M.; TRENKEL, C.; GERARDI, D.; CHWALLA, M.; BURKHARDT, J.; JOHANN, U.; HESKE, A.; WILLE, E.; GEHLER, M.; CACCIAPUOTI, L.; GÜRLEBECK, N.; BRAXMAIER, C.; AND RASEL, E., 2015. Design of a dual species atom interferometer for space. *Experimental Astronomy*, 39, 2 (2015), 167–206. doi:10.1007/s10686-014-9433-y. <http://dx.doi.org/10.1007/s10686-014-9433-y>. (cited on page 132)
213. SCHUMM, T.; ESTÈVE, J.; FIGL, C.; TREBBIA, J.-B.; AUSSIBAL, C.; NGUYEN, H.; MAILLY, D.; BOUCHOULE, I.; WESTBROOK, C. I.; AND ASPECT, A., 2005. Atom chips in the real world: the effects of wire corrugation. *The European Physical Journal D - Atomic, Molecular, Optical and Plasma Physics*, 32 (2005), 171–180. doi:10.1140/epjd/e2005-00016-x. <http://dx.doi.org/10.1140/epjd/e2005-00016-x>. (cited on page 82)
214. SCHUMM, T.; HOFFERBERTH, S.; ANDERSSON, L.; WILDERMUTH, S.; GROTH, S.; BAR-JOSEPH, I.; SCHMIEDMAYER, J.; AND KRÜGER, P., 2005. Matter-wave interferometry in a double well on an atom chip. *Nature Physics*, 1 (Sep 2005), 57. doi:10.1038/nphys125. <http://www.nature.com/nphys/journal/v1/n1/full/nphys125.html>. (cited on page 82)
215. SEARS, V., 1989. *Neutron optics: an introduction to the theory of neutron optical phenomena and their applications*. Oxford series on neutron scattering in condensed matter. Oxford University Press. ISBN 9780195046014. <http://books.google.com.au/books?id=iNXvAAAAMAAJ>. (cited on page 1)
216. SHIN, Y.; SABA, M.; PASQUINI, T. A.; KETTERLE, W.; PRITCHARD, D. E.; AND LEANHARDT, A. E., 2004. Atom interferometry with Bose-Einstein condensates in a double-well potential. *Phys. Rev. Lett.*, 92 (Feb 2004), 050405. doi:10.1103/PhysRevLett.92.050405. <http://link.aps.org/doi/10.1103/PhysRevLett.92.050405>. (cited on page 82)
217. SHIN, Y.; SANNER, C.; Jo, G.-B.; PASQUINI, T. A.; SABA, M.; KETTERLE, W.; PRITCHARD, D. E.; VENGALATTORE, M.; AND PRENTISS, M., 2005. Interference of Bose-Einstein condensates split with an atom chip. *Phys. Rev. A*, 72 (Aug 2005), 021604. doi:10.1103/PhysRevA.72.021604. <http://link.aps.org/doi/10.1103/PhysRevA.72.021604>. (cited on page 82)
218. SIMMONDS, R. W.; MARCHENKOV, A.; HOSKINSON, E.; DAVIS, J. C.; AND PACKARD, R. E., 2001. Quantum interference of superfluid ^3He . *Nature*, 412, 6842 (07 2001), 55–58. <http://dx.doi.org/10.1038/35083518>. (cited on page 1)

219. SIMONS, B., 2009. Advanced quantum mechanics. *University of Cambridge Lecture Notes*, (2009). <http://www.tcm.phy.cam.ac.uk/~bds10/aqp.html>. (cited on page 24)
220. SMITH, D. A.; AIGNER, S.; HOFFERBERTH, S.; GRING, M.; ANDERSSON, M.; WILDERMUTH, S.; KRÜGER, P.; SCHNEIDER, S.; SCHUMM, T.; AND SCHMIEDMAYER, J., 2011. Absorption imaging of ultracold atoms on atom chips. *Opt. Express*, 19, 9 (Apr 2011), 8471–8485. doi:10.1364/OE.19.008471. <http://www.opticsexpress.org/abstract.cfm?URI=oe-19-9-8471>. (cited on page 82)
221. SORRENTINO, F.; BERTOLDI, A.; BODART, Q.; CACCIAPUOTI, L.; DE ANGELIS, M.; LIEN, Y.-H.; PREVEDELLI, M.; ROSI, G.; AND TINO, G. M., 2012. Simultaneous measurement of gravity acceleration and gravity gradient with an atom interferometer. *Applied Physics Letters*, 101, 11 (2012), 114106. doi:<http://dx.doi.org/10.1063/1.4751112>. <http://scitation.aip.org/content/aip/journal/apl/101/11/10.1063/1.4751112>. (cited on page 3)
222. SORRENTINO, F.; BODART, Q.; CACCIAPUOTI, L.; LIEN, Y.-H.; PREVEDELLI, M.; ROSI, G.; SALVI, L.; AND TINO, G. M., 2014. Sensitivity limits of a Raman atom interferometer as a gravity gradiometer. *Phys. Rev. A*, 89 (Feb 2014), 023607. doi:10.1103/PhysRevA.89.023607. <http://link.aps.org/doi/10.1103/PhysRevA.89.023607>. (cited on pages 3 and 115)
223. SORRENTINO, F.; BONGS, K.; BOUYER, P.; CACCIAPUOTI, L.; DE ANGELIS, M.; DITTUS, H.; ERTMER, W.; HARTWIG, J.; HAUTH, M.; HERRMANN, S.; HUANG, K.; INGUSCIO, M.; KAJARI, E.; KÖNEMANN, T.; LÄMMERZAH, C.; LANDRAGIN, A.; MODUGNO, G.; DOS SANTOS, F. P.; PETERS, A.; PREVEDELLI, M.; RASEL, E. M.; SCHLEICH, W. P.; SCHMIDT, M.; SENGER, A.; SENGSTOCK, K.; STERN, G.; TINO, G. M.; VALENZUELA, T.; WALSER, R.; AND WINDPASSINGER, P., 2011. The space atom interferometer project: status and prospects. *Journal of Physics: Conference Series*, 327, 1 (2011), 012050. <http://stacks.iop.org/1742-6596/327/i=1/a=012050>. (cited on page 123)
224. SPENCE, J. C., 2009. Electron interferometry. In *Compendium of Quantum Physics* (Eds. D. GREENBERGER; K. HENTSCHEL; AND F. WEINERT), 188–195. Springer Berlin Heidelberg. ISBN 978-3-540-70622-9. doi:10.1007/978-3-540-70626-7_61. http://dx.doi.org/10.1007/978-3-540-70626-7_61. (cited on page 1)
225. STAUDENMANN, J. L.; WERNER, S. A.; COLELLA, R.; AND OVERHAUSER, A. W., 1980. Gravity and inertia in quantum mechanics. *Phys. Rev. A*, 21 (May 1980), 1419–1438. doi:10.1103/PhysRevA.21.1419. <http://link.aps.org/doi/10.1103/PhysRevA.21.1419>. (cited on page 1)
226. STECK, D. A. Alkali D line data. <http://steck.us/alkalidata/>. (cited on page 68)
227. STECK, D. A., 2001. Quantum chaos, transport, and decoherence in atom optics. *Ph.D. dissertation, The University of Texas at Austin*, (Nov 2001). <http://steck.us/dissertation/>. (cited on pages 35 and 36)

228. STOCKTON, J. K.; WU, X.; AND KASEVICH, M. A., 2007. Bayesian estimation of differential interferometer phase. *Phys. Rev. A*, 76 (Sep 2007), 033613. doi:10.1103/PhysRevA.76.033613. <http://link.aps.org/doi/10.1103/PhysRevA.76.033613>. (cited on page 137)
229. STRECKER, K. E.; PARTRIDGE, G. B.; TRUSCOTT, A. G.; AND HULET, R. G., 2002. Formation and propagation of matter-wave soliton trains. *Nature*, 417 (2002), 150. doi:<http://dx.doi.org/10.1038/nature747>. (cited on pages 123 and 127)
230. STRECKER, K. E.; PARTRIDGE, G. B.; TRUSCOTT, A. G.; AND HULET, R. G., 2003. Bright matter wave solitons in Bose-Einstein condensates. *New Journal of Physics*, 5, 1 (2003), 73. <http://stacks.iop.org/1367-2630/5/i=1/a=373>. (cited on pages 123 and 127)
231. STRELTSOV, A. I.; ALON, O. E.; AND CEDERBAUM, L. S., 2011. Swift loss of coherence of soliton trains in attractive Bose-Einstein condensates. *Phys. Rev. Lett.*, 106 (Jun 2011), 240401. doi:10.1103/PhysRevLett.106.240401. <http://link.aps.org/doi/10.1103/PhysRevLett.106.240401>. (cited on page 146)
232. SU, E. J.; WU, S.; AND PRENTISS, M. G., 2010. Atom interferometry using wave packets with constant spatial displacements. *Phys. Rev. A*, 81 (Apr 2010), 043631. doi:10.1103/PhysRevA.81.043631. <http://link.aps.org/doi/10.1103/PhysRevA.81.043631>. (cited on page 82)
233. SZIGETI, S. S.; DEBS, J. E.; HOPE, J. J.; ROBINS, N. P.; AND CLOSE, J. D., 2012. Why momentum width matters for atom interferometry with Bragg pulses. *New Journal of Physics*, 14, 2 (2012), 023009. <http://stacks.iop.org/1367-2630/14/i=2/a=023009>. (cited on pages 5, 6, 33, 85, 98, 109, and 126)
234. TARALLO, M. G.; MAZZONI, T.; POLI, N.; SUTYRIN, D. V.; ZHANG, X.; AND TINO, G. M., 2014. Test of Einstein equivalence principle for 0-spin and half-integer-spin atoms: Search for spin-gravity coupling effects. *Phys. Rev. Lett.*, 113 (Jul 2014), 023005. doi:10.1103/PhysRevLett.113.023005. <http://link.aps.org/doi/10.1103/PhysRevLett.113.023005>. (cited on page 132)
235. TINO, G.; SORRENTINO, F.; AGUILERA, D.; BATELIER, B.; BERTOLDI, A.; BODART, Q.; BONGS, K.; BOUYER, P.; BRAXMAIER, C.; CACCIAPUOTI, L.; GAALOUL, N.; GÜRLEBECK, N.; HAUTH, M.; HERRMANN, S.; KRUTZIK, M.; KUBELKA, A.; LANDRAGIN, A.; MILKE, A.; PETERS, A.; RASEL, E.; ROCCO, E.; SCHUBERT, C.; SCHULDIT, T.; SENGSTOCK, K.; AND WICHT, A., 2013. Precision gravity tests with atom interferometry in space. *Nuclear Physics B - Proceedings Supplements*, 243, 0 (2013), 203 – 217. doi:<http://dx.doi.org/10.1016/j.nuclphysbps.2013.09.023>. <http://www.sciencedirect.com/science/article/pii/S0920563213005471>. Proceedings of the IV International Conference on Particle and Fundamental Physics in Space. (cited on page 123)

236. TOGAWA, Y.; KOUSAKA, Y.; NISHIHARA, S.; INOUE, K.; AKIMITSU, J.; OVCHINNIKOV, A. S.; AND KISHINE, J., 2013. Interlayer magnetoresistance due to chiral soliton lattice formation in hexagonal chiral magnet CrNb₃S₆. *Phys. Rev. Lett.*, 111 (Nov 2013), 197204. doi:10.1103/PhysRevLett.111.197204. <http://link.aps.org/doi/10.1103/PhysRevLett.111.197204>. (cited on page 121)
237. TONYUSHKIN, A. AND PRENTISS, M., 2010. Straight macroscopic magnetic guide for cold atom interferometer. *Journal of Applied Physics*, 108, 9 (2010), 094904. doi:10.1063/1.3506685. <http://link.aip.org/link/?JAP/108/094904/1>. (cited on page 82)
238. TREBBIA, J.-B.; GARRIDO ALZAR, C. L.; CORNELUSSEN, R.; WESTBROOK, C. I.; AND BOUCHOULE, I., 2007. Roughness suppression via rapid current modulation on an atom chip. *Phys. Rev. Lett.*, 98 (Jun 2007), 263201. doi:10.1103/PhysRevLett.98.263201. <http://link.aps.org/doi/10.1103/PhysRevLett.98.263201>. (cited on page 82)
239. VAN ZOEST, T.; GAALOUL, N.; SINGH, Y.; AHLERS, H.; HERR, W.; SEIDEL, S. T.; ERTMER, W.; RASEL, E.; ECKART, M.; KAJARI, E.; ARNOLD, S.; NANDI, G.; SCHLEICH, W. P.; WALSER, R.; VOGEL, A.; SENGSTOCK, K.; BONGS, K.; LEWOCZKO-ADAMCZYK, W.; SCHIEMANGK, M.; SCHULDIT, T.; PETERS, A.; KÖNEMANN, T.; MÜNTINGA, H.; LÄMMERZAH, C.; DITTUS, H.; STEINMETZ, T.; HÄNSCH, T. W.; AND REICHEL, J., 2010. Bose-Einstein condensation in microgravity. *Science*, 328, 5985 (2010), 1540–1543. doi:10.1126/science.1189164. <http://www.sciencemag.org/content/328/5985/1540.abstract>. (cited on page 82)
240. VERETENOV, N.; ROZHDESTVENSKY, Y.; ROSANOV, N.; SMIRNOV, V.; AND FEDOROV, S., 2007. Interferometric precision measurements with Bose-Einstein condensate solitons formed by an optical lattice. *The European Physical Journal D*, 42, 3 (2007), 455–460. doi:10.1140/epjd/e2007-00129-2. <http://dx.doi.org/10.1140/epjd/e2007-00129-2>. (cited on page 123)
241. VOLZ, U. AND SCHMORANZER, H., 1996. Precision lifetime measurements on alkali atoms and on helium by beam-gas-laser spectroscopy. *Physica Scripta*, 1996, T65 (1996), 48. <http://stacks.iop.org/1402-4896/1996/i=T65/a=007>. (cited on page 68)
242. WANG, Y.-J.; ANDERSON, D. Z.; BRIGHT, V. M.; CORNELL, E. A.; DIOT, Q.; KISHIMOTO, T.; PRENTISS, M.; SARAVANAN, R. A.; SEGAL, S. R.; AND WU, S., 2005. Atom Michelson interferometer on a chip using a Bose-Einstein condensate. *Phys. Rev. Lett.*, 94 (Mar 2005), 090405. doi:10.1103/PhysRevLett.94.090405. <http://link.aps.org/doi/10.1103/PhysRevLett.94.090405>. (cited on page 82)
243. WILLIAMS, J. G.; TURYSHEV, S. G.; AND BOGGS, D. H., 2012. Lunar laser ranging tests of the equivalence principle. *Classical and Quantum Gravity*, 29, 18 (2012), 184004. <http://stacks.iop.org/0264-9381/29/i=18/a=184004>. (cited on page 132)

244. WOOD, A. A.; BENNIE, L. M.; DUONG, A.; JASPERSE, M.; TURNER, L. D.; AND ANDERSON, R. P., 2014. Magnetic tensor gradiometry using Ramsey interferometry of spinor condensates. *ArXiv e-prints*, (Aug. 2014). (cited on page 3)
245. WU, S.; ROOIJAKKERS, W.; STRIEHL, P.; AND PRENTISS, M., 2004. Bidirectional propagation of cold atoms in a “stadium”-shaped magnetic guide. *Phys. Rev. A*, 70 (Jul 2004), 013409. doi:10.1103/PhysRevA.70.013409. <http://link.aps.org/doi/10.1103/PhysRevA.70.013409>. (cited on page 82)
246. WU, S.; SU, E.; AND PRENTISS, M., 2007. Demonstration of an area-enclosing guided-atom interferometer for rotation sensing. *Phys. Rev. Lett.*, 99 (Oct 2007), 173201. doi:10.1103/PhysRevLett.99.173201. <http://link.aps.org/doi/10.1103/PhysRevLett.99.173201>. (cited on page 82)
247. YAN, D.; CHANG, J. J.; HAMNER, C.; KEVREKIDIS, P. G.; ENGELS, P.; ACHILLEOS, V.; FRANTZESKAKIS, D. J.; CARRETERO-GONZÁLEZ, R.; AND SCHMELCHER, P., 2011. Multiple dark-bright solitons in atomic Bose-Einstein condensates. *Phys. Rev. A*, 84 (Nov 2011), 053630. doi:10.1103/PhysRevA.84.053630. <http://link.aps.org/doi/10.1103/PhysRevA.84.053630>. (cited on page 123)
248. YE, J.; SWARTZ, S.; JUNGNER, P.; AND HALL, J. L., 1996. Hyperfine structure and absolute frequency of the ^{87}Rb $5\text{P}_{3/2}$ state. *Opt. Lett.*, 21, 16 (Aug 1996), 1280–1282. doi:10.1364/OL.21.001280. <http://ol.osa.org/abstract.cfm?URI=ol-21-16-1280>. (cited on page 68)
249. ZHAI, Y.; ZHANG, P.; CHEN, X.; DONG, G.; AND ZHOU, X., 2013. Bragg diffraction of a matter wave driven by a pulsed nonuniform magnetic field. *Phys. Rev. A*, 88 (Nov 2013), 053629. doi:10.1103/PhysRevA.88.053629. <http://link.aps.org/doi/10.1103/PhysRevA.88.053629>. (cited on page 98)
250. ZHOU, M.-K.; PELLE, B.; HILICO, A.; AND PEREIRA DOS SANTOS, F., 2013. Atomic multiwave interferometer in an optical lattice. *Phys. Rev. A*, 88 (Jul 2013), 013604. doi:10.1103/PhysRevA.88.013604. <http://link.aps.org/doi/10.1103/PhysRevA.88.013604>. (cited on page 97)